Connecting Internal and Surface Properties of Massive Stars

Author:

Eoin Farrell

Supervisor:

Prof. Jose Groh

A thesis submitted for

PhD in Astrophysics

2022

Summary

Massive stars have an important impact on the universe. They are responsible for the generation of many of the chemical elements such as oxygen and silicon. They can produce core collapse supernovae which impact the chemical enrichment of the interstellar medium and galaxies, triggering of star formation and release of energy into the surroundings. They also produce neutron stars and black holes which can merge in binary systems and emit detectable gravitational waves. The evolution of massive stars is affected by a variety of physical processes including convection, rotation, mass loss and binary interaction. Because these processes modify the internal chemical abundance profiles in multiple ways simultaneously, it can be challenging to connect the properties of the internal abundance profile to the location in the HR diagram.

We developed a new stellar modelling approach called SNAPSHOT that allows us to systematically compute stellar structure models in hydrostatic and thermal equilibrium. Using our approach, we computed numerical stellar structure models in thermal equilibrium covering key phases of stellar evolution. We applied our SNAPSHOT method to explore several topics. We first studied the properties of red supergiants and of stars stripped of their envelopes in binary systems and constrained the mass of one of these stripped stars in a binary system, HD 45166. Second, we investigated the connections between the surface properties and the masses of progenitors of core collapse supernovae and direct collapse black holes. Finally, we constructed a series of numerical experiments to isolate the key features of the internal abundance profile that drive the evolution of massive stars. We discussed why massive stars expand after the main sequence and the fundamental reasons for why they become red, blue or yellow supergiants.

We also conducted several other investigations into other aspects of stellar evolution. We investigated the possibility that Following the observation of a surprisingly massive 85 $M_\odot$ black hole in the binary black hole merger GW190521 by the LIGO Virgo Collaboration, we investigated whether such a black hole could be produced by the first stellar generations. Our models suggested the possibility of black hole masses of up to 75 $M_\odot$, but uncertainties related to convective mixing, mass loss, H-He shell interactions and pair-instability pulsations could increase this limit to 85 $M_\odot$. Secondly, we investigated the impact of binary interaction on the evolution of blue supergiants and how this affects the use of these stars for distance determination. Finally, we combined observations with theoretical models of magnetic field evolution to infer the initial distribution of magnetic fields for 1.4 - 3.4 $M_\odot$ AB stars. We inferred an initial field distribution with a mean of ~ 800 G and a width of ~ 600 G.

Acknowledgements

First, I have been very lucky to have an excellent supervisor, Jose Groh. Thank you so much for the constant support and encouragement, and for all the interesting discussions along the way! Thanks to Georges Meynet for hosting me on my visits to Geneva and for your inspiration and help in our collaborations together. To my other collaborators, JJ Eldridge, Rolf Kudritzki, Sung-Chul Yoon, Raphael Hirschi and Etienne Kaiser, thank you for all the advice and guidance. Thanks to everyone at the Geneva Observatory for making my visits there enjoyable experiences, especially to Sylvia Ekström, Cyril Georgy, Sébastien Martinet, Camilla Pezzotti, Manos Zapartas and Arthur Choplin. Thanks to Adam Jermyn and Matteo Cantiello for making my remote internship at the CCA so enjoyable and insightful. Thanks to Rich Townsend for the help and supervision during the summer internship program at the Flatiron Institute. Thanks also to the Simon's Foundation for funding my research at the CCA. Thanks to Ioana, Laura and Andrew for creating such an enjoyable research group to be a part of. Finally, to Dúalta, Stephen, Rob, Amanda and Maxime, thanks for making the office a fun place to be.

List of Publications

First-authored publications

1. **Eoin Farrell**, Jose Groh, Georges Meynet, JJ Eldridge, *The uncertain masses of progenitors of core-collapse supernovae and direct-collapse black holes*, MNRAS Letters, 494, 1, 53, May 2020
2. **Eoin Farrell**, Jose Groh, Georges Meynet, JJ Eldridge, Sylvia Ekström, Cyril Georgy, *SNAPSHOT: connections between internal and surface properties of massive stars*, MNRAS, 495, 4, 4659, July 2020
3. **Eoin Farrell**, Jose Groh, Raphael Hirschi, Laura Murphy, Etienne Kaiser, Sylvia Ekström, Cyril Georgy, Georges Meynet, *Is GW190521 the merger of black holes from the first stellar generations?*, MNRAS Letters, 502, 1, L40, March 2021
4. **Eoin Farrell**, Jose Groh, Georges Meynet, JJ Eldridge, *Numerical experiments to help understand understand the evolution of massive stars*, MNRAS submitted
5. **Eoin Farrell**, Adam Jermyn, Matteo Cantiello, Dan Foreman-Mackey *The initial fossil field distribution for AB stars*, ApJ in prep.
6. **Eoin Farrell**, Jose Groh, Georges Meynet, Rolf Kudritzki, JJ Eldridge, Cyril Georgy, Sylvia Ekström, Sung-Chul Yoon *Impact of binary interaction on the evolution of blue supergiants. The flux-weighted gravity luminosity relationship and extragalactic distance determinations*, A&A 621, A22, Jan. 2019

Co-authored publications

7. Jose Groh et al. (including **Eoin Farrell**), *Grids of stellar models with rotation - IV. Models from 1.7 to 120*$M_\odot$ *at Z=0.0004*, A&A, 627, A24, July 2019
8. Jose Groh, **Eoin Farrell**, Georges Meynet, Nathan Smith, Laura Murphy, Andrew Allan, Cyril Georgy, Sylvia Ekström, *Massive Black Holes Regulated by Luminous Blue Variable Mass Loss and Magnetic Fields*, ApJ, 900, 2, 98, Sept. 2020
9. Daria Kubyshkina et al. (including **Eoin Farrell**), *Coupling thermal evolution of planets and hydrodynamic escape in MESA*, MNRAS, 499, 1, 77, Nov. 2020
10. Sébastien Martinet et al. (including **Eoin Farrell**) *Convective core sizes in rotating massive stars. I. Constraints from solar metallicity OB field stars*, A&A, 648, A126., April 2021

11. Patrick Eggenberger et al. (including **Eoin Farrell**) *Grids of stellar models with rotation - VI. Models from 0.8 to 120*$M_\odot$ *at a metallicity Z=0.006*, A&A, 652, A137, Aug. 2021
12. Laura Murphy et al. (including **Eoin Farrell**) *Grids of stellar models with rotation - V. Models from 1.7 to 120* $\mathrm{M}_\odot$ *and zero metallicity*, MNRAS, 501, 2, 2745, Feb. 2021
13. Laura Murphy, Jose Groh, **Eoin Farrell**, Georges Meynet, Sylvia Ekström, Sophie Tsiatsiou, Alexander Hackett, Sébastien Martinet *Ionizing photon production of Population III stars: effects of rotation, convection, and initial mass function*, MNRAS, 506, 4, 5731, Oct. 2021
14. Maxime Deckers, Jose Groh, Ioana Boian, **Eoin Farrell** *The origins of low-luminosity supernovae: the case of SN 2016bkv*, MNRAS, 507, 3, 3726, Nov. 2021
15. Norhasliza Yusof et al. (including **Eoin Farrell**) *Grids of stellar models with rotation - VII. Models from 0.8 to 300*$M_\odot$ *at super-solar metallicity (Z=0.020)*, accepted in MNRAS

Contents

Chapter 1

Introduction

1.1 Thesis Motivation

Stars are highly relevant for our overall understanding of the universe. Massive stars are responsible for the generation of many of the chemical elements such as oxygen and silicon. They have an important impact on the evolution of galaxies and of the universe and on cosmic re-ionisation. Mergers of the remnants of massive stars in binary systems emit gravitational waves. The study of exoplanets and their environments depends on our understanding of low mass stars. Stars are vital for distance measurements which are important for all areas of astrophysics. They are also interesting environments to understand from a physics standpoint because all four fundamental forces are relevant: gravity, electromagnetism and the strong and weak nuclear forces.

A century of research has produced well-established descriptions of how stars evolve. However, many interesting challenges and observations continue to spark new research. Some of these open directions include: What are the formation channels for binary black hole systems detected by LIGO/Virgo? Which massive stars produce which transients? What are the important evolutionary sequences for massive stars as a function of mass and metallicity? What are the internal differences between blue and red supergiants? What is the origin of magnetic fields in stars and the distribution of initial magnetic field strengths? Making progress towards answering these questions requires a detailed understanding of stellar structure and evolution.

Stars are challenging to understand and study for several reasons. The conditions inside a star are extreme, with a large range of pressures, temperatures and densities, turbulent mixing, lots of difficult physics (including nuclear reactions) and broad range of relevant timescales. These complex, uncertain physics can make them extremely difficult to model, as well as numerical challenges relating to the highly non-linear nature of the equations of stellar structure. In addition, it is difficult to obtain direct observational data about stellar interiors, so we are mostly left with trying to observe the surface properties of stars. Unfortunately, observational samples are often limited in size and incomplete, especially for massive stars. This can make it very difficult to draw definitive conclusions and can bias our view in a particular direction before subsequent detections change the picture. However, it is these challenges that make stars interesting and exciting to study!

One of the key tools used to study the interiors of stars and understand how they change in time is one-dimensional stellar evolution models. These models allow us to infer what the interiors of stars look like based on the surface properties. Outputs from the models can help to provide physical explanations for astronomical observations, based on our general understanding of the laws of physics and other astronomical observations. The research in this thesis uses state-of-the-art stellar evolution models, and develops a new stellar modelling technique (SNAPSHOT), to study the connection between stellar interiors and surface properties, understand the properties of red supergiants at the pre-supernova stage, distinguish cause and effect in stellar evolution, suggest a plausible astrophysical formation scenario for an 85 $M_\odot$ black hole and to infer the initial fossil field distribution of intermediate mass stars.

1.2 Evolution of Massive Stars

Stars exist in a mechanical equilibrium between the inward gravitational force, set by the mass, and the outward pressure, set by the properties of the gas and the radiation field. As a result, the mass strongly affects the equilibrium structure and the resulting internal temperature and density profiles. Stars that are massive enough to burn carbon are classified as 'massive stars'. They have initial masses of $\gtrsim 8$ $M_\odot$ and undergo a very different evolution to lower mass stars.

As well as being interesting to study because of their complex, extreme environments, massive stars have a wide variety of impacts on the rest of the universe. The evolution of massive stars is a key driver of the overall abundance of the elements as a function of time in the universe and the population of the periodic table. Throughout their evolution, the interiors of massive stars are hot enough to generate many of the chemical elements up to ^{56}Fe (e.g. Arnett, 1978; Woosley & Weaver, 1995). These elements are released into the surroundings by stellar winds and eruptions. The deaths of massive stars in core collapse supernovae are dramatic and explosive, releasing large quantities of energy and material into the galaxy and also drive further nucleosynthesis. Core collapse supernovae can leave behind neutron stars, which can later merge and drive further nucleosynthesis (Abbott et al., 2017a,c) and black holes, which can emit gravitational waves in mergers (Abbott et al., 2016d). Massive star feedback in the form of chemical elements, ionising radiation and kinetic energy drives the evolution of galaxies (Vogelsberger et al., 2014). Therefore, to fully capture the processes that are necessary for modelling the evolution of galaxies, an understanding of massive star evolution is vital.

It is generally thought that the massive stars were a significant source of cosmic reionisation in the intergalactic medium (Haiman & Loeb, 1997; Haehnelt et al., 2001; Loeb & Barkana, 2001; Faucher-Giguère et al., 2008, 2009; Conroy & van Dokkum, 2012; Becker

& Bolton, 2013; Wise et al., 2014) Massive stars in binary systems with stripped envelopes can be important sources of ionising photons, which has implications for the cosmological history of the universe and the evolution of galaxies (e.g. Götberg et al., 2017, 2020). Through their stellar winds, massive stars trigger the formation of new stars (Elmegreen, 2011). Massive stars produce gamma-ray bursts and pair-instability supernovae which might be probes of the early universe (Savaglio et al., 2009; Tanvir et al., 2009; Cucchiara et al., 2011; Whalen et al., 2013; Kozyreva et al., 2014). Some massive stars undergo pulsations in their envelope which result in explosive eruptions that release tens of solar masses of material into the interstellar medium. Their high luminosities also mean they can be used to measure distances, which is vitally important for all areas of astrophysics (e.g. Kudritzki et al., 2003, 2012). Massive stars are also the precursors to the black holes and neutron stars which produce gravitational waves that are observed by the Ligo/Virgo Collaboration. Massive stars are more luminous that low mass stars because they need to produce a higher luminosity for support against gravity. The scaling of the luminosity L with the mass M on the main sequence, L$\propto M^3$, means that, despite being significantly outnumbered, they can outshine lower mass stars in clusters and galaxies.

Despite their importance, massive stars are relatively rare compared to low mass star. Only about 1% of stars are born with an initial mass of > 8M$_\odot$ (Salpeter, 1955; Scalo, 1986; Kroupa, 2001; Chabrier, 2003). This is a consequence of star formation processes, in which higher radiation pressure is expected to hinder accretion (Tan et al., 2014; Krumholz, 2015; Motte et al., 2018). Massive stars also have much shorter lifetimes than low mass stars. For example, a 1 M$_\odot$ star has a lifetime of around 10^{10} yr, compared to 10^7 yr for a 16 M$_\odot$ star. The combined effect of the initial mass function and their shorter lifetimes means there are far fewer massive stars than lower mass stars in the universe. The intrinsically small numbers of massive stars make it very challenging to obtain large and complete sample sizes. This makes them difficult to understand and requires significant efforts to model. The challenge of understanding how they work and putting together the limited available information to form a cohesive overall picture of massive star evolution is part of the fun of it all. Our current overall picture of massive star evolution is summarised in Sec. 1.2 and 1.3 below.

1.2.1 Main Sequence

Stars evolve because of changes in their internal chemical abundances, ultimately driven by nuclear fusion. The most common way to represent the evolution of the surface properties of stars is the Hertzsprung-Russell (HR) diagram (Hertzsprung, 1911; Russell, 1914a). Fig. 1 presents classical evolutionary tracks in the HR diagram for massive single star models with masses ranging from 9 to 120 M$_\odot$ at solar metallicity (Z = 0.020) with and without rotation from Meynet & Maeder (2000).

The core hydrogen burning phase is the first and longest phase in a star's evolution. Stars in this phase form a band that extends across the HR diagram known as the Main

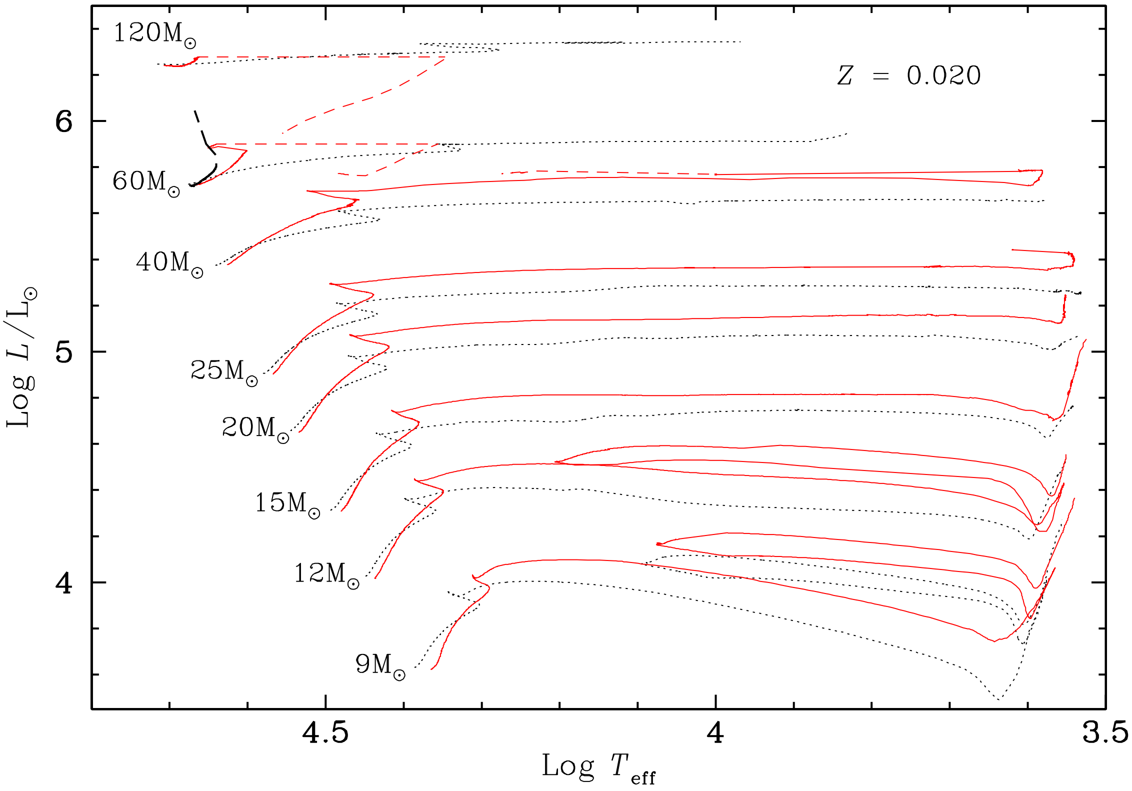

Figure 1: Evolutionary tracks in the Hertzsprung-Russell diagram for single star models (Meynet & Maeder, 2000) at solar metallicity. Dotted black lines indicate non-rotating models and solid red lines indicate rotating models with an initial velocity of $v_{\rm ini}$ = 300 km s^{-1}. Short–dashed lines indicate a Wolf-Rayet phase. Long–dashed 60 M$_\odot$ track indicates a MS rotating model with $v_{\rm ini}$ $\sim$ 400 km s^{-1}.

Sequence (MS). For this reason, the core hydrogen burning phase is often referred to as the MS phase. Stars typically spend about 90% of their total lifetime in their MS phase, during which they convert hydrogen into helium by nuclear fusion reactions in their cores. In massive stars, the nuclear burning takes place in a convective core via a series of reactions described by the carbon-nitrogen-oxygen (CNO) cycle. This is in contrast to low mass stars that burn hydrogen via the proton-proton (PP) chain reactions and have radiative cores. During the MS phase, massive stars generally fall into the O-type or B-type spectroscopic classifications. Some more massive MS stars close to the Eddington limit with strong stellar winds are classified as WNh stars (de Koter et al., 1997).

The evolution during the MS phase has a very important impact on the structure of the star in later evolutionary phases. The mass of the convective core and the internal hydrogen profile left behind after the MS determine the helium core mass which sets the subsequent evolution beyond core hydrogen burning. Relatively small changes in the MS phase can have large impacts on the stellar structure and evolution in later evolutionary phases. Therefore, a detailed, quantitative understanding of the MS phase is critical to building on overall picture of stellar evolution.

In the absence of strong amounts of internal mixing or mass loss, massive stars increase in luminosity and expand during the MS phase. L increases by ~ 0.2 dex and T_{eff} decreases by ~ 0.1 dex as they evolve upwards and to the right in the HR diagram (Fig. 1). These changes in L and T_{eff} are ultimately a consequence of the changes in the mean molecular weight in the core, μ_{core}, as hydrogen is converted to helium by nuclear fusion. The increase in μ_{core} causes an increase in the temperature and density in the core, through the equation of state, which increases the rate of energy generation. This increase in the luminosity from nuclear burning, L_{nuc}, relative to the luminosity that the envelope can transport, L_{actual}, causes the star to expand. The increase in the surface luminosity L is a result of the increased rate of energy generation in the core. The combined increase in L and R cause the decrease in T_{eff}.

The conversion of hydrogen to helium in the core and the evolution to higher L and T_{eff} continues until about 5% of the hydrogen remains in the core. At this point, the entire star contracts, causing the star to evolve to the left in the HR diagram (Fig. 1). This creates a kink in the evolutionary tracks known as the Henyey hook. hook is caused by the decrease in the central fuel supply, which decreases luminosity from nuclear burning. The total surface luminosity continues to increase due to the additional energy released from the gravitational contraction in the outer layers of the star. As the star contracts and heats up, the increase in temperature just above the hydrogen-depleted core forms a new nuclear burning region - a hydrogen burning shell. During the evolution to the left in the HR diagram, the star burns the remaining hydrogen in its core, marking the end of the core hydrogen burning phase. The star will now leave the MS and evolve elsewhere in the HR diagram as it goes through several further nuclear burning phases.

The evolution during the MS phase can be affected by several factors. Stars of lower metallicity are more compact and have a higher L and T_{eff} at the beginning of the MS phase. The effect of metallicity on stellar structure of stars at this mass is composed of two significant components, the CNO abundance in the core and the metal abundance in the envelope. A lower metallicity also causes a lower mass loss rate, which can significantly alter the evolution during this phase. Very strong internal mixing in MS stars due to e.g. rotation, convection or binary interaction, can result in chemically homogenous evolution (CHE). In these stars, helium is mixed from the core to the outer layers and hydrogen is mixed into the core. The decreased opacity of helium compared to hydrogen in the outer layers can cause the star to contract and evolve to the left in the HR diagram. Models with fast rotation can reproduce observations of stars to the left of the ZAMS in the HR diagram (e.g. 60 $\mathrm{M}_{\odot}$ $v_{\mathrm{ini}} \sim 400$ km s^{-1} model in Fig. 1 or the blue evolutionary tracks in the upper HR diagram in Fig. 2. This is a classical result from stellar evolution (e.g. Maeder, 1987, 2009).

The evolution of L and T_{eff} during the MS can be described in a simplified way by considering the equations of stellar structure and using the assumption of homology. Homology assumes that going from one stellar model to another, all mass shells are compressed or expanded by the same factor. Under this assumption, one can show that L and

R depend on the mass M and μ such that $L \propto M^3\mu^4$ and $R \propto M^{0.78}\mu^{0.61}$ for massive stars (e.g. Kippenhahn & Weigert, 1990; Maeder, 2009).

While the MS evolution is relatively simple compared to the later evolutionary phases, there are important uncertainties and open questions that have consequences for the MS phase and beyond. First, the convective core mass of massive MS stars are uncertain due to uncertainties in convective boundary mixing and rotational mixing. This is important as the MS convective core mass determines the helium core mass during the post-MS, which sets the subsequent evolution and the final fate. As the convective core masses cannot be computed a priori using 1D stellar evolution models, the free parameter $\alpha_{\rm ov}$ is used to parameterise the extent of convective overshooting. In non-rotating models, $\alpha_{\rm ov}$ acts a de-facto parameterisation of the convective core mass on the MS. The evolution of the convective core mass affects the location of the right-most point in the HR diagram, known as the terminal-age main sequence (TAMS). Another significant uncertainty during the MS phase is the amount of mass that is lost by stellar winds (Vink et al., 2001). The mass loss rates for these hot OB stars have been uncertain for some time (Smith, 2014) although there has been much recent work in that direction may help reduce uncertainties (Vink & Sander, 2021). MS mass-loss rates can have a significant impact on the evolution in the HR diagram during the MS phase and also the final remnant masses. Rotation also alters the position of evolutionary tracks, and the location of the TAMS. Fig. 1 shows that the evolutionary tracks in the HR diagram are different for rotating models vs. non-rotating models. For example in Fig. 1, the rotating models at the TAMS have a higher luminosity than the non-rotating models. Rotation may boost stellar wind mass loss if the angular momentum transport within the star is efficient enough. There are also feedback effects, for example rotation can boost the luminosity which can affect mass loss rates.

Even for the relatively simple MS phase, current grids of stellar evolution models have some difficulty reproducing observations in the HR diagram. For instance, the width of the MS is different in observations and models. There are many efforts to use observations to constrain the convective boundary mixing and rotational mixing, but it is a complex problem (e.g. Maeder, 1974; Castro et al., 2014, 2018; Martinet et al., 2021; Scott et al., 2021). Another example is that observations of the location of the zero-age main sequence in the HR diagram appear to be inconsistent with standard stellar evolution models (Holgado et al., 2020).

1.2.2 Post Main Sequence

The evolution of massive stars after the main sequence phase is complicated and many aspects are not fully understood. Despite accounting for only about 10% of stars, the post main sequence evolutionary phases produce the majority of the different types of massive stars. The diversity in surface properties is caused by variation in the stellar interior, driven by many different physical processes, including nuclear burning, convection, rotation, mass loss and binary interaction (Langer, 2012). The well accepted picture of post-MS evolution is outlined below.

The post main sequence evolution begins after core hydrogen depletion causes the entire star to contract, forming a hydrogen burning shell above the hydrogen depleted core. Due to the feedback effect of nuclear burning, the hydrogen burning shell acts to limit any further contraction in its vicinity (Maeder et al., 2009). As the core cannot produce nuclear energy to support itself, it must contract. The core contraction has two main effects. Firstly, it converts the core's gravitational potential energy partly to internal energy and partly to the luminosity which supports the core. The total energy (gravitational + internal) of the core drops. Secondly, the contraction of the core also changes the hydrostatic structure of the star, increasing the temperature and density at the base of the hydrogen-shell burning region. This increases the rate of nuclear energy generation in the shell. The extra energy produced in the shell cannot be transported by the envelope in a timescale shorter than the core contraction timescale, so it goes into the envelope causing it to cool and expand. The expansion proceeds on the Kelvin-Helmholtz (KH) timescale of the core. The cooling and expanding of the envelope is reflected in the evolution of the star across the HR diagram to form a blue or red supergiant (Fig. 1). When the central temperature and density are high enough to burn helium via the triple-alpha reaction, the core stops contracting. This stops the increase in temperature and density at the base of the hydrogen burning shell. As a result, the envelope stops expanding and the star begins to evolve on a nuclear burning timescale once more. Massive stars typically expand by factors of 10 - 100 during this post-MS expansion phase.

During core helium burning, massive stars burn helium via two main reaction pathways. The first the triple alpha reaction. This is a series of reactions which convert three ^{4}He particles to a ^{12}C nucleus. The second is the carbon alpha-capture reaction $^{12}C(\alpha,\gamma)^{16}O$ in which a ^{12}C nucleus and an alpha particle combine to produce an ^{16}O nucleus. As a result of these two reactions, ^{12}C and ^{16}O build up in the core throughout core helium burning. Core helium burning typically accounts for about 9% of the total stellar lifetime. After core helium is exhausted, the core contracts once again and core carbon burning begins. At this point, a helium burning shell often forms around the helium depleted core. The remaining burning phases account for the remaining 1% of the stellar lifetime. From this point onwards, the core is hot enough for neutrino pair emission to become significant ($> 3 \times 10^8$K) and stars produce a large fraction of their luminosities in neutrinos. As neutrinos do not really interact with the star, they act as an energy sink and remove energy from the star. After core carbon burning, the core is composed of a mixture of oxygen, neon and magnesium. Following a contraction, the core undergoes neon photo-disintegration which converts ^{20}Ne to ^{16}O via emission of an alpha particle. The next burning phase is oxygen burning which produces ^{28}Si and ^{32}Si and lasts about 3 months. Finally, silicon is fused to form the iron group elements including ^{56}Fe. At this point, the star enters its final stages before core collapse.

Depending on a variety of factors, massive stars can evolve to become blue, yellow or red supergiants, go through an LBV phase, lose their envelope and become Wolf-Rayet stars or several of the above. The most important of these factors is the mass, the effect of which can be seen in the HR diagram in Fig. 1. For instance, the 15 $M_\odot$ model expands across the HR diagram after the MS and begins core helium burning as a RSG. It remains a RSG for the rest of its lifetime and will explode in a type II-Plateau (II-P) supernova. The 9 $M_\odot$ model exhibits a similar expansion to the beginning of core helium burning but then exhibits a loop in the HR diagram during the core-helium burning phase, first back towards higher $T_{\rm eff}$ and then back to lower $T_{\rm eff}$ These loops are caused by a change in the helium profile above the hydrogen core (Lauterborn et al., 1971a; Walmswell et al., 2015) The evolutionary tracks for these loops pass through the Cepheid instability strip. These blue loops can serve as key comparisons between observations of Cepheids and stellar evolution models. At higher masses, the 25 and 40 $M_\odot$ rotating models also become RSGs after the MS. However, due to strong mass loss in the RSG phase, they subsequently evolve back towards the blue region of the HR diagram. The 40 $M_\odot$ model becomes a Wolf-Rayet star. At even higher masses, e.g. the 60 and 120 $M_\odot$ models do not even become RSGs.

At these masses, increased radiation pressure modifies the efficiency of energy transport in convective regions of the envelope. This change in stellar structure limits the radius and, in addition to mass-loss effects prevent the star from expanding to become a RSG. The structure of the envelope in radiation dominated convective envelopes is very uncertain and one of the major uncertainties in stellar models.

Rotation can have a significant impact on the post-MS evolution. Rotating models tend to have higher luminosities during the post-MS (Fig. 1). This is caused by their larger helium core masses produced by enhanced mixing during the MS. Rotational mixing affects the helium profile in the hydrogen shell which is a key property that affects L and $T_{\rm eff}$. For example, this causes the 12 $M_\odot$ rotating model in Fig. 1 to exhibit a blue loop, while the non-rotating model does not. Rotating models can also undergo enhanced mass loss due to rotationally-induced mass loss and stronger stellar wind mass loss rates as a result of the higher luminosities.

The metallicity of the star can have a significant effect on post-MS evolution in the HR diagram and on the structure of the envelope. The metallicity impacts the surface properties both directly and indirectly. The direct impact comes in two components: (i) the effect of opacity in the envelope and (ii) the effect on the CNO abundances in the hydrogen burning shell. Metallicity also has several indirect impacts. The most significant of these is that mass loss by stellar winds is significantly reduced a lower metallicities. For example, a 60 $M_\odot$ non-rotating model can lose 80 % of its mass at solar metallicity compared to 25% of its mass at Z = 0.004 and 0% at Z = 0 (e.g. Ekström et al., 2012; Groh et al., 2019; Murphy et al., 2021). The change in mass as a function of time has a significant feedback effect on its overall evolution.

There are several other factors that affect the post-MS evolution of massive stars, each of which could be the subject of a PhD thesis on its own. A few of these are summarised below: Interaction with a binary companion can result in many different evolutionary pathways. Mass loss to a binary companion via Roche-Lobe Overflow (RLOF) can can cause stars to lose their hydrogen envelope and thus evolve to the blue region of the HR diagram producing stripped stars (Götberg et al., 2017) and possibly WR stars (Sander et al., 2020). Common envelope evolution may lead to the ejection of the envelope of a star, resulting in a hot stripped star. Stellar mergers may produce massive blue supergiants (Schneider et al., 2014). The proximity to the Eddington limit also impacts post-MS evolution (Agrawal et al., 2021b,a) It is possible that the high luminosities of massive stars may cause an inflation of the envelope to very large radii and a large variation in the effective temperature (Gräfener et al., 2012). Conti (1975) proposed a standard evolutionary picture for the evolution of massive stars above 30 $M_{\odot}$. They evolve from OB-type stars, go through a short-lived LBV phase lose mass to become WR stars before exploding in a core collapse supernova. The discover that most massive stars exist in binary systems (Sana et al., 2012) has changed the paradigm on the overall evolutionary scenarios for post-MS massive stars and it remains highly uncertain.

1.2.3 Final Stages

There are currently thought to be several possibilities for the final fate of massive stars, depending on the mass, density structure and composition of the core. Most massive stars explode in core collapse supernovae. While the details of how the star actually explodes are uncertain, the following is believed to occur: An $\sim 1M_{\odot}$ iron core is formed by the end of silicon burning. Due to thermodynamics of the nuclear structure, no further exothermic nuclear fusion reactions can occur with iron nuclei. At this point, the iron core is supported by electron degeneracy pressure. Iron and helium nuclei disintegrate by high energy photons. The electrons that supported the star against gravity are captured by photons, the star loses pressure support and the core collapses. The collapse of the core takes about 1 second. As it is compressed by gravity, the core reaches a density similar to an atomic nucleus and stiffens. As a result, the collapsing material rebounds and produces a shockwave that travels outwards through the star. The shockwave stalls after 10s of milliseconds as the outflowing gas meets the inflowing material. Most of the energy emitted during the supernova is in the form of neutrinos. These neutrinos travel outwards from the core and transfer some of their energy to allow the stalled shockwave to be revived and facilitate a successful explosion. The shockwave then propagates to the surface, expelling a significant amount of energy into the surroundings producing a core-collapse supernova. After the collapse and explosion, the remains of the core forms a neutron star or black hole depending on their mass. Neutron stars have been observed at the centre of supernova remnants providing a definitive link between the two. Neuton stars and black holes are now routinely observed merging in binary systems via their gravitational wave emission (The LIGO Scientific Collaboration et al., 2021c).

While most massive stars are expected to produce a core-collapse supernova, depending on their mass and internal structure, some might collapse directly to black holes. This has been postulated to occur following so-called 'failed supernova' in which insufficient energy is supplied to the envelope of the star and the entire mass of the star collapses inwards onto the newly formed compact remnant. Some higher mass stars ($\gtrsim 60\mathrm{M}_{\odot}$) are expected to experience a pair-instability in their cores. This pair-instability is caused by the creation of electron-positron pairs which can cause the core to lose support, the temperature to increase, causing greatly accelerated oxygen burning in a runaway process. This can cause a pulsational pair instability supernova or a pair instability supernova. Observational evidence for these supernovae is difficult to find, although several candidates exist (e.g. Gal-Yam et al., 2009)

1.2.4 Classical Studies in Massive Star Evolution

The current description of massive star evolution is the result of many decades of observational and theoretical work. It is worth understanding the key studies and developments to understand how the field of stellar physics got to where it is today.

The first distance to a star (61 Cyg) was measured using parallax by Bessel (1838) who recorded a distance of about 11 lightyears, in good agreement with current distance estimates. As the knowledge of physics advanced through the end of the 1800s, there was much speculation about what stars and how they work. Early studies of stellar structure and evolution were limited by lack of observations and a poor understanding of the relevant physics of stellar interiors (e.g. Emden, 1907). However, an improvement in observational samples, progress in other areas of physics and the development of computers that could compute detailed stellar models allowed the development of the theories of stellar evolution that we have today. One of the first analyses to start this was a detailed analysis and classification of a sample of stellar spectra of in the northern sky by Maury & Pickering (1897), later extended to the southern sky by Cannon & Pickering (1901). These studies led to the analysis of the relationship between the luminosity and effective temperature of stars (Hertzsprung, 1905, 1907) and published in the form of what is now called a Hertzsprung-Russell diagram first by Rosenberg (1910) and then by Hertzsprung (1911) for stars in the Pleiades and Hyades clusters. Independently, Russell (1914a) published the same type of diagram using a much larger sample of stars. The development of the Hertzsprung-Russell (HR) diagram was a key step in putting together a picture of stellar evolution as it allowed different types of stars to be distinguished. Around this time, there was much speculation and debate on the order of stellar evolution. Many attempts were made to build an overall picture of stellar evolution (Russell, 1914b; MacMillan, 1918; Russell, 1925; Jeans, 1925). Eddington (1924) worked on the internal structure of stars and produced a mass-luminosity relationship for stars assuming an ideal gas. This relationship was compared to the observed relationship. This comparison might be one of the first successful comparisons between observations and a theoretical understanding of stellar structure. However, most of the relevant information needed to build that picture was still unavailable. It was widely thought at the time that stars began their lives as red giants and evolved down the main sequence, which we now know is the exact opposite to how they actually evolve. There were many works throughout this time trying to understand the internal structure of stars (Emden, 1907; Eddington, 1926; Emden, 1927; Cowling, 1935; Hoyle & Lyttleton, 1942). However, all of this was made extremely difficult by the fact that the source of energy production in stars was unknown.

The first suggestions that the fusion of hydrogen to helium is the source of energy in the sun was made by Eddington (1920) and Perrin (1922). During in the 1930s, it became clear that the stars produced energy by converting hydrogen to helium via nuclear reactions. Detailed explanations of the proton-proton chain (von Weizsacker, 1938) and the CNO cycle (Bethe, 1939) were produced. Bethe received the Nobel Prize in physics in 1967, partly for this discovery. This prompted new investigations into the overall picture of stellar evolution (Gamow, 1938, 1939a,b; Gamow & Schoenberg, 1941; Schönberg & Chandrasekhar, 1942). Due to the lack of detailed stellar models, the details of the evolution of the stellar interior were still relatively speculative. For example, it was unclear what fraction of the star was available for nuclear burning. Stellar physics advanced over the next two decades with a range of advances from both observations and theory. The importance of rotation in stars was investigated (Sweet, 1950; Mestel, 1953). Böhm-Vitense (1958) introduced mixing length theory for modelling convection in stars. New methods to solve the equations of stellar structure were developed (Hoyle, 1945). Nuclear reactions in stars and nucleosynthesis were further detailed (Cameron, 1957; Hoyle, 1954). Hoyle (1954) improved the understanding of nucleosynthesis in stars and predicted the existence of a resonant reaction, the triple alpha reaction. Advances in observations and larger sample sizes (e.g. Johnson & Hiltner, 1956; Johnson & Mitchell, 1958; Sandage & Eggen, 1959) provided more information that was previously available. The initial mass function for stars was inferred from observations by Salpeter (1955). New pictures of stellar evolution were suggested (Hoyle & Schwarzschild, 1955; Schwarzschild & Härm, 1958; Schwarzschild, 1958; Eddington, 1959). Hoyle & Schwarzschild (1955) produced a paper of the full evolution of low mass stars through the main sequence, through to the tip of the red giant branch. Burbidge et al. (1957) described all the known nuclear reactions that occur in stars from hydrogen burning up to the later burning phases in massive stars and proposed that all elements above lithium were once synthesised in stellar interiors and released into space by supernovae and stellar winds. Fowler and Chandrasekhar received the Nobel Prize in 1983 for these advances in the theory of stellar evolution.

All of these advances in understanding of stellar interiors and the development of computers allowed the construction of more detailed stellar evolution models through the 1950s and 1960s. Many of these papers made important contributions to the fundamentals of stellar evolution with a surprising amount of accuracy given the nature of their models and the computational power available. Some of these findings are discussed below. Sandage

& Schwarzschild (1952) computed models to show that stars expand rapidly at the end of the main sequence after core hydrogen exhaustion, consistent with observations of the main sequence, the red giant regions in the HR diagram and the turnoff from the MS in the HR diagram of globular clusters.

> *"As the cores contract, the envelopes greatly expand. From the initial configuration, which is near the main sequence, the stars evolve rapidly to the right in the H-R diagram, amply covering the giant region. A comparison of this theoretical evolution with the observed H-R diagram for globular clusters appears to explain the sudden turnoff from the main sequence to the giant region".*

Härm & Schwarzschild (1955) studied the impact of the distribution of chemical composition within the star, compared to models with a discontinuous jump in composition, and pointed out the following.

> *"The variation of the composition throughout the interior has to be determined in fair detail by considerations of the evolution, before the radius can be computed with sufficient accuracy to warrant comparison with observed radii or effective temperatures."*

Schwarzschild et al. (1957) computed a solar model to compare to observations of the sun and concluded that

> *"a pronounced inhomogeneity in composition must exist in the present sun."*

The amount of information that early, quite simplified stellar evolution models were able to provide is impressive.

The main sequence phase was studied using a range of stellar evolution models and compared to observations (e.g Tayler, 1954; Kushwaha, 1957; Reiz & Otzen Petersen, 1964; Sakashita et al., 1959). For MS models, Sakashita et al. (1959) found that

> *the convective core retreats as its hydrogen content decreases, setting up the intermediate zone of continuously varying composition and a thin convective unstable region between the radiative envelope and the intermediate zone*

The difficulties of understanding the post-MS evolution of massive stars in the HR diagram were realised by Hayashi et al. (1959). Hayashi & Cameron (1962) found that the principle effect of mass loss on a red supergiant model to be a very slightly lowering of the effective temperature.

Henyey et al. (1959b) presented a new method for computing stellar evolution models using *"high-speed digital computers"* (later updated in Henyey et al., 1964). They described a method for solving the equations of stellar structure and evolution:

> *"A method is described for obtaining time sequences of stellar configurations automatically by means of high-speed digital computers. The time-dependent*

> *differential equations of stellar structure are replaced by second-order difference equations. These nonlinear difference equations, together with the boundary conditions, are solved by an iterative method which is a generalization of the Newton-Raphson method for obtaining roots of functions."*

This is the underlying method used to compute stellar evolution models today. Their method was used to compute an evolutionary model specific to Sirius (Henyey et al., 1955).

Henyey et al. (1959b) produced a detailed analysis of the main sequence phase over a wide range of stellar masses (1.5 to 30 $M_\odot$) by computing the first such grid of stellar evolution models and comparing to observations in the HR diagram. The evolution of massive O-type stars was investigated in a new series of models for the main sequence phase (Stothers, 1963), the expansion after the main sequence (Stothers, 1964) and the helium burning phase (Stothers, 1966). Stothers (1964) and Stothers (1966) made great effort to understand the post-MS evolution of the 30 $M_\odot$ star in the HR diagram. Henyey et al. (1965) discuss the challenges of modelling stellar envelopes.

As the understanding of the importance of mass loss became important, stellar evolution models were computed to study the impact of mass loss on the evolution. Stellar evolution models showed that mass loss can modify the location of the terminal-age MS in the Hertzsprung-Russell (HR) diagram (Forbes, 1968; Chiosi & Nasi, 1974; Chiosi, 1986; Meynet et al., 1994; De Loore et al., 1977; Chiosi et al., 1978). They also found that higher mass loss favours a lower $T_{\rm eff}$ during core helium burning, near the Hayashi line (Hayashi et al., 1962; Stothers & Chin, 1979; Maeder & Meynet, 1987). Significant mass loss in higher mass stars can cause evolution to higher $T_{\rm eff}$ during core helium burning if the envelope becomes stripped from the star (Maeder, 1981a; Sreenivasan & Wilson, 1985; Maeder & Meynet, 1987; Meynet et al., 2015a).

It also became clear that mixing at the convective boundaries of MS stars was required, both from observational and theoretical backgrounds. Convective mixing is one of the most important (and uncertain) physical processes that changes the internal abundance profile over time is (e.g Shaviv & Salpeter, 1973; Stothers & Chin, 1973; Maeder, 1985). Both the convective stability criterion and the nature of convective boundary mixing were found to have important impacts on the evolution of L and $T_{\rm eff}$. For example, a moderate amount of convective core overshooting during core hydrogen burning results in higher L and lower $T_{\rm eff}$ at the end of the main sequence and therefore an extended main sequence width in the HR diagram (Maeder, 1975, 1976, 1981b; Alongi et al., 1993). The choice of the Ledoux or Schwarzschild criterion for convective stability affects L and $T_{\rm eff}$ during core helium burning (Oke & Schwarzschild, 1952; Saslaw & Schwarzschild, 1965; Stothers & Chin, 1975, 1976). Convective overshooting in envelopes and the value of the mixing length parameter can also impact the evolution of $T_{\rm eff}$, particularly for red supergiants (Alongi et al., 1991). In regions that are stable with respect to the Schwarzschild criterion, but unstable to the Ledoux criterion, semi-convection can occur (Langer et al., 1983). Semi-convection was then included in stellar evolution models and found to affect the evolution of L and T_{eff} in multiple ways including favouring core helium ignition as a red supergiant rather than a blue supergiant (Langer et al., 1985).

Stellar rotation was also found to be important for massive star evolution (Heger & Langer, 2000; Maeder & Meynet, 2000). In general, moderate rotation favours evolution to higher luminosities and lower T_{eff} during both the hydrogen and helium burning phases (Meynet & Maeder, 2000). Fast rotation can produce evolution towards higher T_{eff} during hydrogen burning if the star becomes chemically homogeneous (e.g. Maeder & Meynet, 1987; Yoon & Langer, 2005).

The paradigm of massive star evolution was changed once again when observations by Sana et al. (2012) indicated that a majority of massive stars will interact with a binary companion at some point. Interaction with a binary companion greatly complicates the possible evolutionary pathways that stars can follow (Paczyński, 1967a; Sana et al., 2012; de Mink et al., 2013; Moe & Di Stefano, 2017). The implementation of binary interaction in massive star evolution models and population synthesis models has proved vital to interpret gravitational wave detections of black hole mergers and neutron star mergers by the LIGO Virgo Collaboration (Abbott et al., 2016b, 2017a).

1.3 Observational Classifications of Massive Stars

Stars are classified based on their spectral and photometric appearance (Walborn & Fitzpatrick, 2000). Their appearance changes as they evolve. As one of the tasks of stellar evolution modelling is to figure out how to make evolutionary connections between different types of stars, understanding the observational classifications of massive stars is vitally important.

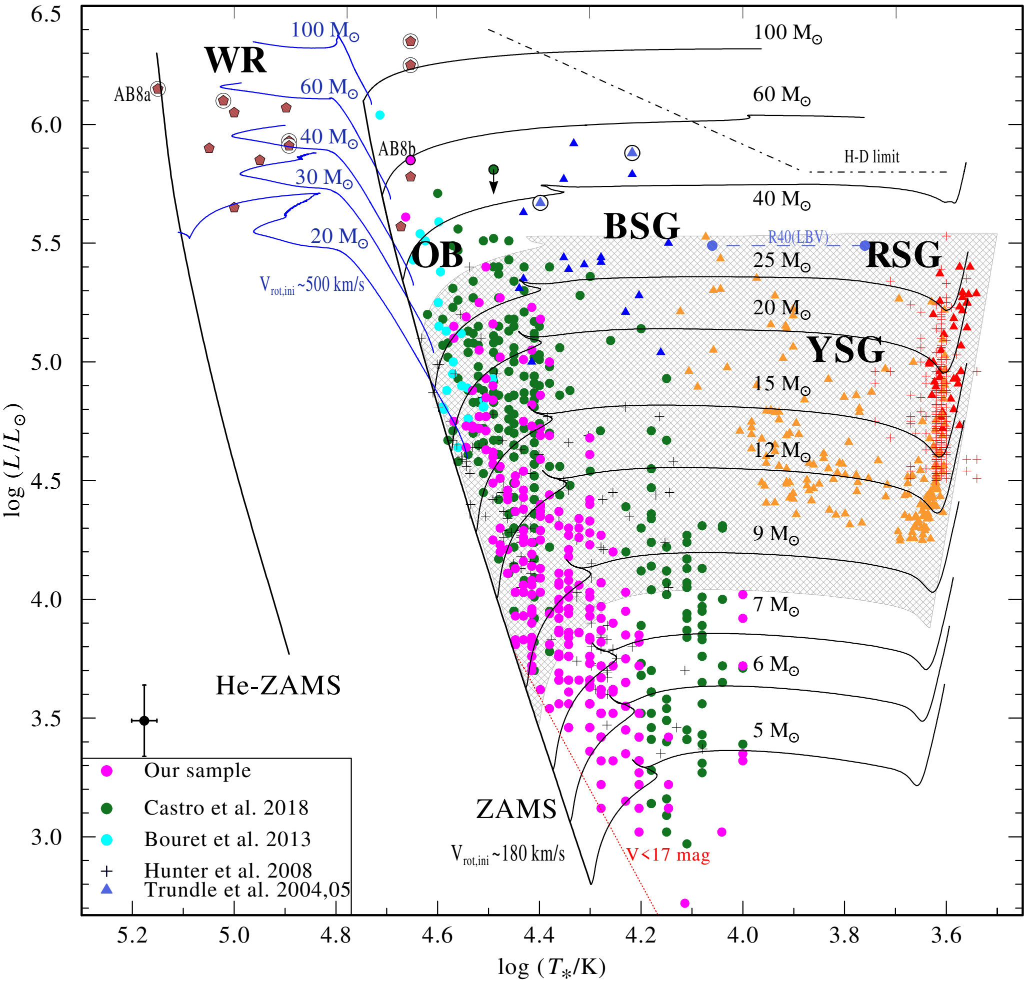

Figure 2: Hertzsprung-Russell Diagram for massive stars in the Small Magellanic Cloud (SMC) taken from Ramachandran et al. (2019). The different stellar classifications are represented by green, pink and cyan circles for OB stars (Ramachandran et al., 2019; Castro et al., 2018; Bouret et al., 2013; Hunter et al., 2008a), blue triangles for BSGs (Trundle et al., 2004; Trundle & Lennon, 2005), yellow symbols stand for YSGs (Neugent et al., 2010), red crosses (Davies & Beasor, 2018) and red triangles (Levesque et al., 2006) for RSGs and brown pentagons for Wolf-Rayet stars (Hainich et al., 2015; Shenar et al., 2016). Evolutionary tracks with $v_{\rm init} \approx 180\,{\rm km\,s^{-1}}$ are shown by solid black and blue lines (Brott et al., 2011a; Köhler et al., 2015). The initial masses are indicated above each track. The black tracks show standard evolutionary paths, while the blue tracks with $v_{\rm ini} \approx 550\,{\rm km\,s^{-1}}$ show the tracks of quasi-chemically homogeneously evolving (QCHE) stars. The shaded gray area indicates the luminosity range in which single stars are expected to die as RSGs according to models from Brott et al. (2011a).

1.3.1 OB-type Main Sequence Stars

Most massive stars are OB-type stars (Sota et al., 2011). OB-type stars span the upper region of the Main Sequence in the HR diagram (Sana et al., 2013; Dunstall et al., 2015; Almeida et al., 2017; Martins & Palacios, 2021). They range in luminosity from about $\log \mathrm{L}/\mathrm{L}_{\odot} = 3.0$ to about 6.0 and in effective temperature from about T_{eff} = 10 000 K to about 40 000K.

1.3.2 Blue Supergiants

Blue Supergiants (BSGs) are massive luminous stars with large radii and high T_{eff}. They have luminosities of $\log \mathrm{L}/\mathrm{L}_{\odot} = 3.5$ to 5.5, T_{eff} of between 8 000 and 20 000 K and typical radii of about 20 - 200 $\mathrm{R}_{\odot}$. Most OB-type main sequence stars with masses of 8 to 30 $\mathrm{M}_{\odot}$ will evolve to become BSGs after core hydrogen exhaustion. BSGs are interesting because it is often unclear exactly which phase of evolution they belong to. Stars can appear as BSGs during the short-lived expansion phase between the MS and helium burning, the core helium burning phase, the core carbon burning phase or even directly prior to core collapse. A BSG was famously observed as the progenitor to SN 1987A in the LMC (Arnett et al., 1989). Because BSGs are typically the brightest stars in their galaxies in optical light, they are ideal candidates for determining extragalactic distances (Kudritzki et al., 1999). The flux-weighted gravity luminosity relationship (FGLR) is a powerful method which has been used to determine extragalactic distances with BSGs, both within the Local Group (Urbaneja et al., 2008; U et al., 2009) and beyond (Kudritzki et al., 2003, 2012, 2014, 2016; Bresolin et al., 2016). Blue supergiants are also of interest in studies of binary interaction. Mass-gainers and mergers are often predicted to appear as BSGs rather than RSGs (Schneider et al., 2014).

1.3.3 Yellow Supergiants

Yellow Supergiants (YSGs) are a rare type of massive evolved star that have T_{eff} in between blue and red supergiants (Drout et al., 2009, 2012; Neugent et al., 2010, 2012a; Drout et al., 2012). It is a short lived phase and their envelopes are thought to be quite unstable (Stothers & Chin, 2001; Kienzle et al., 1998; Nieuwenhuijzen et al., 2012). Stellar evolution models suggest that YSGs are post red supergiant stars (Georgy, 2012; Stothers & Chin, 2001; Gordon et al., 2016). YSGs are also thought to be supernova progenitors. A YSG progenitor of SN 2011dh which was found in archival imaging before explosion (Maund et al., 2011; Soderberg et al., 2012; Van Dyk et al., 2013; Maund, 2019). Stellar evolution models have also pointed in this direction (e.g. Georgy, 2012; Groh, 2014). However, due to their short lifetimes, their place in the evolutionary sequence of massive stars is uncertain.

1.3.4 Red Supergiants

Red Supergiants (RSGs) are large, luminous, evolved massive stars with $T_{\rm eff}$ of 3500 - 5000 K (e.g. Davies et al., 2007, 2008). Their interiors consist of a dense helium core with a deep convective envelope. Most massive stars at high metallicity are expected to evolve into RSGs after core hydrogen depletion (de Mink et al., 2014; Sana et al., 2012; Eldridge et al., 2008; Massey & Olsen, 2003; Maeder & Meynet, 2001; Langer & Maeder, 1995; Humphreys & Davidson, 1979; Humphreys, 1978; Paczyński, 1969; Stothers & Chin, 1968) Additionally, the majority of CCSNe come from red supergiants (RSGs) with H-rich envelopes which explode as type-IIP SNe (Smartt et al., 2004; Smith et al., 2011; Eldridge et al., 2013; Groh et al., 2013b; Davies, 2017).

RSGs sit near the Hayashi line in the HR diagram. They have deep convective envelopes which can be quite difficult to model. In general the approach in 1D stellar evolution models is to use mixing length theory (Böhm-Vitense, 1958) with a free parameter called $\alpha_{\rm MLT}$. In these models, the radius and effective temperature depends on the value of $\alpha_{\rm MLT}$. The value of $\alpha_{\rm MLT}$ and its dependence on mass and metallicity which can be constrained using observations (González-Torà et al., 2021; Chun et al., 2018). This is difficult to do as both the envelope mass and metallicity affect $T_{\rm eff}$ independent of the value of $\alpha_{\rm MLT}$. There is significant hope that new 3D hydrodynamical simulations will improve our understanding of the nature of the envelopes of RSGs (e.g. Goldberg et al., 2021). These new results suggest that the mixing length parameter is different for RSGs and solar metallicity models.

The Humphreys-Davison (HD) limit is an observed upper luminosity limit to stars in HR diagram (Humphreys & Davidson, 1979). Reproducing the HD limit at different metallicities using stellar evolution models has been a topic of recent research and may be quite useful for constraining the properties of stellar interiors (McDonald et al., 2021; Massey et al., 2021; Ren et al., 2021; Gilkis et al., 2021; Higgins et al., 2021; Neugent et al., 2020; Schootemeijer & Langer, 2018). Recent research by Davies & Beasor (2018) revised the HD limit downwards to $\log {\rm L/L_\odot} = 5.5$ Connected to the HD limit, the luminosity function of RSGs is a good testbed for stellar evolution as well and has also been a topic of recent research using models and observations. Again, at higher masses closer to the HD limit, turbulent convection and energy transport in the envelopes of more massive stars can be difficult to model.

RSGs have also been observed in binary systems in the LMC (Neugent et al., 2020) and M31 and M33 (Neugent, 2021). They can be used to measure the metallicity of distant galaxies (Davies et al., 2010). The number ratio of BSGs to RSGs has used a diagnostic to test stellar evolution models (Langer et al., 1985; Maeder & Meynet, 2000). This is a very sensitive test as BSGs and RSGs can exist close to the transition between a blue and a red location in the HR diagram. Thus even small changes in mass loss, convection or other mixing processes greatly affect the evolution and the balance between the red and the blue. Several other open research directions regarding RSGs have been investigated.

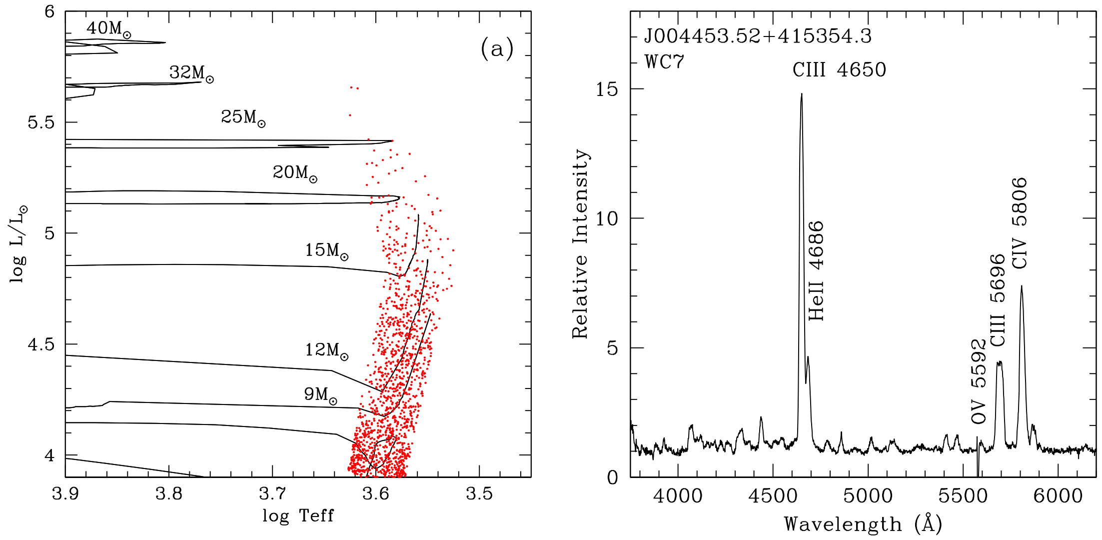

Figure 3: *Panel (a)*: Red Supergiants in the HR diagram in M31 from Neugent et al. (2020). The Geneva stellar evolution tracks are plotted in black. *Panel (b)*: Representative optical spectrum of a WC star in M31 from Neugent et al. (2012a).

For instance, do some RSGs evolve back to blue regions of the HR diagram due to mass loss (Yoon & Cantiello, 2010; Georgy et al., 2012; Georgy, 2012; Groh et al., 2013b,a)? Does this evolution explain the location of blue supergiants observed in high metallicity clusters (Meylan & Maeder, 1983; Eggenberger et al., 2002)? Are they the precursors to low-luminosity WC stars (Georgy et al., 2012), to low luminosity LBV SN progenitors Groh et al. (2013b) or YSG SN progenitors Georgy et al. (2012) such as 2011dh (Van Dyk et al., 2013)?

1.3.5 Luminous Blue Variables

Luminous Blue Variables (LBVs) are a class of bright, blue massive star that exhibit spectral and photometric variability (Humphreys & Davidson, 1994). Their L and $T_{\rm eff}$ can be significantly variable over the timescale of months or years, often causing them to move across the HR diagram. The Galactic LBVs span a range of luminosities, with $\log \mathrm{L/L}_\odot$ = 5.2 - 6.5 (Clark et al., 2005), corresponding to stars with masses $\gtrsim 20\mathrm{M}_\odot$. Examples of LBVs in our Galaxy include P Cygni in the 1600s (de Groot, 1988; Lamers & de Groot, 1992) and η Car in the 1800s (Davidson & Humphreys, 1997; Smith & Frew, 2011)

LBVs are surrounded by massive circumstellar nebulae of dust and gas, rich in processed material, indicative of stellar mass ejected by an evolved object through extensive stellar winds and outbursts (Morse et al., 1998; Smith, 2013; Thackeray, 1950; Davies et al., 2005; Vamvatira-Nakou et al., 2015; Buemi et al., 2017; Agliozzo et al., 2019). They are possibly an important source of dust in galaxies (Agliozzo et al., 2021). LBV variability is caused by instabilities that are not yet understood (Conti et al., 1984; Conti, 1997; Humphreys & Davidson, 1994). Outbursts with very high mass loss rates are required

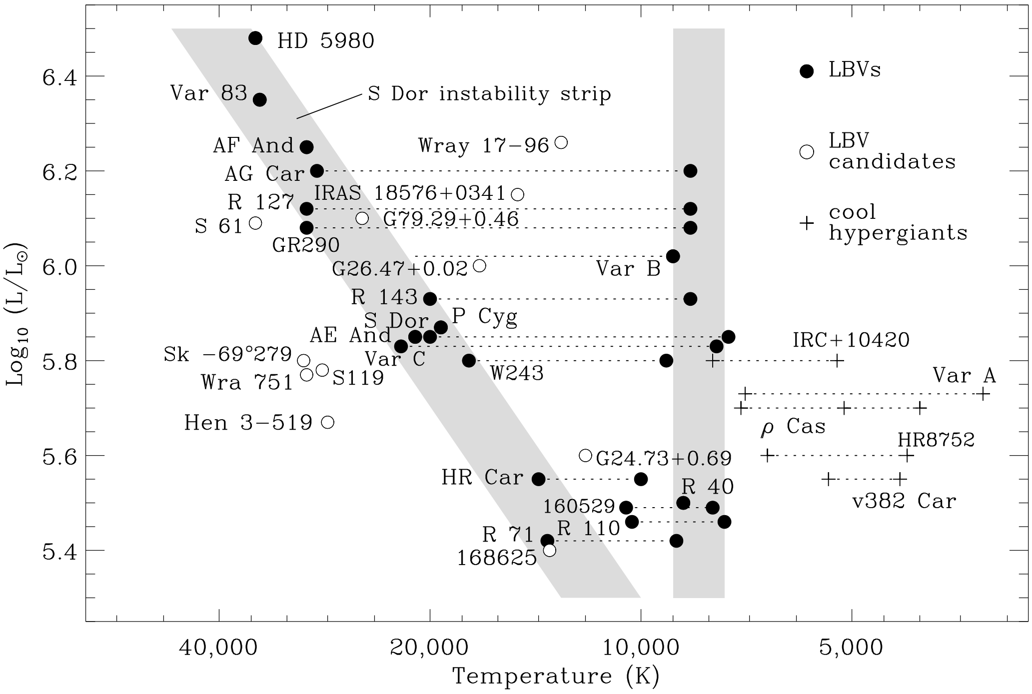

Figure 4: HR diagram for LBVs, LBV candidates and other cool hypergiants from Smith et al. (2004). The grey bands indicate the location of the S Doradus instability strips.

to form these nebulae of dust and gas (Kochanek, 2011). The high stellar luminosities near the Eddington limit probably enable instabilities in the envelope (Vink & de Koter, 2002; Owocki, 2015; Lovekin & Guzik, 2014). 3d hydrodynamical simulations by Jiang et al. (2018) suggest that variations in the helium opacity may explain LBV outbursts. Another possible factor is whether LBV outbursts are affected by proximity to a binary companion. LBVs can undergo huge eruptions, losing significant amounts of mass in the process, and moving across the HR diagram. Stellar evolution models indicate that LBV mass loss may regulate the maximum mass of black holes (Groh et al., 2020).

Recent research has also investigated whether LBVs are produced by single stars or by stars in binary systems (e.g. Aghakhanloo et al., 2017; Smith, 2019). Some argue that LBVs could be mass gainers in binary systems that receive a kick when the primary explodes (Justham et al., 2014; Smith et al., 2015; Portegies Zwart & van den Heuvel, 2016). However, this has been highly debated in the literature (e.g. Portegies Zwart & van den Heuvel, 2016). LBVs have a high Eddington factor Γ in their envelope. As $\Gamma \propto L/M$, a decrease in mass may be the best way to produce an LBV so they could possibly be the mass donors in binary systems.

LBVs have classically been considered as transitions between O-type stars and WR stars, during which large amounts of mass is lost (e.g. Conti, 1975). More recently, LBVs have also been connected to supernova progenitors. Stellar evolution models and synthetic spectra presented by (Groh et al., 2013a) suggest relatively low-luminosity LBVs could explode as supernovae without binary interaction. Additionally, observations of the radio light-curve (Kotak & Vink, 2006) and line profiles (Groh et al., 2011), the presence of a dense circumstellar medium (Smith, 2007) and photometry of progenitors (Gal-Yam et al., 2009; Mauerhan & Smith, 2012) all suggest that LBVs could be the final evolutionary phase for some massive stars. Whether LBVs are actually direct progenitors to core-collapse supernovae is still unknown. Additionally, some of these eruptions could be bright non-terminal eruptions (Allan et al., 2020).

1.3.6 Wolf-Rayet Stars and Stripped Stars

If massive stars lose their hydrogen envelopes either through wind mass loss, LBV eruptions, binary interaction or CHE, they can evolve to the blue side of the HR diagram and can become stripped stars or classical Wolf-Rayet (WR) stars (Conti, 1975; Chiosi, 1986; Abbott & Conti, 1987). Wolf-Rayet stars are hot, compact massive stars that exhibit broad emission lines with typical widths of a few hundreds to thousands of km/s. Depending on the amount of mass the star has lost, and hence its spectral appearance, WR stars can be sub-classified into nitrogen-rich (WN), carbon-rich (WC) and oxygen-rich (WO) stars. Some high mass stars on the main sequence have high enough mass loss rates to appear as WR stars. These are classified separately as WNh stars, indicating the presence of hydrogen in the spectra (de Koter et al., 1997).

The WR content of several nearby galaxies has been studied including M33 (Neugent & Massey, 2011), M31 (Neugent et al., 2012b). WR stars can appear in binary systems (Neugent & Massey, 2014) Classical WR stars can probe some of the least understood phases of massive stars prior to their core-collapse into neutron stars or black holes. WR stars play an important role in astrophysics, as signatures of star formation in galaxies and starbursts, as sources of kinetic energy for the ISM and possibly as SN progenitors and progenitors of GRBs.

WR stars were discovered by Charles Wolf and Georges Rayet, who observed spectra with broad emission lines in three stars in Cygnus (Wolf & Rayet, 1867). Beals (1929) proposed that the spectrum can be interpreted as a signal of strong mass loss of matter from the star. With increased sample sizes, it was discovered that the spectra of WR stars form a continuum with the O-type stellar spectra. Subsequently, it was suggested that WR stars are formed from O type stars that lose mass via strong stellar winds (Rublev, 1965; Conti, 1975). Classical WR stars require envelope stripping to be formed. This stripping increases the L/M ratio and the proximity to the Eddington limit. This allows the launching of a powerful wind (Castor et al., 1975; Gräfener et al., 2011). This envelope stripping can occur via stellar winds or via binary interaction. Lower mass binary-stripped He stars (Paczyński, 1967a; Podsiadlowski et al., 1992; Groh et al., 2008; Götberg et al., 2017, 2018) have been discussed as a source of cosmic re-ionisation (Stanway et al., 2016; Götberg et al., 2020).

1.4 Supernovae and Compact Objects

We may not be sure of the order of stellar evolution or of how the different stellar types connect with each other. Whatever the order of stellar evolution is, and whatever phase they go through, massive stars eventually run out of fuel to burn. What sort of explosion and remnant they produce depends primarily on the masses of the helium core and the hydrogen envelope at death. Most of them explode in bright explosions called core collapse supernovae.

1.4.1 Core Collapse Supernovae

Core Collapse Supernovae (CCSNe) are energetic explosions generated by the explosion of a massive star (Minkowski, 1964; Woosley & Weaver, 1986). They mark the transition of an ordinary star into a neutron star or a black hole (Baade & Zwicky, 1934). They are so luminous that they can outshine their entire galaxy for a short period of time. When they occur in our Galaxy, which happens about once per century (Adams et al., 2013), they can be visible to the naked eye. Indeed, several CCSNe are known to have been observed historically. CCSNe have distinct light curves with a sharp rise over a few days to weeks and a gradual decline that can last several years. Their spectra show velocities of $10\,000 - 15\,000$ km/s. They have typical energies of 10^{53} erg in neutrinos and 10^{53} erg in photons and are associated with cosmic rays and long gamma ray bursts. The majority of CCSNe are type II-P produced by red supergiants with hydrogen rich envelopes (e.g. Smartt, 2009; Smith et al., 2011; Eldridge et al., 2013; Groh et al., 2013c). CCSNe leave behind neutron stars and remnants like the Crab nebula.

Supernovae are classified based on the properties of their light curve and spectra in a system first introduced by Minkowski (1941) and later updated by Filippenko (1997) If the spectrum with weak or no hydrogen lines it is classified as a Type I SN, otherwise it is classified as a Type II SN. Type I SNe are sub-classified into Type Ia if silicon lines are present in the spectrum (these are thermonuclear explosions of white dwarfs, e.g. Maguire et al. 2012), Type Ib if helium is present but silicon is not, and Type Ic if neither helium or silicon are present. Type II SNe are sub-classified into Type II-P if the light curve exhibits a plateau for a few months or Type II-L if the light curve decreases linearly with time after the peak. These classifications exist mainly for historical reasons, because it was (and is) useful to initially place things into categories to try to understand them. As more supernovae were discovered, it has become clear that there are no sharp transitions between the different classifications. In addition, many peculiar transients have been discovered that do not fit neatly into these classifications (e.g. Prentice et al., 2021).

CCSNe have significant impacts across many areas of astrophysics, including the direct chemical enrichment of the interstellar medium and of galaxies, the triggering of star formation and the release of energy into the surroundings. They have also been used for distance measurement in cosmological studies (Maguire et al., 2010) Determining which stars explode and their final properties such as mass and chemical composition is an important open question in stellar astrophysics. Connecting observations of massive stars with photometry and spectroscopy of supernovae and the compact remnant left behind is an excellent way to do this.

The progenitors and power source of hydrogen-poor super-luminous supernovae is currently unknown (Gal-Yam et al., 2009; Pastorello et al., 2010; Chomiuk et al., 2011; Gal-Yam, 2012). Several energy sources have been proposed including production of significant amounts of radioactive material and large ejecta masses from pair-instability explosions (Heger & Woosley, 2002), interaction of the SN ejecta with a dense circumstellar medium that spans a range of mass loss rates and timescales (Chevalier & Irwin, 2011; Chatzopoulos et al., 2013), and powering by a magnetar central engine (Kasen & Bildsten, 2010; Woosley, 2010; Blanchard et al., 2021).

1.4.2 Pair-instability Supernovae

In stars with massive CO cores, $M_{\rm CO} \gtrsim 30{\rm M}_\odot$, ($M_{\rm init} \gtrsim 60{\rm M}_\odot$) the late nuclear burning phases are expected to be interrupted by the production of electron-positron pairs in the core (Fowler & Hoyle, 1964; Rakavy et al., 1967). For stars with CO core masses of $30{\rm M}_\odot \lesssim M_{\rm CO} \lesssim 60{\rm M}_\odot$, this can result in a series of energetic pulses followed by a collapse to a BH called a pulsational pair instability supernovae (PPISN) (Chatzopoulos & Wheeler, 2012; Chen et al., 2014; Woosley, 2017; Marchant et al., 2019; Leung et al., 2019). For $60{\rm M}_\odot \lesssim M_{\rm CO} \lesssim 120{\rm M}_\odot$, pair creation can result in a complete disruption of the star in a pair-instability supernova (PISN), leaving behind no remnant (Glatzel et al., 1985; Fryer et al., 2001; Umeda & Nomoto, 2002; Kasen et al., 2011). For even higher $M_{\rm CO}$, energy losses due to photo-disintegration are expected to result in a direct collapse to a BH (Fowler & Hoyle, 1964; Ober et al., 1983; Heger et al., 2003; Woosley & Heger, 2007). The combined effect of pulsational pair instability (PPI) and pair instability (PI) is predicted to produce a gap in the BH birth mass distribution between $\sim 55-130{\rm M}_\odot$ (Heger et al., 2003; Belczynski et al., 2016; Woosley, 2019; Giacobbo et al., 2018). The exact boundaries of the mass gap are uncertain due to uncertainties in stellar evolution, core-collapse supernovae, PPISNe and PISNe (Woosley, 2017; Mapelli et al., 2020; Marchant et al., 2019; Farmer et al., 2019; Stevenson et al., 2019; Renzo et al., 2020b). Farmer et al. (2019) found that the lower boundary of the mass gap is quite robust against uncertainties in the metallicity ($\sim 3{\rm M}_\odot$), internal mixing ($\sim 1{\rm M}_\odot$) and stellar wind mass loss ($\sim 4{\rm M}_\odot$). However, they found that varying the $^{12}C(\alpha,\gamma)^{16}O$ reaction rate within 1σ uncertainties shifts the location of the lower-boundary of the mass gap between 40 and 56 ${\rm M}_\odot$. van Son et al. (2020) investigated the possibility of super-Eddington accretion forming BHs in the mass gap, however they found no binary black hole (BBH) with a combined mass $> 100{\rm M}_\odot$. Additionally, Marchant & Moriya (2020) investigated the impact of stellar rotation on the location of the mass gap and found that the lower boundary may be shifted upwards by 4 - 15% depending on the efficiency of angular momentum transport.

The boundaries of the PI mass gap have also been proposed as a mechanism to place constraints on nuclear reaction rates (Farmer et al., 2020), particle physics (Croon et al., 2020) and in cosmological studies (Farr et al., 2019).

1.4.3 Supernova Progenitors

The progenitors of CCSNe and PISNe are massive stars at the end of their evolution. This has been well established by finding stars located at the location of a supernova that are no longer present after the explosion (e.g. Arnett et al., 1989). However, the exact connections between supernovae and stellar evolution channels are still uncertain. The light curve and spectra of CCSNe an offer a lot of information about the stars that produced them. The key advantage of studying stars at the pre-supernova stage is that their evolutionary state is known. This is in contrast to direct observations of stars, which require models to constrain the evolutionary state. For stars at any other evolutionary phase, we rely on models to determine the evolutionary state. It is often quite difficult to determine to determine the evolutionary state. But one of the main points of producing stellar evolution models is to connect the dots and therefore to know the evolutionary stages.

One of the exciting advancements in the last two decades is the direct imaging of CCSNe progenitors in pre-explosion archival images (see reviews from Smartt 2015, Van Dyk 2017, and references therein). The analysis of these observations, in combination with other techniques such as SN light curve modelling, can help us to make connections between CCSNe and their progenitor stars and to improve our understanding of the complexities and uncertainties in the evolution of massive stars. The fact that we know the evolutionary stage of CCSNe progenitors (i.e. they are the end stages of their lives) makes them especially useful for comparisons with stellar models. (Maund et al., 2011; Fraser, 2016) for RSG supernova progenitors (Adams et al., 2017a,b) search for direct collapse black hole

Around 20 progenitors of CCSNe have been detected in pre-explosion images, the majority of which are RSGs. From these photometric observations, and with a distance, it is possible to obtain the bolometric luminosity L_{bol} and effective temperature T_{eff} immediately before core collapse. To obtain an initial mass M_{ini} from L_{bol} and T_{eff}, it is necessary to use a stellar evolution model. Comparisons between the pre-explosion images and stellar evolution models have suggested that stars with $M_{\text{ini}} \gtrsim 18\ \text{M}_{\odot}$ may not explode as supernovae (e.g. Smartt, 2009). However, some stellar evolution models predict that some stars with $M_{\text{ini}} \gtrsim 18\ \text{M}_{\odot}$ will die as RSGs. This discrepancy has been called the 'red supergiant problem'. To explain this, several authors have proposed that RSGs with M_{ini} between 18 and 30 $\text{M}_{\odot}$ may collapse directly to a black hole without a luminous supernova explosion (e.g. Smartt, 2015; Sukhbold et al., 2016; Sukhbold & Adams, 2020). Others have offered suggestions related to underestimated bolometric corrections (Davies & Beasor, 2018), uncertain extinction (Walmswell & Eldridge, 2012), and increased mass loss of luminous RSGs near the Eddington limit compared to older stellar models (e.g. Groh et al., 2013c; Meynet et al., 2015b). The statistical significance of the RSG problem is far lower than the original claim if late-type bolometric corrections are used (Davies & Beasor, 2018).

In addition to direct imaging of SN progenitors, other properties of the SN progenitors can be inferred from the SN spectra and light curve. Significant mass loss immediately before the SN can impact the spectrum. It can result in narrow lines in the spectrum and is classified as SN IIn. This can help to infer properties of the progenitors and the end stages of the evolution (Smith, 2007; Pastorello et al., 2007; Kiewe et al., 2012; Ofek et al., 2014; Moriya et al., 2014) and in SN IIb and Ibc using X-ray and radio observations (Chevalier & Fransson, 2006; Soderberg et al., 2012) LBV or yellow hypergiant (YHG) could be SN progenitors (Groh, 2014). Models from Groh et al. (2013b) indicate that the pre-mortem LBV phase is short (about 5000 years), which is consistent with the observed rarity of LBVs (Humphreys & Davidson, 1994; van Genderen, 2001; Clark et al., 2005). The properties of SN progenitors can be constrained using several complementary techniques. These include direct imaging of the progenitor in pre-explosion images (e.g. Smartt, 2009), hydrodynamical modeling of the lightcurve (Nomoto et al., 1993) and spectrum (Dessart & Hillier, 2011), and analysis of the progenitor's environment (e.g. Modjaz et al., 2008), among others. To extract all the information about the progenitor contained in the observations, these techniques are often used in combination with stellar evolution models.

Possibly the best progenitor detection was of the B0.7-B3 blue supergiant Sanduleak -69° 202 ° which exploded as SN 1987A (Arnett et al., 1989; McCray & Fransson, 2016). The star had an initial mass of $\approx 20\mathrm{M}_{\odot}$, although could have gone through a binary interaction phase. The detection of a BSG progenitor to a Type II SN was somewhat surprising as it was, and still is, thought that most Type II SN would be produced by RSG progenitors.

Uncertainties in stellar evolution models related to physical processes such as mass loss, convection, rotation and binary interaction mean that it is difficult to make a robust connection between observed surface properties of a progenitor and M_{ini}. For instance, Groh et al. (2013c) found that changes in the initial rotational velocity alone can cause an uncertainty of ± 2 $\mathrm{M}_{\odot}$ in the determination of the initial mass. We should also keep in mind that it is possible that a significant fraction of RSG progenitors will have gained mass from a binary companion (e.g. Zapartas et al., 2019). This would produce RSGs with different core to envelope mass ratios than in single stars.

1.4.4 Neutron Stars

Neutron stars are the remains of the cores of massive stars that had masses of 8 - 25 $\mathrm{M}_{\odot}$ on the MS (Duncan & Thompson, 1992; Ruderman & Sutherland, 1975; Akmal et al., 1998; Hirata et al., 1987; Eichler et al., 1989; Sturrock, 1971; Heger et al., 2003; Lattimer

& Prakash, 2004; Li & Paczyński, 1998; Hawking, 1971; Lattimer, 2012) They typically have masses of 1 - 2 $M_\odot$ and are some of the densest manifestations of massive objects in the universe. This makes them ideal astrophysical laboratories for testing theories of dense matter physics. The maximum mass of NS is thought to be around 2.5 $M_\odot$, but this depends on the nuclear matter fluid equation of state which is uncertain and the topic of current research. Because of the movement of free charges, neutron stars are highly magnetised with fields in excess of 10^{13} G. Rapidly rotating neutron stars called pulsars can also be produced following CCSNe (Goldreich & Julian, 1969).

Neuton stars have also gathered a lot of recent attention as a result of gravitational-wave observations. The first detection of neutron stars via gravitational waves was made by Abbott et al. (2017a). They found component masses in the range 1.17 to 1.60 $M_\odot$. The Fermi-GBM detected a gamma ray burst 1.7 s after the coalescence (Goldstein et al., 2017), consistent with the hypothesis of a neutron star merger and provided the first direct evidence of a link between NS-NS mergers and short gamma ray bursts.

1.4.5 Black Holes from Massive Stars

Massive stars with initial masses $M \gtrsim 25 M_\odot$ can form a black hole after the supernova (e.g. Heger et al., 2003). Black holes were predicted as a consequence of general relativity. They were confirmed to exist in nature when the compact object in the X-ray binary Cygnus X-1 was determined to have a mass greater than the maximum mass of a neutron star (Webster & Murdin, 1972; Bolton, 1972). Over 20 BHs have since been discovered in similar compact binary systems where they accrete matter from a stellar companion (McClintock & Remillard, 2006). Such observations are very useful for understanding massive star evolution and how they evolve in binary systems. More recently, black holes have been observed via gravitational waves (Abbott et al., 2016b,d)

1.4.6 Gravitational Waves

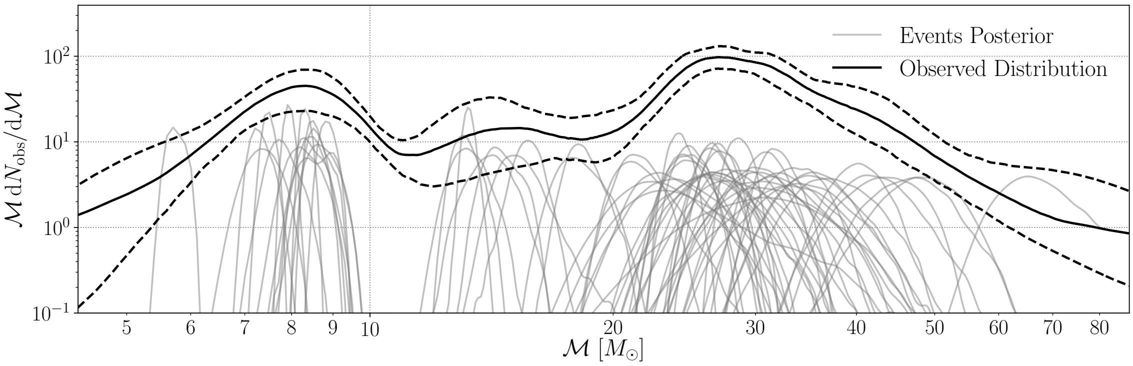

Figure 5: The latest updated catalogue from LIGO Virgo Collaboration of the posterior distribution of chirp masses of compact object mergers detected up to O3 (The LIGO Scientific Collaboration et al., 2021c). An inferred distribution of the observed chirp mass distribution is plotted in black with the 90% confidence interval indicated by dashed lines.

Gravitational waves are ripples in spacetime released with significant amplitudes when very large masses are accelerated very quickly, e.g. when neutron stars or black holes merge with one another in a binary system. Einstein predicted the existence of gravitational waves shortly as a consequence of the field equations of general relativity (Einstein, 1916, 1918). 100 years later, The LIGO Scientific Collaboration and The Virgo Collaboration achieved the first direction detection of gravitational waves (Abramovici et al., 1992; Abbott et al., 2009, 2016b). The latest updates from LIGO/Virgo provided a catalogue of 90 detections of compact object mergers that produced gravitational waves (The LIGO Scientific Collaboration et al., 2021c,d). Fig. 5 shows the latest updated catalogue from The LIGO Scientific Collaboration et al. (2021d) of the distribution of chirp masses of compact object mergers detected up to observing run O3. The black line shows the inferred distribution of the observed chirp mass distribution with 90% confidence intervals. Based on these observations, The LIGO Scientific Collaboration et al. (2021c) inferred the total merger rate as a function of primary BH mass (Fig. 6). These observations provide no evidence of a PI mass gap, but do suggest a peak in the power-law distribution at around 32 $\mathrm{M}_{\odot}$. This peak may be explained by pair-instability explosions.

Gravitational waves offer a fundamentally new way of observing the universe and for understanding massive star evolution. Observations of binary BH-BH have revealed the properties of the stellar mass BBH population (Abbott et al., 2016a, 2020c; The LIGO Scientific Collaboration et al., 2021d), been used to test general relativity (Abbott et al., 2016c). NS-NS mergers have confirmed the association between kilonovae and NS mergers and led to the birth of the age of multi-messenger astronomy (Abbott et al., 2017d,a,c). Observations of the NS-NS merger can also help constrain their equation of state (Abbott et al., 2018; The LIGO Scientific Collaboration et al., 2021d,c). GW observations have also been use as cosmological probes, e.g. for the Hubble constant (Abbott et al., 2017b) and been used to test the association with short and long gamma ray bursts (The LIGO Scientific Collaboration et al., 2021a,b). One possible advantage of GW observations is that they are subject to different observational biases than those that can affect typical observational samples in photometric or spectral surveys. For instance, events are observed independent of their location in the sky. In addition to the wealth of new information and observational constraints available for compact remnants of massive stars, gravitational wave observations have also directly challenged massive star evolutionary models (e.g. Abbott et al., 2020d,b).

1.4.7 GW190521 & the 85 Solar Mass Black Hole

In 2019, the LIGO Virgo Collaboration reported the detection of a BBH merger with unusually high component masses of 85^{+21}_{-14} and $66^{+17}_{-18}\mathrm{M}_{\odot}$ (Abbott et al., 2020a). These black hole masses lie within the mass gap predicted by standard PPI SNe theory. Based on the BH mass function predicted by PPISNe and PISNe, the observation of a pre-merger $\sim 85\mathrm{M}_{\odot}$ BH as in GW190521 is unexpected. Several possibilities to create BHs with

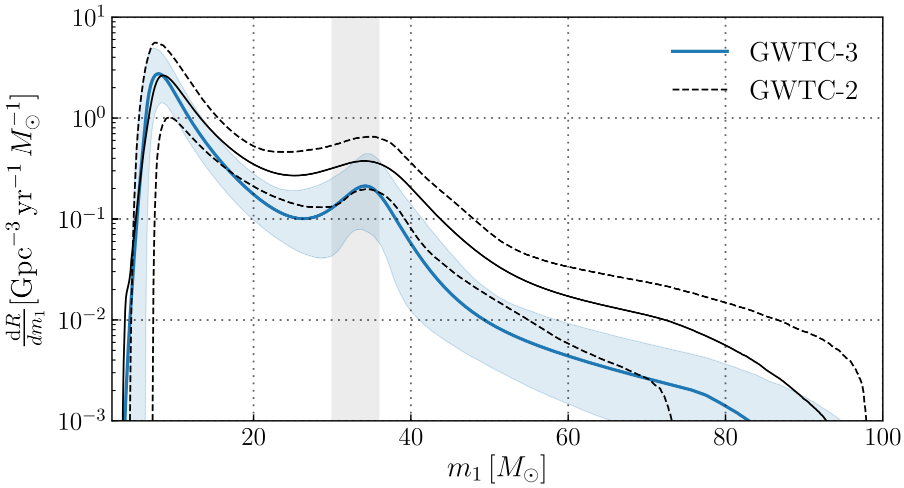

Figure 6: The total merger rate as a function of primary BH mass reported by the Ligo Virgo Collaboration O3 (The LIGO Scientific Collaboration et al., 2021c).

the reported mass are presented in previous works. The BH could form as a result of hierarchical mergers in dense stellar clusters, i.e. it is the result of the prior merger of two or more other BHs (e.g. Miller & Hamilton, 2002; Gerosa & Berti, 2017; Fishbach et al., 2017; Rodriguez et al., 2019; Romero-Shaw et al., 2020; Gayathri et al., 2020; Fragione et al., 2020). Other possible explanations include a stellar merger between a post-main sequence star and a MS binary companion (Spera et al., 2019; Di Carlo et al., 2019), a primordial origin (De Luca et al., 2021), different assumptions for stellar wind mass loss Belczynski (2020), Population III stars in binary systems (Kinugawa et al., 2020, 2021; Tanikawa et al., 2021), an alternative prior in the gravitational wave analysis (Fishbach & Holz, 2020) and modifications to the Standard Model of particle physics (Sakstein et al., 2020). Alternative explanations for the source of GW190521 were found to be highly unlikely (Abbott et al., 2020b), including a strongly gravitationally lensed merger or a highly eccentric merger. Given the widely predicted existence of the mass gap and the apparent robustness of the boundary of the gap with respect to uncertainties in stellar evolution models, the question of whether a single star produce a BH remnant with a mass around 85M$_\odot$ is worth investigating further. The possibility exists that stars at low or zero metallicity could retain most of their hydrogen envelope until the pre-supernova stage, avoid the pulsational pair-instability regime and produce a BH with a mass in the pair-instability mass gap.

1.5 Evolution of Low and Intermediate Mass Stars

Low and intermediate mass stars evolve very differently to high mass stars. Their lower masses mean they do not need to produce as much luminosity for support against gravity. As a result, they burn through their fuel slower and have longer lifetimes. Due to their lower core temperatures, low mass stars achieve hydrogen fusion on the MS via the PP chain and do not go through the nuclear burning phases beyond helium burning. During the MS, their cores are radiative and they have convective envelopes. When they exhaust hydrogen in their cores, they leave the MS and a hydrogen burning shell outside the core is formed. As the shell burns outwards, the helium rich core becomes degenerate and isothermal and the surface luminosity increases by a factor of ~ 100 as it ascends the red giant branch. A consequence of degeneracy is that core contraction is not connected with heating. Helium burning begins degenerately in a sudden process known as the helium flash and then settles on the horizontal branch. When core helium is exhausted, they evolve up the asymptotic giant branch. Here, shed their envelopes, sometimes driven by common envelope evolution with a binary, and can form planetary nebulae. In the end, they produce white dwarfs.

Intermediate mass stars ($2 < M_{\mathrm{init}} < 8$) develop a non-degenerate helium core after core hydrogen exhaustion. They expand across the HR diagram to produce red giants and ignite helium without a flash. After central helium burning, they form a carbon-oxygen core that becomes degenerate. Similar to low mass stars, they shed their envelopes by a strong stellar wind and form CO white dwarfs at the end of their evolution.

Stars with masses of 3 - 12 $\mathrm{M}_{\odot}$ may evolve to become Cepheid variable stars during their post-MS evolution. Cepheids occupy a well-defined region in the HR diagram called the classical instability strip. Cepheids famously obey a tight statistical relationship between the pulsation period and luminosity (Leavitt, 1908; Leavitt & Pickering, 1912). They are among the most precise standard candles for distance measurements. They are used for calibrating supernova based direct measurements of the local Hubble constant (e.g. Riess et al., 1998; Freedman et al., 2001; Riess et al., 2011). Cepheids are excellent examples for testing stellar evolution models because they occur on blue loops in the HRD. The properties of blue loops can be very sensitive to changes in the input physics in stellar models. In fact, one of the most fantastic comparisons between observations and models is the rate of change of period of Cepheids matches blue loops forming. There is also debate about the Cepheid mass discrepancy related to systematically overestimated masses inferred from stellar evolution models as compared to observations (e.g Christy, 1968; Stobie, 1969a,b; Bono et al., 2006; Keller, 2008).

1.5.1 Magnetic Fields & Sub-Surface Convection

Magnetic fields are thought to play several key roles in the evolution of stars. They affect the internal transport of angular momentum (Spruit, 2002; Fuller et al., 2019). They can impact the properties of stellar winds (Weber & Davis, 1967; Ud-Doula et al., 2009), which in turn can affect planetary evolution (Vidotto et al., 2013). Magnetic fields can alter heat transport and produce star spots (Cantiello & Braithwaite, 2011), influence accretion (Bouvier et al., 2007). They can also enhance (Harrington & Garaud, 2019) or inhibit chemical mixing (Gough & Tayler, 1966).

Near the surface, stellar models indicate that the opacity peaks due to hydrogen and helium can cause convective layers to appear. These convective layers do not have a huge impact on the overall structure of the star or the location in the HR diagram. However, they can interact with magnetic fields and remove evidence of large scale magnetic fields at the surface of the star. Magnetic fields make the criterion for convective instability more strict (Gough & Tayler, 1966; MacDonald & Mullan, 2009; MacDonald & Petit, 2019). Jermyn & Cantiello (2020) discussed in detail the relationship between magnetic fields and subsurface convective zones and derived the following expression for the critical magnetic field strength $B_{\rm crit}$:

$$B^2_{\rm crit} = \frac{4\pi\rho c_s^2 Q(\nabla_{\rm rad} - \nabla_{\rm ad})}{1 - Q(\nabla_{\rm rad} - \nabla_{\rm ad} + d\ln\Gamma_1/d\ln p} \tag{1.1}$$

where c_s is the sound speed, Γ_1 is the first adiabatic index, ρ is the density, $\nabla_{\rm rad}$ is the radiative temperature gradient, $\nabla_{\rm ad}$ is the adiabatic temperature gradient

$$Q = \frac{4 - 3p_{\rm gas}/p}{p_{\rm gas}/p}. \tag{1.2}$$

where $p_{\rm gas}$ is the gas pressure. For magnetic field strengths above the critical field strength ($B > B_{\rm crit}$), the magnetic field is expected to suppress convection. For $B < B_{\rm crit}$, strong surface magnetic fields are thought to be erased by convection. The process involves magnetic re-connections in subsurface convective layers, and the subsequent expulsion of overlying magnetic fields (Jermyn & Cantiello, 2020). Stable fossil fields can survive underneath the convective regions, but they are not detectable at the surface using spectropolarimetry. For intermediate mass stars, the (sub)surface convective regions are driven by helium ionisation, either the He I or He II convective zone (HeICZ, HeIICZ) (Cantiello & Braithwaite, 2019). The critical field is of order 10^3 G and is set by the helium ionisation convection zone (HeCZ). A visual representation of these subsurface envelope convective zones is presented in Fig. 9.

1.5.2 Initial Fossil Magnetic Field Distribution

Stars are expected to form with a range of fossil magnetic field strengths. The distribution of fossil fields is currently unknown and an important open question in stellar astrophysics. Direct observation of this initial fossil field distribution is precluded, as magnetic fields interact with convective regions and can be erased by subsurface convection layers as a star evolves (e.g. Gough & Tayler, 1966; Jermyn & Cantiello, 2020). By combining the theoretical results from Jermyn & Cantiello (2020) with observations by Sikora et al.

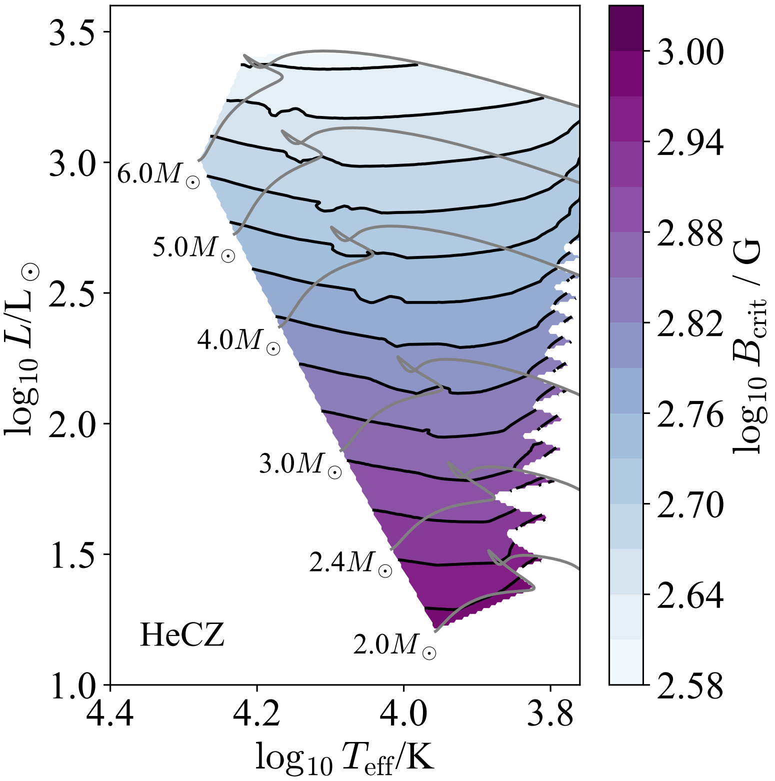

Figure 7: The critical magnetic field B_{crit} given by Equation 1.1 for stellar models ranging from 2 to 6 $\mathrm{M}_\odot$ in which the HeCZ is the most important convection zone from Jermyn & Cantiello (2020). The critical magnetic field decreases in strength with increasing mass and also as the star evolves during the MS phase.

(2019b), we are able to infer the initial distribution of fossil magnetic fields for AB stars in the mass range 1.6 to 3.4 $\mathrm{M}_\odot$.

Observations of early-type stars (OBA stars) have revealed a bimodal distribution of surface magnetic field strengths. Stars are observed either with strong fossil fields, in excess of about 300 G, or ultra-weak fields, with amplitudes below a few G. Few or no stars are observed with field strengths in between (Aurière et al., 2007; Grunhut et al., 2017; Fossati et al., 2015). The bi-modal distribution raises the possibility of two different origins for magnetism in early-type stars. Strong magnetic fields could be the relic of fossil field generation during star formation (e.g. Donati & Landstreet, 2009) or during a stellar merger (Schneider et al., 2016, 2019). Weak magnetic fields could be the result of ongoing dynamo processes (Cantiello & Braithwaite, 2011, 2019).

This picture was supported by the conclusions of Jermyn & Cantiello (2020) who studied the interaction of magnetic fields with subsurface convection layers. They concluded that a bimodal distribution of field strengths, as well as the approximate field strengths of the magnetic desert, can be naturally produced by considering a criterion for a magnetic field to suppress convection. They also found that the critical magnetic field required to prevent the onset of subsurface convection depends on the stellar mass and changes slightly throughout the main sequence. For instance, at the beginning of the main sequence, the value of B_{crit} ranges from about 1000 G for 1.6 $\mathrm{M}_{\odot}$ to 700 G for 3.4 $\mathrm{M}_{\odot}$. These critical fields can be used to infer the initial fossil magnetic field distribution.

1.6 Physics of Stellar Interiors

One of the reasons stars are interesting to study is the wide variety of physical processes that take place in their interior. From nuclear fusion, to turbulent convection, to eruptive mass loss, these key mechanisms have a range of important impacts on stellar evolution and the impact of stars on the universe.

1.6.1 Nuclear Reactions

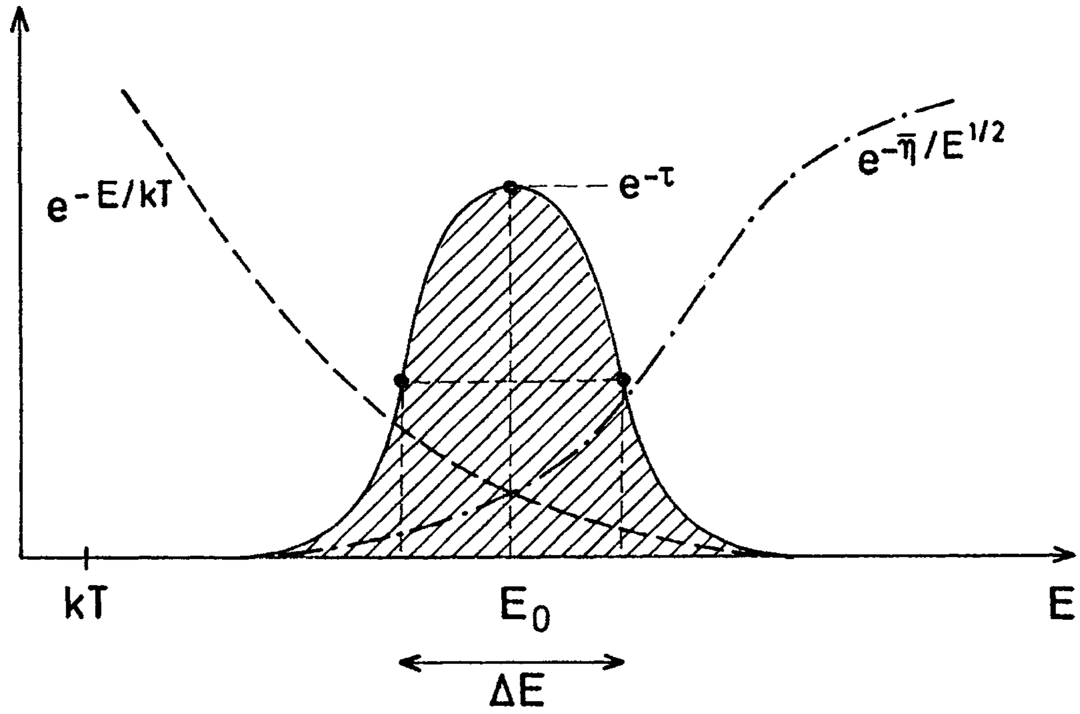

Figure 8: Approximate curves illustrating the range of the strong nuclear force and the electromagnetic force as a function of energy. The hatched region shows the region in which nuclear reactions take place known as the Gamow peak (Gamow, 1938). The $e^{rm-E/kt}$ term represents the Maxwell-Boltzmann distribution and the $e^{-\eta/E^{1/2}}$ term represents the penetrability of the Coloumb barrier by tunnelling.

Stars evolve due to changes in their internal abundance profiles, ultimately driven by nuclear fusion reactions in their interiors. The nuclear reactions are responsible for the creation of the majority of the chemical elements from carbon to iron. The only way that two charged nuclei can be brought close enough to overcome the repulsive Coulomb force and achieve fusion via the shorter-range nuclear forces is through quantum tunnelling (Fig. 8). It is interesting that one of the many strange quantum behaviours, that are totally different to physics at everyday scales, is fundamentally important for stars to evolve and produce the elements. It was first suggested that fusion of protons could provide the energy source for the sun in 1919. This was shown by Atkinson & Houtermans (1929) after the quantum tunnelling effect was discovered by Gamow. In the late 1930s, the pp chain was discovered by Bethe & Critchfield (1938) and the CNO cycle was discovered by von Weizsacker (1938). The core helium burning reactions were described by Salpeter (1952). An overview of these developments was presented by Burbidge et al. (1957). A detailed understanding of nuclear reactions and their dependence on temperature and density is vital for accurately modelling the structure and evolution of stars.

Massive stars on the MS fuse hydrogen into helium using the CNO cycle. This is a chain of nuclear reactions in which the CNO elements essentially act as catalysts to allow the fusion to take place. It has a steep dependence on temperature ($\epsilon_{\rm nuc} \propto X X_{\rm CNO} T^{19.9}$, where $\epsilon_{\rm nuc}$ is the energy generation, X is the abundance of hydrogen, $X_{\rm CNO}$ is the abundance of CNO and T is the temperature.). The net effect from the CNO cycle is that hydrogen is converted to helium, the total CNO abundance stays constant, but the nitrogen abundance goes up while carbon and oxygen go down. This nitrogen enrichment has observational consequences. Because N is enriched, if this material is mixed to the surface or the outer layers of the star are stripped away by winds or binary interaction, we can observe so-called CNO enriched material, which matches the expected pattern from nuclear burning in stellar interiors.

Stellar evolution codes use nuclear reaction networks which provide the nuclear reaction pathways as well as their rates and dependence on temperature and pressure. The nuclear reaction rates are difficult to determine. STELLA is a large project that has worked to measure reaction rates (Heine et al., 2018). For some reactions, the cross section of the reaction at temperatures and densities relevant for helium burning in stars is very small (An et al., 2015, 2016). Therefore, experiments are performed at much higher temperatures where the reaction cross section is higher, and the results are extrapolated down to the relevant energies for stars. However, it can be difficult to extrapolate to lower temperatures because the cross section can have a complex energy dependence. Ongoing lab measurements continue to improve the uncertainties in nuclear reaction rates. In addition, improved theoretical modelling of the $^{12}C(\alpha,\gamma)^{16}O$ rate (Hammer et al., 2005; An et al., 2016; Hammache et al., 2016; deBoer et al., 2017; Shen et al., 2020) with the goal of measuring the reaction rate closer to the temperatures of stars (Holt et al., 2018; Friščić et al., 2019). In MESA (Paxton et al., 2011), the nuclear reaction rates are from JINA REACLIB (Cyburt et al., 2010), combined with additional tabulated weak reaction rates (Fuller et al., 1985; Oda et al., 1994; Langanke & Martínez-Pinedo, 2000).

In some cases, there are significant uncertainties in our understanding of the relevant nuclear reaction rates. For example, the pp chain (Villante & Serenelli, 2021) (Villante & Serenelli 2021), the ^{12}C + ^{12}C reaction in carbon burning (Patterson et al., 1969; High & Čujec, 1977; Becker et al., 1981; Aguilera et al., 2006; Barrón-Palos et al., 2006; Spillane et al., 2007; Bucher et al., 2015), the fusion of oxygen in massive stars (Holt et al., 2019) and the $^{12}C(\alpha,\gamma)^{16}O$ rate. The $^{12}C(\alpha,\gamma)^{16}O$ rate has a significant impact on the post-MS evolution of stars across the HR diagram. In low mass stars, it can impact the the C/O ratio in white dwarfs (Salaris et al., 1997; Straniero et al., 2003; Fields et al., 2016). In massive stars, it may affect whether a star will form a NS or a BH (Brown et al., 2001; Heger & Woosley, 2002; Woosley et al., 2002; Tur et al., 2007; West et al., 2013; Sukhbold & Adams, 2020) and the amount of ^{12}C and ^{16}O in the universe (Boothroyd & Sackmann, 1988; Weaver & Woosley, 1993; Thielemann et al., 1996).

Nuclear reactions in stars prevent gravitational contraction by allowing the pressure gradient to be maintained over very long timescales. The temperature dependence of nuclear reactions impacts the temperature structure of the star. However, during the nuclear burning phases, the nuclear energy released per unit time and mass cannot change significantly. This is due to the feedback of nuclear burning. Any decrease of nuclear energy generation will result in a small contraction, a very slight increase in temperature, and the establishment of thermal equilibrium. Similarly, an increase of nuclear energy generation will result in a small expansion and cooling, and therefore a decrease of nuclear energy generation rates. When a nuclear reaction rate important for the production of energy is changed in the models, the energy released stays approximately constant, while the temperature changes. However, only a very small change in temperature is required, especially for massive stars, as the nuclear reaction rates are very sensitive to temperature.

Monpribat et al. (2021) tested the impact of an updated ^{12}C + ^{12}C reaction rate. Although some of the new reaction rates differ by more than an order of magnitude, the effect on stellar evolution is relatively small. The length of the carbon burning phase is shortened by a factor of two In contrast, there are other situations where an uncertainty in the nuclear reaction rates may have a significant impact on stellar evolution. For example, Farmer et al. (2020) computed a detailed grid of models to show that the boundary of the pair instability black hole mass gap depends strongly on the uncertain $^{12}C(\alpha,\gamma)^{16}O$ reaction rate. This can completely change the expected masses of black holes which has implications for interpreting gravitational wave detections (The LIGO Scientific Collaboration et al., 2021c).

1.6.2 Opacity

Radiation produced by nuclear fusion deep in stellar interiors interacts with the gas. This interaction has a wide variety of effects on the stellar structure and surface properties (Carson, 1976). The opacity in stellar interiors is typically dominated by electron scattering $\kappa_{\rm sc}$. Electron scattering opacity can be approximated by $\kappa_{\rm sc} = 0.20(1+{\rm X})$. Other significant sources of opacity include free-free transitions, bound-free transitions, bound-bound transitions, H$^-$ and molecular opacities. When solving the stellar-structure equations in stellar evolution models, numerical opacity tables for different chemical mixtures are used. For example, MESA uses radiative opacities are primarily from OPAL (Iglesias & Rogers, 1993, 1996), with low-temperature data from Ferguson et al. (2005) and the high-temperature, Compton-scattering dominated regime by Buchler & Yueh (1976) and with electron conduction opacities from Cassisi et al. (2007).

Opacity has significant impacts for the stellar structure. The values in the opacity tables can significantly modify the evolution in the HR diagram (e.g. Schaller et al., 1992). Opacity effects are also very important in wide range of different kinds of pulsating stars across the HR diagram (Zhevakin, 1963; Christy, 1966; Gautschy & Saio, 1995, 1996). Opacity can also cause the appearance of convective layers in the outer envelopes of stars across a wide range of masses (Fig. 9). If the ratio of luminosity to mass, L/M, is sufficient, the envelopes of massive stars $\gtrsim 60 M_\odot$ can be pushed close to what is called the Eddington limit. Beyond the Eddington limit, the material is unstable. As Eddington (1926) pointed out, *"... the radiation observed to be emitted [by stars] must work its way through the star, and if there were too much obstruction it would blow up the star"*. Near the Eddington limit, instabilities can manifest in the outer envelopes of OB stars, where the iron opacity can cause density and gas pressure inversions in 1D models (Schultz et al., 2021). These instabilities may explain observations of stochastic low-frequency variability in massive OB stars.

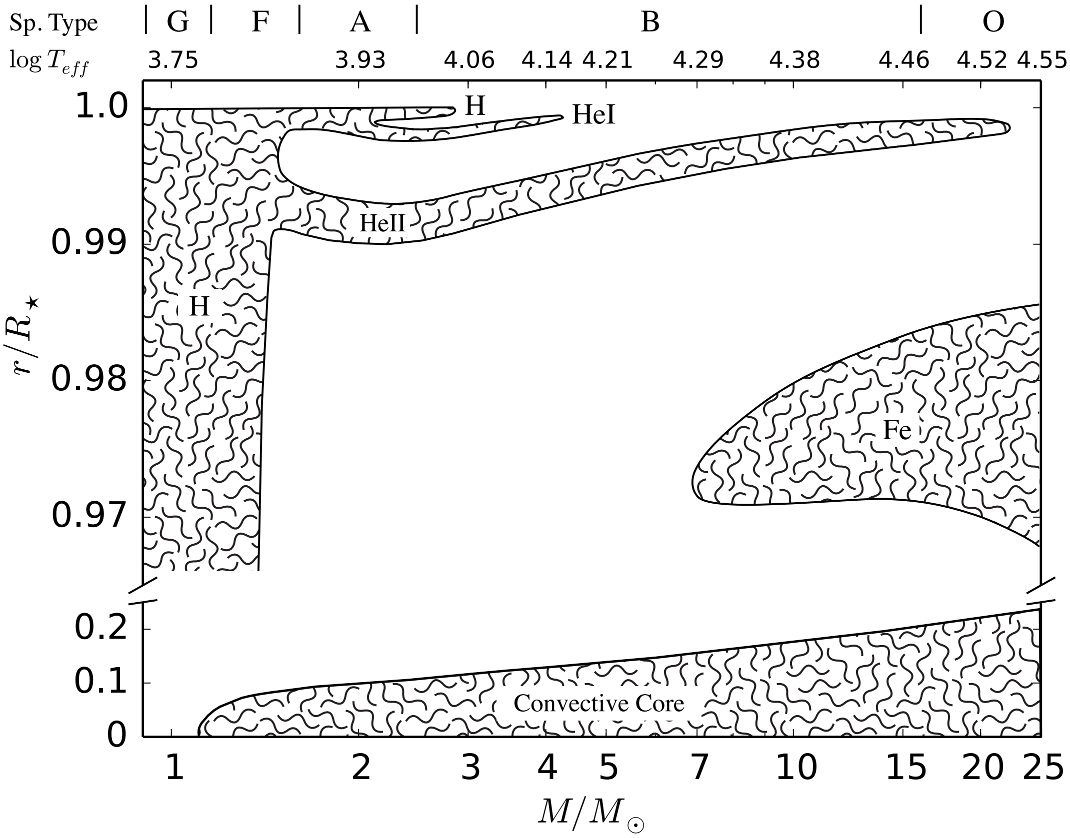

Figure 9: Normalised radial extension of core, surface, and subsurface convection zones for stars in the mass range 0.9 - 25 at $X_c = 0.5$ from Cantiello & Braithwaite (2019). Convective regions are associated with the ionisation of H, He (He I and He II), and ironpeak elements (Fe). The stellar surface r/R* = 1 is defined as the location corresponding to optical depth $\tau = 2/3$.

1.6.3 Convection

Convection is perhaps the most important large-scale physical process that takes place in stars. Convection in stellar interiors impacts the structure and evolution in two ways: it (i) transports energy and (ii) causes internal mixing. Convection develops in stars when energy transport by convection requires a shallower temperature gradient than energy transport by radiation. It is usually caused by nuclear burning or regions of increased opacity, e.g. CNO burning in the cores of massive MS stars, or iron opacity bumps near sub-surface convective layers. Many of the important open questions in massive star evolution ultimately come down to the nature of convection in stellar interiors. As convection is inherently a 3D process, one of the best theoretical routes to understand how it affects stars is through 3D hydrodynamical models. Unfortunately, these models are extremely computationally intensive. In addition, due to the short convective turnover timescale relative to the total stellar lifetime, it is not possible to compute such a model for a star's entire evolution. Therefore, to model the entire evolution of a star, we are stuck to adopting prescriptions for convection in 1D stellar evolution models.

The most common method to model convection in 1D stellar evolution codes is mixing-length theory (MLT, Böhm-Vitense, 1958) combined with a criterion for stability against convection. The basic assumption of MLT is that fluid elements can be represented by bubbles which move outwards in the star over a distance denoted the mixing length. In stellar evolution codes, a free parameter $\alpha_{\rm mlt}$ is used to determine the mixing length in units of the pressure scale height (Maeder & Meynet, 1989). To determine convective stability, the Ledoux or Schwarzschild criteria are commonly used. Mixing at convective boundaries between convective and radiative zones is expected to occur and is usually implemented via a free parameter $\alpha_{\rm ov}$ or $f_{\rm ov,core}$ that allows convection to 'overshoot' the original location of the boundary. These free parameters are constrained using observations.

Convective mixing in stars has a wide variety of evolutionary effects. Different values for $\alpha_{\rm ov}$ or $f_{\rm ov,core}$ are adopted in different models (e.g. Brott et al., 2011a; Ekström et al., 2012; Choi et al., 2016; Higgins & Vink, 2019), depending on the calibration method. For a given initial mass, the choice of $\alpha_{\rm ov}$ can significantly affect the mass of the convective core during the MS phase and the mass of the He-core during subsequent burning stages. As well as the value adopted for $\alpha_{\rm ov}$, the exact implementation of core-overshooting in the stellar evolution code can also modify a star's evolution (Martins et al., 2013). The dependence of $\alpha_{\rm ov}$ on mass and metallicity is also uncertain (Castro et al., 2014). In addition, the value of $\alpha_{\rm mlt}$ in stellar evolution models can significantly affect the $T_{\rm eff}$ of RSGs. A higher value of $\alpha_{\rm mlt}$ produces RSGs with lower values of $T_{\rm eff}$. Chun et al. (2018) compared observations of RSGs to stellar evolution models and found that models $\alpha_{\rm mlt} = 2$ or 2.5 best reproduced the observations.

Both the convective stability criterion and the nature of convective boundary mixing are known to have important impacts on the evolution of L and $T_{\rm eff}$ in stellar evolution models. For example, a moderate amount of convective core overshooting during core hydrogen burning results in higher L and lower $T_{\rm eff}$ at the end of the main sequence and therefore an extended main sequence width in the HR diagram (Maeder, 1975, 1976, 1981b; Alongi et al., 1993). The choice of the Ledoux or Schwarzschild criterion for convective stability affects L and $T_{\rm eff}$ during core helium burning (Oke & Schwarzschild, 1952; Saslaw & Schwarzschild, 1965; Stothers & Chin, 1975, 1976; Georgy et al., 2014b, 2021). Convective overshooting in envelopes and the value of the mixing length parameter can also impact the evolution of $T_{\rm eff}$, particularly for red supergiants (Alongi et al., 1991; Chun et al., 2018). New astero-seismological studies may provide important insights into convective boundary mixing in massive stars (e.g. Pedersen et al., 2021).

In regions that are stable with respect to the Schwarzschild criterion, but unstable to the Ledoux criterion, semi-convection can occur (Langer et al., 1983). Semi-convection is implemented in stellar evolution codes as a time-dependent, diffusive process, with a diffusion coefficient (Langer et al., 1985). Semi-convection can affect the evolution of L and $T_{\rm eff}$ in multiple ways and has been shown to favour core helium ignition as a red supergiant rather than a blue supergiant (Langer et al., 1985; Schootemeijer et al., 2019). The range of values of $\alpha_{\rm semi}$ varies by orders of magnitude throughout literature from 0.1-100 (e.g. Langer, 1991; Yoon et al., 2006; Charbonnel & Zahn, 2007; Cantiello & Langer, 2010; Schootemeijer et al., 2019).

1.6.4 Mass Loss

Stars lose mass by stellar winds as they evolve. Some of the first evidence that stars lose matter as they evolve was provided by Beals (1929) who suggested that the spectra of WR stars could be understood if a continuous wind of matter was flowing out from the star (Kosirev, 1934). Mass loss from different types of stars was later discovered (Deutsch, 1956; Neugebauer & Snyder, 1962) The stellar winds of massive MS stars were first observed by Morton (1967a,b) by spectrographs on balloons and rockets in space (not possible to observe from ground due to atmospheric UV absorption). Following these observations, the first complete theories of line driven stellar winds describing how these strong and fast winds are driven were published by Lucy & Solomon (1970) and Castor et al. (1975). It is now well understood that mass loss has a significant impact on the evolution of massive stars, particularly for stars with initial masses of $> 20{\rm M}_{\odot}$ (e.g. Smith, 2014). Mass can be lost from stars across the HR diagram in a variety of ways. Hot massive stars lose mass via line driven stellar winds (Lucy & Solomon, 1970; Castor et al., 1975). The very high luminosities of massive stars generates a large number of high energy photons that interact with the spectral lines when escaping from the star. The transfer of momentum from photons to atoms in the stellar atmosphere can accelerate the particles beyond the escape velocity, producing an outwards mass flux forming the stellar winds. This can be caused by iron atoms in hot massive stars or dust in cool giants. Mass can also be lost via massive eruptions, e.g. in LBVs, in which several ${\rm M}_{\odot}$ can be lost at a time. Other mechanisms for mass loss in low mass and cooler stars include coronal wind theory (Cranmer & Saar, 2011), the dust driven wind theory (Morris, 1987), the line driven wind theory (Abbott, 1982), the magnetic rotator theory (Holzwarth & Jardine, 2007). Additionally, there is increasing theoretical and observational evidence that massive stars may undergo eruptive and explosive mass-loss events during the late nuclear burning stages before core-collapse (e.g. Kotak & Vink, 2006; Smith, 2007; Pastorello et al., 2007; Gal-Yam et al., 2009; Fraser et al., 2013; Gal-Yam et al., 2014; Smith, 2014; Groh, 2014; Fuller, 2017; Yaron et al., 2017; Boian & Groh, 2018). Despite their potential significance, the nature of these eruptions is very uncertain and they are not usually accounted for in stellar evolution models.

Stellar wind mass loss are difficult to infer directly from observations and difficult to estimate from models. There are several methods to infer wind mass loss rates. These include the strength of wind free-free emission in the IR or radio, the strength of blue-shifted P Cygni absorption features in unsaturated UV resonance lines (Morton, 1967b) and recombination emission lines e.g. H_α. The latest models of hot line driven winds from Vink & Sander (2021). Other models mass-loss rates for O-type stars also suggest lower mass loss rates than previously thought (Björklund et al., 2021) and empirical mass loss rates are in agreement (Hawcroft et al., 2021). Stellar winds may or may not have large inhomogeneities, often referred to as clumps. Depending on what the unknown structure of the wind is, the inferred mass loss rates can vary by up to a factor of 2-3 (Smith 2014). At high luminosities, mass loss rates probably depend on the proximity to the Eddington limit (Bestenlehner, 2020). O-type stars can produce spherical nebulae that surround the star thought to be produced by stellar winds (Weaver et al., 1977; Castor et al., 1975). Discrepancies between theoretical models and values inferred from observations for wind mass loss rates exist (e.g. Puls et al., 2008; Muijres et al., 2012; Gvaramadze et al., 2012) For massive stars close to the Eddington limit ($\gtrsim 60\mathrm{M}_\odot$), mass loss rates may depend on how close they are to the Eddington limit (Gräfener & Hamann, 2008; Gräfener et al., 2011; Vink et al., 2011; Bestenlehner et al., 2014) In massive, evolved stars when radiation pressure is important, line-driven winds may transition into continuum-driven winds, possibly resulting in giant eruptions that eject several solar masses e.g, LBVs.

Mass loss from cooler massive stars is not as well understood. Their mass loss rates have been a topic of recent research (Beasor et al., 2020; Kee et al., 2021). One difficulty with understanding their mass loss properties, both observationally and theoretically, is that RSG mass loss may occur in short outbursts, rather than a steady stellar wind. For example, VY CMa has a dusty circumstellar envelope (Humphreys et al., 2007) that produces a reflection nebula at optical wavelengths, suggesting that it went through phase of high mass-loss about 1000 years ago (Decin et al., 2011). RSG mass loss has commonly been implemented in stellar evolution codes using a prescription for the time-averaged mass-loss rate from de Jager et al. (1988). These rates have been challenged by more recent observations with larger sample sizes (e.g. Beasor et al., 2020). If mass-loss rates are large enough, RSG mass loss can have an important impact the evolution of stars

(Davies & Plez, 2021; Moriya, 2021; Hiramatsu et al., 2021; Wang et al., 2021; Beasor et al., 2020; Renzo et al., 2017; Meynet et al., 2015b; Smith, 2014; Georgy et al., 2012; Yoon & Cantiello, 2010; van Loon et al., 2005). If a RSG loses about 1 $M_\odot$, it will usually remain a RSG. If it loses 5 to 10 $M_\odot$, whether due to winds or binary interaction, it can evolve back to the blue region of the HR diagram. At high masses, RSGs may turn into Wolf-Rayet stars due to mass loss (Maeder, 1981b).

Mass loss rates are very different at different masses (Vink et al., 2001). Mass loss rates increases as a function of luminosity and, therefore, as a function of initial mass. Stellar wind mass loss is significant for initial masses of $> 20 M_\odot$. Below 20 $M_\odot$, the fraction of mass lost over the total lifetime of the star is $< 5\%$ and generally does not have a significant impact on the overall evolution. At 40 $M_\odot$, stars can lose up to 20 % of its mass in mass over its lifetime, while a 100 $M_\odot$ star can lose up to 80 %. Line driven winds are also strongly dependent on the initial metallicity of the star. For example, a 60 $M_\odot$ non-rotating model can lose 80 % of its mass at solar metallicity compared to 25% of its mass at $Z = 0.004$ and 0% at $Z = 0$ (e.g. Ekström et al., 2012; Groh et al., 2019; Murphy et al., 2021). Mass loss affects the evolution of the surface properties, the angular momentum content (Aerts et al., 2019) and the appearance of a supernova. Stellar evolution models show that mass loss can modify the location of the terminal-age main sequence in the Hertzsprung-Russell (HR) diagram (De Loore et al., 1977; Chiosi et al., 1978) and favours a lower T_{eff} during core helium burning, near the Hayashi line (Hayashi et al., 1962; Stothers & Chin, 1979; Maeder & Meynet, 1987). Significant mass loss in higher mass stars can cause evolution to higher T_{eff} during core helium burning if the envelope becomes stripped from the star (Maeder, 1981a; Sreenivasan & Wilson, 1985; Maeder & Meynet, 1987; Salasnich et al., 1999; Vanbeveren et al., 2007; Yoon & Cantiello, 2010; Georgy, 2012; Groh et al., 2013b; Meynet et al., 2015a).

Stellar winds are important for the evolution and final fate of stars and for the evolution and chemical enrichments of galaxies (e.g. Chiosi, 1986). They can help explain the formation of Wolf-Rayet stars, affect supernova spectra and cause feedback of kinetic energy into the ISM. Stellar winds expel chemical elements synthesised in stellar interiors into the interstellar medium. In addition to supernova explosions, the chemical abundance of newly enriched ISM impacts the formation of new generations of stars and planets. Mass loss can produce stars without hydrogen or helium and the end of their lives, resulting in Type Ib/c Supernovae.

1.6.5 Rotation

Stars rotate because they form from large molecular clouds, which rotate as they collapse in the star formation process. Rotation modifies the internal structure of stars in several ways.

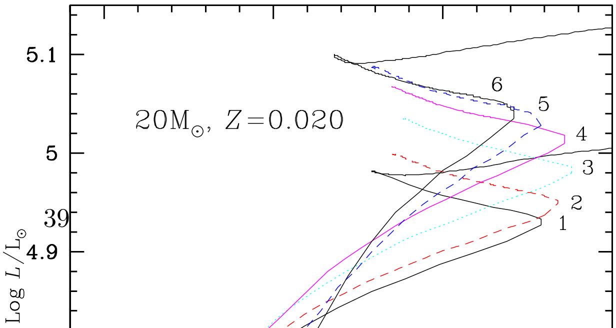

The hydrostatic equilibrium is modified due to the additional support of the centrifugal force. Local thermal equilibrium is broken causing to large scale meridional currents to develop. These currents transport angular momentum (Aerts et al., 2019) and transport material through advection processes. Indirectly, they produce differential rotation which triggers shear instabilities. The surface properties are also modified as the shape of the star becomes oblate and T_{eff} varies with the latitude. This produces a change of the mass loss rates and can induce anisotropies of the winds.

Stellar rotation can significantly affect the evolution of massive stars (e.g. Maeder & Meynet, 2000; Meynet & Maeder, 2000; Heger & Langer, 2000; Heger et al., 2005; Maeder et al., 2009; Brott et al., 2011a,b; Chieffi & Limongi, 2013a). Massive stars exhibit a range of rotational velocities (Huang et al., 2010; Hunter et al., 2008a; Ramírez-Agudelo et al., 2013, 2015; Dufton et al., 2019). In addition to the effect hydrostatic on hydrostatic equilibrium, rotation is expected to have a qualitatively similar evolutionary effect on the convective core mass to convective overshooting (Fig. 10). In general, moderate rotation favours evolution to higher luminosities and lower T_{eff} during both the hydrogen and helium burning phases (Meynet & Maeder, 2000; Chieffi & Limongi, 2013a). Fast rotation can produce evolution towards higher T_{eff} during hydrogen burning if the star becomes chemically homogeneous (e.g. Maeder & Meynet, 1987; Langer, 1992; Yoon & Langer, 2005; Brott et al., 2011a). The behaviour of stellar structure under extreme rotation has recently been suggested to be significantly different than previously thought, with consequences for the late stages of stellar evolution and the explosion (Aguilera-Dena et al., 2018). 2D models suggest that rotation can also cause enhanced mass loss and modify the angular momentum (Gagnier et al., 2019a,b).

1.6.6 Magnetic Fields

About 7% of massive OB stars exhibit strong, large scale magnetic fields (Morel et al., 2015; Fossati et al., 2015; Wade et al., 2014, 2016; Grunhut et al., 2017; Shultz et al., 2018). These fields are on the order of kG and stable on long time-scales. The origin of these fields is unknown. They are thought to be of fossil origin (Donati & Landstreet, 2009). One possibility is that these strong fields are produced in a stellar merger with a binary companion (Ferrario et al., 2009; Langer, 2012). The discovery of a strong B-field in the mass-accreting secondary star of the O-type binary HD 47129 adds evidence to this formation scenario (Grunhut et al., 2013). Another possibility is that many stars are formed with strong magnetic fields but evidence of their existence is removed at the surface e.g. by subsurface convective layers. These strongly magnetised stars are interesting for studies of the progenitors of magnetars and whether they form super-luminous supernovae at the end of their evolution. Surface magnetic fields can also greatly limit mass loss by stellar winds and may therefore play a role in setting the maximum BH mass at high metallicity (Groh et al., 2019). Magnetic fields may influence internal mixing and the transport of angular momentum. Magnetic braking can greatly deplete the core angular momentum resovoir on the MS and modify the chemical enrichment (Meynet et al., 2011). In massive stars, magnetic fields may also cause differences in the surface abundances (Keszthelyi et al., 2020, 2021).

In low and intermediate stars, magnetic fields are thought to play several key roles. They affect the internal transport of angular momentum (Spruit, 2002; Fuller et al., 2019). They can impact the properties of stellar winds (Weber & Davis, 1967; Ud-Doula et al., 2009), which in turn can affect planetary evolution (Vidotto et al., 2013). Magnetic fields can alter heat transport and produce star spots (Cantiello & Braithwaite, 2011), influence accretion (Bouvier et al., 2007). They can also enhance (Harrington & Garaud, 2019) or inhibit chemical mixing (Gough & Tayler, 1966).

1.6.7 Metallicity

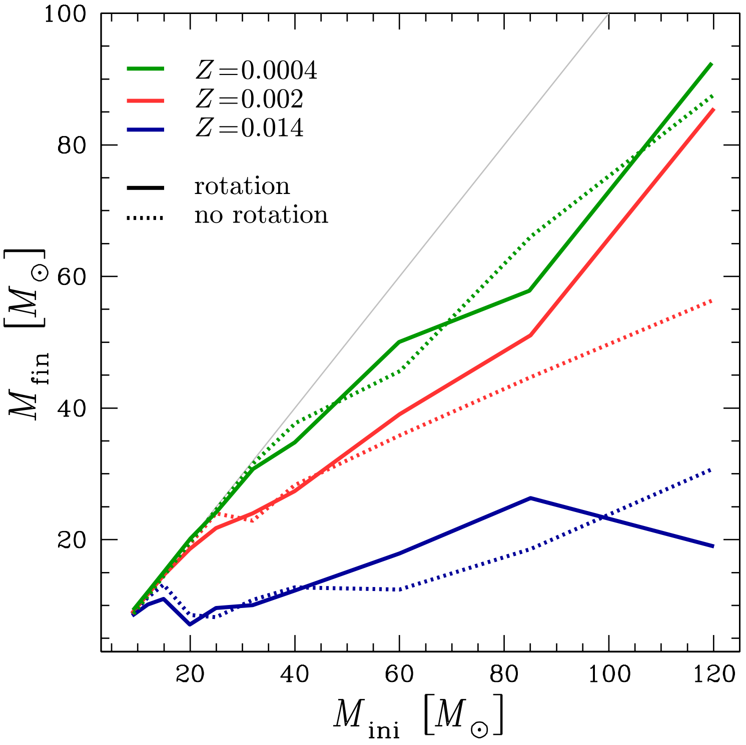

Figure 11: Impact of metallicity on the initial-final mass relationship for massive stars with and without rotation from Groh et al. (2019).

Stars are born with the chemical composition of the molecular cloud in which it forms. Solar metallicity stars have about a metal abundance of about 1.4% - 2%, while the LMC and SMC have metal compositions of about 0.6 % and 0.3 % respectively. Lower metallicity stars evolve differently to solar metallicity stars in several ways. First, lower metallicity stars are more compact and have higher $T_{\rm eff}$, both during the MS and the post-MS. This is due to (i) the effect of opacity in the envelope and (ii) the effect on the CNO abundances in the hydrogen burning shell. Mass loss by stellar winds is significantly reduced at lower metallicities (Fig. 11). For example, a 60 $M_\odot$ non-rotating model can lose 80 % of its mass at solar metallicity compared to 25% of its mass at Z = 0.004 and 0% at Z = 0 (e.g. Ekström et al., 2012; Groh et al., 2019; Murphy et al., 2021). The metallicity of a star affects the amount of mass it will lose in a binary system (Klencki et al., 2020, 2021) through its impact on the radius. The evolution of the mass as a function of time has a significant feedback effect on its evolution in the HR diagram and the final fate of the star.

Stellar evolution at low metallicity has a significant impact in many topics of astrophysics, such as the photometric and chemical evolution of metal-poor galaxies at different redshifts (e.g. Tolstoy et al., 2009; Stark, 2016), the observable properties of intergrated stellar populations (e.g. Vazdekis et al., 2010; Eldridge et al., 2017), the nature of supernovae and gamma ray burst progenitors (eg. Modjaz et al., 2008; Schulze et al., 2018), the amount of ionising flux at high redshift (e.g. Levesque et al., 2012; Götberg et al., 2017, 2018), nucleosynthesis (e.g. Chiappini et al., 2011) and the rates of gravitational wave signals from merging black holes. (e.g. Abbott et al., 2016b,a; Belczynski et al., 2017) and neutron star systems (e.g. Abbott et al., 2017a)

1.6.8 Binary Interaction

Observational evidence that a large number of stars exist in binary systems has been around for many decades (Garmany et al., 1980), but recently our understanding of the importance of binaries has rapidly increased (Kobulnicky & Fryer, 2007; Mason et al., 2009; Chini et al., 2012; Sana et al., 2013; Sota et al., 2014; Kobulnicky et al., 2014; Dunstall et al., 2015; Moe & Di Stefano, 2017; Almeida et al., 2017). Massive stars, in particular, have found to have a very high binary fraction. Observations by Sana et al. (2012) reported an interacting binary fraction of 0.69 ± 0.09 for O-type stars in open clusters in the Galaxy. They estimate that 24% will merge, 33% will have their H envelopes stripped before death, 14% will be spun up by accretion, and only about 29% of massive stars do not interact with a companion (or don't have one). Subsequently, Sana et al. (2013) and Dunstall et al. (2015) studied the Tarantula region in the LMC as part of the VLT-FLAMES survey, reporting interacting binary fractions of 0.51 ± 0.04 for O-type stars and 0.58 ± 0.11 for B-type stars respectively. The observed binary fraction of evolved cool supergiants in the LMC and SMC has been found to be smaller than for the MS (Dorda & Patrick, 2021) suggesting that earlier binary interaction e.g. a merger,

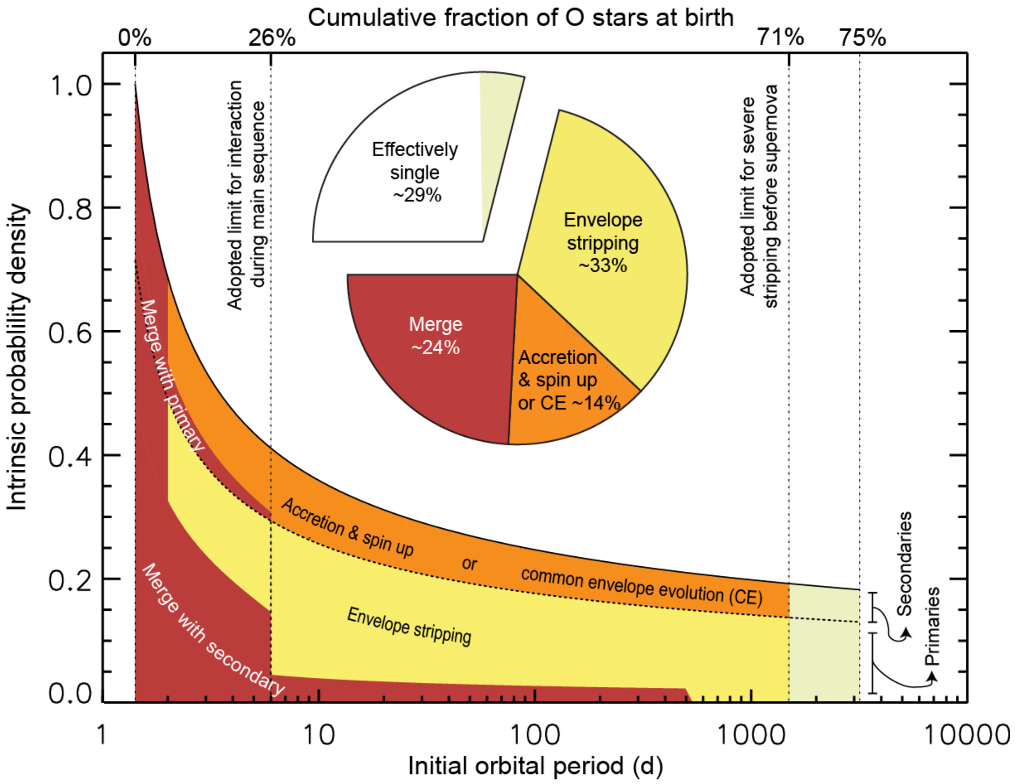

Figure 12: Schematic representation of the relative importance of different binary interaction processes from Sana et al. (2012). Percentages are expressed in terms of the fraction of all stars born as O-type stars.

may make stars appear single during later evolutionary phases. Moe & Di Stefano (2017) compiled observations of early-type binaries and reported a single star fraction of 16% for $9-16\ M_{\odot}$ stars and 6% for $>16\mathrm{M}_{\odot}$ stars (these values include non-interacting long period binaries). Understanding the effects of binary interactions on both the primary and the secondary is critical to understanding the evolution of massive stars and their impact on host galaxies.

Stars generally expand as the evolve. If stars expand beyond their Roche-lobe (the region of space surrounding the star in which material is gravitationally bound to the star), this can lead to interaction with a close binary companion. The possible range of evolutionary outcomes for massive stars is greatly complicated by the possibility of binary interaction (e.g. Paczyński, 1967b; Paczyński & Ziółkowski, 1967; Paczyński, 1967a, 1971; Podsiadlowski et al., 1992; Eldridge & Stanway, 2009; de Mink et al., 2014; Yoon, 2015; Eldridge et al., 2017; Zapartas et al., 2019). Roche-lobe overflow can lead to mass transfer episodes, typically classified into Case A (pre-core hydrogen exhaustion), Case B (post-core hydrogen exhaustion) or Case C (post-core He burning) mass transfer (Paczyński, 1966; Kippenhahn & Weigert, 1967). Mass transfer from a companion can have have interesting implications for the observational signatures (e.g. Hellings, 1983). Massive stars in binary systems have been suggested as the source of abundance anomalies in globular clusters (de Mink et al., 2009b)

If a star continues to expand into the orbit of its companion, the two stars can merge into a single star, producing a modified new stellar structure. Mergers have been directly observed e.g. V1309 Sco in which both stars are in physical contact in a 1.4 day orbit (Tylenda et al., 2011) The merger is accompanied by an brightening of about 5 mag in the I band (Munari et al., 2002) called a luminous red nova. These novae are frequently observed in distant galaxies (Kulkarni et al., 2007; Kasliwal et al., 2011). If a star gains mass from a companion either as a mass-gainer or in a merger, it can appear as a more massive, younger star. These stars are classified as 'blue stragglers', such as τ Sco (Schneider et al., 2016, 2019). Assuming single star evolution, τ Sco has an inferred age of $< 5\,\mathrm{Myr}$ appearing anomalously young compared to other stars of $\sim 11\,\mathrm{Myr}$ which are thought to have formed together in the Upper Scorpius association. If stars are close enough to each other, they can go into contact, e.g. VFTS 352 in the Tarantula Nebula. This can modify the T_{eff} (Abdul-Masih et al., 2019) and luminosity (Abdul-Masih et al., 2021) as compared to single stars.

Binary interaction has been linked to a wide range of observed phenomena. Binary interaction has been linked to the formation of Be stars (Porter & Rivinius, 2003; de Mink et al., 2013; Rivinius et al., 2013; Klement et al., 2017). Stars that lose mass via RLOF can also have modified core structures which may impact their explodability (Laplace et al., 2021). Late stage expansion of stripped stars can result in a second phase of mass transfer (Laplace et al., 2020). If a star gains mass from a companion either as a mass-gainer or in a merger, it can appear as a more massive, younger star. These stars are classified as 'blue stragglers', such as τ Sco (Schneider et al., 2016, 2019). Assuming single star evolution, τ Sco has an inferred age of $< 5\,\mathrm{Myr}$ appearing anomalously young compared to other stars of $\sim 11\,\mathrm{Myr}$ which are thought to have formed together in the Upper Scorpius association. Among the key results of these works are increased fractions of stripped WR stars (Eldridge et al., 2008) and higher rotational velocities due to binary interaction (de Mink et al., 2013). Given the prevalence of binaries among massive stars, such works are crucial in understanding how binary interaction impacts stellar evolution and final fates.

Massive close binary systems can also produce stellar winds that collide which allow estimates of the properties of the stellar wind (Bestenlehner et al., 2021). New, updated mass-loss rates for O-type stars suggest lower mass loss rates than previously thought (Björklund et al., 2021) and empirical mass loss rates are in agreement (Hawcroft et al., 2021). This has impacts for stellar evolution and the masses of compact remnants produced by massive stars in the Galaxy. If stars are close enough to each other, they can go into contact, e.g. VFTS 352 in the Tarantula Nebula. This can modify the T_{eff} (Abdul-Masih et al., 2019) and luminosity (Abdul-Masih et al., 2021) as compared to single stars. Large uncertainties regarding the nature and efficiency of the internal mixing mechanisms in these post-merger systems still exist and how these would manifest in observations. In addition, stellar evolution models and population synthesis of massive stars have also concluded that some observations are better explained by incorporating binaries (Vanbeveren et al., 1998; van Bever & Vanbeveren, 1998; Petrovic et al., 2005; Eldridge et al., 2008; de Mink et al., 2013; Zapartas et al., 2017; Yoon et al., 2017) Stellar mergers and mass transfer may impact the colour-magnitude diagrams of young clusters (Beasor et al., 2019; Britavskiy et al., 2019; Wang et al., 2020).

1.7 Aims of the Thesis

This thesis presents the results from six research papers, the goals of which are outlined below. Three of these projects make use a new stellar modelling technique that we developed called SNAPSHOT. This modelling approach allows us to systematically isolate key features of the internal abundance profile that impact the structure and surface properties of stars, in a way that is difficult to obtain from classical stellar evolution models, without fine-tuning of free parameters governing processes such as mass loss, overshooting etc.

1. The SNAPSHOT approach allows us to systematically investigate the connections between properties of the stellar interior and the surface properties explore over a wider range of stellar structures than are usually explored using single star (or binary) evolutionary models and apply these models to understand the properties of red supergiants and stripped stars (Chapter 3).

2. The systematic nature of the SNAPSHOT approach can help us to study how many different internal structures could correspond to a given set of L and $T_{\rm eff}$. This can allow us to investigate the degree of degeneracy between observable and non-observable stellar properties, e.g. RSGs at the pre-supernova stage (Chapter 4).

3. The evolution of massive stars is affected by a variety of physical processes including convection, rotation, mass loss and binary interaction. Because these processes modify the internal chemical abundance profiles in multiple ways simultaneously, it can be challenging to determine which properties of the stellar interior are primarily driving the overall evolution. The SNAPSHOT approach allows us to isolate the key features of the internal abundance profile that drive the evolution of massive stars (Chapter 5).

4. Given the widely predicted existence of the pair-instability mass gap and the apparent robustness of the boundary of the gap with respect to uncertainties in stellar evolution models, can a single star produce a BH remnant with a mass around 85 $M_\odot$? (Chapter 6)

5. Are blue supergiants in binary systems affect distance determinations using the observed flux-weighted gravity luminosity distribution?

6. What is the initial distribution of fossil magnetic fields for AB stars with masses of 1.6 to 3.4 $M_\odot$? (Chapter 7)

Chapter 2

Methods

There are several different codes that are used to model the evolution of stars, for example GENEC (e.g. Ekström et al., 2012), MESA (Paxton et al., 2011), FRANEC (e.g. Chieffi & Limongi, 2013b), STERN (e.g Heger et al., 2000), the Padova code (Bertelli et al., 2009), and the STAREVOL code (Decressin et al., 2009). The models presented in this thesis are computed using the MESA and GENEC stellar evolution codes.

2.1 Overview of MESA

MESA is an open-source software package capable of modelling the structure and evolution of stars. It was first presented in Paxton et al. (2011) and updated capabilities have been subsequently discussed in several instrument papers (Paxton et al., 2013, 2015, 2018, 2019). MESA can be now used to model the evolution of stars from the pre-main sequence to the white dwarf phase or to just before core collapse. It has a range of additional in-built modelling capabilities including for astero-seismology using `GYRE`, for nonlinear radial stellar pulsations that characterise RR Lyrae, Cepheids using `RSP`, for supernova light curves using a coupling with `STELLA` and for giant planets. MESA is organised into a suite of modules that provide a variety of numerical and physical data and routines. The physical modules include the `eos` module for the equation of state, `kap` for the opacity, `atm` for atmospheric boundary conditions, `chem` for the properties of elements and isotopes, `net` for nuclear reaction networks, `rates` for nuclear reaction rates, `neu` for thermal neutrino processes and `turb` for various mixing processes. The numerical modules include `auto_diff` for analytic derivaties, `const` for mathematical and astronomical constants and `math` and `mtx` for linear algebra routines. The `star` module solves the equations of stellar structure and evolution using the numerical and physical modules. The `binary` module models the evolution and interaction between stars in a binary system.

2.1.1 Equations of Stellar Structure and Evolution

The standard equations used to model the structure and evolution of stars are described below (e.g. Kippenhahn & Weigert, 1990). The equation for hydrostatic equilibrium can be expressed as:

$$\frac{\partial P}{\partial m} = -\frac{Gm}{4\pi r^4 \rho} \tag{2.1}$$

for a pressure P, radius r, mass coordinate m and density ρ. This equation can be modified to account for rotation (e.g. Maeder, 2009) or for cases when hydrostatic equilibrium is not an accurate assumption and an acceleration term must also be included e.g. the late nuclear burning phases of massive stars. The equation of mass continuity, which describes the conservation of mass throughout the star, can be expressed as:

$$\frac{\partial r}{\partial m} = \frac{1}{4\pi r^2 \rho} \tag{2.2}$$

The energy sources and sinks within the star are contained in the equation for energy conservation, which can be expressed as:

$$\frac{\partial l}{\partial m} = \epsilon_{\rm nuc} - \epsilon_{\nu} - \epsilon_{\rm grav} \tag{2.3}$$

where l is the luminosity at a given point inside the star, ϵ_{nuc} is a term describing the energy produced due to nuclear reactions, ϵ_{ν} is the energy lost due to neutrinos, T is the temperature. $\epsilon_{\rm grav}$ accounts for energy released or absorbed due to gravitational contraction or expansion within the star and can be expressed as:

$$\epsilon_{\rm grav} = c_{\rm P} T \left(\frac{1}{T}\frac{\partial T}{\partial t} - \frac{\nabla_{\rm ad}}{P}\frac{\partial P}{\partial t} \right) \tag{2.4}$$

where $\nabla_{\rm ad}$ is the adiabatic gradient, c_P is the heat capacity at constant pressure and t is time. Energy is transported in stars primarily by convection or radiation. The equation for energy transport can be expressed as:

$$\frac{dT}{dm} = -\frac{GmT}{4\pi r^4 P}\nabla \tag{2.5}$$

where κ is the opacity, a is the radiation constant and c is the speed of light. For transport by radiation, $\nabla = \nabla_{\rm rad}$ in Equation 2.5,

$$\nabla_{\rm rad} = \frac{3}{16\pi a c G}\frac{\kappa L_{\rm actual} P}{m T^4} \tag{2.6}$$

while for transport by convection ∇ is equal to $\nabla_{\rm ad}$ or the gradient that is obtained from mixing-length theory. Finally, the conversion of elements from one isotope to another by nuclear fusion for I elements can be expressed as:

$$\frac{\partial X_i}{\partial t} = \frac{m_i}{\rho}\left(\sum_j r_{ji} - \sum_j r_{jk}\right), i = 1, ..., I \tag{2.7}$$

In general, an element i can be affected simultaneously by many reactions, some of which create it (r_{ji}) and some of which destroy it (r_{jk}). These reaction rates give directly the change per second.

Stellar evolution code solves these equations to model the interior and surface properties of a star and how it evolves in time. To go with the equations of stellar structure and evolution, we need a set of boundary conditions for the radius r, mass r, luminosity l and temperature T. A range of physical effects need to be implemented to compute stellar evolution models, including convection, rotation, mass loss and binary interaction. As these processes cannot be computed a priori, stellar evolution codes contain a list of free parameters to include these processes in the model. Many of these parameters can be constrained to some reasonably small range based on theory or observations. However, all these free parameters create the potential for significant degeneracy in the output. As a result, the outputs of stellar evolution models should be interpreted carefully.

2.1.2 Microphysics inputs

A range of micro-physical inputs are required to compute a stellar evolution model, including nuclear reactions, opacities and an equation of state. In MESA, the nuclear reaction rates and the reaction pathways are provided by the Joint Institute for Nuclear Astrophysics (JINA) REACLIB library (Cyburt et al., 2010) as well as other tabulated weak reaction rates (Fuller et al., 1985; Oda et al., 1994; Langanke & Martínez-Pinedo, 2000), thermal neutrino loss rates from Itoh et al. (1996) and screening via the prescription of Chugunov et al. (2007).

The interaction of the radiation with the matter inside the star is modelled using the opacity κ. The opacity in the interior of stars is typically dominated by electron scattering $\kappa_{\rm sc}$ which can be approximated by $\kappa_{\rm sc} = 0.20(1+{\rm X})$, where X is the mass fraction of ^{1}H. Other sources of opacity include free-free transitions, bound-free transitions, bound-bound transitions, H minus and molecular opacities. Stellar evolution models use numerical opacity tables that provide the values of $\kappa(\rho, T)$ for a wide range of densities ρ and temperatures T are used. In MESA, radiative opacities are primarily from OPAL (Iglesias & Rogers, 1993, 1996), with low-temperature data from Ferguson et al. (2005). The high-temperature, Compton-scattering dominated regime by Buchler & Yueh (1976). Electron conduction opacities are from Cassisi et al. (2007).

An equation of state relating the pressure, temperature and density is also necessary to construct a solution to the stellar structure equations. The combination of the ideal gas and radiation pressure is usually a relatively good approximation for much of the stellar interior,

$$P = \frac{\rho k T}{\mu m_H} + \frac{1}{3} a T^4 \tag{2.8}$$

however in practice more detailed equations of state are usually used, to be applicable over a wide range of temperatures and pressures. The EOS in MESA is constructed using a blend of the EOS from OPAL (Rogers & Nayfonov, 2002), SCVH (Saumon et al., 1995), FreeEOS (Irwin, 2004), HELM (Timmes & Swesty, 2000), and PC (Potekhin & Chabrier, 2010). In evolutionary models of massive stars, inputs due to nuclear reaction rates, opacities and the EOS are generally not considered to be a source of significant uncertainty compared to other physical inputs. However, in some cases they may produce significant effects (e.g. Farmer et al., 2020; Chieffi et al., 2021) and should therefore be kept in mind when interpreting outputs from stellar evolution models.

2.1.3 Treatment of Convection

Energy is generated deep in stellar interiors by nuclear reactions and transported to the surface in two main ways: radiation and convection. Along with the effects of the hydrostatic structure and nuclear energy generation, the properties of the energy transport mechanism set the stellar structure and the surface properties. Despite its importance, the nature and efficiency of the energy transport in stars is often quite uncertain. This is because it is difficult to model convection in stellar interiors or to infer its behaviour from observations.

Convection is an intrinsically 3-D process that transports energy and mix material. In stars, convection develops when radiation is insufficient to transport the energy outwards. For the purpose of 1-D stellar evolution models, this limit is usually described by the Ledoux and Schwarzschild criteria (Kippenhahn & Weigert, 1990) which define the position in a star where there is a balance between the force from gravity and the buoyancy force. The Ledoux criterion states that a region remains stable against convection if

$$\nabla_{\rm rad} < \nabla_{\rm ad} + \frac{\varphi}{\delta} \nabla_\mu \tag{2.9}$$

where $\nabla_{\rm rad}$ and $\nabla_{\rm ad}$ are the radiative and adiabatic temperature gradients, ∇_μ is the gradient of the mean molecular weight, $\varphi \sim 1$ and $\delta \sim 1$ are derivatives of thermodynamic quantities. If Equation 2.9 is not satisfied, convection will occur. For homogenous regions with $\nabla_\mu = 0$, we have the Schwarzschild criterion,

$$\nabla_{\rm rad} < \nabla_{\rm ad} \tag{2.10}$$

If the criteria in Equation 2.9 and 2.10 favour stability, no convection will occur and all the energy will be transported by radiation. Stellar evolution models often assume instantaneous mixing within convective regions as the convective turnover timescale is (usually) much shorter than the time-step in the model. The usual method for modelling convection in 1-D stellar evolution codes is mixing-length theory (MLT). The basic hypothesis of MLT is that the fluid elements can be represented by an average cell, which moves over an average vertical distance l called the mixing length, before dissipating its energy excess. The mixing length l is a free parameter in stellar evolution models and is usually taken to be

$$l = \alpha_{\mathrm{MLT}} \, H_{\mathrm{P}} \tag{2.11}$$

where $\alpha_{\mathrm{MLT}} \sim 2$ is a free parameter. The value of α_{MLT} is uncertain and probably varies as a function of mass and metallicity (Chun et al., 2018). MLT can be implemented in stellar evolution models in several different ways (Böhm-Vitense, 1958; Cox & Giuli, 1968; Henyey et al., 1965). These may require the addition of further free parameters (e.g. $y \sim 1/3$ that sets the temperature gradient in a rising bubble and $\nu \sim 8$, a mixing length velocity multiplier). Further modifications to MLT by stellar evolution codes may be required in some cases, e.g. radiation dominated envelopes of massive stars in which the assumptions of MLT break down. The advantage of MLT is that it expresses the non-local phenomenon of convection in terms of local quantities, which facilitates the computation of stellar models. Although it can mimic convective energy transport, MLT is a significant simplification of how convection will actually behave.

Another significant difficulty with implementing convection in 1-D stellar evolution models is understanding how convection behaves at and near the boundaries of convective regions. When the Ledoux or Schwarzschild criteria are used, the velocity of the convective material at convective boundaries is non-zero, suggesting that the material could overshoot the convective region. However, due to the turbulent 3-D nature of convection, it is uncertain how large this overshooting distance is, or how efficient the mixing and energy transport are in the overshooting region. Efforts to investigate this behaviour with 3-D hydrodynamical models are in progress, however the high Reynolds numbers (high ratio of inertial forces to viscous forces) in these regions make the calculations extremely computationally intensive. In the absence of a robust 3-D hydrodynamical treatment of convection, mixing at convective boundaries is implemented in 1-D stellar evolution models by a convective overshooting prescription and the addition of a free parameter. The overshoot region is usually modelled in one of two ways. It can be modelled as a step-overshoot in which the convective boundary is extended by a distance d_{ov}, usually expressed as a fraction of the pressure scale height via a free parameter α_{ov}

$$d_{\mathrm{ov}} = \alpha_{\mathrm{ov}} \, H_{\mathrm{P}} \tag{2.12}$$

Alternatively, it can be modelled as an exponential diffusive overshoot (Herwig et al., 1997; Paxton et al., 2011) in which the diffusion coefficient in the overshoot region is given by

$$D_{\mathrm{OV}} = D_0 \exp\left(\frac{-2z}{f_{\mathrm{ov}} \, H_{\mathrm{P}}}\right) \tag{2.13}$$

where $f_{\rm ov} \sim 0.016$ is a free parameter. Many efforts have been made to constrain these parameters using observations (e.g. Brott et al., 2011b; Martinet et al., 2021), but this is a difficult process. It is likely that $\alpha_{\rm ov}$ and $f_{\rm ov}$ vary as a function of mass (Castro et al., 2014) and possibly depend on other factors such as metallicity.

The implementation of convection in 1-D stellar evolution models, with certain choices for the free parameters, can reproduce a wide range of observations of stars. However, large uncertainties in the values of the free parameters remain. In addition, 3-D simulations show that MLT does not capture certain important effects (e.g. Arnett et al., 2018, 2019; Cristini et al., 2019) . Meakin & Arnett (2007) used 3-D simulations to show that the assumption of zero net up/down kinetic energy flux by MLT is inaccurate. Cristini et al. (2017) computed 3-D models of convective carbon burning in a 15 $\mathrm{M}_\odot$ star using the Implicit Large Eddy Simulation paradigm (Margolin et al., 2006) and found that mass entrainment could be represented by its dependence on the luminosity, which drives convection, and the bulk Richardson number ($Ri_{\rm B}$), which defines the stiffness of the convective boundary. The relationship between the bulk Richardson number and mass entrainment from Cristini et al. (2017, 2019) were implemented in 1-D stellar evolution models by Scott et al. (2021) who found that convective boundary mixing increases with mass, consistent with results based on observations of the main sequence width (Castro et al., 2014; Martinet et al., 2021).

2.1.4 Numerical Methods

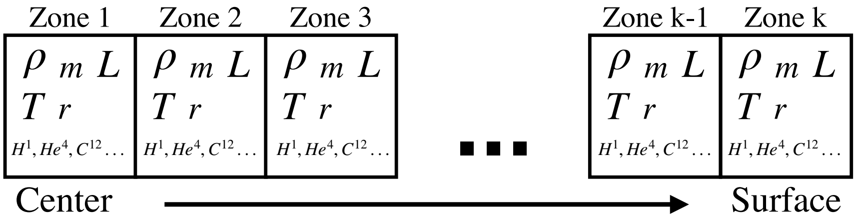

Figure 13: Schematic for division of star into k zones with several quantities tracked in each zone.

1-D stellar evolution codes use a variety of methods and numerical techniques. In general, the star is divided up into about 1 000 discrete concentric mass shells. Several basic variables are computed and tracked for each shell, including the mass, radius, temperature, density, luminosity and the mass fraction of each isotope. The basic strategy to evolve from one time-step to the next is to iteratively adjust a candidate solution to the equations of stellar structure using a Newton method until the residual is smaller than some acceptable threshold. Each time step, a block tridiagonal Jacobian matrix of partial derivates is computed using a candidate solution, a block tridiagonal system of linear equations is solved for the corrections to the candidate solution and the new residual is calculated. In MESA, the equations are written in the form $F($`basic_vars`$) = 0$ where F is the vector-valued function of the residuals and `basic_vars` is the solution attempt. The values of `basic_vars` are iteratively adjusted to reduce F, until the magnitude of F or the relative

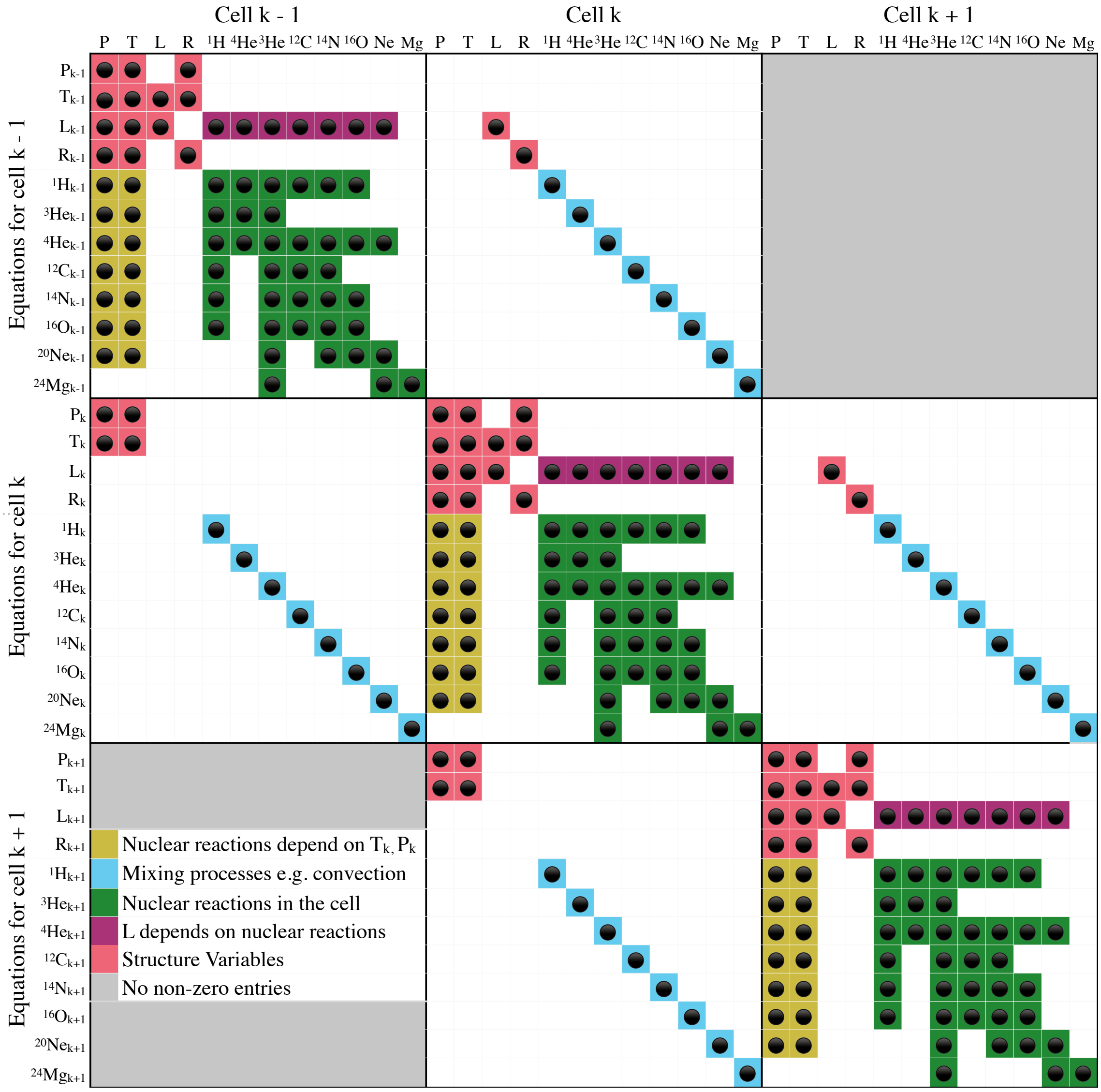

Figure 14: A sketch of the structure of a 3x3 subset of the tri-diagonal Jacobian matrix used to solve the equations of stellar structure. All non-zero entries are indicated by black circles. Inspired by Kippenhahn & Weigert (1990) and Paxton et al. (2013).

size of the adjustments to `basic_vars` fall below some acceptable threshold. The iterative adjustments to `basic_vars` are chosen using a Jacobian matrix of partial derivatives of the F equations with respect to the values of `basic_vars`.

The Jacobian matrix is a block tri-diagonal matrix with a size N equal to the number of zones in the model times the number of basic variables per zone. Fig. 14 shows the structure of a 3 x 3 subset of the block tri-diagonal Jacobian matrix representing the equations of stellar structure for 8 different chemical species. Note that usually at least 21 species are tracked. All non-zero entries are indicated by black circles. Regions shaded in light red indicate variables related to the structure of the star, i.e. pressure, temperature, luminosity and radius. Yellow regions represent the fact that the abundance of each isotope depend on nuclear reaction rates which depend on the values of temperature and pressure in that cell. Blue regions indicate that the abundances of each isotope depends on the abundance of the isotope in neighbouring cells due to the possibility of convective mixing. Green regions indicate the possible nuclear reaction pathways. Purple regions represent the fact that the luminosity depends on the abundances of each isotope through the nuclear reactions. Finally, grey regions indicate areas where all entries are equal to zero. Each block of the tri-diagonal matrix is indicated by black lines. The centre left block shows the dependency of the equations for cell k on the variables of cell $k-1$. The upper centre block shows the dependency of the equations for cell $k-1$ on the variables of cell k. The middle block shows the dependency of the equations for cell k on the variables of cell k. Given a candidate solution, the Jacobian matrix elements from microphysics (EOS, opacity, nuclear reaction rates), rotation and MLT are evaluated in parallel to speed up the computation time. In high resolution models, that can have up to 15 000 zones, or with large nuclear reaction nets, the size of the Jacobian matrix can be very large, with $N > 100\,000$, which can make it very difficult to converge to a solution.

At the beginning of the computation of a model, MESA `star` reads the input files are read and allocates memory space for the model. The modules related to the isotope data, nuclear reactions, the equation of state, opacity and physical constants are initialised and the relevant starting model is loaded into memory. The model is now ready to evolve forward in time. Each time step, MESA first checks to see if the spatial mesh needs to be modified. This allows more zones to be inserted if necessary and unnecessary zones to be removed. Various quantities are calculated, including thermodynamic gradients and the properties of the overshooting regions and the total amount of mass to be added/removed from the star during the time step. After these preparations, the mass is added or removed from the star and the Lagrangian mass derivatives are updated. The new structure and composition of the star is then solved for using repeated Newton iterations as described above. If the candidate solution is satisfactory and consistent with the desired spatial and temporal resolution, the model is accepted. The outputs of the model calculation are written to a file and the duration of the following time-step is calculated.

Control of the spatial mesh and the time step is very important for computing stellar evolution models. The properties stellar interior can sometimes change significantly over a small region. These regions need to be resolved at a high resolution. The timescales involved in different stages of a star's life vary over many orders of magnitude, from 10 Gyr for the lifetime of a $1\,\mathrm{M}_\odot$ star to 1 day for the silicon burning phase of a massive star. The time step in a stellar evolution model must be small enough to allow convergence in a small number of iterations but large enough to allow the full evolution of a star to be computed in a practical amount of time. At the end of each time step, MESA calculates the value of the time step in years for the model's next time step. This calculation takes a number of factors into account, such as the length of the previous time step and the likely change in the stellar model from one time-step to the next.

2.2 SNAPSHOT Stellar Structure Models: Our New Approach

2.2.1 Motivation

Stellar evolution models have lead to great advances in the understanding of the evolution of massive stars. In addition to standard evolutionary models, a range of additional stellar modelling techniques have been used to understand how stars behave. In Farrell et al. (2020b, 2021a), we introduced our method called SNAPSHOT which allow us to systematically isolate the effect of one property of the internal abundance profile at a time. SNAPSHOT models are static stellar structure models in hydrostatic and thermal equilibrium computed in such a way that allows significant flexibility in how the models are computed. SNAPSHOT models are static stellar structure models in hydrostatic and thermal equilibrium. They are a snapshot at just one moment during a star's evolution, so they are not evolving in time. This type of approach to stellar models was first used by Cox & Giuli (1961). It was further developed by Giannone & Weigert (1967) and Giannone et al. (1968) to study core-Helium burning stars at low and intermediate masses, and by Lauterborn et al. (1971a,b) to study the occurrence of blue loops of intermediate mass stars in the HR diagram. Some of these earlier approaches used very simple internal structures. In Farrell et al. (2020a,b, 2021a), we take advantage of the advancements in stellar evolution and computational capabilities over the last decades to produce grids of state-of-the-art SNAPSHOT models in a systematic and comprehensive way. The main purpose of Farrell et al. (2020b) was to systematically produce a grid of stellar structure models in hydrostatic and thermal equilibrium, based on three important structural properties: $M_{\rm core}$, $M_{\rm env}$ and the core composition. The models were constructed in a way that allows us to vary the value of one structural property, while keeping the other properties constant, e.g. varying $M_{\rm env}$ while keeping $M_{\rm core}$, $X_{\rm c}$ and $Y_{\rm c}$ constant. This allows us to isolate the effect of each structural property on the surface properties of the star. These models were applied to study stars stripped of their envelope through binary interaction (Farrell et al., 2020b) and the properties of red supergiants at the pre-supernova stage in (Farrell et al., 2020a). In Farrell et al. (2021a), we extended our SNAPSHOT method to try to isolate the key features of the internal abundance profile that drive the evolution of massive stars. The SNAPSHOT approach has several advantages:

1. The surface properties of a star depend on its internal structure. The SNAPSHOT approach allows us to make direct connections between the properties of the internal abundance profile, e.g. $M_{\rm core}$, $M_{\rm env}$, $Y_{\rm c}$ or helium profile in the hydrogen shell, and the surface properties, L and $T_{\rm eff}$. For example, with this approach we can directly compare between two core-He burning stars with exactly the same Helium core, but with different $M_{\rm env}$. These types of comparisons are difficult to obtain from classical stellar evolution models without fine-tuning of processes such as mass loss,

overshooting etc.

2. It is often difficult to disentangle cause and effect in stellar evolution. The equations of stellar structure and evolution are non-linear and processes such as rotation, convection etc. can combine and interact to produce complex effects on the evolution of a star. It is often challenging to connect these evolutionary effects to a particular physical process or combination of processes. Our approach using SNAPSHOT stellar models is not subject to such complex evolutionary effects, which allows us to more easily disentangle connections between internal and surface properties. These connections can then be used to help establish cause and effect in stellar evolution models.

3. A wider range of stellar structures can be produced with SNAPSHOT models than are currently obtained in stellar evolution calculations. Stellar evolution calculations always include prescriptions for computing effects such as mass loss and effects of close binary interactions such as Roche-Lobe Overflow. These prescriptions may limit the range of stellar structures that are produced in evolutionary calculations. Our method allows us to compute stellar structures that may not be produced in stellar evolution calculations and to see if they correspond to observations.

4. SNAPSHOT models can help us to study how many different internal structures could correspond to a given set of observed properties (such as L and $T_{\rm eff}$). This is very important, as it will allow us to determine the degree of degeneracy between observable and non-observable stellar properties. For instance, the actual/initial mass of a stars is often deduced from its observed position in the HR diagram using stellar evolution models. The result from this procedure depends on the set of stellar evolution models that are used and their assumptions about convection, binary interaction etc. The SNAPSHOT model approach may allow a better estimate of the degree of uncertainty of these deductions. It may also provide some hints into what kinds of additional observations could help to reduce the degeneracy.

5. The results from SNAPSHOT models may be useful for improving the approximations used in rapid stellar evolution algorithms to compute single and binary population synthesis models (e.g., Eggleton & Tout, 1989; Pols et al., 1995; Tout et al., 1996, 1997; Hurley et al., 2000, 2002).

6. The SNAPSHOT models also allow an investigation of the sensitivity of the position of stellar models in the HR diagram with respect to changes in the internal abundance profile in a quantitative way. Understanding the key properties that set the luminosity and effective temperature can provide a new way to interpret observations of individual stars and stellar populations in terms of the structural properties that favour a given set of observed properties. This cannot be done by more simplified

techniques such as homology relations or polytropic models. Many different properties of the internal abundance profile can be studied in this way including aspects governed by mixing processes, e.g. the quantity of helium in the hydrogen burning shell, or by mass loss processes, e.g. the mass of the envelope.

2.2.2 How SNAPSHOT Models are Computed

Our SNAPSHOT models are computed using the MESA software package (r15140, Paxton et al., 2011, 2013, 2015, 2018, 2019), but the underlying method can be implemented with any stellar evolution code. Our method can be summarised in the following steps:

1. We first compute a stellar evolution model at a given mass and metallicity and then save a snapshot at the desired evolutionary stage (a `.mod` file in MESA). The purpose of this is to generate a starting stellar model which will then be modified. For these evolutionary models, we use a standard set of physical ingredients, the same as described in Farrell et al. (2020b). However, the exact choices for the physical inputs such as convective overshooting, rotation or even binary interaction are not very important because the model will be modified in the next step.

2. Once we have an appropriate starting stellar model, we directly modify part of the model file by hand (the `.mod` file in MESA). For example, we might modify the abundance profile in a specific region, or add or remove mass. This part can easily be done in a controlled way, varying only one property at a time.

3. We then insert the model file back into MESA to find a solution to the stellar structure equations in hydrostatic and thermal equilibrium with the new abundance profile. During this stage, we make the following changes to the usual stellar evolution inputs to prevent the star from evolving as usual:

   (a) The changes in abundances of the chemical elements due to nuclear burning are turned off. This can be achieved in MESA by setting `dxdt_nuc_factor = 0`. This allows the energy produced by nuclear reactions to remain the same, but prevents the chemical abundances from changing which prevents the star from evolving.

   (b) All mixing is turned off by setting `mix_factor = 0`. In addition, element diffusion is turned off by setting `do_element_diffusion = 0`.

   (c) All mass loss is turned off.

   As long as the abundance profile or mass was not modified too much, we found that MESA usually converged to a stable solution relatively quickly. As the model is not evolving in time due to nuclear reactions, a long time-step in MESA indicates that the model has reached thermal equilibrium. Therefore, we stop once the model has reached a time of 10^7 yr.

4. We then allow convective mixing to briefly take place under standard evolutionary conditions so that the new solution is consistent with the criterion for convection. Sometimes this causes mixing and changes the chemical profiles inside the model. During this phase, we apply several stopping criteria to establish when the model has reached thermal equilibrium:

    (a) The total energy released/absorbed from gravitational contraction/expansion, i.e. from the $\epsilon_{\rm grav}$ term, must be less than 1% of the total energy from nuclear reactions.

    (b) The maximum value of $\epsilon_{\rm grav}$ must be less than 10% of the maximum value of $\epsilon_{\rm nuc}$.

    (c) The maximum relative change in the internal luminosity profile from one cell to the next must be 25%.

    We performed tests to verify that our models are in equilibrium by evolving them for a short amount in time to check that they don't change significantly.

These steps are repeated many times as required to construct a series of models in which one feature of the internal abundance profile is changed at a time, e.g. the envelope mass (e.g. Farrell et al., 2020b) or the hydrogen abundance in the envelope (e.g. Farrell et al., 2021a). If the envelope mass is the quantity being isolated, an alternative option to step 2 is to use a routine in MESA called `mass_change` which allows an arbitrary mass-loss rate or mass-accretion rate from/to the surface of the star. Once can set a very low rate of mass loss/accretion to be $10^{-12}\mathrm{M}_{\odot}$/yr, which allows the model to remain close to thermal equilibrium when possible, and then use steps 3 and 4 as normal to ensure that the final model is in thermal equilibrium. This allows the envelope mass to be smoothly and efficiently changed in very small steps, which can help MESA to find a solution to the equations.

Chapter 3

SNAPSHOT: Connections between Internal and Surface Properties of Massive Stars

The contents of this chapter were published in Farrell et al. (2020), MNRAS, 495, 4, 4659.

3.1 Method

A systematic method to compute stellar structure models with a range of core compositions, core masses and envelope masses requires an alternative approach to the usual methods for computing stellar evolution models*. In Fig. 15, we provide a schematic outline of our approach to compute SNAPSHOT stellar structure models. We use the MESA software instrument (r10398; Paxton et al., 2011, 2013, 2015, 2018, 2019) to compute our models. Our method can be summarised in the following three steps:

1. To produce the initial stellar structures with a given $M_{\rm core}$, $M_{\rm env}$ and core composition, we compute a stellar evolution model with MESA from the zero-age main sequence until the end of core-He burning.
2. Using the stellar structures produced in (i), we modify some of the input controls to allow us to change the total mass of the star, without the star evolving.
3. We allow the modified structures from (ii) to relax to hydrostatic and thermal equilibrium.

---

*In principle, it is possible to compute a stellar evolution model and fine-tune the input parameters governing various physical processes e.g. mass loss, convective core-overshooting or binary interaction to achieve a desired combination of core composition, $M_{\rm core}$ and $M_{\rm env}$. However, this would be difficult to do in a systematic way as these processes often have complex interactions and feedback effects that affect the evolution of the star. For example, larger convective core overshooting produces a more massive core, a higher luminosity and higher mass-loss rates which can then affect the mass of the core.

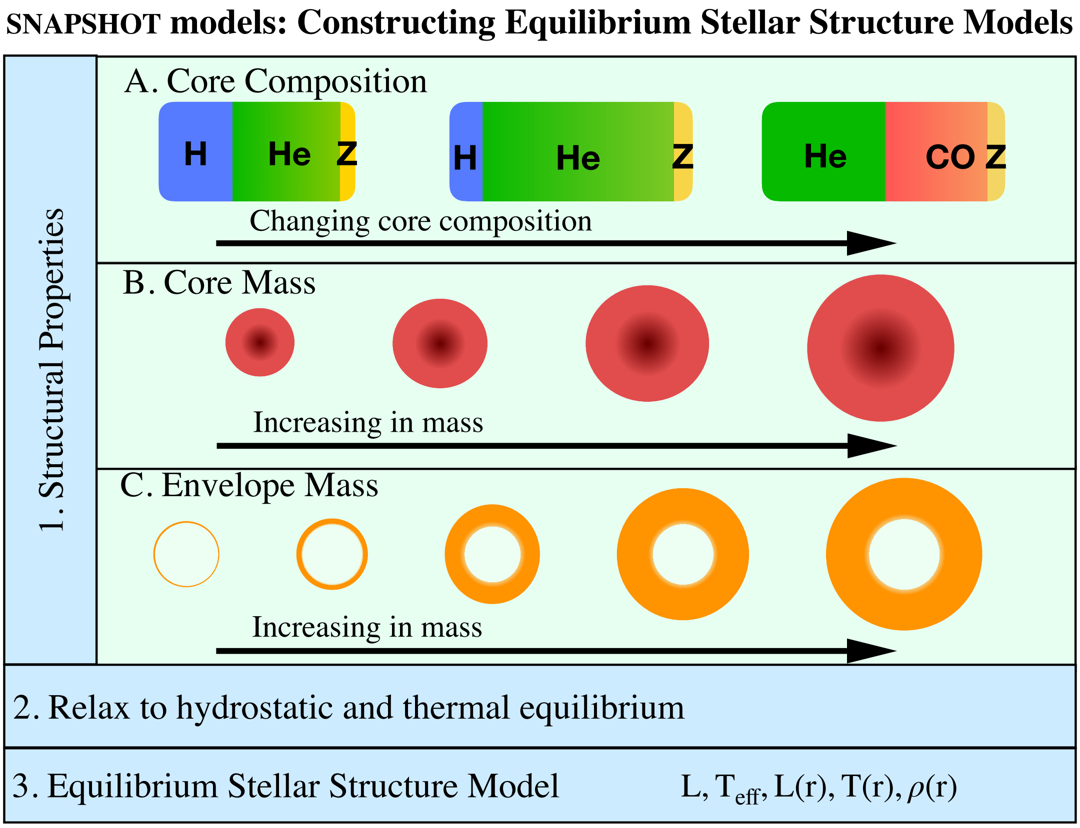

Figure 15: Schematic outline of the construction of SNAPSHOT stellar structure models with different core compositions, core masses and envelope masses. We first select a core composition (1A). Secondly, we select a core mass to go with this core composition (1B). Finally, we select an envelope mass (1C). Using a stellar evolution code, the models are allowed to relax to a state of hydrostatic and thermal equilibrium (2). The final stellar model produces both the surface properties, e.g. luminosity and effective temperature, as well as the interior profiles of the standard quantities, e.g. temperature, luminosity, and density (3). See Sec. 3.1 for more details.

We would like to emphasise that our approach is very flexible and can easily be updated to include new physics. Secondly, we will provide all our input files online and, as MESA is open-source, the SNAPSHOT method can easily be implemented by others. Thirdly, our method also benefits from the active development in the MESA code in improving and updating the physical ingredients in the models.

The first step involves computing a stellar evolution model with MESA from the zero-age main-sequence until the end of core-He burning. For these models, we adopt similar physical inputs as in the MIST grid of stellar evolution models (Choi et al., 2016), which were also computed using MESA. We discuss the potential effects of the input physics in Sec. 3.4.3. We choose to apply this technique to study massive stars ($> 8M_{\odot}$) at solar metallicity for this paper, but the same technique can also be applied to intermediate and low mass stars and also to stars at different metallicities. This simply requires computing a suitable initial stellar evolution model. Our core-He burning stellar structure models have Helium core masses of 2 to $9M_{\odot}$. These cores correspond to stellar evolution models with initial masses of 8 to 25$\mathrm{M}_{\odot}$ assuming our physical inputs detailed below. We explore a wide range of M_{env} from 0 to 50$\mathrm{M}_{\odot}$, so that the total masses of our core-H and core-He burning models range from 2 to 59$\mathrm{M}_{\odot}$. We explore core-H burning stellar structure models with values of X_{c} from 0.70 to 0.05 and core-He burning models with $Y_{\mathrm{c}} = 0.50$ and 0.01. We summarise the physical ingredients that we use below.

1. We adopt a solar metallicity of Z = 0.020 (with the solar abundance scale from Grevesse & Sauval (1998)) for all models, with an initial He abundance of 0.26. The exact value of the metallicity, C, N, O and Fe abundances affect the stellar properties.
2. For mass loss, we use the 'Dutch' wind scheme in MESA with the default scaling factor of 1.0. This wind scheme combines mass-loss rates from Vink et al. (2001) and Nugis & Lamers (2000) for hot stars ($> 10^4$K) and from de Jager et al. (1988) for cool stars ($< 10^4$K).
3. We use the Ledoux criterion for convective stability, with a semi-convective efficiency of $\alpha_{\mathrm{sc}} = 0.1$.
4. We use a time-dependent, diffusive convective core-overshooting parameter (Herwig, 2000; Paxton et al., 2011). We adopt the same overshooting parameters as in the MIST models (Choi et al., 2016) with core overshooting of $f_{\mathrm{ov,core}} = 0.016$ (roughly equivalent to $\alpha_{\mathrm{ov}} = 0.2$ in the step overshoot scheme), and $f_{\mathrm{ov,shell}} = f_{\mathrm{ov,env}} = 0.0174$.
5. For most of the models, we use the standard mixing-length theory to model convective mixing, with a mixing-length parameter of $\alpha_{\mathrm{mlt}} = 1.82$. For some of the higher mass models, in order to allow the models to converge it was necessary to use a modified treatment of convection known as MLT++ (Paxton et al., 2013). MLT++ reduces the temperature gradient in some radiation-dominated convective regions to make it closer to the adiabatic gradient. This boosts the efficiency of energy transport which allows the model to run with reasonable timesteps.
6. As a surface boundary condition, we use the `simple_photosphere` option in MESA (Paxton et al., 2011).
7. We adopt the `mesa_49.net` nuclear network in MESA which tracks and solves for the abundances of 49 species.
8. The models are all non-rotating.

For each stellar evolution model, we save snapshots at two points during core-H burning (for $X_{\mathrm{c}} = 0.35$ and 0.05) and two points during core-He burning (for $Y_{\mathrm{c}} = 0.50$ and 0.01). In principle, any core composition can be studied, as long as the star is in thermal equilibrium. We take the snapshot models we saved from the stellar evolution models and change the value of M_{env} without the star evolving. To do this, we modify the following inputs in MESA to effectively pause the evolution of the star:

1. We turn off changes in abundances of the chemical elements due to nuclear burning by setting `dxdt_nuc_factor = 0` in MESA. This allows the nuclear energy generation rates to remain the same, but prevents the chemical abundances from changing.
2. We turn off element diffusion by setting `do_element_diffusion = 0` and turn off all other mixing by setting `mix_factor = 0`.
3. We turn mass loss off.

While the evolution of the star is paused, we use a routine in MESA called `mass_change` which allows an arbitrary mass-loss rate or mass-accretion rate from/to the surface of the star. We set the rate of mass loss/accretion to be $10^{-12}\mathrm{M}_\odot/\mathrm{yr}$. This low value ensures that the star will remain in thermal equilibrium while it is accreting or losing mass. We set the chemical abundance of the accreted material to be the same as the surface abundances. For each of the core masses and core compositions, we allow the star to lose mass until the H-rich envelope is stripped entirely, and to accrete mass until the star reaches an envelope mass of $50\mathrm{M}_\odot$ (as defined when we start to modify the mass). For each core, we save models for a range of M_{env}.

We allow every model to relax to hydrostatic and thermal equilibrium by restarting the evolution, with mass loss turned off but with all other physical inputs unchanged from the initial stellar evolution. This allows the convective core to readjust to the modified structure. We set a stopping criterion for these models based on $L_{\mathrm{nuc}}/L_{\mathrm{total}}$, the ratio of the total nuclear energy generation to the total luminosity of the star. The time for the models to mix by convection and relax to thermal equilibrium is typically on the order of ~ 1 kyr or less.

3.2 Application to Main Sequence Stars

In this section, we apply our SNAPSHOT method to MS stars i.e. core-H burning stellar structures. We analyse our core-H burning models in terms of three structural properties, the convective core mass (M_{core}), the envelope mass (M_{env}) and the central hydrogen abundance (X_{c}). We define the envelope as the rest of the star above the convective core. For models to which we have added mass, we find that the size of the convective core adjusts to the new stellar structure during the relaxation procedure. Material from the H-rich envelope mixes with H-depleted material in the core, the convective core increases in mass and the value of X_{c} increases. This so-called "rejuvenation" phenomenon in MS stars, in which a star can accrete from its companion and end up with a higher value of X_{c} than before the mass transfer episode, has been well studied in various stellar evolution contexts (e.g., Hellings, 1983, 1984; Schneider et al., 2014). Whether or not rejuvenation will take place depends on the treatment of convective stability and the choice of the semi-convective efficiency α_{sc} (Braun & Langer, 1995).

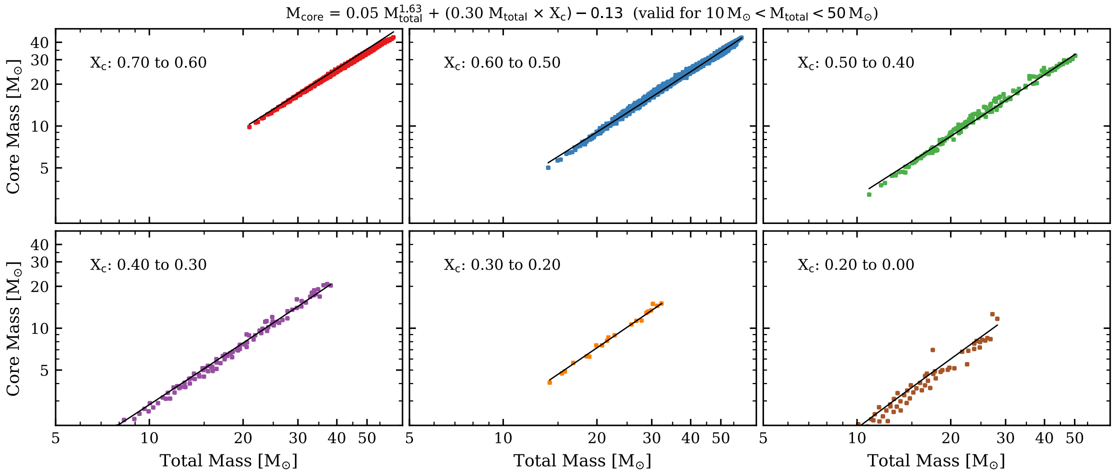

Figure 16: Convective core mass as a function of the total mass for core-H burning models. The models are divided up into bins according to X_c as indicated in each plot. The best fit line for each X_c is plotted in black and corresponding equations relating M_{core} and the total mass M_{total} are indicated in the upper left of each subplot.

Our core-H burning structure models have M_{core} ranging from 1 to 45M$_\odot$, M_{env} from 6 to 18M$_\odot$ and X_c from 0.70 to 0.05. We find that the combinations of M_{core}, M_{env} and core composition are quite limited (Figs. 75 and 16). We indicate the values of M_{core}, M_{env} and X_c in Fig. 75 in Appendix 10.1, where we plot the values of M_{env} and M_{core} for different values of X_c. In Fig. 16, we plot the relationship between M_{core} and M_{total}. For a core-H burning star, the value of M_{core} is determined by the total mass of the star and the value of X_c. We fit the following function relating the total stellar mass M_{total}, the convective core mass M_{core} and X_c:

$$M_{core} = aM_{total}^{d} + bM_{total}X_c + c \tag{3.1}$$

We obtain best fit values of a = 0.045, b = 0.304, c = -0.133 and d = 1.627. For a star of a given total mass, the convective core mass is lower for models with lower X_c, as expected from stellar evolution models. Furthermore, the dependence of M_{core} on X_c is steeper for larger stellar masses. While the value of the convective core mass for a given total mass depends on our assumptions for convective overshooting, the overall trends observed in Fig. 16 do not depend on overshooting assumptions.

The mass of the convective core in core-H burning stars as a function of mass has been studied before for models at the beginning of the main sequence (Schwarzschild & Härm, 1958; Schwarzschild, 1961; Stothers, 1970, 1974; Maeder, 1980; Maeder & Mermilliod, 1981; Maeder & Meynet, 1987, 1988, 1989; Langer et al., 1989; Pols et al., 1998), by Stothers & Chin (1985) at the beginning and end of the MS, and by many others as in the context of stellar evolution models. Here, we make a connection between the M_{core}, the total stellar mass and X_c (Fig. 16), providing fits for the convective core mass for a range of stellar masses and core compositions that can be easily used by the community. These calculations are useful for a number of reasons, for instance in rapid binary stellar evolution algorithms for computing population synthesis models (e.g., Belczynski et al., 2002; van Bever & Vanbeveren, 1998; Hurley et al., 2000, 2002; Izzard et al., 2006; Belczynski et al., 2008; Eldridge et al., 2008; Eldridge & Stanway, 2009; de Mink & Belczynski, 2015; Eldridge et al., 2017) where stellar properties need to be updated after a mass transfer episode.

We have compared the location of our core-H burning SNAPSHOT models in the HR diagram to standard MESA stellar evolution models (Choi et al., 2016) and they are consistent, as expected. For the sake of brevity we do not include these comparisons here, as it is a well known result (e.g Henyey et al., 1959a). Further tests show that the luminosity and $T_{\rm eff}$ of core-H burning SNAPSHOT stellar structure models not depend very much on the amount of overshooting. Models with no overshooting and with the the overshooting assumptions we adopt in this paper differ by about 0.01 dex in $\log \mathrm{L/L_\odot}$ and $\log T_{\rm eff}$ despite the differences in convective core masses.

3.3 Application to Post-Main Sequence Stars

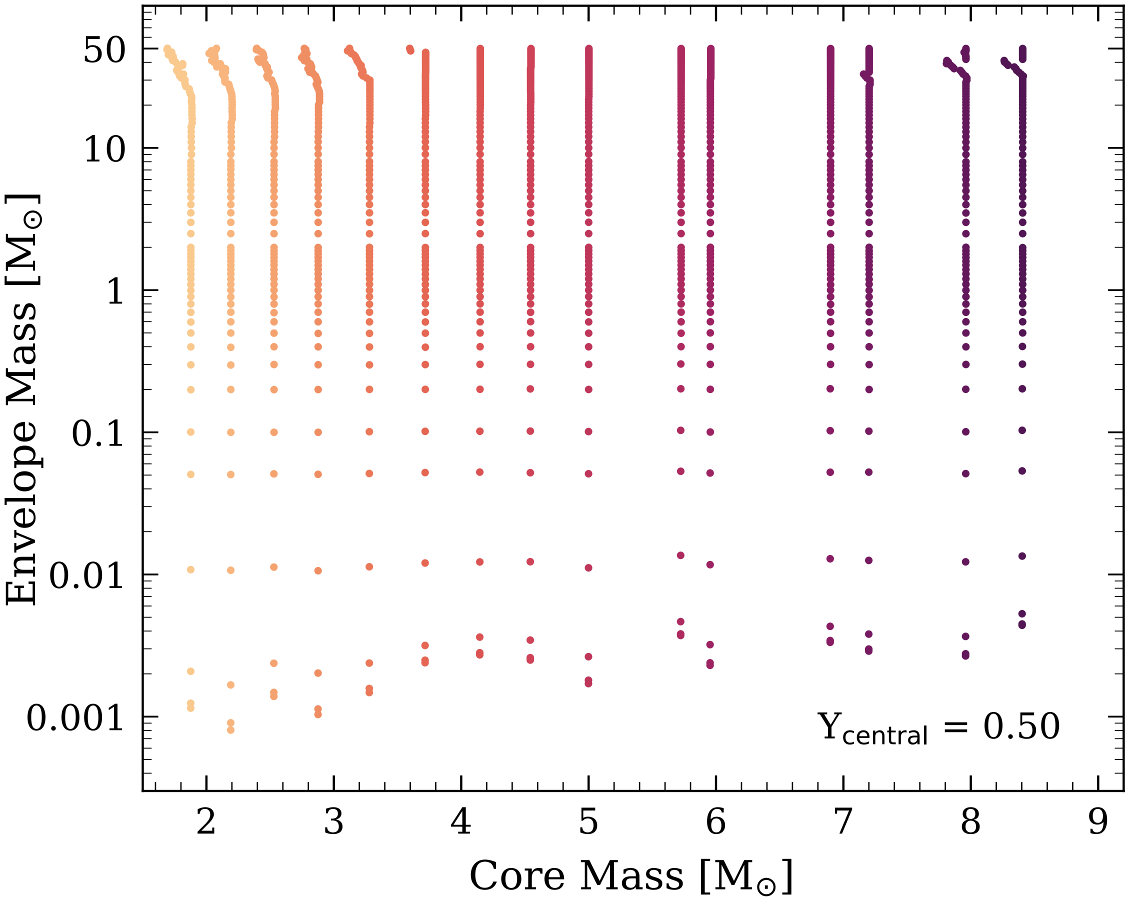

Figure 17: Envelope mass as a function of the core mass for our core-He burning models with $Y_{\rm c} = 0.50$. The colours indicate structure models with the same core mass.

In this section, we apply our SNAPSHOT technique to post-MS core-Helium burning stars. We construct core-He burning SNAPSHOT structure models based on three structural properties: the Helium core mass $M_{\rm core}$, the H-rich envelope mass $M_{\rm env}$ and the central He abundance $Y_{\rm c}$. The He-core is defined as the central Hydrogen depleted region where $X < 10^{-4}$. The H-envelope is defined as the rest of the star above the He-core. Our models have He-core masses ranging from $M_{\rm core} = 2$ to $9{\rm M}_{\odot}$[†], envelope masses of $M_{\rm env} = 0.001$ to $50{\rm M}_{\odot}$ and a central Helium abundance of $Y_{\rm c} = 0.50$ and 0.01.

Figure 17 shows the values of $M_{\rm core}$ and $M_{\rm env}$ for our core-He burning models with $Y_{\rm c} = 0.50$. Each point corresponds to an individual SNAPSHOT stellar structure model. A similar figure for models with $Y_{\rm c} = 0.01$ is included in Appendix 10.2. In contrast to core-H burning stars (Figs. 16 and 75), core-He burning stars in thermal equilibrium can have a wide range of combinations of $M_{\rm core}$, $M_{\rm env}$ and $Y_{\rm c}$ (Fig. 17). The difference in the variety of stellar structures for core-He and core-H burning stars is due to the fact that there are (usually) two nuclear burning regions in core-He burning stars (the He-core and H-shell), while there is only one burning region in core-H burning stars. To understand the difference, we can consider what happens if we begin with a star in hydrostatic and thermal equilibrium with a given $M_{\rm core}$ and $M_{\rm env}$, and then very slowly increase $M_{\rm env}$, such that the star remains in thermal equilibrium. The star must respond by readjusting its structure to support the increased mass. With only one nuclear burning region, a core-H burning star can respond only by producing more energy in its core. An increased mass changes the mechanical equilibrium structure of the star. The pressure and temperature gradients inside the star must increase to support the increased mass. As a result, the central temperature increases and hence the nuclear reaction rates in the core increase.This will generally cause an increase in the mass of the convective core, depending on the assumptions for mixing, particularly semi-convection. In contrast, a core-He burning star, with two nuclear burning regions (the He-core and the H-shell), could respond to the increased mass by modifying its mechanical equilibrium in a way that results in an increase in the the energy production in either the He-core, the H-shell or some combination. Our models show that, in almost all cases, core-He burning stars respond to an increase in the total mass in a way that increases the energy production in the H-shell. The value of $M_{\rm env}$ can change over a wide range without significantly modifying the conditions in the He-core, such as the central temperature (Appendix 10.3). This leads to the wide variety of combinations of $M_{\rm core}$ and $M_{\rm env}$ for core-He burning stars.

In Fig. 18, we summarise the results we obtain for our core-He burning models by plotting the value of $T_{\rm eff}$ as a function of the core mass ratio. Each line consists of models with constant $M_{\rm core}$, a constant $Y_{\rm c} = 0.50$ and $M_{\rm env}$ varying from 0 to $50{\rm M}_{\odot}$ (same models as Fig. 26d). Dashed lines indicate a sharp transition from red supergiants to hotter, more luminous stellar structures due to a bi-stability in the stellar structure equations. To put our results in context, we discuss connections between our SNAPSHOT models

---

[†] These He-core masses correspond to initial masses of $8 - 25{\rm M}_{\odot}$, assuming single star evolution with our physical ingredients.

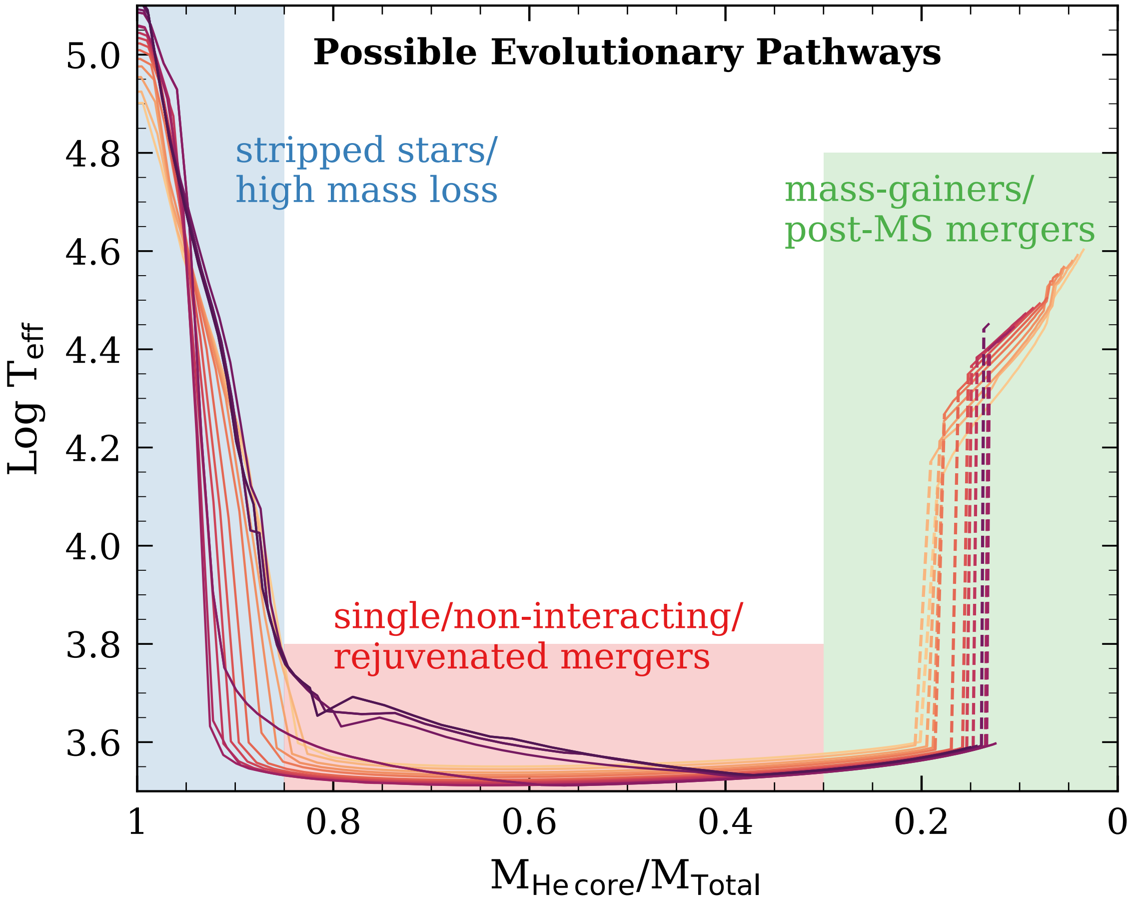

Figure 18: Effective temperature as a function of the core mass ratio for core-He burning models with constant $M_{\rm core}$, $Y_{\rm c} = 0.01$ and $M_{\rm env}$ varying from 0 to 50M$_\odot$ (same models as in panel d of Fig. 26). We roughly sketch possible binary evolutionary pathways which may produce the same stellar structures as these models.

and stellar evolution pathways.

Stellar structures with high core mass ratios (shaded in blue in Fig. 18) correspond to stripped stars with low values of $M_{\rm env}$. Most stripped stars are expected to form in binary systems when the primary star expands after the MS, fills its Roche-Lobe and is stripped of its envelope by the secondary (Podsiadlowski et al., 1992). Some may also form due to high mass loss from a single star (Groh et al., 2013b). These stars correspond to Regime I of the core-He burning models discussed in Sec. 3.3.1. Stellar structures with intermediate core mass ratios (shaded in red in Fig. 18) are mostly red supergiants. They are expected to be formed by single stars, non-interacting stars in binary systems or stars that rejuvenate after accreting mass. These stars correspond to Regime II in Sec. 3.3.1. Stars with lower core mass ratios $\lesssim 0.2$ probably only form in binary systems, either as the product of mass-accretion or a post-MS merger (e.g., Eldridge et al., 2017; Zapartas et al., 2019). For example, a merger between a core-He burning star and a relatively massive main sequence companion could produce a star with a small He-core and a very high mass H-rich envelope (e.g., Justham et al., 2014). These stars may resemble OB-type stars or

Table 3.1: Summary of surface properties for Models A – G with a He-core mass of $4.1 M_\odot$ and a central Helium abundance of 0.50. $M_{\rm env}$ indicates the mass of the H-rich envelope above the He-core. $F_{\rm H-shell}$ refers to the fraction of the total nuclear energy that is generated by H-Shell burning.

Model	$M_{\rm core}$ [$M_\odot$]	$M_{\rm env}$ [$M_\odot$]	$M_{\rm total}$ [$M_\odot$]	$\log T_{\rm eff}$ [K]	$T_{\rm eff}$ [K]	$\log {\rm L/L_\odot}$	$\log g$	$\log {\rm R/R_\odot}$	$F_{\rm H-shell}$
A	4.1	0.0	4.1	4.96	91700	4.37	5.48	-0.21	0.00
B	4.1	0.5	4.6	4.45	28000	4.53	3.32	0.89	0.17
C	4.1	2.0	6.1	3.53	3390	4.58	-0.28	2.76	0.28
D	4.1	6.0	10.1	3.54	3460	4.59	-0.04	2.74	0.30
E	4.1	17.0	21.1	3.58	3800	4.61	0.42	2.67	0.34
F	4.1	18.0	22.1	4.29	19620	5.04	2.87	1.46	0.75
G	4.1	50.0	54.1	4.51	32590	5.73	3.44	1.36	0.95

blue supergiants (BSGs) and they correspond to Regime III from Sec. 3.3.1. They lie to the right of the MS in the HR diagram which may help to explain observations of a large number of stars in this location in the HR diagram (Castro et al., 2014).

In the following sections, we discuss our core-He burning models in detail and describe the connections between internal and surface properties when varying $M_{\rm env}$ (Sec. 3.3.1), $M_{\rm core}$ (Sec. 3.3.2), and $Y_{\rm c}$ (Sec. 3.3.3).

3.3.1 Effect of Envelope Mass

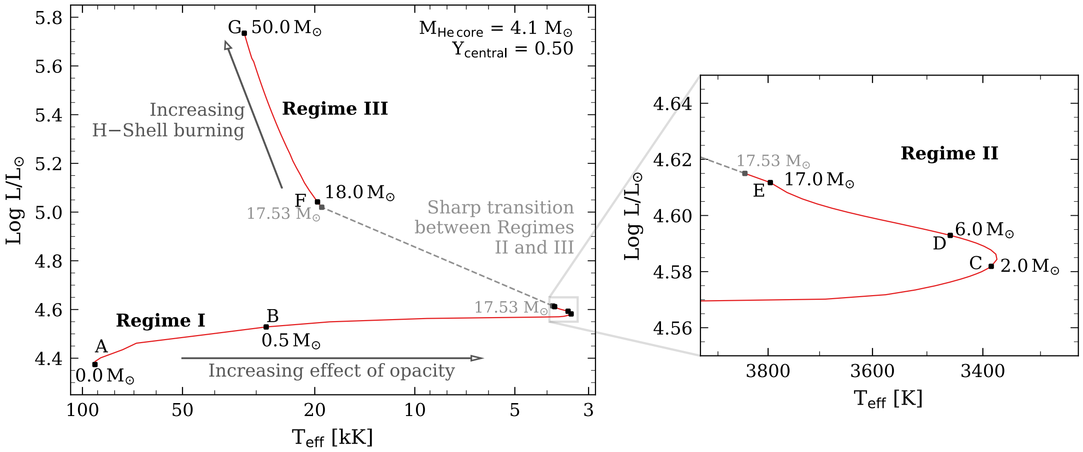

Figure 19: HR diagram showing core-He burning models with $M_{\rm core} = 4.1 {\rm M}_\odot$, $Y_{\rm c} = 0.50$ and varying H-rich envelope mass in the range $0 - 50 {\rm M}_\odot$ ($M_{\rm env}$ indicated in brackets). We label 7 representative models (A – G) to discuss the trends in the surface properties as a function of envelope mass (Sects. 3.3.1, 3.3.1 and 3.3.1). The right panel shows a zoom-in of the RSG region (models C, D and E).

To analyse how the surface properties of a core-He burning star depend on the mass of the H-envelope, we discuss a representative set of models with the same He-core mass and composition ($M_{\rm core} = 4.1 {\rm M}_\odot$ and $Y_{\rm c} = 0.50$) and different envelope masses ($M_{\rm env}$ ranges from 0.0 to $50.0 {\rm M}_\odot$). We choose this particular set of models as its core properties are representative of massive core-He burning stars. A He-core mass of $4.1 {\rm M}_\odot$ corresponds to an initial mass of $\sim 14 {\rm M}_\odot$, assuming single star evolution and our physical ingredients. Additionally, $Y_{\rm c} = 0.50$ corresponds to the middle of core-He burning phase.

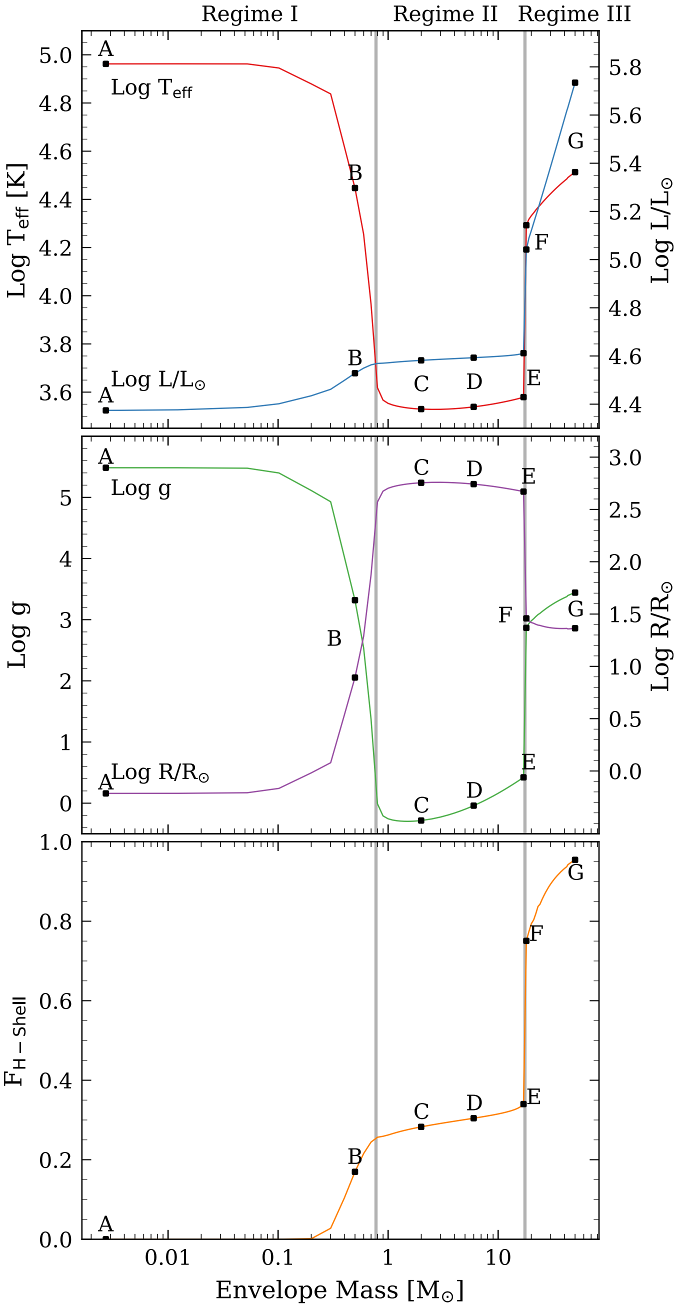

Figure 20: *Upper Panel*: Effective temperature (red curve) and luminosity (blue) as a function of $M_{\rm env}$ for the same models as in Fig. 19 (a constant He-Core mass of 4.1M$_\odot$, $Y_{\rm c} = 0.50$ and envelope mass varying from $0 - 50{\rm M}_\odot$). Models A – G from Fig. 19 are indicated with black dots and labelled. *Middle Panel*: Surface gravity, $\log g$ and the stellar radius as a function of envelope mass for the same models as in the upper panel. *Lower Panel*: Proportion of the total nuclear energy that is produced by the H-burning shell as a function of envelope mass for the same models as in the upper panel.

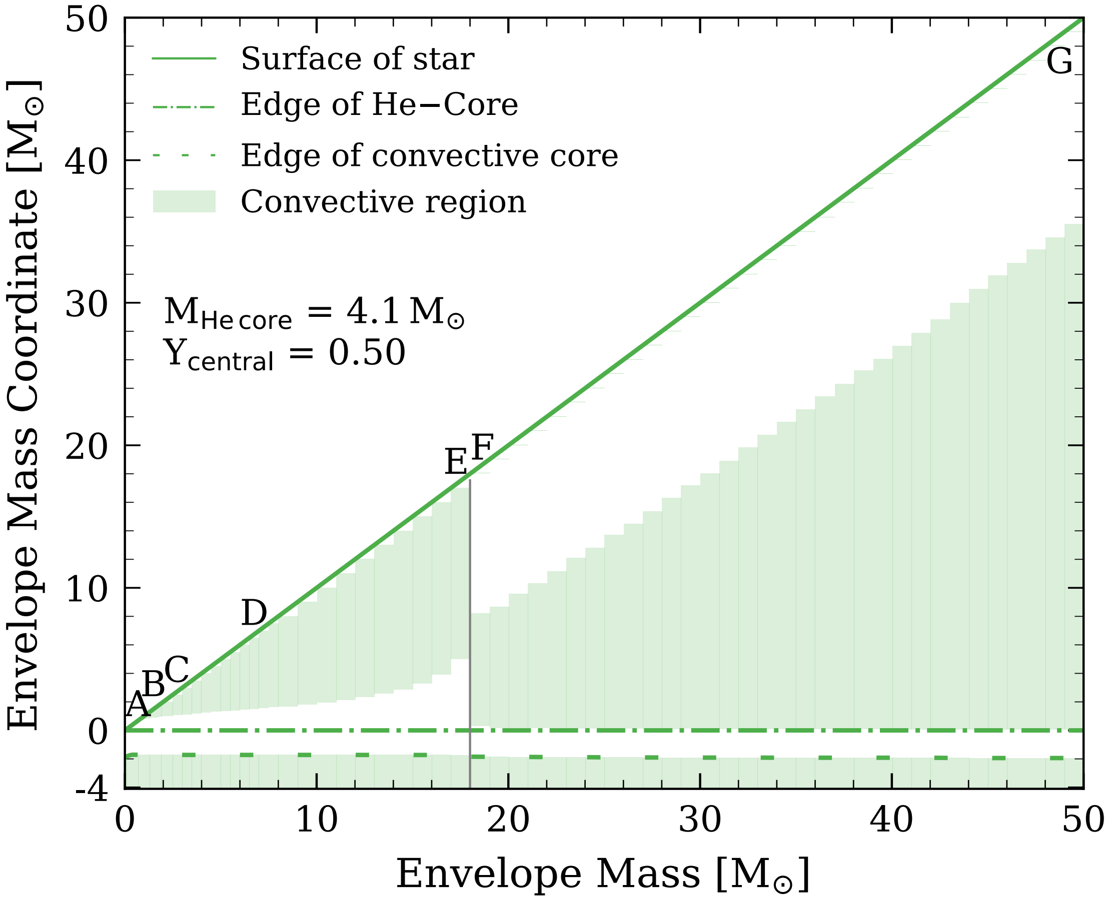

Figure 21: Kippenhahn-like diagram for the models in Figs. 19 and 20 with the envelope mass on the x-axis and the envelope mass coordinate on the y-axis, where 0 corresponds to the edge of the He-core and −4.1 corresponds to the centre of the $4.1M_\odot$ core. The convective regions are shaded in green and the boundary of the convective core, the He-core and the surface of the star are indicated with dashed, dash-dot, and solid lines respectively. A grey vertical line indicates the transition between Regimes II and III. Moving from left to right in this figure corresponds to increasing envelope mass.

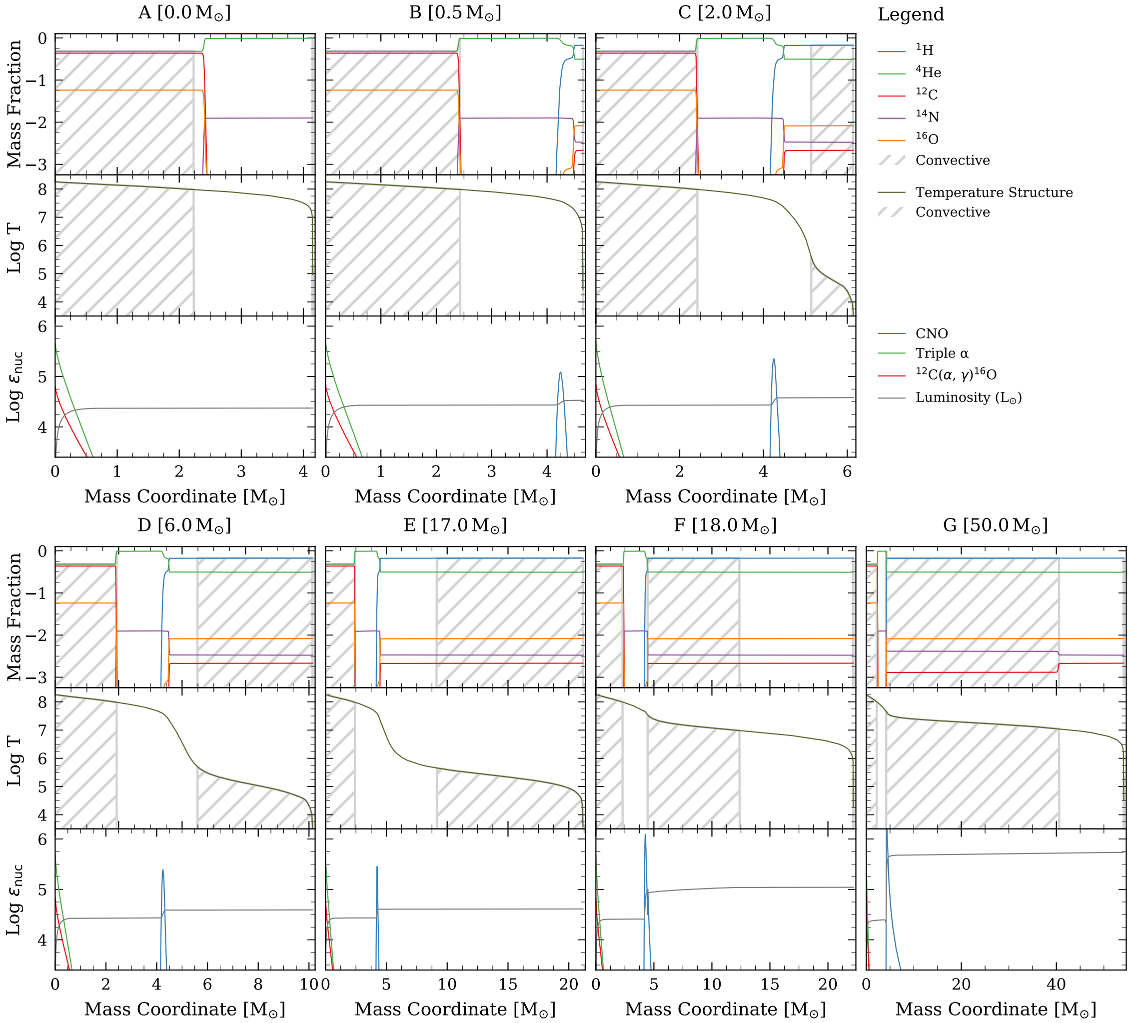

Figure 22: Internal structure of models from points labelled A to G in Figs. 19 and 20. The models have $M_{\rm core}$ =4.1M$_\odot$ and $Y_{\rm c}$ =0.50. The values of $M_{\rm env}$ are indicated above each sub-figure. The convective regions are hashed in the upper and middle panels. The upper panels show the internal abundance profile of H (blue), He (green), C (red), N (purple) and O (orange). The middle panels show the internal temperature structure (solid line). The lower panels show $\log \epsilon_{\rm nuc}$ in units of erg g^{-1}s^{-1} for different reactions, and $\log L$, in units of L$_\odot$.

In Fig. 19, we plot this set of models in the HR diagram. From these, we select 7 models, labelled A – G, which represent the qualitative trends in surface properties as a function of $M_{\rm env}$. We indicate the location in the HR diagram and the value of $M_{\rm env}$ for each of the models A-G in Fig. 19. We summarise the internal and surface properties for models A-G in Table 3.1.

Based on the location in the HR diagram, we divide the models plotted in Fig. 19 into Regimes I, II and III. Regime I consists of stars with no H-envelope or low envelope masses and with mostly high effective temperatures $T_{\rm eff}$. We define the transition between Regimes I and II at $\log(T_{\rm eff}) = 3.7$ or $T_{\rm eff} = 5\,011$ K. Regime II consists of stars with intermediate envelope masses, a radiative H-burning shell and a convective outer envelope. They are located near the Hayashi line in the HR diagram. The transition between Regime

II and III is defined by an abrupt change in the solution of the stellar structure equations from a cool star with a convective outer envelope to a hotter, more luminous star with a convective H-burning shell and a radiative outer envelope. Stars with envelope masses above this transition are defined to be in Regime III.

In Fig. 20, we plot the surface luminosity, T_{eff}, surface gravity ($\log g$), radius (R) and $F_{\mathrm{H-shell}}$ (the fraction of the total nuclear energy that is generated in the H-burning shell) as a function of M_{env} for the same set of models in Fig. 19. The transitions between Regimes I, II and III are indicated by grey vertical lines. We also label models A-G in each panel. Models A and B are in Regime I with envelope masses of 0.0 and 0.5M$_{\odot}$ respectively. Models C, D and E are in Regime II, close to the Hayashi line, with envelope masses of 2.0, 6.0 and 17.0M$_{\odot}$ respectively. Models F and G are in Regime III with envelope masses of 18.0 and 50.0M$_{\odot}$ respectively.

To investigate the presence of convective regions as a function of M_{env}, we plot in Fig. 21 the envelope mass on the x-axis and the Lagrangian envelope mass coordinate on the y-axis for the same representative set of models as in Fig. 19. This is similar to a normal Kippenhahn plot, with convective regions indicated in solid color. In Fig. 22, we plot internal abundance profiles, internal temperature profiles and internal nuclear burning profiles for models A – G. Convective regions are hashed in the abundance and temperature profile plots.

In Sections 3.3.1 – 3.3.1 below, we discuss Figs. 19, 20, 21 and 22 in detail. We analyse the trends in surface properties as a function of envelope mass and establish connections between the internal and surface properties.

Regime I – Stripped Stars (Models A and B)

We begin by discussing a model with a 4.1M$_{\odot}$ He-core and no envelope (Model A). It has a high T_{eff} of 92 000K, is highly compact with a radius of $R = 0.62$R$_{\odot}$ and has a high surface gravity of $\log g = 5.48$ (middle panel of Fig. 20). The 4.1M$_{\odot}$ He-core is composed of a 2.2M$_{\odot}$ convective core, with $Y_{\mathrm{c}} = 0.50$, and a 1.9M$_{\odot}$ Helium rich shell (Fig. 22).

For only a modest increase in the envelope mass from $M_{\mathrm{env}} = 0$ to 0.5M$_{\odot}$ (Model B), the value of T_{eff} drops sharply from 92 000 K to 28 000 K. This is because the effect of opacity in the envelope increases with increasing M_{env}. The increased effect of opacity produces a larger stellar radius and a lower T_{eff}. While this effect has been identified before in stellar evolution models (e.g., Groh et al., 2014; Meynet et al., 2015a), with our models we can investigate this behavior in a more systematic way as a function of M_{env}, M_{core}, and Y_{c}. We find that the luminosity increases slightly when increasing M_{env} from 0 (model A) to 0.5 M$_{\odot}$ (model B). This is due to the presence of a second nuclear energy generation region, i.e. the H-burning shell. In model B, 17 per cent of the total energy is generated in the H-shell, compared to 0 per cent in model A (see Fig. 20 and Table 3.1). The presence of the H-burning shell and its contribution to the total luminosity can also be seen by comparing the energy generation profiles for models A and B in Fig. 22.

Regime II – Red Supergiants (Models C, D, E)

As the value of $M_{\rm env}$ increases, the star responds to the increased mass by increasing the energy generation in the H-burning shell. As the value of $M_{\rm env}$ increases from 2 to $17{\rm M}_{\odot}$ (i.e. from model C to E), $F_{\rm H-shell}$ increases from 0.28 to 0.34 (Fig. 20). As well as the increased energy generation in the H-shell, the mass of the convective region in the envelope increases greatly from model C to E (Figs. 21 and 22). Over a wide range of $M_{\rm env}$, the mass of the convective region in the outer envelope increases with $M_{\rm env}$ almost as fast as $M_{\rm env}$ (Fig. 21). These changes in internal properties as a function of $M_{\rm env}$ can help to explain the trends in the HR diagram as a function of $M_{\rm env}$.

The right panel of Fig. 19 shows a zoom-in of Regime II in the HR diagram. For $M_{\rm env} < 2.5{\rm M}_{\odot}$, $T_{\rm eff}$ decreases with increasing $M_{\rm env}$. It reaches a minimum of $T_{\rm eff} = 3380$K at $M_{\rm env} = 2.5{\rm M}_{\odot}$ and increases with increasing $M_{\rm env}$ for $M_{\rm env} > 2.5{\rm M}_{\odot}$. Conversely, the radius increases with $M_{\rm env}$ to a maximum at $M_{\rm env} = 2.5$ and then decreases with further increasing $M_{\rm env}$ (Fig. 20). The value of $T_{\rm eff}$ is affected by two factors in this regime. Firstly, the effect of opacity increases with increasing $M_{\rm env}$ because there is more material in the envelope. This produces a larger radius and lower $T_{\rm eff}$. Secondly, as $M_{\rm env}$ and $F_{\rm H-shell}$ increases, the interior temperature profile changes and a larger mass of material is convective (Fig. 21). For stars on the Hayashi track, we expect the stellar radius to decrease with increasing mass (Eggleton, 2006), resulting in a higher $T_{\rm eff}$. The combination of these factors causes $T_{\rm eff}$ to decrease to a minimum and subsequently increase.

For a given $M_{\rm core}$ and $Y_{\rm c}$, our models show that the surface properties of a RSG change very little over a wide range of envelope masses (Figs. 19, 20, 23, 24). For example, for $M_{\rm core} = 4.1{\rm M}_{\odot}$, as $M_{\rm env}$ increases from 2 to $17{\rm M}_{\odot}$, the value of $T_{\rm eff}$ increases from 3390 K to 3800 K and the luminosity increases from ${\rm Log}({\rm L}/{\rm L}_{\odot}) = 4.58$ to 4.61 (Fig. 19). This means that there is a lot of degeneracy in the value of a stellar mass derived from a particular luminosity and $T_{\rm eff}$ for RSGs.

Our models indicate that the minimum envelope mass required to produce a RSG with $T_{\rm eff} < 5000$ K is $M_{\rm env} = 0.6{\rm M}_{\odot}$ for $M_{\rm core} = 1.9{\rm M}_{\odot}$ and $M_{\rm env} = 1.7{\rm M}_{\odot}$ for $M_{\rm core} = 8.9{\rm M}_{\odot}$. In addition, they show that over a wide range of $M_{\rm core}$, the minimum $T_{\rm eff}$ and maximum radius of a RSG occurs for a core mass ratio of $M_{\rm core}/M_{\rm total} \approx 0.60$.

Although we only plot the convective regions for models with one core mass ($M_{\rm core} = 4.1{\rm M}_{\odot}$) in Fig. 21, our models show that the mass of the convective region in the envelope depends only on $M_{\rm env}$ and is independent of $M_{\rm core}$ for a wide range of core masses, from $\sim 2 - 7{\rm M}_{\odot}$.

Transition between Regime II and III

As we keep increasing $M_{\rm env}$, we find a bi-stability in the solution of the stellar structure equations at an envelope mass of $M_{\rm transition} = 17.532{\rm M}_{\odot}$ (the exact value depends on the input physics). For $M_{\rm env}$ ¡ $M_{\rm transition}$, the star has a RSG structure with a radiative H-burning shell and a convective envelope (Figs. 21 and 22). As $M_{\rm env}$ increases towards

$M_{\rm transition}$, the pressure and temperature in the H-burning shell increase. This is accompanied by slightly increased nuclear energy generation in the H-burning shell (comparing models D and E in Fig. 22). At $M_{\rm transition}$, the base of the envelope becomes unstable to convection due to the increased H-shell nuclear burning and the solution of the stellar structure changes. For $M_{\rm env} > M_{\rm transition}$, the star is more condensed and hotter, with a convective H-burning shell and a radiative envelope (see Fig. 21 and compare models E and F in Fig. 22). Although we have only included structure models at intervals of $1{\rm M}_{\odot}$ in Figs. 19, 20 and 21, we observe in our paused models that the star 'jumps' from a RSG solution to a BSG solution with no change in mass.

Regime III – High Envelope Mass (Models F and G)

For $M_{\rm env} \geq 18{\rm M}_{\odot}$, our models present a hot, convective H-shell above the He-core and a radiative envelope (models F and G). The presence of a convective region at the base of the envelope results in a modified internal structure with a greatly increased temperature and nuclear energy generation rate in the H-shell. This increased energy production in the H-shell causes a much higher surface luminosity as compared to models with lower $M_{\rm env}$ in Regime II. The modified structure of the envelope also results in a much smaller stellar radius and a higher $T_{\rm eff}$ compared to Regime II.

The energy generation of models in Regime III is dominated by H-shell burning (see Fig. 20 and energy generation profiles in Fig. 22). More than 75 per cent of the total nuclear energy generation occurs in the H-shell, compared to Regime II stars which have $F_{\rm H-shell} \sim 0.30$. The mass of the region that is convective increases with increasing $M_{\rm env}$ (Fig. 21). For $M_{\rm env} = 50{\rm M}_{\odot}$ (model G), the envelope dominates the structure and surface properties of the star. The value of $F_{\rm H-shell} \sim 0.90$ and the star has a similar structure to a core-H burning star but with a $4.1{\rm M}_{\odot}$ He-core in the centre. Regime III stars will appear as blue stars in the HR diagram with $\log g$ of $1.8 - 3.9$ dex. Models with lower core masses can produce blue stars with lower values of $\log g$. Some may resemble OB-type stars and others may resemble blue supergiants.

3.3.2 Effect of Core Mass

We now discuss stellar structure models with $M_{\rm core}$ ranging from 1.9 to $8.9{\rm M}_{\odot}$, $M_{\rm env}$ ranging from 0.0 to $50.0{\rm M}_{\odot}$, and $Y_{\rm c}$ of 0.50 (corresponding to the middle of core-He burning).

We plot these models in the HR diagram in Fig. 23a, and Fig. 24a shows the effect of $M_{\rm env}$ on $T_{\rm eff}$ for models with the same $M_{\rm core}$ and $Y_{\rm c} = 0.50$. Qualitatively, models with $M_{\rm core} < 7{\rm M}_{\odot}$ show similar trends as a function of $M_{\rm env}$ as the model with $M_{\rm core} = 4.1{\rm M}_{\odot}$ (Sec. 3.3.1). We discuss these models below and examine models with $M_{\rm core} > 7{\rm M}_{\odot}$ in Sec. 3.3.2.

For models with $M_{\rm env} \lesssim 0.5{\rm M}_{\odot}$, the value of $T_{\rm eff}$ increases with $M_{\rm core}$ at constant $M_{\rm env}$ (Fig. 24a). This is due to an increase in luminosity with $M_{\rm core}$ at constant $M_{\rm env}$, mostly

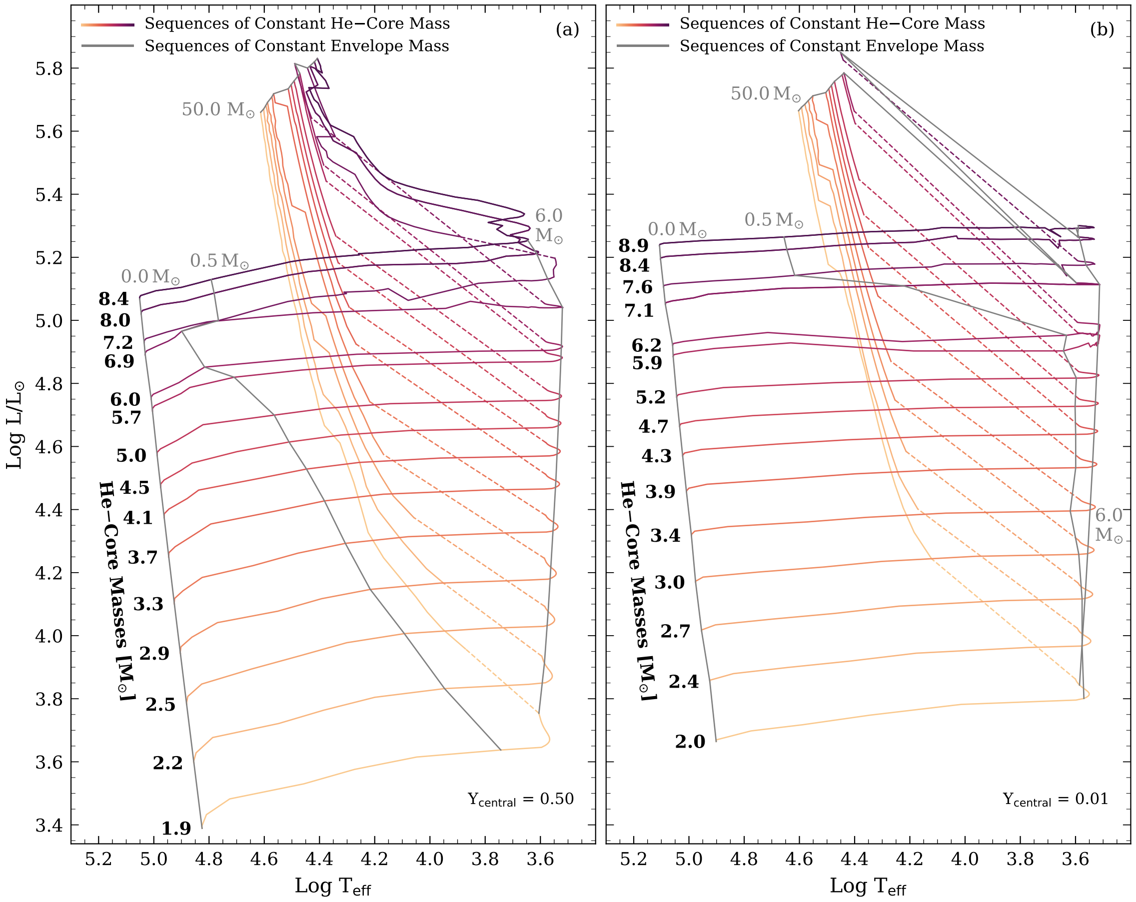

Figure 23: *Left Panel:* Coloured lines indicate constant He-core mass, constant $Y_c = 0.50$ and envelope masses varying from 0.0 to 50.0M$_\odot$ (colours indicate different He-core masses). The He-core masses are indicated in bold along the left-hand side. We also plot four lines of constant envelope mass and varying He-core mass in grey, with the envelope mass in M$_\odot$ indicated in grey text above each line. As in Fig. 19, the dashed coloured lines indicate a transition between two stable solutions of the stellar structure equations. *Right Panel:* Same as left panel but for models with $Y_c = 0.01$.

due to higher energy generation in the He-core. For some models, there is also an increase in energy generation in the H-Shell with increasing M_{core} at constant M_{env}, which also contributes to the higher luminosity.

As the envelope mass increases from 0.1 to 1M$_\odot$, the value of T_{eff} decreases sharply. This is due to the increasing effect of opacity with increasing M_{env}. The value of M_{env} at which T_{eff} begins to decrease increases with M_{core} (Fig. 24a). Additionally, the rate of decrease of T_{eff} as a function of M_{env} increases with M_{core}. The value of T_{eff} depends on the structure of the envelope and, in particular, on the presence and mass of any convective regions in the outer envelope. Models with higher M_{core} can support a higher M_{env} before the outer envelope becomes convective. This allows the envelope to remain compact (i.e. higher T_{eff}) up to a higher M_{env}.

For intermediate envelope masses from ~ 1 to 10M$_\odot$, models with higher M_{core} have lower T_{eff} for the same M_{env} (Fig. 24a). Models with higher M_{core} have more extended,

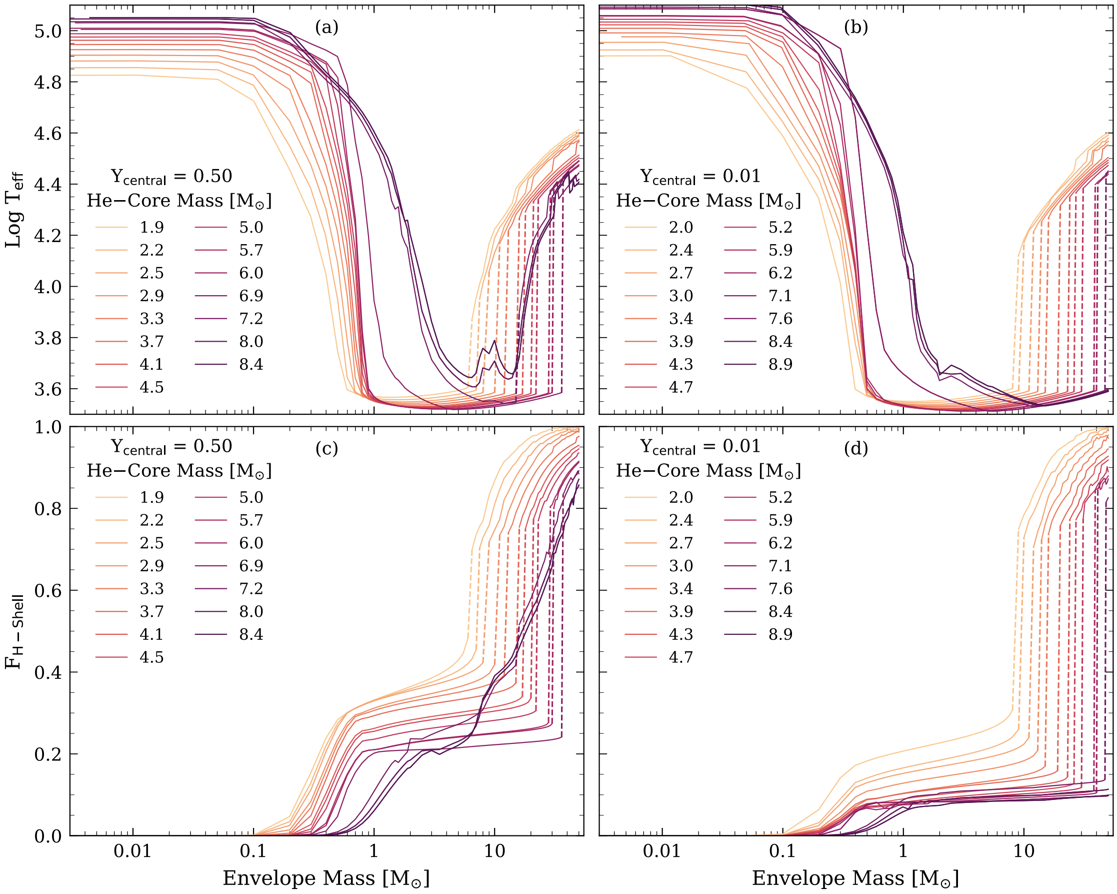

Figure 24: *(a)*: Effective temperature vs. envelope mass for models with constant He-core mass and $Y_{\rm c} = 0.50$. The dashed lines indicate the bi-stability between Regimes II and III. *(b)*: Same as (a) but for models with $Y_{\rm c} = 0.01$. *(c)*: The fraction of the total nuclear energy generated in the H-Shell ($F_{\rm H-shell}$) vs. envelope mass for the same models as in (a). *(d)*: Same as (c) but for models with $Y_{\rm c} = 0.01$.

lower density envelopes, larger radii which results in a lower $T_{\rm eff}$.

For each value of $M_{\rm core}$, the location of the bi-stability of the stellar structure equations at the transition between Regimes II and III is indicated in Fig. 24a by dashed lines. At this point, the solution of the stellar structure transitions from a RSG structure with a convective envelope and radiative H-shell to a structure with a radiative envelope and a convective H-shell. The value of $M_{\rm env}$ at which the transition occurs increases with $M_{\rm core}$. Models with higher $M_{\rm core}$ are able to support a higher $M_{\rm env}$ before the base of the envelope becomes unstable to convection.

Models with higher envelope mass generally converge towards a similar $T_{\rm eff}$ as a function of $M_{\rm env}$, independent of $M_{\rm core}$. In this regime, $\gtrsim 80$ per cent of the mass of the star is contained in the envelope and the surface properties are dominated by the nature of the H-shell burning, which depends mostly on $M_{\rm env}$.

To assess the relative contributions of the core and the envelope to the overall structure of the star, we compute the fraction of the total nuclear energy that is generated in the

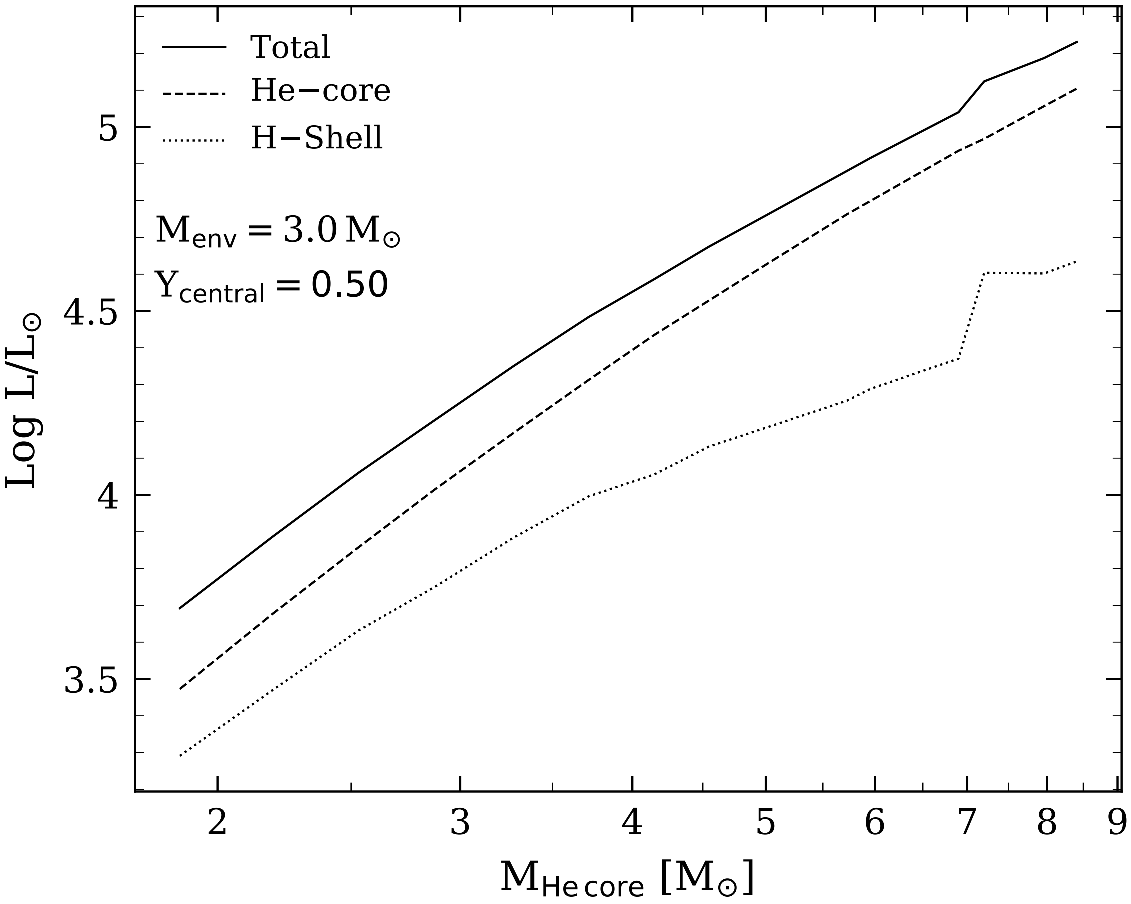

Figure 25: Luminosity vs. core mass for models with the same $Y_c = 0.50$ and $M_{env} = 3.0M_\odot$ and with core masses ranging from $M_{core} = 2$ to $8M_\odot$. The luminosities of the He-core, the H-shell and the total luminosity are indicated by a dash-dot, dotted and solid lines respectively.

H-shell ($F_{H-shell}$) as a function of M_{env} for models with constant M_{core} (Fig. 24c). In all models, the value of $F_{H-shell}$ is ≈ 0 for $M_{env} \lesssim 0.1M_\odot$. For stars with these envelope masses, very little burning takes place in the H -shell. As the value of M_{env} increases from $\sim 0.1 - 1M_\odot$, $F_{H-shell}$ increases sharply from 0 up to $F_{H-shell} \approx 0.1 - 0.3$ for $M_{env} = 1M_\odot$. As M_{env} further increases, the star must respond to support the extra mass. It does this by producing more energy in the H-shell. For models with M_{env} of $1 - 10$, the value of $F_{H-shell}$ increases only slightly (by a factor of ~ 0.25) over a large range of M_{env} (a factor of ~ 10). The value of $F_{H-shell}$ decreases with M_{core} at constant M_{env} (Fig. 24c). The luminosity generated in the core and in the H-shell both increase with increasing M_{core} at constant M_{env}. However, the luminosity generated in the core increases at a higher rate as a function of core mass than the H-shell (see Sec. 3.3.2 and Fig. 25). As a consequence, for models with higher M_{core}, a lower fraction of the overall energy comes from the H-shell.

For models in Regime III (high envelope mass), > 70 per cent of the total energy production occurs in the H-shell (Fig. 24c). The envelope has a structure similar to a massive core-H burning star with a nuclear burning region at the base, and a radiative outer region. The structure of the star is dominated by the H-shell burning at the base of

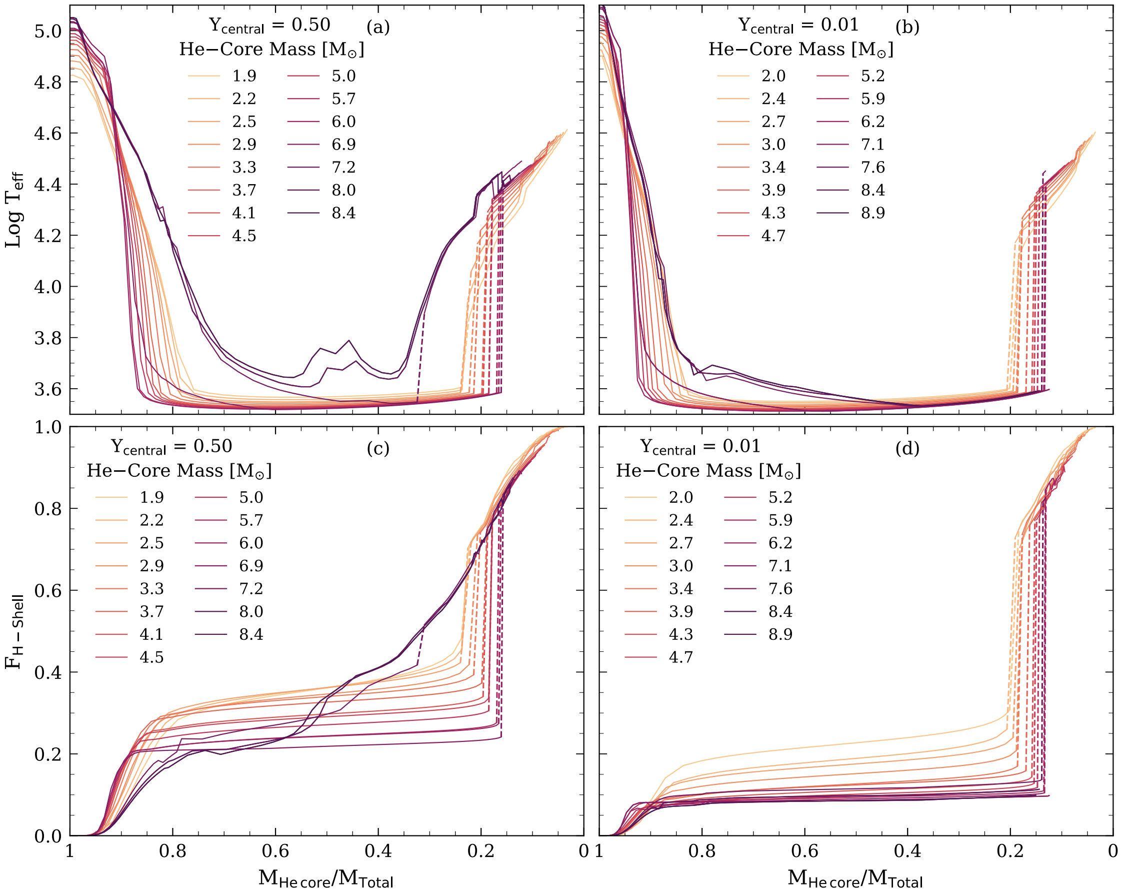

Figure 26: *(a)*: Effective temperature vs. core mass ratio ($M_{\rm core}/M_{\rm total}$) for models with constant He-core mass and $Y_{\rm c} = 0.50$. The dashed lines indicate the bi-stability between Regimes II and III. *(b)*: Same as (a) but for models with $Y_{\rm c} = 0.01$. *(c)*: The fraction of the total nuclear energy generated in the H-Shell ($F_{\rm H-shell}$) vs. envelope mass for the same models as in (a). *(d)*: Same as (c) but for models with $Y_{\rm c} = 0.01$.

the envelope, and the energy generated in the H-shell increases with increasing $M_{\rm env}$.

In Fig. 24a, c, we see that the bi-stability between RSG structures and more luminous, blue stars occurs over a very wide range of $M_{\rm env}$ for different $M_{\rm core}$. To further explore this transition, we plot $T_{\rm eff}$ and $F_{\rm H-shell}$ as a function of the core mass ratio, i.e. $M_{\rm core}$ divided by total mass (Fig. 26a, c). Moving from left to right in this figure corresponds to increasing envelope mass.

In Fig. 26a, $T_{\rm eff}$ shows similar trends as a function of $M_{\rm core}/M_{\rm total}$ for each $M_{\rm core}$. The value of $T_{\rm eff}$ decreases sharply from a core mass ratio of 1.0 to about 0.8. For core mass ratios $\approx 0.8 - 0.2$, most models have a RSG structure (Regime II). For models with $M_{\rm core} < 7{\rm M}_\odot$, the transition from Regime II to III occurs at a core mass ratio of ≈ 0.2. We can also see the different behaviour of models with $M_{\rm core} > 7.0{\rm M}_\odot$, the value of $T_{\rm eff}$ decreases much more slowly than models with lower $M_{\rm core}$.

Looking in more detail at Fig. 24a, we notice that for models with $M_{\rm core} \lesssim 3{\rm M}_\odot$ and very high envelope masses of $M_{\rm env} \approx 20 - 50{\rm M}_\odot$, there are some small sharp increases in

$T_{\rm eff}$. This is due to a small amount of convective mixing of material from the edge of the He-core into the envelope for some models with particularly extreme core mass ratios. The mixing occurs only for some models with a core mass ratio of $M_{\rm core}/M_{\rm total} \lesssim 0.15$ and it results in a slight decrease in $M_{\rm core}$ and slight increase in $M_{\rm env}$.

Our SNAPSHOT models indicate that the maximum core mass ratio that a RSG can have increases with increasing He-core mass. We note that Eggleton et al. (1998) finds a maximum allowed core mass ratio of ≈ 0.64 for composite polytropic models of red giants, which is consistent with the trend as a function of $M_{\rm core}$ that we observe in our models.

Models with $M_{\rm core} > 7{\rm M}_{\odot}$ and $Y_{\rm c} = 0.50$

These models exhibit qualitatively different behaviour to models with $M_{\rm core} < 7{\rm M}_{\odot}$. Unlike models with lower $M_{\rm core}$, they do not easily develop an outer convective envelope. Small convective shells are formed in the envelope for intermediate $M_{\rm env} \approx 6-20$. The location and mass of the convective shells in the envelope affect the radius R and hence $T_{\rm eff}$. These cause the small 'bumps' visible for models with $M_{\rm core} = 8.0$ and $8.4{\rm M}_{\odot}$ in Fig. 24c. Interestingly, models with $Y_{\rm c} = 0.01$ and $M_{\rm core} > 7{\rm M}_{\odot}$ do produce a convective envelope, suggesting that whether or not a star with a given core produces a RSG may depend on $Y_{\rm c}$.

The value of $M_{\rm env}$ at which models with $M_{\rm core} > 7{\rm M}_{\odot}$ form a convective H-burning shell with a radiative outer envelope is much lower than the models with $M_{\rm core} = 5.7$, 6.0 and 6.9. This is the opposite to the trend for lower core masses. The increase in $F_{\rm H-shell}$ as a function of $M_{\rm env}$ is different for these core masses as well.

Effect of Core Mass on H-Shell

The grey lines in Fig. 23a indicate that the surface luminosity increases with $M_{\rm core}$ for constant $M_{\rm env}$ and $Y_{\rm c}$. This is not unexpected, as a higher mass core is typically hotter, can generate more energy and produce a higher surface luminosity. Many authors have provided relationships between the luminosity and $M_{\rm core}$ for core-He burning stars (e.g., Eggleton et al., 1989; Tout et al., 1997; Hurley et al., 2000).

Our grid of SNAPSHOT models allows us to test the separate contributions from the core and H-shell to the luminosity. In Fig. 25, we plot the surface luminosity, the luminosity of the He-core and the luminosity of the H-shell against $M_{\rm core}$ for a set of models with $M_{\rm env} = 3.0{\rm M}_{\odot}$ and $Y_{\rm c} = 0.50$ and $M_{\rm core}$ from $2-9{\rm M}_{\odot}$. As we observed in Fig. 23, the surface luminosity increases with $M_{\rm core}$ for constant $M_{\rm env}$ and $Y_{\rm c}$. However the increased luminosity does not all originate in the He-core. The energy produced in both the He-core and the H-shell increases with increasing $M_{\rm core}$. The value of $M_{\rm core}$ modifies the temperature structure in the H-shell in two ways. Firstly, the temperature of the H-shell increases (by a small amount) with $M_{\rm core}$, because the higher mass He-cores are hotter and produce a higher temperature just above the core. Secondly, the mass of the region in which significant energy generation takes place increases. These two changes result in hotter, higher mass H-shells and higher nuclear energy generation rates in the H-shell.

3.3.3 Effect of Core Composition

Our grid of SNAPSHOT stellar structure models also allows us to isolate the effect of the core composition on the surface properties of the star, independent of the effects of the core mass and envelope mass. This analysis is difficult to accomplish with stellar evolution models, in which the three interior quantities listed above change simultaneously. Models with $Y_\mathrm{c} = 0.50$ and 0.01 exhibit qualitative differences in the internal and surface properties (Figs. 24 and 26). In this section, we discuss the effect of the core composition.

Figure 27a, b, c compares the surface luminosity as function of M_core at constant M_env for core compositions of $Y_\mathrm{c} = 0.50$ (dashed line) and $Y_\mathrm{c} = 0.01$ (solid line). The models in panel A have $M_\mathrm{env} = 0\mathrm{M}_\odot$. For these models, the surface luminosity is higher for models with $Y_\mathrm{c} = 0.01$ than for $Y_\mathrm{c} = 0.50$. This is due to the higher mean molecular weight of the core (μ_core) for models with $Y_\mathrm{c} = 0.01$ compared to 0.50. For the same core mass, a higher μ_core results in a higher central temperature, T_central, through the equation of state, and hence higher nuclear energy generation rates, ϵ_nuc, in the core. As these models have no H-envelope, the He-core is the only region of nuclear energy generation. This means that a higher ϵ_nuc in the core caused by with higher μ_core corresponds to a higher surface luminosity. We find mass-luminosity relationships of $\mathrm{L} \propto \mathrm{M}^{2.56}$ for $Y_\mathrm{c} = 0.50$ and $\mathrm{L} \propto \mathrm{M}^{2.43}$ for $Y_\mathrm{c} = 0.01$. These are consistent with the mass-luminosity relationships found by Langer (1989).

In contrast, for models with $M_\mathrm{env} = 3\mathrm{M}_\odot$, the value of Y_c (and thus μ_core) does not affect the surface luminosity (Fig. 27b). For these models, there are two regions of nuclear energy generation, the He-core and the H-shell. The surface luminosity depends on the energy from both of these regions. While a lower Y_c corresponds to a higher μ_core, T_central and ϵ_nuc in the core, it does not correspond to a higher surface luminosity. This is because the energy generation in the H-shell decreases with decreasing Y_c. To illustrate this, we plot the total luminosity generated in the He-core, L_core and the total luminosity generated in the H-shell, $L_\mathrm{H-shell}$ (Fig. 28) for models with $M_\mathrm{env} = 3\mathrm{M}_\odot$. Models with $Y_\mathrm{c} = 0.50$ and 0.01 are indicated in dashed and solid lines respectively. For the same core mass, the L_core is lower for $Y_\mathrm{c} = 0.50$ than for $Y_\mathrm{c} = 0.01$. In contrast, the $L_\mathrm{H-shell}$ is lower for $Y_\mathrm{c} = 0.50$ than for $Y_\mathrm{c} = 0.01$. These effects nearly cancel out so that the total luminosity at the surface is similar for $Y_\mathrm{c} = 0.50$ and 0.01. For example, models with the same values of M_core and M_env and Y_c of 0.50 and 0.01, the luminosity differs by ~ 0.02dex and T_eff differs by $\sim 0.007\,$dex. The same effect is observed for $M_\mathrm{env} = 6\mathrm{M}_\odot$ and for a wide range of envelope masses. This means that changes in the luminosity of a RSG as it evolves are due mostly to changes in M_core and not due to changes in Y_c or M_env.

We also study the trend in T_eff as a function of M_core for $Y_\mathrm{c} = 0.50$ and 0.01 (Fig. 27d, e, f). For models with no H-envelope (Fig. 27d), the luminosity and T_eff are higher for models with $Y_c = 0.01$ compared to $Y_c = 0.50$, while the radius is smaller. For models with $M_{\rm env} = 3$ and $6{\rm M}_\odot$ and a convective envelope, the value of $T_{\rm eff}$ does not depend on Y_c. This result holds for a wide range of envelope masses. In some cases for $M_{\rm core} > 7{\rm M}_\odot$, $T_{\rm eff}$ is slightly higher for $Y_c = 0.50$ than 0.01. This is due to differences in the formation of convective shells in the envelope.

In Fig. 27g, h, i, we plot the radius of the core as a function of the core mass. For a given core mass, models with $Y_c = 0.50$ have cores with larger radii than models with $Y_c = 0.01$. For the same $M_{\rm core}$, cores with lower values of Y_c must be denser and hotter to produce the same amount of energy to compensate for the decreasing Y_c. This results in a smaller core radius. We also plot the radius of the envelope against the core mass for the same $M_{\rm env}$ (Fig. 27j, k, l). The envelope radius increases with $M_{\rm core}$ at constant $M_{\rm env}$ and Y_c. For the same $M_{\rm env}$, the mass of the outer envelope that is unstable to convection decreases with increasing $M_{\rm core}$. At constant $M_{\rm env}$, envelopes with a more massive outer convective region have lower radii.

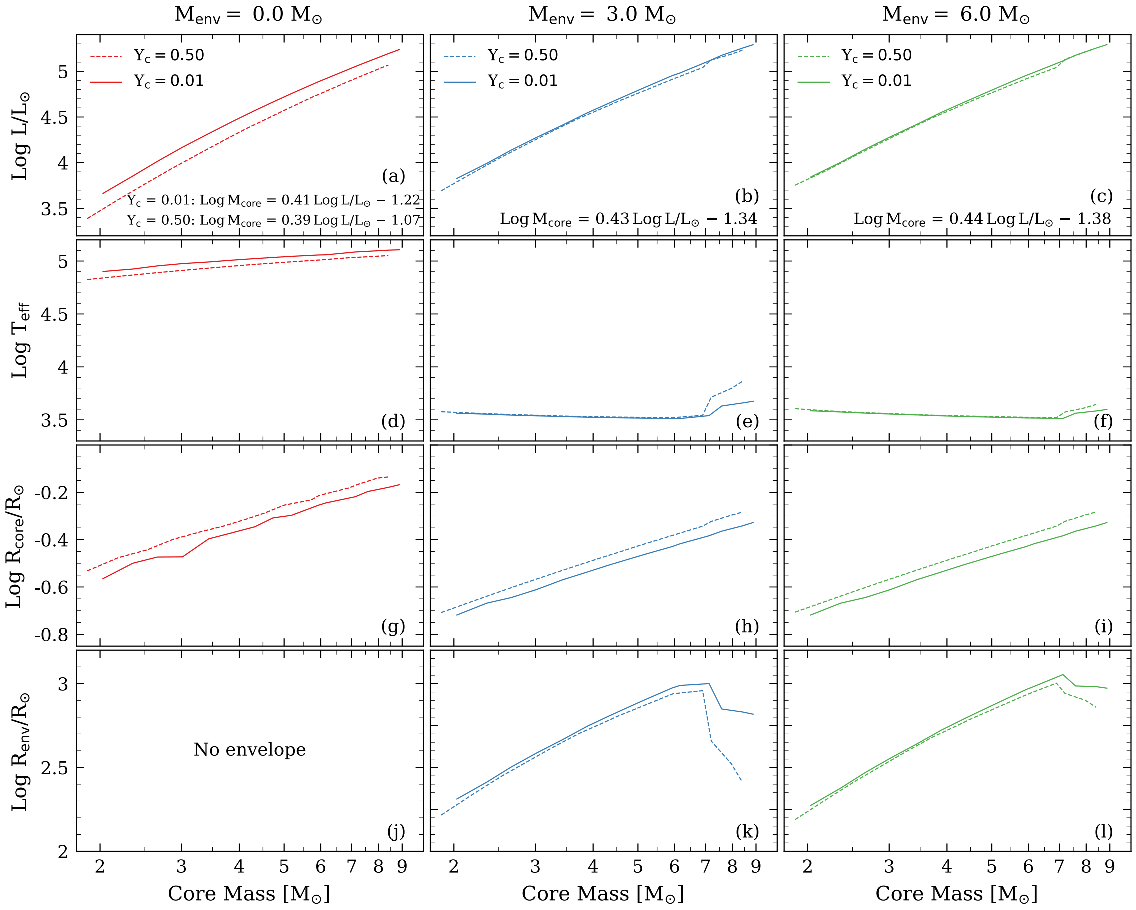

Figure 27: *Left panels (a, d, g, and j)*: Surface luminosity, effective temperature, radius of the core and radius of the envelope as a function of core mass for models with no H-envelope. The dashed lines and solid lines indicate models with $Y_c = 0.50$ and $Y_c = 0.01$) respectively. *Middle panels (b, e, h, and k)*: Same as left panels but for models with a constant envelope mass of $3{\rm M}_\odot$ and varying core mass. *Right panels (c, f, i, and l)*: Same as left panels but for models with a constant envelope mass of $6{\rm M}_\odot$ and varying core mass.

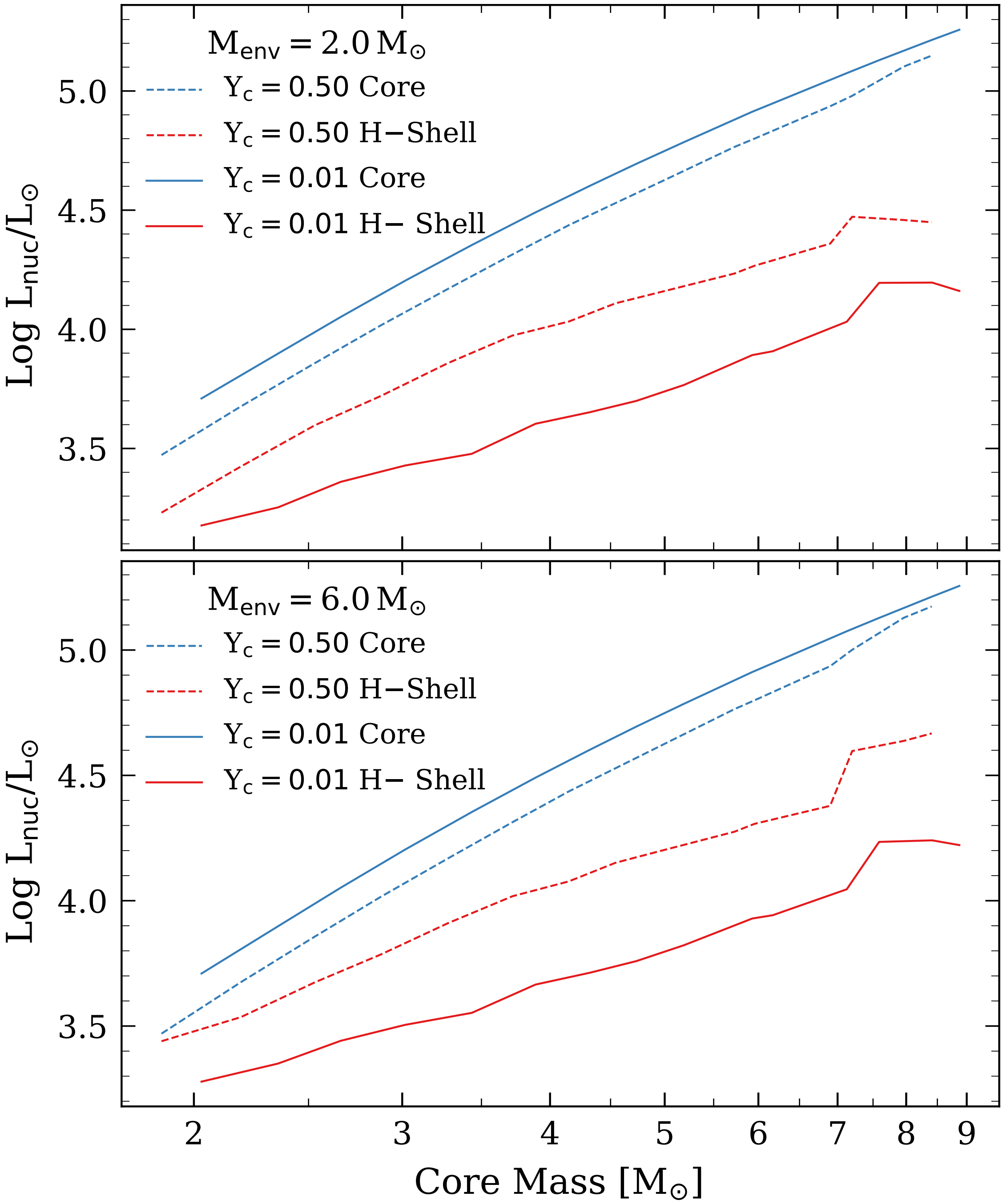

Figure 28: *Upper panel*: Luminosity from the core (blue) and the H-shell (red) as a function of core mass for a constant envelope mass of $3M_\odot$ and for $Y_c = 0.50$ (dashed line) and $Y_c = 0.01$ (solid line) – the same models as panels b, e, h, and K in Fig. 27. *L*ower panel: Same as upper panel but for models with a constant envelope mass of $6M_\odot$ – the same models as panels c, f, i, and l in Fig. 27

3.4 Discussion

3.4.1 Uncertain Masses of Red Supergiants

For a RSG with a given luminosity and T_{eff}, our models show that there is a large range of allowed total masses. This means that for all known RSGs in the Galaxy, it is impossible to know the current mass based on the luminosity and T_{eff} alone. For instance, Betelgeuse and VY CMa may have quite different current masses to what we think they do. This degeneracy may be broken with an accurate measure for the surface gravity. However, this quantity is typically derived from evolutionary mass and either angular diameter (if the star can be resolved) or luminosity and T_{eff} in spectroscopic analyses of RSGs, rather than derived based on diagnostics.

The core of a RSG is mostly unaffected of the presence of the envelope. The luminosity of the core is determined by M_{core} and Y_{c}, which is the classical result obtained for Helium stars (Maeder & Meynet, 1987; Langer et al., 1989). However, the envelope is affected by the core. The energy produced in the H burning shell depends on the temperature profile at the base of the envelope, which in turn depends on M_{core} and Y_{c}. It contributes 10 – 30 per cent of the total luminosity (for $0.50 < Y_{\text{c}} < 0.01$ and $M_{\text{core}} < 7\text{M}_{\odot}$) in such a way that the role of Y_{c} in the total energy production is almost eliminated. This means that the mass of the RSG envelope does not significantly impact the total luminosity.

Our finding about the uncertain current value of M_{env} of a RSG (and thus total current mass) has several implications for massive star evolution. First, two RSGs at a similar location in the HR diagram may have very different M_{env} and total mass. Second, not knowing the value of M_{env} makes it difficult to estimate the fraction of the envelope that will be lost as the star evolves during He core burning. This has effects on the duration of the plateau in the supernova lightcurve for those stars that are able to retain their H envelope. This is particularly relevant in light of the recent downward revision of the mass-loss rates of RSGs (e.g., Beasor et al., 2020). Our SNAPSHOT models open the possibility that RSGs could have much lower or much higher M_{env} than currently thought, however binary population synthesis models are needed to assess the distribution of M_{env}. The distribution of allowed M_{env} is not flat and based on our current knowledge of single and binary star evolution, some masses are preferred (Zapartas et al., 2019).

This analysis can be extended to RSGs at the end of their lives, which is especially interesting for the fate of the star, supernova light curve properties and the compact remnant mass. Farrell et al. (2020a) applied the SNAPSHOT model approach to investigate RSGs at the end of their lives and found that it is not possible to determine the final mass of a red supergiant (RSG) at the pre-supernova (SN) stage from its luminosity L and effective temperature T_{eff} alone. This result applies to RSG progenitors of core collapse supernovae, failed supernovae and direct collapse black holes.

We now turn our attention to the radius and T_{eff} of RSGs. These quantities have significant impact on the morphological appearance of these stars and on the post-explosion properties, such as the early time lightcurve (e.g., Dessart et al., 2013; González-Gaitán et al., 2015; Morozova et al., 2015, 2018; Hillier & Dessart, 2019). Because of their deep convective envelopes, RSGs are also ideal laboratories for studying the properties of convective mixing. For instance, it is well known that the $T_{\rm eff}$ of RSGs in stellar models are strongly affected by the choice of mixing length parameter, $\alpha_{\rm mlt}$ (e.g., Henyey et al., 1965; Stothers & Chin, 1995; Chun et al., 2018). In the models of Chun et al. (2018), the $T_{\rm eff}$ of RSGs varies by up to $\sim 800\,{\rm K}$ for different choices of $\alpha_{\rm mlt}$. Our models show that, in addition to convective mixing, different envelope masses produce a variation of up to $\sim 400\,K$ for the same core mass. This suggests that when calibrating the mixing length parameter $\alpha_{\rm mlt}$ by using the $T_{\rm eff}$ of RSGs, it may be important to consider that the core and envelope masses may be substantially different to what is predicted by stellar evolution models. Possible processes that would modify $M_{\rm core}$ and $M_{\rm env}$ include convective overshooting on the MS or mass loss during the RSG phase.

Our results about the behavior of the stellar radius as a function of envelope mass are also relevant for RSGs in binary systems, of which there are many observations (e.g., Vinter Hansen, 1944; McLaughlin, 1950; Wright, 1970; Stencel et al., 1984; Hagen Bauer & Bennett, 2014; Harper et al., 2016; Neugent et al., 2018, 2019).When a RSG undergoes RLOF, it often results in non-conservative mass-transfer. As the star loses mass via RLOF, the radius of the star increases faster than the Roche-Lobe increases (Eggleton, 2006).

Our models show that the maximum radius of RSGs occurs for a core mass ratio of ≈ 0.6. This means that even in thermal equilibrium, as envelope mass is lost from the star, we expect that the envelope will continue to increase in radius until the core mass ratio increases above 0.6. For higher core mass ratios, the radius decreases with decreasing $M_{\rm env}$ and the mass transfer episode may finish.

3.4.2 Stripped stars

Based on the number of stars in binary systems, we expect a large number of stars to exist that are stripped of their hydrogen-rich envelope (Sana et al., 2012). However, only a small number have actually been observed (e.g., Gies et al., 1998; Groh et al., 2008; Peters et al., 2013; Wang et al., 2017; Chojnowski et al., 2018), This may be due to the presence of companion stars that are brighter at visual wavelengths (Götberg et al., 2018) or as a result of biases and selection effects (de Mink et al., 2014; Schootemeijer & Langer, 2018).

Our results have implications for the detectability of stripped stars. Our results show that the surface properties of stripped stars, in particular the effective temperature, strongly depend on the mass of the envelope left after binary interaction. This will change the flux distribution in different filters, and impact the completeness limit of future observing surveys that will aim to detect those objects.

By interpolating between our SNAPSHOT models, it is possible to determine the allowed values of $M_{\rm core}$ and $M_{\rm env}$ for a given observed luminosity and $T_{\rm eff}$ of a stripped star. Knowledge of the core and envelope masses of stripped stars can provide constraints

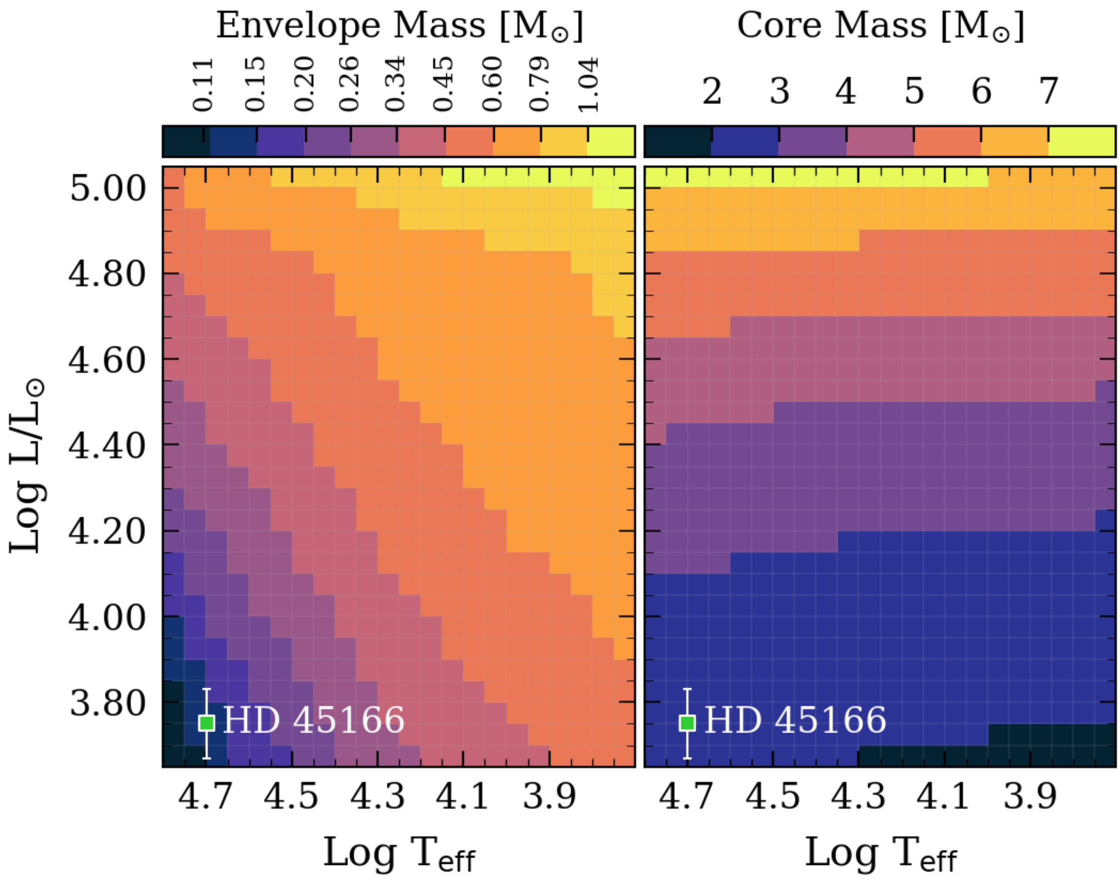

Figure 29: *Left*: Envelope Mass $M_{\rm env}$ that we derive by interpolating between our SNAPSHOT models of stripped stars (with $Y_{\rm c} = 0.50$) for a range of luminosities and $T_{\rm eff}$. *Right*: Same as *left* but for the Core Mass $M_{\rm core}$.

on the physics of RLOF in binary models. When combined with a mass-loss rate, the values of $M_{\rm core}$ and $M_{\rm env}$ can be used to infer their final fates. Depending on the mass of hydrogen left in the envelope at the end of their evolution, these stripped stars are likely to produce SNe IIb or Ib (Podsiadlowski et al., 1993; Woosley & Weaver, 1994; Filippenko, 1997; Stancliffe & Eldridge, 2009; Gal-Yam, 2012; Götberg et al., 2017).

Most stripped stars detected so far have low mass, with HD 45166 being the most massive and only detected system within the mass range that can be compared to our models. Based on orbital dynamics, the primary star has a current mass of 4.2 M$_\odot$ (Steiner & Oliveira, 2005). Spectroscopic analysis using CMFGEN radiative transfer models derived a luminosity of $\log {\rm L/L_\odot} = 3.75$, $T_{\rm eff}$ of 50 000K and mass-loss rate of $2.2 \times 10^{-7} {\rm M_\odot/yr}$ (Groh et al., 2008). Using our models, and assuming $Y_{\rm c} = 0.50$ (the middle of core-He burning), we derive $M_{\rm core} = 2.30 \pm 0.15 {\rm M_\odot}$ and $M_{\rm env} = 0.15 \pm 0.02 {\rm M_\odot}$. Taking into account the range of possible values of $Y_{\rm c}$ from 0.98 to 0.00, we obtain $M_{\rm core} = 2.30^{+0.35}_{-0.23} {\rm M_\odot}$ and $M_{\rm env} = 0.15^{+0.11}_{-0.08} {\rm M_\odot}$.

This mass is consistent with detailed binary models (e.g., Götberg et al., 2018). However it is lower than the mass of $4.2 \pm 0.7 {\rm M_\odot}$ obtained by Steiner & Oliveira (2005). There are several possibilities for this discrepancy. First, it may be due to the assumptions for the secondary star to HD 45166, which is assumed to be $4.8\mathrm{M}_\odot$ based on its B7V spectral type (Steiner & Oliveira, 2005). For example, the secondary star may be out of thermal equilibrium. Assuming our primary mass is correct, the secondary star has a mass of $2.70\mathrm{M}_\odot$ based on the mass ratio derived by Steiner & Oliveira (2005). Secondly, it is possible that the primary star is out of thermal and/or hydrostatic equilibrium, in which case our models would not be applicable. It is also possible, but less likely, that HD45166 is a post core-He burning star, but in this case the derived value of M_{core} and total mass would be even lower. Regardless of the exact mass of HD 45166, its He core is massive enough to explode as a CCSN. We expect that this mass discrepancy is much larger than potential uncertainties in our SNAPSHOT models (see Sec. 3.4.3.)

The energy generation of core-He burning stripped stars is dominated by M_{core}. For stripped stars with high T_{eff}, a given luminosity and T_{eff} could correspond to a high value of M_{core} and high Y_{c} or a lower value of M_{core} and low Y_{c}. For a given luminosity and T_{eff}, most of the uncertainty in the value of M_{core} is due to the degeneracy between M_{core} and Y_{c}, rather than the observational uncertainty in the luminosity and T_{eff}. For a given T_{eff}, the value of M_{core} and M_{env} increases with increasing luminosity while for a given luminosity, the value of M_{core} increases and M_{env} decreases with increasing T_{eff}. This behaviour is illustrated in Fig. 29, where we show the different values allowed for M_{env} and M_{core} for a given position in the HR diagram.

We will provide an online tool to derive the values of M_{core}, M_{env} of stripped stars and the associated uncertainties based on the luminosity and T_{eff} which we hope will be of great benefit to interpret future observations of stripped stars. When such further observations are available, by deriving the values of M_{core} and M_{env} of a population of stripped stars, and with knowledge of the lifetimes of these burning stages, it may be possible to estimate a mass loss rate for hot, stripped stars.

3.4.3 Additional Caveats

One of the advantages of studying SNAPSHOT stellar structure models is that they are independent of many of the usual sources of uncertainty that affect stellar evolution models. These include mass loss by stellar winds, mass-exchange during a binary interaction, the evolutionary effects of rotation and of convective overshooting. However, our approach is still subject to uncertainties of physical inputs to the models. We discuss these below.

We use Type I and Type II opacities from OPAL (Iglesias & Rogers, 1993, 1996) at high temperatures and opacities from Ferguson et al. (2005) at low temperatures. The opacities for H, He, C, N and O are quite well known. Most of the uncertainty arises in the Fe opacities (Bailey et al., 2015) and these can have quite substantial effects on the structure of the star. Changes to the opacities could in some cases systematically shift the T_{eff} of our models.

The equation of state (EOS) used in MESA is from OPAL (Rogers & Nayfonov, 2002), SCVH (Saumon et al., 1995) and the HELM EOS (Timmes & Swesty, 2000). For stars during core-H and core-He burning, the EOS is expected to be relatively accurate (Timmes & Swesty, 2000). Therefore, it is likely that any uncertainties associated with the EOS do not have large effects on the models in this grid.

The nuclear reaction rates are a third potential source of uncertainty. The uncertainties in the reactions during the CNO-cycle and in the triple alpha reaction are relatively small, however there is some uncertainty in the rate of $^{12}C(\alpha,\gamma)^{16}O$ (deBoer et al., 2017). The effect of any uncertainties associated with these nuclear reaction rates on the SNAPSHOT structure models in this work is likely small.

We use MESA's `simple_photosphere atmosphere` boundary condition which applies a simple grey atmosphere. This treatment of the outer boundary is likely appropriate for our models as they are still far from the Eddington limit. Stellar evolution models have shown that the treatment of the outer boundary will have a larger effect on the radius for high mass stars close to the Eddington limit (Langer, 1989; Schaerer et al., 1996; Schaerer, 1996; Gräfener et al., 2012; Groh et al., 2014).

All of our models are non-rotating. Massive stars exhibit a range of rotational velocities (Hunter et al., 2008b; Huang et al., 2010; Ramírez-Agudelo et al., 2013, 2015; Dufton et al., 2019) and rotation can have an important impact on their evolution (Maeder & Meynet, 1987; Meynet & Maeder, 2000; Heger et al., 2005; Brott et al., 2011b). However as our models are not evolving, only the hydrostatic effect of rotation could potentially affect the results in this paper. This effect is small, except for fast rotating stars (Maeder & Meynet, 2000).

Our models do not take into account the effect of internal or surface magnetic fields. However, as we consider only structure models in this paper, the evolutionary effects of magnetic fields on mass-loss rates and angular momentum loss rates (e.g., Meynet et al., 2011; Keszthelyi et al., 2019) likely do not have significant effects on our analysis. The hydrostatic effect of a magnetic field may have a small impact on the structure and energy transport inside the star, but further work is needed to properly address this effect.

We adopt a mixing length parameter of $\alpha_{\rm mlt} = 1.82$ for the models in this paper. This value was calibrated based on solar observations by Choi et al. (2016). The choice of $\alpha_{\rm mlt}$ can significantly affect the $T_{\rm eff}$ of RSGs. A higher value of $\alpha_{\rm mlt}$ produces RSGs with lower values of $T_{\rm eff}$. Chun et al. (2018) compared observations of RSGs to stellar evolution models and found that models $\alpha_{\rm mlt} = 2$ or 2.5 best reproduced the observations.

In this paper, we select 3 key structural properties, i.e. the $M_{\rm core}$, $M_{\rm env}$ and core composition in terms of $X_{\rm c}$ and $Y_{\rm c}$, and draw connections with the surface properties. However, these structural properties clearly do not fully describe the interior of a star. Other structural properties, such as different abundance profiles in the envelope due to mixing, mass-accretion from a companion or mergers, may have important effects on the surface properties. For example, Schootemeijer et al. (2019) studied the properties and lifetimes of red and blue supergiants in terms of the H-gradient outside the He-core.

Most stars are in hydrostatic and in thermal equilibrium, that is the radial acceleration is zero and that the luminosity emitted at the surface is equal to the rate of energy production by nuclear reactions in the interior. The method described in this paper to construct SNAPSHOT stellar structure models is only appropriate for stars that are in hydrostatic and thermal equilibrium. It is not possible to construct stellar structure model after the end of core-He burning or close to core-collapse as the envelope is out of thermal equilibrium during these stages. The latest stage in the evolution of a star at which is is possible to consistently construct SNAPSHOT structure models is the end of core-He burning.

3.4.4 Directions for Future Work

Our SNAPSHOT model approach provides the foundation for several possible directions for future work. We briefly outline some of them below.

In this work, we studied models at solar metallicity. Our analysis can be extended for stars at lower metallicity. Several papers have studied the evolution of stars at different metallicities (e.g., Brott et al., 2011a; Yoon et al., 2012; Szécsi et al., 2015; Choi et al., 2016; Groh et al., 2019). SNAPSHOT models may help us to understand the effects of metallicity on stellar structure, independent of the evolutionary effects of mass loss, rotation and binaries.

While we cannot compute stellar structure models in hydrostatic and thermal equilibrium at the end of central carbon burning (due to the fact that the envelopes are out of thermal equilibrium at this point), the structure models at the end of core-He burning could be evolved to the end of core-C burning to study the surface properties of supernova progenitors. Furthermore, these models could be evolved to core-collapse and exploded in 1-D explosion models, similar to the approach of Ugliano et al. (2012), Sukhbold et al. (2016) and others. This would allow us to systematically study the appearance of supernovae as a function of progenitor structure.

SNAPSHOT stellar structure models may help to shed light on what affects the T_{eff} of post-main sequence massive stars. As well as insight into stellar evolution, understanding which stars live as BSGs and RSGs has implications for the number of ionising photons emitted by stars, the kinetic energy feedback to a galaxy and chemical yields from massive stars.

Our SNAPSHOT models will benefit greatly from current and future astero-seismological results for massive stars, such as from the TESS and PLATO space missions. In particular, improvements in our understanding of stellar structure from astero-seismological studies (Buldgen et al., 2015; Eggenberger et al., 2017; Aerts et al., 2019) could be implemented in our models in the future. SNAPSHOT stellar structure models could also be applied to low mass stars which benefit from larger observational samples.

Gravitational wave observations of double neutron star mergers (Abbott et al., 2017a,c) and double black hole mergers (Abbott et al., 2016b) have opened a new frontier in astrophysics. These observations have provided new insights into compact objects and the endpoints of massive stars. Our SNAPSHOT stellar structure models could be used to study the mass function of compact remnants and the boundaries between white dwarfs and neutron stars, and neutron stars and black holes.

3.5 Conclusions

In this paper, we introduced our SNAPSHOT technique to construct stellar structure models in hydrostatic and thermal equilibrium. We then applied our approach to study the surface properties of core-H and core-He burning stars with a range of core and envelope masses and core compositions.

1. We find that there is a limited range of core masses, envelope masses and core compositions that can form core-H burning structures in hydrostatic and thermal equilibrium. We quantified the relationship between the convective core mass and the total mass for different central H mass fractions.
2. Over a wide range of He-core masses ($M_{\rm core} \approx 2 - 9 {\rm M}_{\odot}$), core-He burning stars show similar trends in luminosity and $T_{\rm eff}$ as a function of the core mass ratio ($M_{\rm core}/M_{\rm total}$).
3. Our models with core mass ratios of $M_{\rm core}/M_{\rm total} > 0.8$ correspond to stripped stars produced as a consequence of significant mass loss or binary interaction. They show that $T_{\rm eff}$ has a strong dependence on $M_{\rm env}$ (due to the increased effect of opacity from the H-rich envelope), $M_{\rm core}$ and the core composition. When a large observational sample of stripped stars becomes available, our results can be used to constrain their $M_{\rm core}$, $M_{\rm env}$, mass-loss rates and the physics of binary interaction. Our models also show that the surface luminosity of these stars increases slightly with increasing envelope mass due to increased energy generation in the H-shell, in which $0-25$ per cent of the total nuclear energy is generated.
4. Stars with $M_{\rm core}/M_{\rm total}$ from 0.2 to 0.8 have convective outer envelopes, low $T_{\rm eff}$ and will appear as RSGs. They exhibit a small variation in luminosity (0.02 dex) and $T_{\rm eff}$ (~ 400K), over a wide range of envelope masses ($\sim 2-17 {\rm M}_{\odot}$). This means that given current uncertainties in the physics driving stellar evolution, it is not possible to derive red supergiant masses from luminosities and $T_{\rm eff}$ alone. In these stars, we find that 10 to 35 per cent of the nuclear energy generation occurs in the H-shell, depending on the core mass ($M_{\rm core}$) and the central He mass fraction ($Y_{\rm c}$). We derive the following relationship between $M_{\rm core}$ and the total luminosity of a red supergiant during core He burning: $\log M_{\rm core} \simeq 0.44 \log {\rm L/L}_{\odot} - 1.38$.
5. At $M_{\rm core}/M_{\rm total} \approx 0.2$, our models exhibit a bi-stability in the solution of stellar structure equations. The solution of the stellar structure equations switches from

a convective outer envelope with a radiative H-burning shell to a radiative outer envelope with a convective H-burning shell. This switch is accompanied by a large increase in luminosity and $T_{\rm eff}$.

6. Stars with greater than 80 per cent of the mass in the H-envelope correspond to mass gainers and merger products. The luminosity and $T_{\rm eff}$ of these stars are dominated by properties of the envelope. More than 70 per cent of their energy generation comes from the H-shell. Some of these stars may resemble OB-type stars and others may resemble blue supergiants.

7. For a constant envelope mass and He-core composition, the total energy produced in the H-shell increases with increasing core mass. This is because higher mass cores produce a larger, hotter H-burning shell which increases CNO burning in the shell. Despite this, the fraction of energy produced in the H-shell decreases with increasing core mass. This is because higher mass cores are hotter and produce more energy which means the stars requires less energy generation in the H-shell to support an envelope of a given mass.

8. For core-He burning stars with the same core mass ($M_{\rm core}$) and envelope mass ($M_{\rm env}$), the luminosity of the He-core increases with decreasing $Y_{\rm c}$, due to the effect of the mean molecular weight of the core ($\mu_{\rm core}$). For stars with envelope masses of $M_{\rm env} \lesssim 1{\rm M}_{\odot}$, the increased luminosity of the He-core results in an increased surface luminosity. However, for stars with $M_{\rm env} \gtrsim 1{\rm M}_{\odot}$, the increased luminosity in the He-core is nearly cancelled out by a corresponding decrease in the luminosity of the H-shell. As a result, in these stars the luminosity at the surface is not strongly affected by $\mu_{\rm core}$, and is set by $M_{\rm core}$ and $M_{\rm env}$.

In this project, we developed a new approach to modelling stars called SNAPSHOT. We described the details of our method and applied it to the properties of red supergiants and stripped stars during core helium burning. In the next chapter, we will apply our SNAPSHOT method to study the properties of red supergiants and stripped stars at the pre-supernova stage.

Chapter 4

The Uncertain Masses of Progenitors of Core Collapse Supernovae and Direct Collapse Black Holes

The contents of this chapter were published in Farrell et al. (2020), MNRAS Letters, 494, 1, 53.

4.1 Stellar Models

We compute a grid of stellar models at the end of core C burning spanning a range of He core masses $M_{\text{He-core}}$ and envelope masses M_{env}. Our models have $M_{\text{He-core}} = 2.7$, 3.4, 4.3, 5.2 and 6.2 M$_\odot$. For each $M_{\text{He-core}}$ our grid contains models with M_{env} ranging from 0 to ~ 40 M$_\odot$. The envelopes of our models consists of ~ 72 per cent H in mass, except for models with $M_{\text{env}} \lesssim 0.5$ M$_\odot$ where the composition is not homogeneous. We choose this range of masses because they correspond to the majority of the range of observed CCSNe progenitors.

Our method can be summarised as follows. We first compute a stellar evolution model with the MESA software package (r10398, Paxton et al., 2011, 2013, 2015, 2018) from the zero-age main sequence until near the end of core-He burning. For these evolutionary calculations, we use standard physical inputs similar to Choi et al. (2016), with a solar metallicity of Z = 0.02. We pause the models when the central He abundance is $Y_c = 0.01$. We then use a technique that we developed, named SNAPSHOT, which allow us to add or remove mass from the star without the star evolving. In effect, this allows us to systematically modify M_{env} without affecting $M_{\text{He-core}}$. After M_{env} is modified, we allow the models to relax to hydrostatic and thermal equilibrium. Finally, we resume the evolution of these models until central C depletion with mass loss turned off. Our results are independent of mass loss during C burning as it would just change the sampling of our

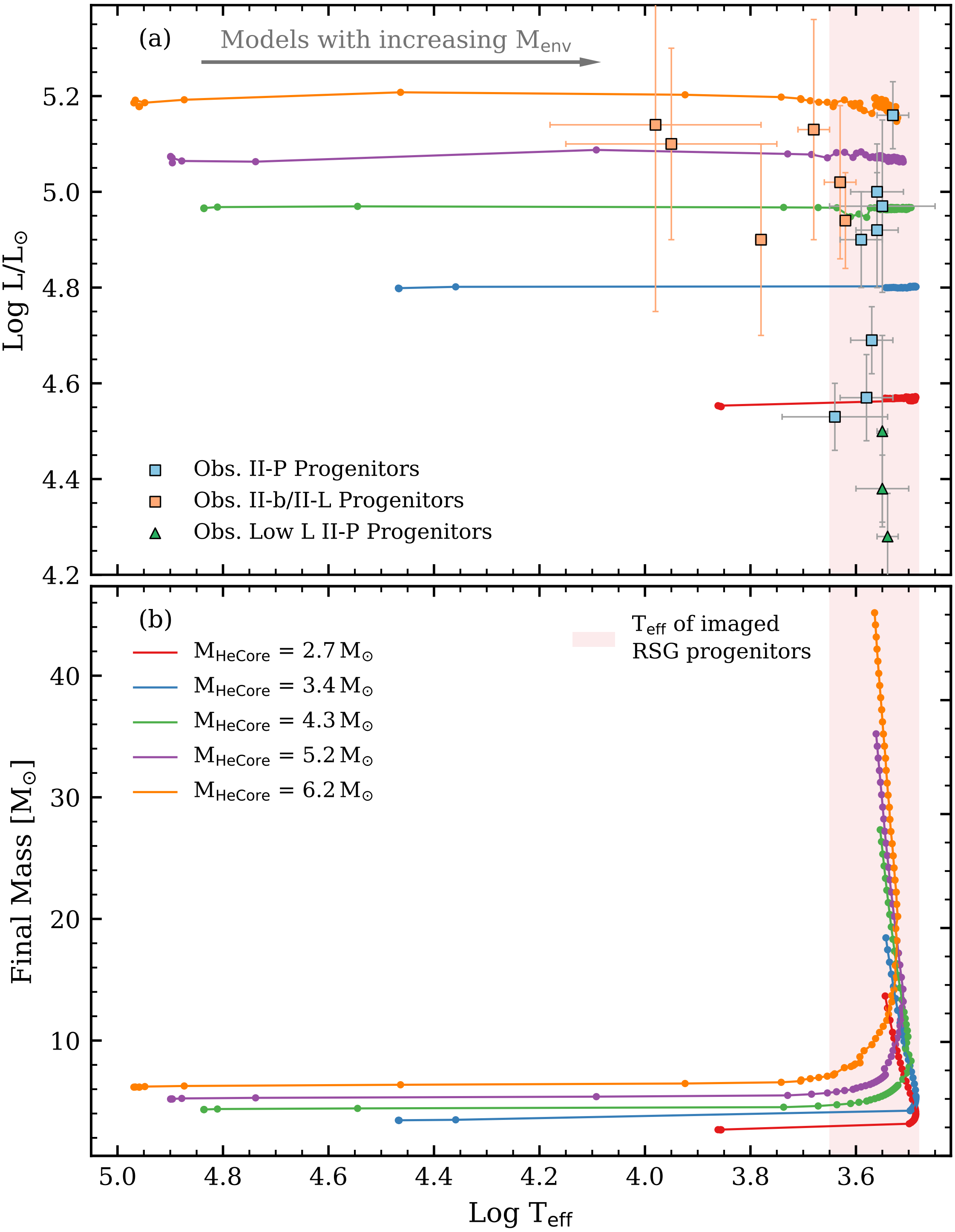

Figure 30: *(a)*: Our grid of models at the end of central Carbon burning in the HR diagram. Lines join models of the same Helium core mass and varying envelope mass from 0 to $\gtrsim 20\,M_\odot$. We also plot the L and $T_{\rm eff}$ derived from pre-explosion images of progenitors of SN II-P (blue squares), IIb/II-L (orange squares) and low luminosity II-P (green triangles). See Table 4.1 for further details. The Helium core masses are indicated in the legend in *(b)*. We shade the range of $T_{\rm eff}$ with which most RSG progenitors are observed (light red). *(b)*: The final mass $M_{\rm fin}$ as a function of $T_{\rm eff}$ for models with constant $M_{\rm He\text{-}core}$ and varying $M_{\rm env}$.

grid in $M_{\rm core}$ and $M_{\rm env}$. The values of luminosity L and $T_{\rm eff}$ at this point are the same as at the pre-supernova stage, as the surface properties are not expected to significantly change after central C depletion (Groh et al., 2013c; Yoon et al., 2017). The final stellar models provide the interior profiles of the standard quantities, e.g. chemical abundances, temperature, density and energy generation, in addition to the surface properties such as L and $T_{\rm eff}$. For a given $M_{\rm core}$ and $M_{\rm env}$, the interior and surface properties of our stellar models do not depend on the mass loss history (see online supplementary appendix).

The results from our models are subject to a number of caveats, which only add to our main conclusion that the initial and final masses of SN II-P progenitors are uncertain. We use standard mixing length theory for convection with a mixing-length parameter of $\alpha_{\rm mlt}$ = 1.82. This treatment of convection may affect the value of the stellar radius, and hence $T_{\rm eff}$. Secondly, we use a time-dependent, diffusive convective core-overshooting parameter (Herwig, 2000; Paxton et al., 2011). We adopt the same overshooting parameters as in the MIST models (Choi et al., 2016) with core overshooting of $f_{\rm ov,core} = 0.016$ (roughly equivalent to $\alpha_{\rm ov} = 0.2$ in the step overshoot scheme), and $f_{\rm ov,shell} = f_{\rm ov,env} = 0.0174$. This may change the masses of the inert He shell and the mass of the CO core, which could have an impact on the core mass luminosity relationship that we derive. The nuclear reaction rates may also affect the core mass luminosity relationship. For instance, there is some uncertainty in the rate of $^{12}C(\alpha,\gamma)^{16}O$ (e.g. deBoer et al., 2017), which may impact the fractions of C and O in the core and hence the relationship between the core mass and L.

4.2 The Uncertain Masses of Supernova Progenitors

Our models predict that it is not possible to determine the final mass, $M_{\rm fin}$ of a RSG supernova progenitor from L and $T_{\rm eff}$ alone. For a given value of L and $T_{\rm eff}$, a RSG can have a range of $M_{\rm fin}$ as wide as 3 to 45 $M_\odot$.

In Fig. 30a, we compare our grid of stellar models at the end of central C burning to the values of L and $T_{\rm eff}$ derived from pre-explosion images of SN progenitors. The observations are taken from the compilation of Smartt (2015). The models with high $T_{\rm eff}$ furthest to the left in Fig. 30a consist of a pure Helium core with no H-rich envelope. Moving from high to low $T_{\rm eff}$ along each line corresponds to increasing $M_{\rm env}$ at constant $M_{\text{He-core}}$. For $M_{\rm env} \lesssim 0.5 M_\odot$, the value of $T_{\rm eff}$ decreases with increasing $M_{\rm env}$ due to the increased effect of opacity in the H-rich envelope. This effect has been seen before in single and binary stellar evolution models (e.g. Meynet et al., 2015a; Yoon et al., 2017; Götberg et al., 2018). For $M_{\rm env} \gtrsim 0.5 M_\odot$, most models have a RSG structure with low $T_{\rm eff}$ and a convective envelope and the value of $T_{\rm eff}$ does not depend very strongly on the value of $M_{\rm env}$. The value of L increases with $M_{\text{He-core}}$, however it does not depend on $M_{\rm env}$ (similar to the behaviour of $T_{\rm eff}$ for RSGs). A given value of L can correspond to a wide range of $M_{\rm fin}$. As a consequence of the relationship between the internal ($M_{\text{He-core}}$, $M_{\rm env}$)

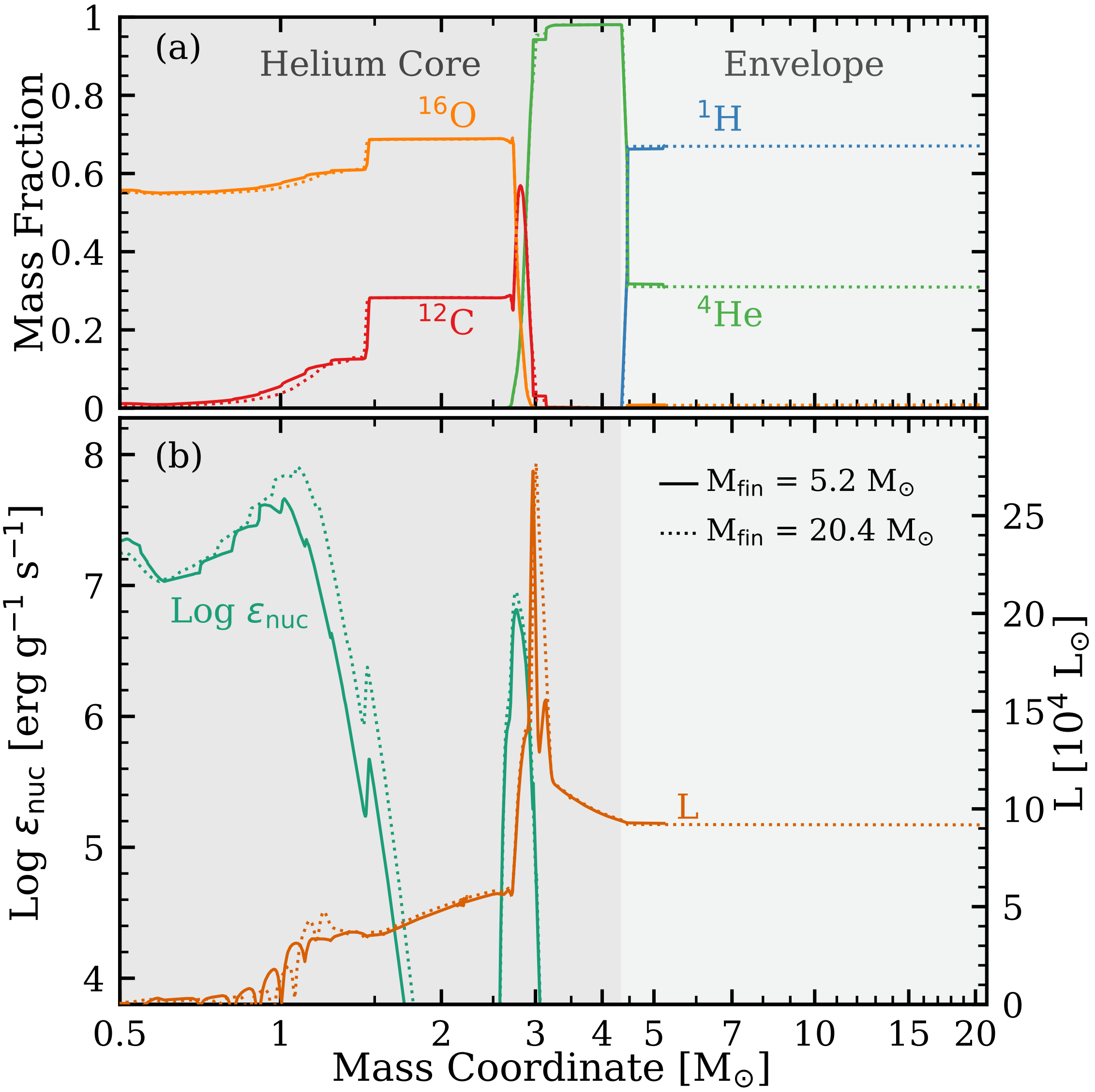

Figure 31: Comparing the interiors of two models at the end of central Carbon burning with the same Helium core mass, $M_{\text{He-core}} = 4.3$ M$_\odot$ and different final masses, $M_{\rm fin} = 5.2$ (solid) and 20.4 M$_\odot$ (dotted). We shade the Helium core in grey and the H rich envelope in light green. *(a)*: The internal abundance profiles of ^{1}H (blue), ^{4}He (green), ^{12}C (red) and ^{16}O (orange) as a function of Lagrangian mass coordinate in log scale. *(b)*: The nuclear energy generation rate $\log \epsilon_{\rm nuc}$ in units of erg g^{-1} s^{-1} (green) and the internal luminosity profile L (orange).

and surface properties (L, $T_{\rm eff}$), there is a wide range of $M_{\rm fin}$ over which L and $T_{\rm eff}$ are very similar.

To more clearly show the range of allowed masses for a given L and $T_{\rm eff}$, we plot the value of $M_{\rm fin}$ against $T_{\rm eff}$ (Fig. 30b). As in Fig. 30a, each line corresponds to a set of models with constant $M_{\text{He-core}}$ and hence constant luminosity. For a given $M_{\text{He-core}}$, i.e. a given L, there is a large range of $M_{\rm fin}$ which produce similar values of $T_{\rm eff}$. Using our models, we estimate the range of allowed $M_{\rm fin}$ for a compilation of directly imaged SN progenitors (Table 4.1).

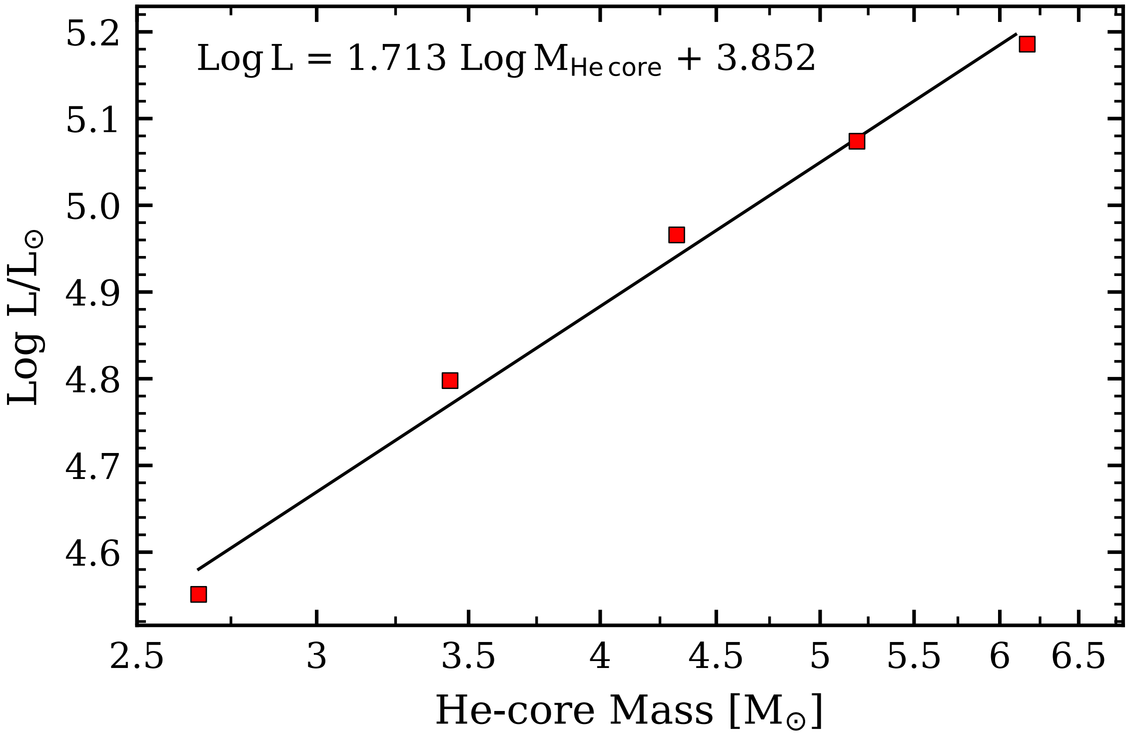

Figure 32: Relationship between final Helium Core Mass $M_{\text{He-core}}$ and luminosity L of our models (red) at the end of central Carbon burning. We also compute and plot the best fit relationship between $M_{\text{He-core}}$ and L.

To explore why the values of L and T_{eff} of RSG progenitors are not strongly affected by M_{env} for a given $M_{\text{He-core}}$, we compare the interior of two models with the same final $M_{\text{He-core}} = 4.3$ M$_{\odot}$ and different final masses $M_{\text{fin}} = 5.2$ (solid) and 20.4 M$_{\odot}$ (dashed) at the end of central Carbon burning (Fig. 31). The abundance profile of the core is very similar for both models (Fig. 31a). The models with $M_{\text{fin}} = 5.2$ and 20.4 M$_{\odot}$ have envelope masses of $M_{\text{env}} = 0.9$ and 16.2 M$_{\odot}$ respectively. Fig. 31b shows the nuclear energy generation rate ϵ_{nuc} (green) and the internal luminosity profile (orange) for each model. In both models, all of the nuclear energy generation occurs inside the Helium core. About 50 per cent of the luminosity from the core is generated by He-shell burning, above the CO core. No burning takes place in the H-shell. As a result, the internal luminosity profiles are very similar inside the core and constant outside the core. This results in the same surface luminosity for both models. The H-rich envelopes are fully convective in both models. This leads to a small change in radius, and hence T_{eff}, over a wide range of M_{fin}.

While our models show that the values of L and T_{eff} alone cannot determine M_{fin}, we can derive $M_{\text{He-core}}$ from L (Table 4.1). The dependence of the luminosity of RSGs on $M_{\text{He-core}}$ has previously been pointed out (e.g. Smartt et al., 2009). Knowledge of $M_{\text{He-core}}$ is important for a number of reasons. For instance, the mass of the core determines the mass of the compact remnant left behind after the supernova, and also affects the nucleosynthesis and chemical yields. We derive the following relationship between the

Table 4.1: Helium core masses $M_{\text{He-core}}$ and range of allowed final masses M_{fin} that we derive from our models for a selection of progenitors type II-P, II-L and IIb supernovae as well as one direct collapse black hole candidate (DCBH, Adams et al., 2017a). We take the values of L and T_{eff} from 1. Aldering et al. (1994), 2. the compilation of Davies & Beasor (2018), 3. the updated distances for 2004et and N6946-BH1 provided by Eldridge & Xiao (2019), 4. the compilation of Smartt (2015) and 5. Kilpatrick et al. (2017). We denote the value of M_{env} for progenitors of SN II-P by '...' as it cannot be constrained by L and T_{eff} alone. We extrapolated our results to lower luminosities for the progenitors in italics. There is some debate about the progenitor of 2009kr (See Maund et al., 2015). We assume a minimum M_{env} of $1\text{M}_\odot$ for progenitors of SN IIP.

SN	Ref	Type	$\log(L/\text{L}_\odot)$	$\log T_{\text{eff}}$	M_{core} [$\text{M}_\odot$]	M_{fin} [$\text{M}_\odot$]	M_{env} [$\text{M}_\odot$]
2003gd	2	II-P	4.28 ± 0.09	3.54	1.8 ± 0.2	2.6 – 13	...
2005cs	2	II-P	4.38 ± 0.07	3.55	2.0 ± 0.2	2.9 – 13	...
2009md	2	II-P	4.50 ± 0.2	3.55	2.4 ± 0.7	2.8 – 18	...
2008bk	2	II-P	4.53 ± 0.07	3.64	2.5 ± 0.2	3.3 – 14	...
2012A	2	II-P	4.57 ± 0.09	3.58	2.6 ± 0.3	3.3 – 14	...
2013ej	2	II-P	4.69 ± 0.07	3.57	3.1 ± 0.3	3.8 – 18	...
2004A	2	II-P	4.90 ± 0.1	3.59	4.1 ± 0.6	4.6 – 28	...
2012aw	2	II-P	4.92 ± 0.12	3.56	4.2 ± 0.7	4.6 – 35	...
2006my	2	II-P	4.97 ± 0.18	3.55	4.5 ± 1.2	4.5 – 45	...
2004et	3	II-P	5.00 ± 0.1	3.56	4.7 ± 0.7	5.1 – 35	...
2012ec	2	II-P	5.16 ± 0.07	3.53	5.8 ± 0.6	6.7 – 41	...
N6946-BH1	3	DCBH?	5.50 ± 0.06	3.51	9.1 ± 0.8	9.4 – 49	...
2011dh	4	IIb	4.90 ± 0.2	3.78	4.1 ± 1.2	$4.2^{+1.3}_{-1.2}$	$0.14^{+0.13}_{-0.03}$
2013df	4	IIb	4.94 ± 0.1	3.62	4.3 ± 0.6	$4.7^{+0.8}_{-0.8}$	$0.38^{+0.25}_{-0.18}$
1993J	1	IIb	5.02 ± 0.16	3.63	4.8 ± 1.1	$5.3^{+2.3}_{-1.4}$	$0.49^{+1.18}_{-0.31}$
2008ax	4	IIb	5.10 ± 0.2	3.95	5.3 ± 1.6	$5.5^{+1.8}_{-1.7}$	$0.22^{+0.2}_{-0.09}$
2009kr	2	II-L	5.13 ± 0.23	3.68	5.6 ± 2.0	$6.1^{+2.7}_{-2.3}$	$0.49^{+0.68}_{-0.32}$
2016gkg	5	IIb	5.14 ± 0.39	3.98	5.6 ± 3.8	$5.8^{+4.0}_{-3.9}$	$0.23^{+0.17}_{-0.11}$

final core mass and the progenitor luminosity (Fig. 32):

$$\log(M_{\text{He-core}}/\text{M}_\odot) = 0.659\log(L/\text{L}_\odot) - 2.630 \tag{4.1}$$

In terms of $M_{\text{He-core}}$, this is

$$\log(L/\text{L}_\odot) = 1.713\log(M_{\text{He-core}}/\text{M}_\odot) + 3.852 \tag{4.2}$$

The exponent in the core mass luminosity relationship of 1.713 is much lower than during core-He burning (~ 2.5) or during the main sequence (~ 3.0). It decreases as a massive star evolves.

For some of the progenitors in Table 4.1, we have extrapolated Equation 4.1 to lower luminosities than we have modelled. We note that this makes those core masses very uncertain. The natures of the progenitors that have the lowest luminosities are uncertain (e.g. Eldridge et al., 2007; Fraser et al., 2011). These stars are close to the minimum core mass for a core-collapse SN and expected to experience second dredge-up after core Helium burning and become AGB stars. If the low Helium core masses that we derive are correct and they do experience core collapse, it suggests that some physical process has slowed or prevented the process of second dredge-up. For example, Fraser et al. (2011) found boosting the carbon-burning rate by a significant factor could prevent second dredge-up before core-collapse. A detailed examination of whether models in this range would go through second dredge-up or not is beyond the scope of this work, but something we will investigate in future. For a review of the uncertain physics and outcomes see Doherty et al. (2017). We don't expect this to change the qualitative conclusion that the $M_{\rm fin}$ of RSG progenitors are uncertain.

We also use our models to derive $M_{\rm He\text{-}core}$ and $M_{\rm env}$ for 5 progenitors of SN IIb and II-L for which pre-explosion images exist (Table 4.1). For models with $M_{\rm env} \lesssim 1$ M$_{\odot}$, the value of $T_{\rm eff}$ depends strongly on $M_{\rm env}$. This allows a determination of $M_{\rm env}$. The derived value of $M_{\rm env}$ depends strongly on both the values of L and $T_{\rm eff}$. The fact that $M_{\rm env}$ is well constrained means that the allowed range of $M_{\rm fin}$ is much smaller for progenitors of SN IIb than for the RSG progenitors of SN II-P.

4.3 Implications

Our models predict that it is not possible to determine the mass of a RSG supernova progenitor from L and $T_{\rm eff}$ alone. Based on the uncertainties in L and $T_{\rm eff}$, the range of allowed $M_{\rm fin}$ can be as wide as $3-45$ M$_{\odot}$ (Table 4.1). While the probability distribution within these limits is not flat, and extreme values are unlikely, any determination of $M_{\rm fin}$ for a specific event based on the surface properties alone will be highly degenerate. RSGs that evolved through binary evolution can have a wider range of $M_{\rm fin}$ than single stars. This is particularly important if the binary fraction is high (Zapartas et al., 2019). Additionally, Eldridge et al. (2018) find that SN II-P like light curves can be produced from RSGs with $M_{\rm fin} \sim 4$M$_{\odot}$, and that stellar mergers can produce RSGs with $M_{\rm fin} \sim 40$M$_{\odot}$. For single stars, there is a much narrower expected range of final masses. However, accurate values are difficult to determine with current state-of-the-art stellar evolution models without making strong assumptions about mass loss, convection, and rotation.

While the value of $M_{\rm fin}$ is degenerate for a given L and $T_{\rm eff}$, it is possible to determine the value of $M_{\rm He\text{-}core}$ from L (Equation 4.1). Using this, we derive values of $M_{\rm He\text{-}core}$ for a compilation of SN progenitors. We include uncertainties in the value of $M_{\rm He\text{-}core}$ based on the reported uncertainties in L. The apparent upper luminosity limit to RSG progenitors reported by Smartt (2015) of $\log L/{\rm L}_{\odot} \simeq 5.1$ dex corresponds to a final $M_{\rm He\text{-}core}$ of 5.3M$_{\odot}$. The distribution of final $M_{\rm He\text{-}core}$ may be a useful constraint for evolution models of massive stars. From the observational side, improvements in distance determination and reddening calculations can help to improve the accuracy of inferred final $M_{\rm He\text{-}core}$.

The mapping between the final $M_{\rm He\text{-}core}$ and the $M_{\rm ini}$ depends on the uncertain physical inputs of the stellar evolution models such as mass loss, rotation, convection and binary interaction. This mapping is likely to be mostly affected by processes that modify the mass of the convective core during the main sequence (MS). The mass of the Helium core of a RSG progenitor is mostly determined at the end of the MS and not strongly affected by subsequent mass loss, binary interaction. Our results suggest that the 'red supergiant problem' can be framed in terms of a mapping between $M_{\rm ini}$ and final $M_{\rm He\text{-}core}$. Uncertainty about the value of $M_{\rm fin}$ of RSG progenitors has several consequences. It means that a RSG progenitor with a given luminosity and $T_{\rm eff}$ can be produced from a wide variety evolutionary histories. This makes it difficult to determine the lifetime of the star and to assign an age. This may be important to consider when assigning an age to a SN progenitor based on its mass and relating the age to the surrounding stellar population.

It is possible to break the degeneracy between L, $T_{\rm eff}$ and $M_{\rm fin}$ of RSGs after they explode. One way is to use the light curve of the supernova to determine the mass of the H-envelope (e.g. Dessart & Hillier, 2019). The value of $M_{\rm env}$ can be added to the value of $M_{\rm He\text{-}core}$ derived from the luminosity of the progenitor to determine $M_{\rm fin}$. It may also be possible to determine $M_{\rm fin}$ from the value of $\log g$, in the unlikely event that a spectrum of the progenitor is available. To make connections between $M_{\rm fin}$ and $M_{\rm ini}$, stellar evolution models are needed. For instance, by combining stellar evolution models of single and binary stars and explosion models, Eldridge et al. (2019) explored a wide range of light curve and progenitor properties of CCSNe.

In contrast to RSG progenitors of SNe IIP , the value of $M_{\rm fin}$ of stripped star progenitors of SN IIb/II-L is more well determined by the values of L and $T_{\rm eff}$ due to the sharp dependence of $T_{\rm eff}$ on $M_{\rm env}$ for $M_{\rm env} \lesssim 1$ M$_\odot$ (Fig. 30b). The maximum $M_{\rm env}$ that we derive for progenitors of IIb is $0.49{\rm M}_\odot$. The range of allowed $M_{\rm fin}$ is mostly due to the uncertainty in $M_{\rm He\text{-}core}$ as a result of uncertain L. In addition, most of the uncertainty in the derived values of $M_{\rm env}$ is due to the uncertainty in the value of L. The derived values of $M_{\rm env}$ can help us to understand and provide useful constraints on stellar evolution, binary interaction and also be used as inputs to hydro-dynamic explosion models. Our models predict that for a star to be a RSG at the end of its evolution (assuming $T_{\rm eff} < 5000$ K), it must have $M_{\rm env}$ of $\gtrsim 0.1-0.5{\rm M}_\odot$, depending on the value of $M_{\rm He\text{-}core}$. Eldridge et al. (2018) found that the minimum hydrogen mass required to produce a SN II-P is $1{\rm M}_\odot$. RSGs with $M_{\rm env}$ of $\sim 0.1-1{\rm M}_\odot$ may produce SN II-L when they explode.

While the degeneracy between $M_{\rm fin}$, L and $T_{\rm eff}$ for progenitors of SN II-P can be broken using SN observations, this is obviously not possible for progenitors of failed supernovae such as N6946-BH1 reported by Adams et al. (2017a).Assuming a RSG structure and the updated distance to its host galaxy reported in Eldridge & Xiao (2019), we derive $M_{\rm He\text{-}core} = 9.1 \pm 0.8$ and an allowed final mass range of $9-49{\rm M}_\odot$. This value is close to the Helium core mass for a black hole forming event assumed by Heger et al. (2003) ($\sim 8{\rm M}_\odot$) and also by Sukhbold et al. (2016). Using the lower distance assumed in Adams et al. (2017a), we derive $M_{\rm He\text{-}core} = 7.2 \pm 0.6$. The core mass determines the outcome of stellar evolution and the lower and upper $M_{\rm He\text{-}core}$ for CCSNe will place tight constraints on stellar models. It is difficult to constrain the initial mass of a progenitor from its final

$M_{\text{He-core}}$. There is no unique solution because of the multiple possible pathways to lead to the same final $M_{\text{He-core}}$.

For values of M_{env} higher than those depicted in Fig. 30b, our models produce blue supergiant (BSG) progenitors, similar to what has been seen in binary evolution models for mass gainers and mergers (e.g. Menon & Heger, 2017). In contrast to the RSG models, we find that the H-shell of BSG models is still generating energy at the end of central Carbon burning. This introduces additional complexities in deriving a relationship between $M_{\text{He-core}}$ and L because there will be a contribution to L from the H-shell which will depend on M_{env}. In the future, we will compute a grid of BSG progenitor models at low metallicities which has implications for the progenitor of SN1987A.

In this chapter, we discussed how the final masses of RSG progenitors of CCSNe, failed SNe and direct collapse black holes are difficult to derive from the luminosity and effective temperature alone. The mass of a RSG at the final stage of its evolution is very uncertain, regardless of the success of the explosion. In the next chapter, we extend our SNAPSHOT method to study cause and effect in massive star evolution.

Chapter 5

Numerical experiments to help understand cause and effect in massive star evolution

The contents of this chapter are submitted for publication in MNRAS.

5.1 Numerical Stellar Models

In Farrell et al. (2020b) we introduced our method to compute SNAPSHOT stellar structure models. These SNAPSHOT models are static stellar structure models in hydrostatic and thermal equilibrium. They are a snapshot at just one moment during a star's evolution, so they are not evolving in time. The key advantage of SNAPSHOT models is that they allow us to systematically isolate the effect of one property of the internal abundance profile at a time, similar to the approach adopted in several previous works (Giannone & Weigert, 1967; Lauterborn et al., 1971a,b; Farrell et al., 2020b,b). In Farrell et al. (2020b), we primarily studied the impact of the core and envelope masses on the surface properties of massive stars. In this work, we expand our method and our focus to a wider range of the key features of internal abundance profiles. Our SNAPSHOT models are computed using the MESA software package (r15140, Paxton et al., 2011, 2013, 2015, 2018, 2019). The steps we take to compute the models are as follows:

1. We compute a stellar evolution model at a given mass and metallicity and then save a snapshot at the desired evolutionary stage. The purpose of this is to obtain a starting stellar model which will then be modified. For these evolutionary models, we use a standard set of physical ingredients, the same as described in Farrell et al. (2020b). However, the exact choices for the physical inputs such as convective overshooting, rotation or even binary interaction are not very important because the models will be modified in the next step. Note that in this study, we don't consider the effects of hydrodynamics, the hydrostatic effect of rotation, magnetic field terms or turbulent

Table 5.1: Sequences of snapshot stellar structure models (S-) and numerical test models (T-) in the paper.

Main Sequence Models	
Sequence	Isolated property
S-1	Average mean molecular weight (μ_{avg})
S-2	CNO abundance in the core ($\mathrm{CNO}_{\mathrm{core}}$)
S-3	Fuel supply in the core ($\mathrm{Fuel}_{\mathrm{core}}$)
S-4	Metal abundance in the envelope ($\mathrm{Z}_{\mathrm{env}}$)
S-5	Total stellar mass
S-6	Homogeneity of hydrogen profile ($\mathrm{H}_{\mathrm{profile}}$)
Core Helium Burning	
Sequence	Isolated property
S-7	Distribution of He in the envelope
S-8	Hydrogen gradient in H-shell
S-9	He mass in H-shell with similar gradient
S-10	H abundance in envelope with same H-shell profile
S-11	H abundance in envelope with same gradient
S-12	H abundance in envelope with same inner envelope
S-13	Helium abundance in the core (Y_{core})
S-14	Core mass ratio with very shallow hydrogen gradient
S-15	Core mass ratio with shallow hydrogen gradient
S-16	Core mass ratio with medium hydrogen gradient
S-17	Core mass ratio with steep hydrogen gradient
S-18	Core mass ratio with very steep hydrogen gradient
S-19	CNO abundance in H-shell ($\mathrm{CNO}_{\mathrm{shell}}$)
S-20	Metal abundance in the envelope (Z_{envelope})
Expansion after the MS phase	
Sequence	Description
T-21	12 $\mathrm{M}_{\odot}$ stellar evolution model
T-22	Artificially suppressing contraction of the core
T-23	Effect of different $\mathrm{Y}_{\mathrm{shell}}$
T-24	Effect of different $\mathrm{CNO}_{\mathrm{shell}}$

pressure.

2. Once we have an appropriate starting stellar model, we directly modify part of the model file by hand (the .mod file in MESA). For example, we might modify the abundance profile in a specific region, or add or remove mass. This can easily be done in a controlled way, varying only one property at a time.

3. We then insert the model file back into MESA to find a solution to the stellar structure equations in hydrostatic and thermal equilibrium with the new abundance profile. As long as the abundance profile or mass was not modified by too much in (ii), we found that MESA usually converged to a stable solution relatively quickly. During this process, we allow convective mixing to briefly take place so that the new solution is consistent with the criterion for convection. Sometimes this causes mixing and changes the chemical profiles inside the model. We also performed tests to verify that our models are in equilibrium by evolving them for a short amount in time to check that they don't change significantly.

Steps (ii) and (iii) are repeated many times as required to construct a series of models in which one feature of the internal abundance profile is changed at a time, e.g. the hydrogen abundance in the envelope (S-10) or the envelope mass (S-16). The advantage of our method is that we can create numerical experiments indicating how a very specific change at a given point in the internal abundance profile affects the position in the HR diagram. This cannot be done by more simplified techniques such as homology relations or polytropic models. Many different properties of the internal abundance profile can be studied in this way including aspects governed by mixing processes, e.g. the quantity of helium in the hydrogen burning shell, or by mass loss processes, e.g. the mass of the envelope.

5.2 A framework to qualitatively understand the evolution of the surface properties of stars

In Sections 5.3 – 5.7, will use our SNAPSHOT modelling approach to investigate the effect of a wide variety features of the internal abundance profile (as listed in Table 5.1). Before presenting the quantitative results from our numerical models, we find it useful to devise a framework to qualitatively understand the evolution of the radius and luminosity based on the usual equations of stellar structure and, in particular, on energy conservation. We describe this framework below.

Classically, expansion and contraction in stars can be encapsulated by ϵ_{grav} in the equation of energy conservation (e.g. Kippenhahn & Weigert, 1990)

$$\frac{dL_{\mathrm{actual}}}{dm} = \epsilon_{\mathrm{nuc}} - \epsilon_{\nu} + \epsilon_{\mathrm{grav}} \tag{5.1}$$

where $\epsilon_{\rm grav}$ can be expressed as

$$\epsilon_{\rm grav} = c_{\rm P} T \left(\frac{1}{T} \frac{\partial T}{\partial t} - \frac{\nabla_{\rm ad}}{P} \frac{\partial P}{\partial t} \right) \tag{5.2}$$

and where $\epsilon_{\rm nuc}$ is the rate of nuclear energy generation per unit mass, ϵ_ν represents neutrino losses. For clarity, we define $L_{\rm actual}$ as the actual internal luminosity profile as a function of mass in a star (note that this quantity is often referred to as $L(m)$ in textbooks). $\epsilon_{\rm grav}$ expresses the change in the thermodynamic properties of the gas resulting from two possibilities: (i) energy that cannot be removed sufficiently quickly by the energy transport mechanism, in which case the energy remains locked in the gas and (ii) an energy deficiency, in which case the temperature gradient is modified by a change of the stellar structure, causing a contraction. A local value of $\epsilon_{\rm grav} > 0$ indicates a local contraction, $\epsilon_{\rm grav} < 0$ indicates a local expansion, while $\epsilon_{\rm grav} = 0$ indicates local thermal equilibrium. These expansions or contractions operate on the thermal timescale. Understanding the behaviour of $\epsilon_{\rm grav}$ is critical to understanding why a star evolves to a particular L and $T_{\rm eff}$.

To get an intuitive understanding for what sets $\epsilon_{\rm grav}$ throughout a star as it evolves, we divide the factors that affect the value of $\epsilon_{\rm grav}$ into two components, $L_{\rm nuc}$ and $L_{\rm actual}$. We define $L_{\rm nuc}$ as the cumulative internal luminosity profile produced by nuclear reactions,

$$L_{\rm nuc}(m) = \int_0^m \epsilon_{\rm nuc}\, dm'. \tag{5.3}$$

$L_{\rm nuc}$ can be affected by anything that changes the nuclear energy generation rates, i.e. the temperature, density or fuel supply in a nuclear burning region. $L_{\rm actual}$ can be affected by (i) the hydrostatic structure of the star and (ii) the energy transport within the star. These are described by the equations for hydrostatic equilibrium and energy transport respectively (e.g. Kippenhahn & Weigert, 1990),

$$\frac{dP}{dm} = -\frac{Gm}{4\pi r^2} \tag{5.4}$$

$$\frac{dT}{dm} = -\frac{GmT}{4\pi r^4 P} \nabla \tag{5.5}$$

$$\nabla_{\rm rad} = \frac{3}{16\pi acG} \frac{\kappa L_{\rm actual} P}{m T^4} \tag{5.6}$$

where κ is the opacity and all other variables have their usual meaning. For transport by radiation, $\nabla = \nabla_{\rm rad}$ in Equation 5.5, while for transport by convection ∇ is equal to $\nabla_{\rm ad}$ or the gradient that is obtained from mixing-length theory. $L_{\rm actual}$ can be affected by any property that affects hydrostatic equilibrium and energy transport including the mass, the opacity or the presence of convection. Rearranging Equation 5.1, and assuming

$\epsilon_\nu << \epsilon_{\rm nuc}$ (which is valid for the vast majority of a star's lifetime), we get

$$\epsilon_{\rm grav} = \frac{dL_{\rm actual}}{dm} - \epsilon_{\rm nuc} = \frac{dL_{\rm actual}}{dm} - \frac{dL_{\rm nuc}}{dm} \tag{5.7}$$

Starting in thermal equilibrium, $\epsilon_{\rm grav} = 0$, an increase in $dL_{\rm nuc}/dm$ or decrease in $dL_{\rm actual}/dm$ will lead to $\epsilon_{\rm grav} < 0$ and expansion, and vice versa. The picture can be simplified by considering that an increase/decrease in $L_{\rm nuc}$ or $L_{\rm actual}$ at a given point in the star will also result in a local increase/decrease in $dL_{\rm nuc}/dm$ or $dL_{\rm actual}/dm$ respectively.

When a star is in perfect hydrostatic and thermal equilibrium, $dL_{\rm nuc}/dm = dL_{\rm actual}/dm$ and $L_{\rm actual} = L_{\rm nuc}$ at all points in the star. Any change that causes either an increase of $L_{\rm nuc}$ or a decrease of $L_{\rm actual}$ will favour evolution to a larger radius (usually lower $T_{\rm eff}$). Conversely, any property that causes a decrease of $L_{\rm nuc}$ or an increase of $L_{\rm actual}$ will favour evolution to a smaller radius (usually higher $T_{\rm eff}$). The evolution of the luminosity is determined by how the surface value of $L_{\rm actual}$ changes when the star relaxes to thermal equilibrium. It typically increases with changes that increase $L_{\rm actual}$, and vice versa. However, the change in luminosity can be difficult to predict a priori due to the possibility of the formation of convective zones. In summary, stars * can contract or expand on nuclear or thermal timescales due to changes in:

1. The temperature, density or fuel supply of a nuclear burning region (affects $L_{\rm nuc}$)
2. The hydrostatic structure of the star e.g. a decrease in the envelope mass due to mass loss (affects $L_{\rm actual}$)
3. The efficiency of energy transport e.g. a change in opacity or the presence of convection (affects $L_{\rm actual}$)

Any change to the internal abundance profile, the hydrostatic structure or the energy transport that causes a mismatch between $L_{\rm nuc}$ and $L_{\rm actual}$ will change the surface properties of a star. The star will relax towards thermal equilibrium and, therefore, a new L and $T_{\rm eff}$.

We now describe a numerical test to demonstrate how a star responds when $L_{\rm nuc} \neq L_{\rm actual}$ and why stellar evolution models are sometimes so sensitive to small changes. The test can be thought of as an accelerated evolution from one specific abundance profile to another on a thermal timescale.

1. The starting state for the test consists of a stellar structure model of a $15\,{\rm M}_\odot$ blue supergiant at the middle of the core helium burning phase (Fig. 33ab). The initial model is in both hydrostatic and thermal equilibrium and $L_{\rm nuc} = L_{\rm actual}$ at all points in the star (Fig. 33c).

---

* Note that we are not considering stars that are out of hydrostatic equilibrium, e.g. pulsating stars or luminous blue variables in eruption, which behave very differently to stars evolving on nuclear or thermal timescales.

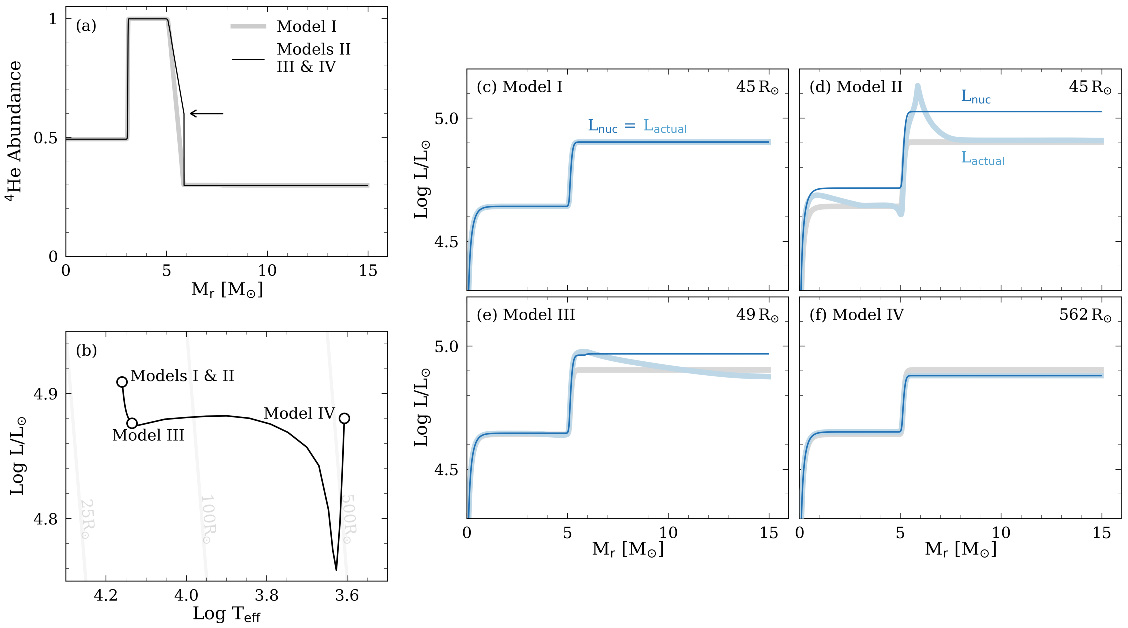

Figure 33: A numerical test to examine the response of a stellar model to changes in its abundance profile. We plot the internal helium abundance profile and the surface properties for the following four models. *Model I*: the original blue supergiant in thermal equilibrium and in which helium will be inserted. *Model II*: stellar model immediately after the helium is inserted to the H-shell by hand, indicated by the black arrow in (a). *Model III*: a few timesteps after Model II after the model has expanded to a radius of 49 $R_\odot$. *Model IV*: when the model has reached thermal equilibrium as a red supergiant. For each model, we plot the cumulative nuclear energy generation profile $L_{\rm nuc}$ and the luminosity imposed by hydrostatic equilibrium $L_{\rm actual}$ in panels.

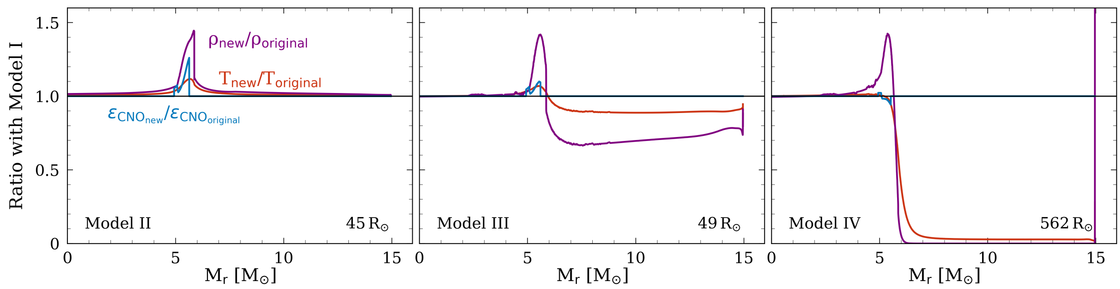

Figure 34: For Models II, III and IV from the test plotted in Fig. 33, we plot the ratio of the internal profiles of temperature, density and $\epsilon_{\rm nuc}$ from CNO burning (scaled by a factor of 0.15) with Model I.

2. We perturb the initial model by modifying the internal abundance profile by hand in the region of the hydrogen burning shell, replacing a small amount of hydrogen with helium (Fig. 33a). This new model could, for example, correspond to what one would obtain assuming a slightly different implementation of the (uncertain) internal mixing processes. We then put the model back into MESA to find a solution to the stellar structure equations, enforcing hydrostatic equilibrium, and study how it relaxes to thermal equilibrium.

3. The new stellar model that we obtain, Model II, is initially out of thermal equilibrium and $L_{\rm nuc} \neq L_{\rm actual}$ (Fig. 33d). The surface properties of Model II have not changed

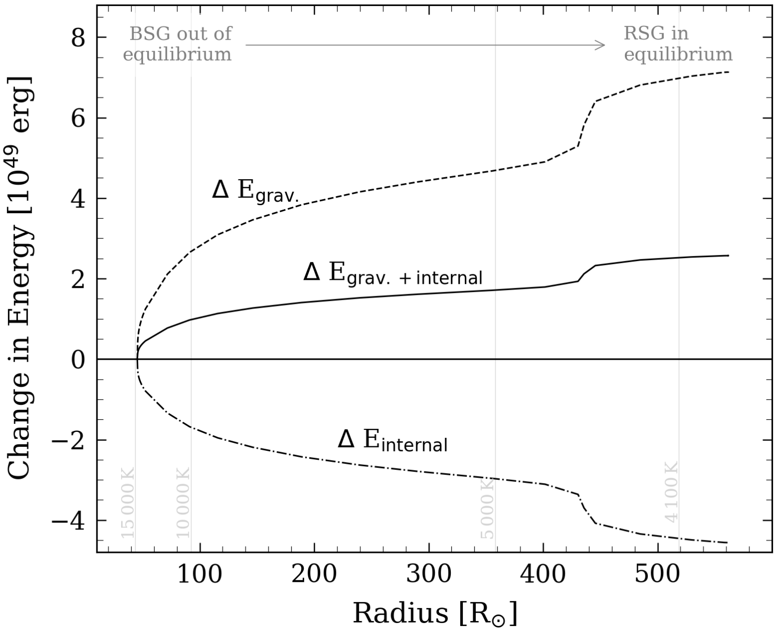

Figure 35: The change in the total internal, gravitational and total (internal + gravitational) energy of the star from the test in Fig. 33 as it expands from a blue to a red supergiant and eventually reaches thermal equilibrium on the right-hand side of the figure. Quantities are defined in the usual way e.g. Kippenhahn & Weigert (1990). The bump at ∼ 440 $R_\odot$ is due to convection in the envelope.

compared to Model I as the changes in the interior have not yet propagated to the surface (Fig. 33b). The value of $L_{\rm nuc}$ in the envelope is larger in Model II than Model I (Fig. 33d). This is because a larger helium abundance increases the mean molecular weight (μ) in the H-shell. For a higher μ, the equation of state requires a higher temperature and/or density to maintain hydrostatic equilibrium. In this case, both the temperature and density in the H-shell are higher in Model II compared to Model I (Fig. 34a). Due to the higher temperature and density, the rate of nuclear energy generation in the H-shell increases, therefore increasing $L_{\rm nuc}$.

4. The value of $L_{\rm nuc}$ is greater than $L_{\rm actual}$ above the H-shell (Fig. 33d). This means the luminosity entering the envelope above the H-shell is greater than the luminosity that can be transported by the envelope with its current structure. The excess energy that cannot be transported will be absorbed into the envelope and cause it to cool and expand. As long as $L_{\rm nuc} \neq L_{\rm actual}$, the star will continue to expand and move to the right in the HR diagram (Fig. 33b). The expansion will stop when the energy produced in the H-shell is exactly equal to the energy that the envelope can transport, i.e. $L_{\rm nuc} = L_{\rm actual}$, and the envelope has a new structure.

5. As the star expands, the values of $L_{\rm nuc}$ and $L_{\rm actual}$ change. $L_{\rm nuc}$ gradually decreases because the expansion of the envelope causes the temperature and density in the outer regions of the H-shell to decrease (Fig. 34). In the envelope, $L_{\rm actual}$ initially decreases and then subsequently increases. This is reflected in the change of the sur-

face luminosity between Model III and IV (Fig. 33b). The initial decrease is a result of the decrease in the temperature gradient dT/dr which decreases the efficiency of energy transport by radiation and, hence, decreases $L_{\rm actual}$. The decrease of $L_{\rm actual}$ actually makes it more difficult for the star to reach thermal equilibrium because it causes the difference between $L_{\rm nuc}$ and $L_{\rm actual}$ to increase. As the radius increases, an increasing proportion of the envelope begins to transport energy by convection. This is a result of cooling of the envelope and an increase in $\nabla_{\rm rad}$. As convection is more efficient at transporting energy, it favours an increase in $L_{\rm actual}$, which occurs once enough of the envelope becomes convective. This is one way to think about why the luminosity of a star increases as it expands along the Hayashi track. It is important to note that the formation of the convective envelope is an effect of the expansion, not the cause. The star will expand regardless of the onset of convection.

6. Another way to think about the expansion is in terms of the change in the internal and gravitational energy (Fig. 35). As discussed above, in Model II the H-shell is producing more luminosity than the envelope can transport. The resulting cooling and expanding of the envelope corresponds to a decrease in the total internal energy of the star of 4.5×10^{49}erg and an increase in its total gravitational potential energy of 7.0×10^{49}erg, reflecting the virial theorem for stars. As a result, the total (gravitational + internal) energy of the star increases by 2.5×10^{49}erg. This net increase comes from nuclear energy generation in the H-shell, so that energy is conserved in total. The increase in the total energy is almost entirely due to the increase in the energy of the envelope. In general, processes which increase the total energy of the envelope also tend to favour an increase in the total stellar radius.

In the following sections, we will use $L_{\rm nuc}$ and $L_{\rm actual}$ to explain what sets the values of L and $T_{\rm eff}$ during core hydrogen burning (Sec. 5.3), core helium burning (Sec. 5.4) and the expansion across the HR diagram between between the hydrogen and helium burning phases (Sec. 5.5).

5.3 The Core hydrogen burning phase

The Main Sequence phase is the most studied and well known phases of the evolution of stars in general (e.g. Schwarzschild & Härm, 1958; Kippenhahn & Weigert, 1990). In this section, we want to (i) verify that our SNAPSHOT models can recover well known results for stars on the MS from simpler methods e.g. homology relations, and to (ii) go beyond what can be done with these simpler approaches by presenting some numerical experiments that shed new light on otherwise well-known behaviour of stars during the MS.

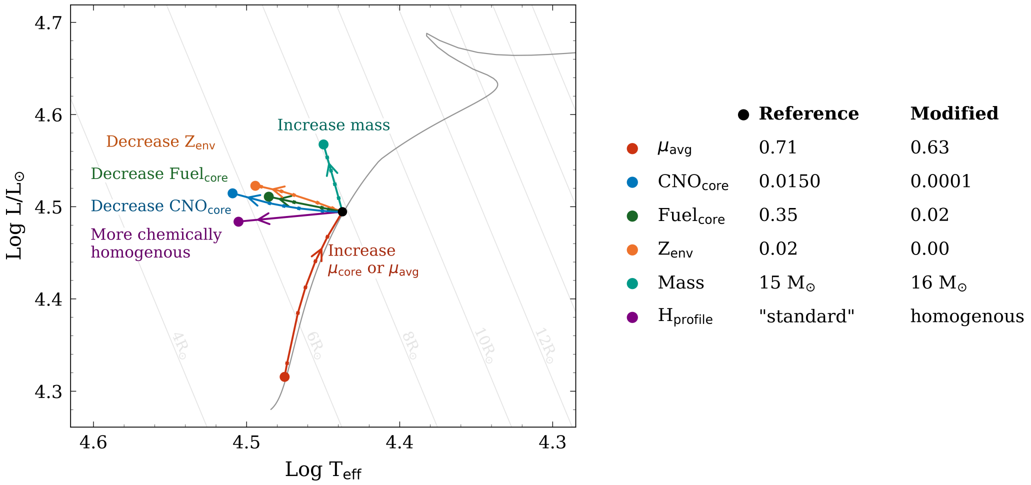

	● Reference	Modified
● $\mu_{\rm avg}$	0.71	0.63
● CNO$_{\rm core}$	0.0150	0.0001
● Fuel$_{\rm core}$	0.35	0.02
● Z$_{\rm env}$	0.02	0.00
● Mass	15 M$_\odot$	16 M$_\odot$
● H$_{\rm profile}$	"standard"	homogenous

Figure 36: The coloured lines represent sequences of models (S-1 to S-6) in which the impact of different properties on the surface properties of a 15 M$_\odot$ main sequence star are isolated. These are the average mean molecular weight ($\mu_{\rm avg}$), the CNO abundance in the convective core (CNO$_{\rm core}$), the fuel supply in the core (Fuel$_{\rm core}$), the metal abundance in the envelope (Z$_{\rm env}$), the total stellar mass and the homogeneity of the hydrogen abundance profile (H$_{\rm profile}$). An evolutionary track of a 15 M$_\odot$ star with solar metallicity (Z = 0.020) is plotted in grey for reference. See Appendix 1 for plots of the internal abundance profiles.

5.3.1 What sets the luminosity and effective temperature of a star on the main-sequence?

We identify six key properties that set L and $T_{\rm eff}$ of massive main sequence stars. These are the average mean molecular weight ($\mu_{\rm avg}$), the CNO abundance in the convective core (CNO$_{\rm core}$), the fuel supply in the convective core (Fuel$_{\rm core}$), the metal abundance in the envelope (Z$_{\rm env}$), the total stellar mass and the homogeneity of the hydrogen abundance profile (H$_{\rm profile}$). To demonstrate the effect of each of these properties, we model their impact on the surface properties with reference to a model of a 15 M$_\odot$ solar metallicity star at the middle of the main sequence phase. To do this, we compute a sequence of models in which only one property of the stellar interior is changed at a time, with the exception of the H$_{\rm profile}$ in which both the hydrogen and helium abundance profiles change. The mean molecular weight and the fuel supply are unusual because they are not simple features of the internal abundance profile. To isolate these properties, we introduce an artificial element called ‘non-burning hydrogen’ which has the mean molecular weight and opacity properties of hydrogen but doesn’t participate in nuclear burning. We achieve this in MESA by modifying the list of isotopes considered in the model to include an artificial isotope with the chemical properties of hydrogen. However, as we do not add this artificial isotope to any of the nuclear reaction networks, it doesn’t participate in nuclear reactions. We verified that this isotope behaves as expected in a stellar evolution model.

Fig. 36 presents the six sequences of models in the HR diagram as well as an evolutionary track of a 15 M$_\odot$ star at Z = 0.020 for comparison. The points on each line indicate the location of each individual snapshot model and the arrows indicate the direction of

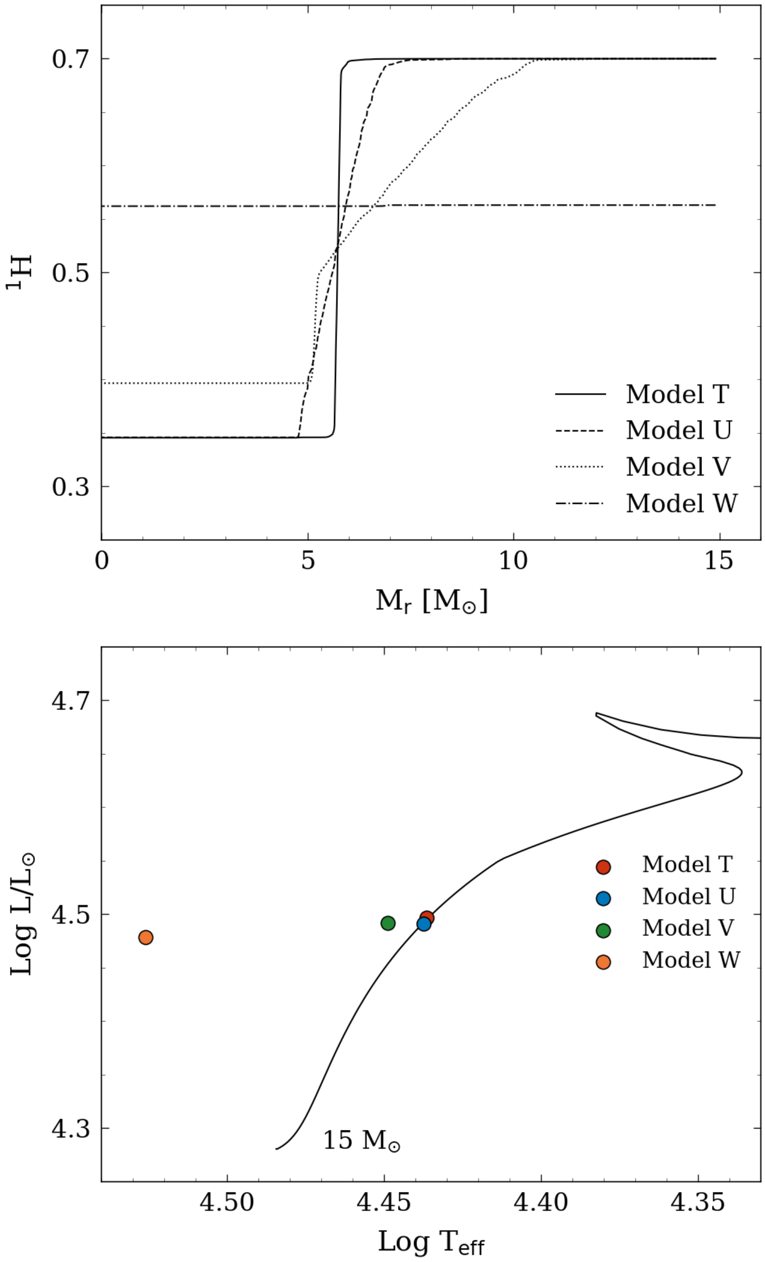

Figure 37: *Upper panel:* Hydrogen abundance profiles of four 15 $M_\odot$ stellar models with the same total hydrogen mass (i.e. same $\mu_{\rm avg}$), but with different internal distributions. *Lower panel:* Location in the HR diagram of the four models from the upper panel with an evolutionary track of a 15 $M_\odot$ plotted for reference.

increase/decrease. The legend on the right lists the numerical values of each property for the reference model plotted in black and for the modified models indicated by the large coloured points at the other end of each model sequence. See Appendix 1 for the internal abundance profiles of the model sequences in Fig. 36. In the following paragraphs, we discuss the effects of each of these properties in detail and consider how they affect $L_{\rm nuc}$ and $L_{\rm actual}$.

To change the average mean molecular weight ($\mu_{\rm avg}$), we convert some fraction of the helium in the convective core to ‘non-burning hydrogen’. This has the desired effect of reducing the mean molecular weight without modifying the fuel supply. It does have the small side effect of changing the opacity in the interior but this has a quantitatively small effect on the overall structure of the stellar model. Note also that while the set of models plotted in Fig. 36 does only modify μ in the convective core, we also computed models in which μ is changed both in and above the core and found similar results. Through the effect of the equation of state, a higher μ_{avg} favours a larger radius R, lower T_{eff} and higher luminosity L. This result can be understood by considering how μ_{avg} affects L_{nuc}. For a higher μ, the equation of state requires a higher temperature and/or density to maintain a given pressure gradient and, therefore, to maintain hydrostatic equilibrium. Due to the higher temperature and density in the nuclear burning region, the rate of nuclear energy generation increases, thus increasing L_{nuc}. This increase in L_{nuc} favours a larger radius, as discussed in Sec. 5.2. The increase in the surface luminosity L with μ_{avg} is due to the higher temperature and density in the central burning region once the model has relaxed to thermal equilibrium. One can derive a consistent conclusion using homologous relations, where $L \propto \mu^4$ (e.g. Kippenhahn & Weigert, 1990). Indeed, one has $L(\mu = 0.71)/L(\mu = 0.63) \approx (0.71/0.63)^4$

We modify the CNO abundances in the core by scaling down the abundances of all the C, N and O isotopes from the reference model (with a solar metallicity) and replacing them with hydrogen. The primary impact of this on the stellar structure is to modify the abundance of CNO isotopes available to act as catalysts in the CNO cycle. We find that a lower CNO abundance in the core (CNO_{core}) favours a smaller R, higher T_{eff} and higher L. The effect on the radius can be understood by considering that a decrease in CNO_{core} decreases L_{nuc} (because the nuclear energy generation rates scale with the abundance of CNO elements, $\epsilon_{\text{nuc}} \propto X_{\text{CNO}}$) which favours a smaller radius. So, why does the luminosity increase? One might have guessed that the higher temperatures in the core required to produce enough luminosity to support the star would exactly balance the effect of the lower CNO abundances. Our models show that the hydrostatic structure of a star in thermal equilibrium with a lower abundance of CNO elements in the core has an internal temperature and density profile that drops off slower as you move away from the center of the star. This results in a higher energy generation rate in the outer parts of the nuclear burning region. An interesting consequence of this is that if you remove fuel, either hydrogen or CNO abundances, from the core, and keep other quantities constant, a star will actually become more luminous.

The fuel supply in the core ($\text{Fuel}_{\text{core}}$) can be modified by converting some fraction of the hydrogen in the core to ‘non-burning hydrogen’. We find that a decrease in $\text{Fuel}_{\text{core}}$, holding everything else constant, favours a smaller R, higher T_{eff} and higher L. Due to the effect on nuclear energy generation a decrease of $\text{Fuel}_{\text{core}}$ will decrease L_{nuc}, favouring a smaller radius. As in the case of the CNO_{core}, because a lower value of $\text{Fuel}_{\text{core}}$ favours a more compact star in thermal equilibrium, the temperatures and densities throughout the nuclear burning region (in particular the outer parts) are slightly higher. This results in a higher surface luminosity.

A lower abundance of metals in the envelope ($\mathrm{Z}_{\mathrm{env}}$) favours a smaller R, higher T_{eff} and higher L. This is due to the effect of $\mathrm{Z}_{\mathrm{env}}$ on the opacity of the envelope. A decrease in opacity affects the energy transport and increases L_{actual} in the envelope, favouring a smaller radius, higher T_{eff} and higher luminosity.

We isolate the effect of the mass by keeping the same abundances at a given normalised mass fraction but modifying the total stellar mass. A larger mass causes a larger R, higher T_{eff} and higher L. While this is very well-known (especially at the zero-age main sequence) and relatively intuitive to understand, it is also worth understanding the result in terms of L_{nuc} and L_{actual}, especially to contrast to helium burning stars later on. A larger mass requires a higher luminosity to maintain hydrostatic equilibrium, resulting in an increase in L_{actual}. This actually favours a contraction to a smaller radius. However due to the magnitude of the increase of L_{actual}, the contraction in the center of the star is large enough to significantly increase the core temperature and the nuclear energy generation rate, causing a feedback effect on L_{nuc}. The balance between the competing effects on L_{nuc} and L_{actual} results in an overall increase in the radius with mass. We will come back to this point when discussing the effects of increasing the envelope mass of a core helium burning star.

Finally, we compare the reference model to a model with the same total mass of hydrogen and helium, but distributed homogeneously throughout the star. While this does increase the fuel supply in the core, it is still a good representation of the effect of the distribution of hydrogen throughout the star ($\mathrm{H}_{\mathrm{profile}}$). The abundance profile of hydrogen in the envelope affects the opacity. Similar to a decrease in $\mathrm{Z}_{\mathrm{env}}$, the decrease in opacity allows a higher luminosity to be transported and increases L_{actual} in the envelope, favouring a smaller radius and higher T_{eff}. Our models indicate that the hydrogen profile has very little impact on the luminosity. We elaborate further on the impact of the internal distribution of hydrogen in Sec. 5.3.3.

5.3.2 Connection to overshooting and metallicity effects

Given the above discussion, we can understand why models with moderately high overshooting or rotation evolve to lower T_{eff} at the terminal-age main sequence. When these models reach the lowest value of T_{eff} on the MS, internal mixing has allowed a larger proportion of the hydrogen in the star to be converted to helium. As a result, the value of μ_{avg} is larger. As we have discussed above, a larger value of μ_{avg} favours a larger radius and lower T_{eff}. Another way of looking at this is to imagine picking up a model with higher overshooting at the TAMS and compressing it so that it is located at the TAMS location of a model with lower overshooting (at higher T_{eff}). The star would then be out of thermal equilibrium as L_{nuc} would be larger than L_{actual}. This would favour an expansion back to larger radii and lower T_{eff}. For more fully mixed models, corresponding to strong rotation or very high overshooting, the competing effect of opacity due to the amount of hydrogen near the surface of the star dominate over the effect of μ_{avg}, favouring a smaller radius and higher T_{eff}. It's also interesting to note that the isolated effect of metallicity on stellar structure of stars at this mass is composed of two significant components, the CNO abundance in the core and the metal abundance in the envelope. Our models show that the effect of opacity is not the only reason that lower metallicity stars have a higher T_{eff}.

5.3.3 Degeneracy between internal hydrogen profile and surface properties

We now examine in more detail the effect of distribution of hydrogen/helium within the star, holding the total mass of hydrogen/helium constant. Fig. 37 compares four core hydrogen burning stellar models with the same mass (15 $\mathrm{M}_{\odot}$) and the same total helium mass, i.e. same μ_{avg}, but with different internal distributions of hydrogen. All of the models are in hydrostatic and thermal equilibrium. Models T, U and V each have different internal distributions of hydrogen (and helium) and different convective core masses. However they have very similar surface properties, differing by at most 0.01 dex in $\log T_{\mathrm{eff}}$ and 0.002 in $\log \mathrm{L}/\mathrm{L}_{\odot}$. These models demonstrates a degeneracy between the internal distribution of hydrogen and the surface properties for stars with the same total mass and μ_{avg}. The degeneracy applies only in the limit that the effects of opacity in the outer layers of the envelope do not dominate. When the star is more fully mixed and homogeneous (Model W), the effects of opacity in the outer layers of the star dominate and it has a significantly higher T_{eff}. Our results here are consistent with conclusions from simplified models of main sequence stars (e.g Schwarzschild & Härm, 1958), but we feel that it is worth re-emphasising and demonstrating this point with more detailed models.

This degeneracy suggests that a given L and T_{eff} could correspond to a lower mass star with higher μ_{avg} or a higher mass star with a lower μ_{avg}. Based on the surface properties alone, it may only be possible to constrain a star to a range of allowed total masses and total hydrogen/helium masses. The degeneracy could be broken by asteroseismology which would provide a better understanding of internal mixing processes. It also suggests that current and future asteroseismology studies with larger sample sizes and higher mass stars will be useful to improve our understanding of convective boundary mixing and rotational mixing beyond what is possible using L and T_{eff} alone. Further study is required to properly quantify this degeneracy across different masses and evolutionary states.

5.4 The Core Helium burning Phase

The evolution of massive stars after the main sequence is complicated. Some of the fundamentals are well understood after decades of research, however many important questions remain unanswered. Stellar evolution models are one of the key tools used to tackle these questions. Understanding exactly what drives a post-main sequence massive stellar model to a blue or red supergiant solution is often very difficult. Stars can evolve to the right and left in the HR diagram in ways that are difficult to understand, sometimes executing loops. The stellar interior changes in multiple ways simultaneously, which makes it difficult to distinguish cause and effect. In addition, very small changes to the stellar interior from earlier evolutionary phases can have a significant effect on the subsequent evolution (Iben, 1974; Weiss, 1989; Chin & Stothers, 1990; Maeder & Meynet, 1994; Ritossa, 1996). For this reason, Rudolf Kippenhahn referred to the post main sequence stage as a “sort of magnifying glass, also revealing relentlessly the faults of calculations of earlier phases” (Kippenhahn & Weigert, 1990). In this section, we isolate and analyse some of the important features of the internal abundance profile that set L and $T_{\rm eff}$ of massive stars during core helium burning. Because stellar interiors can get quite complicated and are ultimately described by a set of vectors describing the internal abundance profiles of each isotope, we cannot fully describe every feature of the internal abundance profile that affects the surface properties. Instead, we try to select the important properties that are modified by evolutionary processes. These are the effect of the helium abundance in the hydrogen shell, the hydrogen abundance in the envelope, the helium abundance in the core, the core mass ratio, the CNO abundance in the hydrogen shell and the metallicity in the envelope which we discuss in Sections 5.4.1 - 5.4.5 below.

5.4.1 Helium Abundance Profile in the Hydrogen Burning Shell

The fact that models with different hydrogen profiles at the interface between the core and the envelope impacts $T_{\rm eff}$ has been known since some of the earliest stellar models were computed (e.g. Lauterborn et al., 1971b). Models with steeper hydrogen gradients are found to favour a bluer star while a shallower gradient favours a redder star (Stothers & Chin, 1968; Robertson, 1971; Fricke et al., 1971; Lauterborn et al., 1971a; Stothers & Chin, 1976; Schlesinger, 1977; Langer et al., 1985; Walmswell et al., 2015; Schootemeijer & Langer, 2018; Schootemeijer et al., 2019). The reason why for this effect is not immediately obvious. An investigation by Walmswell et al. (2015) isolated the effects of the hydrogen profile on the opacity, mean molecular weight and fuel supply and how each affected $T_{\rm eff}$. They found that the increased mean molecular weight and decreased effect of opacity associated with a shallower hydrogen gradient favour a redder star, the reduced fuel supply favours a bluer star, and concluded that the effect of the increased mean molecular weight dominates. Following this, one may still wonder why a gradient of mean molecular weight at the core/envelope interface affects $T_{\rm eff}$ like this. In this section, we investigate this question.

To encapsulate the abundance profile of hydrogen at the core/envelope interface, previous stellar evolution studies have used the term “hydrogen gradient”. This is a simple quantity that is useful for some purposes. However, as is well known, the internal abundance profiles can be quite complicated e.g. due to convective shells during the main sequence phase, semi-convection (Langer et al., 1985), mass gainers (Braun & Langer, 1995) and mergers (Glebbeek et al., 2013). Therefore, we will instead refer to this in a more general way as the helium abundance profile in the region of the hydrogen burning shell, denoted by $\mathrm{Y}_{\mathrm{shell}}$. We will demonstrate why we choose to do this below.

In stellar evolution models, $\mathrm{Y}_{\mathrm{shell}}$ is primarily set by the receding convective core during the MS phase (e.g. Robertson, 1971) and by internal mixing between the end of core hydrogen burning and the beginning of core helium burning (e.g. Langer et al., 1985). During core helium burning, $\mathrm{Y}_{\mathrm{shell}}$ evolves as the hydrogen shell burns through the layers at the base of the envelope. Several different physical processes can modify the shape of the profile. Firstly, the implementation of convective core overshooting during the main sequence phase and choice of the free overshooting parameter (α_{ov} or f_{ov}) can cause a steeper or shallower gradient of hydrogen and helium in the H-shell (Stothers, 1991; Langer, 1991). Semi-convective mixing between core hydrogen depletion and the beginning of helium burning can also have an important effect (Langer et al., 1985; Langer, 1991; Schootemeijer et al., 2019). A combination of reasonable choices for the free parameters for convective overshooting and semi-convective efficiency can produce a very wide variety of hydrogen/helium profiles in the H-shell (Schootemeijer et al., 2019). Rotation has also been shown to modify the helium profile (Maeder & Meynet, 2001) and this depends on the initial rotational velocity and choice of the diffusive mixing parameter. In binary systems, mass gainers and stellar mergers during the MS and the post-MS (e.g. Braun & Langer, 1995; de Mink et al., 2013; Glebbeek et al., 2013) and the reorganisation of the star after a merger event could produce abundance profiles that differ significantly to single stars. In addition, current 1D stellar evolution models likely do not fully or accurately capture the mixing processes that affect $\mathrm{Y}_{\mathrm{shell}}$. These instabilities are inherently multi-dimensional as shown by Cristini et al. (2017); Horst et al. (2021). All of this is to say that the helium abundance profiles in the hydrogen shell that are produced in stellar evolution models are subject to many different uncertain processes.

We compute several sets of snapshot stellar structure models that isolate the effect of $\mathrm{Y}_{\mathrm{shell}}$ on L and T_{eff}, presented in Fig. 38. Each set of models isolates $\mathrm{Y}_{\mathrm{shell}}$ in different ways, keeping some other quantity constant. The lower panels in Fig. 38 show the corresponding values of T_{eff} for each of the three models in the upper panels (black circles) as well as for several intermediate models that are not plotted in the upper panels (white circles). Lines of constant radius are also plotted in grey. The dash-dot lines connect the two models that are closest to the bi-stability transition between a blue and a red supergiant, similar to the one found in Farrell et al. (2020b). This is due to the on-off nature of convection in our stellar models.

The first set of models in Fig. 38, Models A, B and C have the same total mass of helium but distributed differently throughout the envelope. We parameterise the distribution of helium in the envelope in terms of a new parameter A_{He}, where a value of $A_{\mathrm{He}} = 0$ means helium is distributed perfectly evenly throughout the envelope and $A_{\mathrm{He}} = 1$ means all of the helium is concentrated at the base of the envelope and all the hydrogen is at the surface (quite an artificial situation). Models with a higher proportion of helium distributed towards the base of the envelope favour redder stars with larger radii, while those with more evenly distributed helium favour bluer stars with smaller radii. For different distributions of helium, the effective temperature can range from 23 000 K to 4 000 K.

The second set of models, Models D, E and F, have the same core mass (defined here as where $X < 10^{-4}$) and envelope mass and isolate the effect of a linear abundance profile of hydrogen/helium. We choose to parameterise each model in terms of the hydrogen gradient as defined by Schootemeijer & Langer (2018). Models D, E and F indicate clearly that a shallower hydrogen gradient favours a redder star with a larger radius, while a steeper gradient favours a bluer star with a smaller radius. This reproduces the well-known results regarding the hydrogen gradient that we discussed above. For moderate changes in the gradient, our models indicate that the radius can change by a factor of $\sim$ 20 and $T_{\rm eff}$ can vary from 22 000 K to 4 000 K.

The third set of models, Models G, H and I, have similar hydrogen gradients consisting of the same drop in hydrogen abundance between the core and the envelope over the same mass interval, but different total masses of helium. Despite the fact that the hydrogen gradient is very similar, the value of $T_{\rm eff}$ and the stellar radius can vary quite significantly for models with a different mass of helium in the shell. Although this phenomenon is well known from stellar evolution models, Models H and I clearly demonstrate that very small changes in the stellar interior make a huge difference in $T_{\rm eff}$. Although they differ by just 0.05 $M_\odot$ in their total mass of helium, a tiny fraction of the total stellar mass of 15 $M_\odot$, but E is a blue supergiant and F is a red supergiant. The sharp transition between blue and red supergiants due to a small change in stellar structure is similar to the one discussed in Farrell et al. (2020b). The difference between Models G, H and I is smaller than the typical uncertainties in the internal mixing in a stellar evolution model and yet they differ in radius by a factor of 12. As they are located in different parts of the HR diagram, they may be interpreted as having different evolutionary histories, despite their very similar internal structure. Although it has been emphasised by many others, we would like to reiterate the importance of being cautious when using the results of an individual stellar evolution model. A related consequence of these results is that the effect of the helium abundance profile in the shell on the surface properties cannot easily be represented by a single parameter. Even for a very similar hydrogen gradient (e.g. as defined by Schootemeijer et al., 2019), $T_{\rm eff}$ can vary significantly due to the effect of the helium profile (compare our models H and & I).

To understand why the helium abundance profile has these effects on $T_{\rm eff}$, consider how $Y_{\rm shell}$ affects $L_{\rm nuc}$ and $L_{\rm actual}$. An increase of the helium abundance in the region of the H-burning shell causes an increase in the mean molecular weight and, through the equation of state, in the temperature and density (the same effect demonstrated in detail in the numerical test in Sec. 5.2). This causes an increase in the nuclear energy generation rate in the hydrogen burning shell, increasing L_{nuc}. As discussed in Sec. 5.2, an increase in L_{nuc} favours a larger radius and, in this case, a redder star. Any process that causes an increase in the helium abundance in the nuclear burning region of the hydrogen burning shell favours a redder star with a larger radius [†].

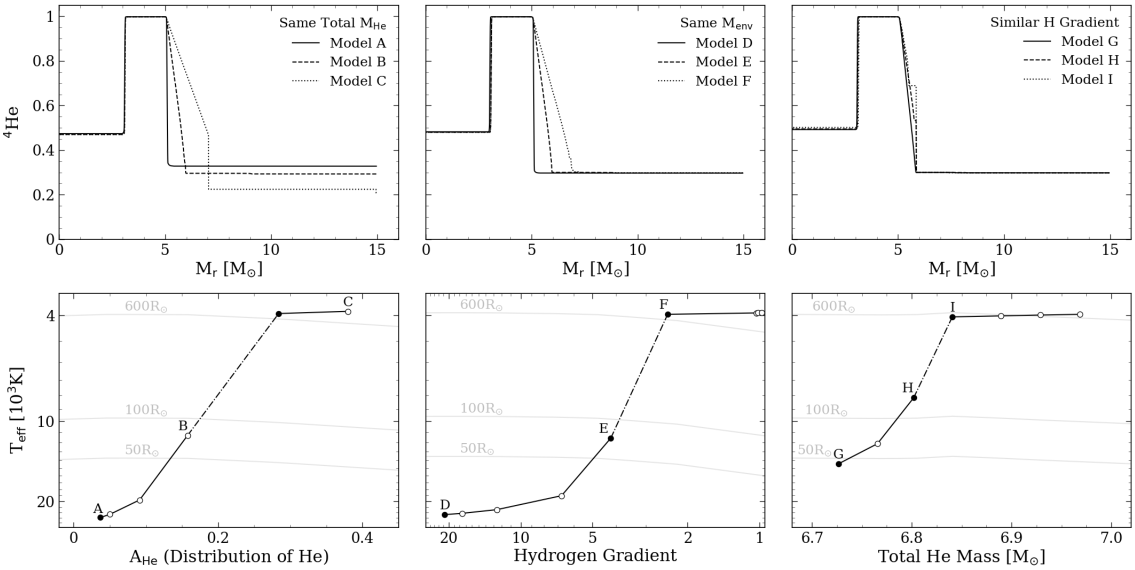

Figure 38: Effect of the helium abundance profile in the shell on L and T_{eff} of core helium burning stars. The upper panels show the internal helium abundance profiles for three snapshot models. The lower panels show the value of T_{eff} for the models from the upper panel (black circles), as well as several similar intermediate models that are excluded from the upper panel for clarity (white circles). The dash-dot lines indicate the bi-stability transition between a blue and red supergiant. *Left Column*: Models with the same total mass of helium mass, distributed differently throughout the envelope (S-7). *Middle Column*: Models with the same envelope mass and with different gradients of hydrogen and helium in the hydrogen burning shell (S-8). *Right Column*: Models with similar hydrogen gradients and different masses of helium in the H-shell (S-9).

5.4.2 Hydrogen Abundance in the Envelope

The abundance profile of hydrogen in the envelope of a core helium burning star (X_{env}) can be affected by several different factors. The initial abundance of hydrogen and helium can vary with metallicity. Internal convective zones and semi-convective mixing in the envelope during the transition between core hydrogen and core helium burning can also alter the hydrogen profile in the envelope. This can also happen, for instance, if a star becomes a red supergiant and its convective envelope extends deep enough to a region

---

[†] We can also consider the framework of L_{nuc} and L_{actual} in the context of the effects of the fuel supply and the opacity on T_{eff} found by Walmswell et al. (2015) (although note that the effect of the mean molecular weight dominates the impact on the overall surface properties). A decreased fuel supply causes a decrease in L_{nuc} which favours a bluer star. A decreased opacity in the H-burning shell initially favours a local increase in L_{actual}, causing a local contraction in the hydrogen burning shell which actually increases L_{nuc}. The increase in L_{nuc} dominates, favouring a redder star. We found the same qualitative results for the effect of the mean molecular weight and fuel supply on the T_{eff} of core hydrogen burning stars in Sec. 5.3 as Walmswell et al. (2015) did for core helium burning stars.

of decreased hydrogen abundance in a dredge-up episode. Accretion of material from a binary companion with a different surface abundance or a merger event could also modify the envelope abundance.

As in Sec. 5.4.1, we compute sets of snapshot stellar structure models to isolate the effect of $\mathrm{X}_{\mathrm{env}}$ on T_{eff} for models with the same M_{core}, M_{env}, Y_{c} and abundance profile in the H-shell, presented in Fig. 39. For clarity, we choose to plot the helium abundance profiles to demonstrate that the helium cores are the same. Models J, K and L have the same (or very similar) abundance profiles in the H-shell but different profiles in the envelope. A larger abundance of hydrogen in the envelope favour a redder star with a larger radius. Models M, N and O isolate the effect of the surface abundance of hydrogen for the same hydrogen gradient. Again, the models with a larger abundance of hydrogen in the envelope favour a redder star. These models present another example of how certain definitions of the hydrogen gradient do not always fully capture the effects on T_{eff}. Models P, Q & R mimic a possible effect of mass accretion or a merger with material of a different average H/He abundance, in which only the outer half of the envelope contains a different hydrogen abundance. A similar effect of $\mathrm{X}_{\mathrm{env}}$ on T_{eff} is found.

While the effect of $\mathrm{X}_{\mathrm{env}}$ will be intuitive to many readers, we can also understand it in terms of how it affects L_{nuc} and L_{actual}. An increase in the hydrogen abundance in the envelope (e.g. compare Models N and O) increases the opacity in the envelope, reducing the ability to transport energy by radiation and decreasing L_{actual}. A decrease in L_{actual} favours an increase in the stellar radius and a decrease in T_{eff}, which is exactly what we see in the models. Although the impact of an increased hydrogen abundance in the envelope on T_{eff} due to opacity effects has been understood for quite some time, our snapshot models clearly isolate the effect of $\mathrm{X}_{\mathrm{env}}$.

5.4.3 Helium Abundance in the Core

During the core helium burning phase, the helium abundance in the core, Y_{c}, is primarily modified by nuclear burning. Its evolution as a function of time can also be affected by processes such as convective core overshooting, rotational mixing and, in evolutionary models, the $^{12}C(\alpha,\gamma)^{16}O$ reaction rate. Using the SNAPSHOT approach, we can isolate the effect of Y_{c} on T_{eff} and the stellar radius for a set of models with identical abundance profiles in the rest of the star outside the convective core Fig. 40. To support our discussion, we also plot the impact of Y_{c} on the radius of the helium core in green, defined as where $X < 10^{-4}$, and the radius of the peak of the hydrogen burning shell in blue.

We find that Y_{c} affects T_{eff} in two competing ways. First, a decrease in Y_{c} causes an increase in the mean molecular weight of the core μ_{core} as helium is converted to C and O. The increase in μ_{core} favours an increase in the radius of the helium core (Fig. 40). This is for the same reason that the radius of a core hydrogen burning star increases with increasing μ_{core}. A higher μ_{core} favours a higher temperature and density through the equation of state, increasing L_{nuc} and therefore favouring a larger helium core radius.

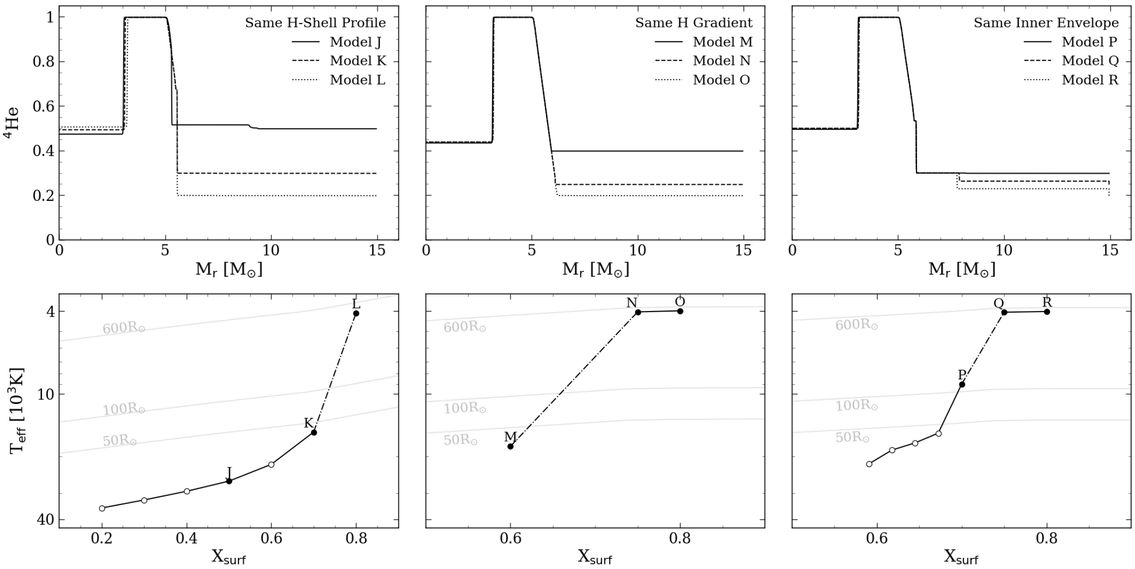

Figure 39: Effect of the Hydrogen profile in the envelope on T_{eff} for helium burning stars. *Left Column*: Models with the same hydrogen profile and different abundances in the envelope (S-10). *Middle Column*: Models with the same hydrogen gradient and with different surface abundances (S-11). *Right Column*: Models with different helium abundances in the outer envelope (S-12).

However, a larger helium core radius favours a smaller total stellar radius. This is because as the core radius increases, so does the radius of the hydrogen burning shell, as it is located just above the helium core. As the radius of the hydrogen shell increases, the temperature and density throughout the burning region decrease, which leads to a decrease in L_{nuc} and favours a smaller radius. The second impact of Y_{c} on T_{eff} is through the decrease in the available fuel supply in the core for the triple alpha reaction. Again, similar to core hydrogen burning stars, a decrease in the fuel supply causes a decrease in L_{nuc} and favours a smaller helium core radius. A smaller helium core radius moves the radius of the hydrogen burning shell inwards, causing an increase in the temperature, density and L_{nuc}, favouring a larger total stellar radius. In summary, as Y_{c} decreases, the increase in μ_{core} initially favours a decrease in the stellar radius while the decrease in the available fuel supply in the core subsequently favours an increase in the stellar radius.

For our 15 M$_\odot$ representative model, the impact of Y_{c} on μ_{core} dominates for $1 < Y_{\text{c}} \lesssim 0.50$ while the impact on the fuel supply dominates for $0.50 \lesssim Y_{\text{c}} < 0$. Therefore, the effect of Y_{c} on the surface properties in non-monotonic. For $1 < Y_{\text{c}} \lesssim 0.50$ a decrease in Y_{c} favours an increase in T_{eff}, while for $0.50 \lesssim Y_{\text{c}} < 0$ a decrease in Y_{c} favours a decrease in T_{eff}. We find that the quantitative impact of Y_{c} on T_{eff} is smaller for large values of Y_{c}, i.e. the beginning of helium burning, and larger towards the end of helium burning for $Y_{\text{c}} < 0.40$. The impact of the fuel supply on T_{eff} in core hydrogen burning stars only dominates over the effect of the mean molecular weight for very low values of $X_{\text{c}} \lesssim 0.05$. However, for core helium burning stars it can dominate for $Y_{\text{c}} \lesssim 0.50$. This is likely related to a combination of the larger relative change in mean molecular weight when converting from ^{1}H to ^{4}He and from ^{4}He to ^{12}C as well as the smaller dependence of the CNO cycle reaction rate on the density of hydrogen compared to the dependence of the triple alpha reaction on the density of He.

We tested our interpretation of the effect of Y_c on T_eff by computing a similar set of snapshot models to those in Fig. 40 but in which we keep the mean molecular weight constant, and just decrease the fuel supply with decreasing Y_c. This is achieved using a similar method as for the core hydrogen burning models described in Sec. 5.3. In these models, we found that the radius of the core and H-shell decreased monotonically with decreasing Y_c and the total stellar radius increased monotonically. This implies that the effect of a decreased fuel supply is indeed to favour an overall increase of the stellar radius in a core helium burning star, supporting our analysis above.

Our snapshot models show the non-monotonic behaviour of R_c and R with Y_c. In the context of blue loops in the HR diagram Lauterborn et al. (1971a) discussed the impact of the radius of the helium core on T_eff in terms of the parameter $\Phi_\mathrm{c} = M_\mathrm{c}/R_\mathrm{c}$, the ratio of the mass of the core to the radius of the core. As found by Lauterborn et al. (1971a), our models show that when R_c decreases, R increases and vice versa. We also provide the main cause for these behaviors.

5.4.4 Core Mass Ratio

The combination of the core mass M_core and envelope mass M_env of a star during helium burning can be affected by many different physical processes. Core masses are intrinsically larger for higher mass stars due to the formation of larger convective core masses during the core hydrogen burning phase. The core mass can also be increased by mixing during core hydrogen burning due to convective boundary mixing and rotation. The envelope mass can decrease due to mass loss and can be dramatically modified by binary interaction via stripping, mass accretion or a merger. In Farrell et al. (2020b), we computed snapshot models to isolate the effect of the envelope mass on the surface properties for constant helium core mass and abundance. Here, we extend this analysis by studying how the helium abundance in the hydrogen shell affects the relationship between the core mass, envelope mass and the surface properties.

We present five sequences of snapshot models, each with the same helium core mass and varying envelope mass. Each sequence has a different hydrogen/helium abundance profile in the hydrogen burning shell, as indicated in Fig. 41. For a given helium core mass, the envelope mass affects T_eff in two competing ways. On one hand, an increase in the mass of hydrogen in the envelope increases the effect of opacity. This decreases the amount of energy that can be transported, causing a decrease in L_actual and favouring a larger radius. On the other hand, an increase in the mass of the envelope modifies the hydrostatic structure of the star and requires a larger value of L_actual in the envelope to support a higher mass. The increase in L_actual favours a bluer star with a smaller radius. For all of the model sequences in Fig. 41, the core mass ratio has a non-monotonic effect on T_eff. For core mass ratios $M_\mathrm{core}/M_\mathrm{total} \gtrsim 0.6$, the effect of opacity dominates and

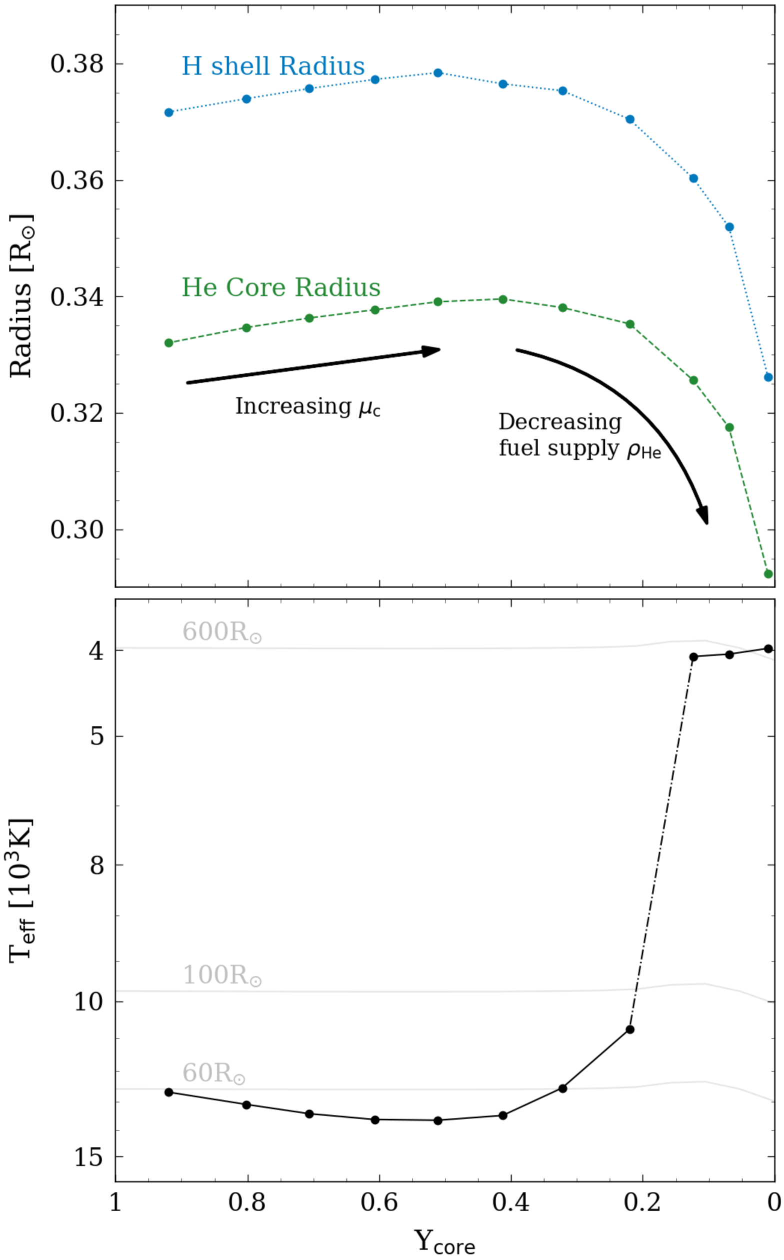

Figure 40: *Top Panel:* Effect of the central helium abundance Y_c on the radius of the helium core, where $X < 10^{-4}$, and the radius of the peak of the H-burning shell for a set of snapshot models with the same core mass, envelope mass and abundance profile in the envelope (S-13). *Bottom Panel:* Effect of Y_c on T_{eff} and the stellar radius for the same models as in the top panel.

therefore T_{eff} decreases with increasing envelope mass (decreasing $M_{\text{core}}/M_{\text{total}}$). For core mass ratios $M_{\text{core}}/M_{\text{total}} \lesssim 0.6$, the effect of increasing mass on the hydrostatic structure dominates and T_{eff} increases with increasing M_{env} (increasing $M_{\text{core}}/M_{\text{total}}$). The fact that massive stars during the post-main sequence with higher envelope masses tend to favour a blue supergiant solution rather than a red supergiant solution has been known in the literature for a long time. However, a simple explanation for this has not always been clear.

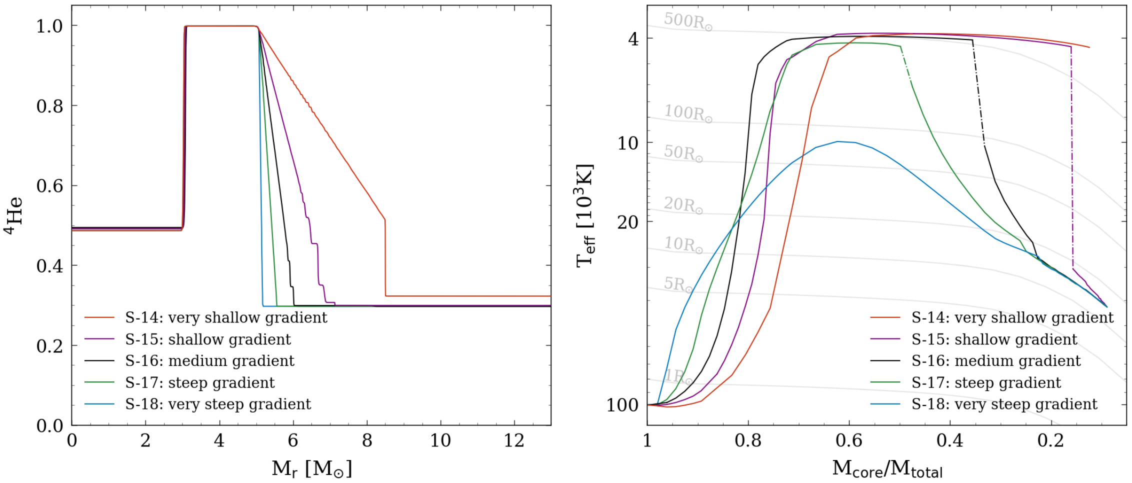

Figure 41: *Left panel:* The helium abundance profile in the hydrogen shell region for each sequence of models (S-14 to S-18). *Right panel:* The effect of the combination of core mass ratio $M_{\rm core}/M_{\rm total}$ on the surface properties. The value of $T_{\rm eff}$ as a function of core mass ratio is plotted for each sequence of models with the same core mass and varying envelope mass.

Fig. 41 also clearly illustrates how the helium profile in the hydrogen burning shell affects the relationship between the core mass ratio and the surface properties. In the stripped star regime (i.e. low envelope masses), at the same core mass ratio a larger abundance of helium in the hydrogen shell favours a bluer star. This is simply due to the fact that the envelope mass is so small that the helium lowers the opacity of the envelope, favouring a smaller radius. For intermediate and higher envelope masses, a high $\rm Y_{shell}$ at the same core mass ratio favours a redder star. In these models, the effect of the helium abundance on the H-shell energy generation dominates, increasing $L_{\rm nuc}$ and favouring a redder star as discussed in Sec. 5.4.1.

At this point, the reader may wonder why it is that if you continue to add mass onto a typical core helium burning star, the radius decreases, but if you add mass to a typical main sequence star, the radius increases? It appears that this is due to a sort of a boundary condition effect. The boundary at the inner edge of the hydrogen burning shell in stars during helium burning is set by the hydrostatic and thermodynamic properties of the helium core. However, the boundary at the center of main sequence stars is not constrained in the same way. This allows the temperature and density to increase with increasing mass, increasing $L_{\rm nuc}$ and favouring a larger radius.

5.4.5 Metallicity: CNO in the hydrogen shell and Z in the envelope

Stellar evolution models show that core helium burning stars with a lower initial metallicity tend to have a higher $T_{\rm eff}$ (e.g. Stothers & Chin, 1968). The initial metallicity of a star can impact its evolution in several ways including by modifying its mass loss rate, the efficiency of rotational mixing, the internal temperature structure and the convective core mass. All of these evolutionary effects have complex feedback effects. Because of this, it is difficult to use evolutionary models to isolate the effect of metallicity on post-MS stellar

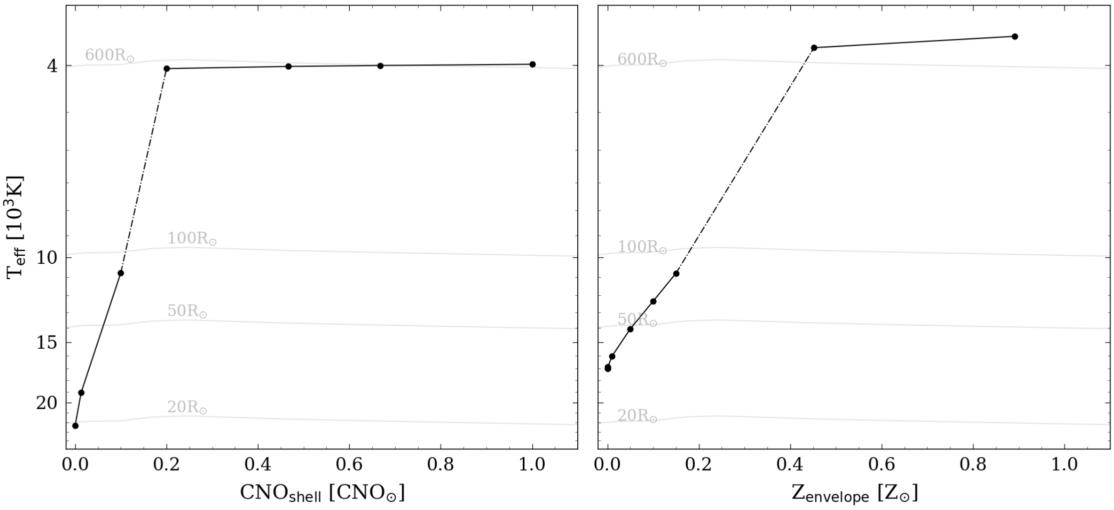

Figure 42: *Left panel:* Effect of the CNO abundance in the hydrogen burning shell on T_{eff} for a representative set of stellar models with the same core mass, envelope mass, core composition and helium abundance profile (S-19). *Right panel:* Effect of the metallicity in the envelope above the hydrogen burning shell (S-20).

structures. Our snapshot models indicate that both the CNO abundance in the hydrogen burning shell ($\text{CNO}_{\text{shell}}$) and the metal opacity in the envelope have important impacts on T_{eff}. The value of $\text{CNO}_{\text{shell}}$ is predominantly determined by the initial metallicity but can be modified by rotational mixing if C and O are mixed from the core into the H-shell. This occurs most dramatically so in the case of low or zero metallicity stars (e.g. Ekström et al., 2008).

Using snapshot models, we isolate the effect of $\text{CNO}_{\text{shell}}$ on T_{eff} for a representative 15 $M_{\odot}$ model, in which we scale the abundance of all the CNO elements in the H-shell, while keeping the rest of the internal abundance profiles the same (Fig. 42). The CNO elements are converted to hydrogen to conserve mass. An increase in $\text{CNO}_{\text{shell}}$ favours an increase in the stellar radius and a lower T_{eff}. This can be understood by considering that a higher $\text{CNO}_{\text{shell}}$ causes a higher L_{nuc} (due to the effect on the CNO cycle), favouring a redder star. We also test the effect of the abundance of the metals in the non-burning region of the envelope, above the hydrogen shell (Fig. 42). As expected, a higher abundance of metals in the envelope increases the effect of opacity, decreases L_{actual} and favours a larger radius. The internal abundance profiles for these models are included in Appendix 2 and 3 in the online supplementary material.

Many previous works have studied and discussed the evolutionary effects of metallicity on T_{eff} of core helium burning stars (e.g Schaller et al., 1992; Langer & Maeder, 1995). It has been pointed out by Stothers & Chin (1968) that the T_{eff} of massive post-main sequence stellar models may be lowered by increasing only the CNO abundances in the star. This can be connected to the effect of $\text{CNO}_{\text{shell}}$. Additionally, Schaller et al. (1992) found that a lower initial metallicity favours a more extended blue loops in the HR diagram during helium burning. This can also be understood by the fact that a lower initial metallicity implies a lower CNO content in the shell and lower metal content in the envelope which, as explained above, favour a more compact, bluer star.

5.4.6 Comparison of effects in the HR diagram

Fig. 43 summarises and compares the effects of the five key features of the internal abundance profile discussed above on the values of L and $T_{\rm eff}$. For each property, we select representative models which demonstrate the important effects. The internal hydrogen and helium abundance profiles of two or three representative SNAPSHOT models are plotted in the left panels and their location in the HR diagram are plotted in the right panels (blue, red and green circles), as well as several intermediate models that are not included in the abundance profiles (empty circles). The dash-dot lines in the HR diagram indicate the approximate location of the bi-stability transition between a blue and a red supergiant, in which intermediate stellar models in hydrostatic and thermal equilibrium do not exist. As these results relate only to the internal structure of stars in hydrostatic and thermal equilibrium, they are not affected by the prior evolution. Therefore, they apply to all stars regardless of the mass loss history, any internal mixing or binary interaction. Fig. 43 is also relevant for the crossing of the HR diagram between the core hydrogen and helium burning phases, as we will discuss in Sec. 5.5.

In summary, Fig. 43 demonstrates the following: First, a larger helium abundance profile in the region of the H-burning shell, $\mathrm{Y}_{\rm shell}$, favours a larger radius and lower $T_{\rm eff}$. In some cases, the stellar radius can change by a factor of 4 for a change in the helium mass of only of 0.05 $\mathrm{M}_{\odot}$. $\mathrm{Y}_{\rm shell}$ does not modify the luminosity significantly except when the star is on the Hayashi track. As $\mathrm{Y}_{\rm shell}$ increases, the stellar radius increases, the envelope cools and more of the envelope becomes convective. A higher convective mass in the envelope increases the rate at which energy can be transported, increasing $L_{\rm actual}$, resulting a higher surface luminosity. Second, the CNO abundance in the shell, $\mathrm{CNO}_{\rm shell}$, has a similar effect on L and $T_{\rm eff}$ to $\mathrm{Y}_{\rm shell}$, for similar reasons. An increase of $\mathrm{CNO}_{\rm shell}$ by a factor of 6 decreases $T_{\rm eff}$ from 11 000K to 4 000K. Third, an increase in $\mathrm{X}_{\rm env}$ also favours a lower luminosity due to the fact that an increase in the opacity causes a decrease in $L_{\rm actual}$, resulting in a lower surface luminosity. A decrease of the hydrogen abundance in the envelope ($\mathrm{X}_{\rm env}$) from 0.70 to 0.60 can cause a very large increase in $T_{\rm eff}$ i.e. from 4 000K to 20 000K. Fourth, the effect of $Y_{\rm c}$ on $T_{\rm eff}$ is non-monotonic but most important during the second half of the core helium burning phase when it favours a decrease in $T_{\rm eff}$ with decreasing $Y_{\rm c}$. The effect on the luminosity is similar to the previous properties, for the same reasons. Finally, the core mass ratio $M_{\rm core}/M_{\rm total}$ also has a non-monotonic effect on $T_{\rm eff}$. For $M_{\rm core}/M_{\rm total}$ decreasing from 1 to ~ 0.6 (i.e. corresponding to increasing envelope mass), the radius increases and $T_{\rm eff}$ decreases. For further decreasing $M_{\rm core}/M_{\rm total}$ (i.e. further increasing envelope mass), the radius decreases and $T_{\rm eff}$ increases. The luminosity gradually increases with increasing envelope mass due to the larger luminosity produced/required by the hydrogen burning shell.

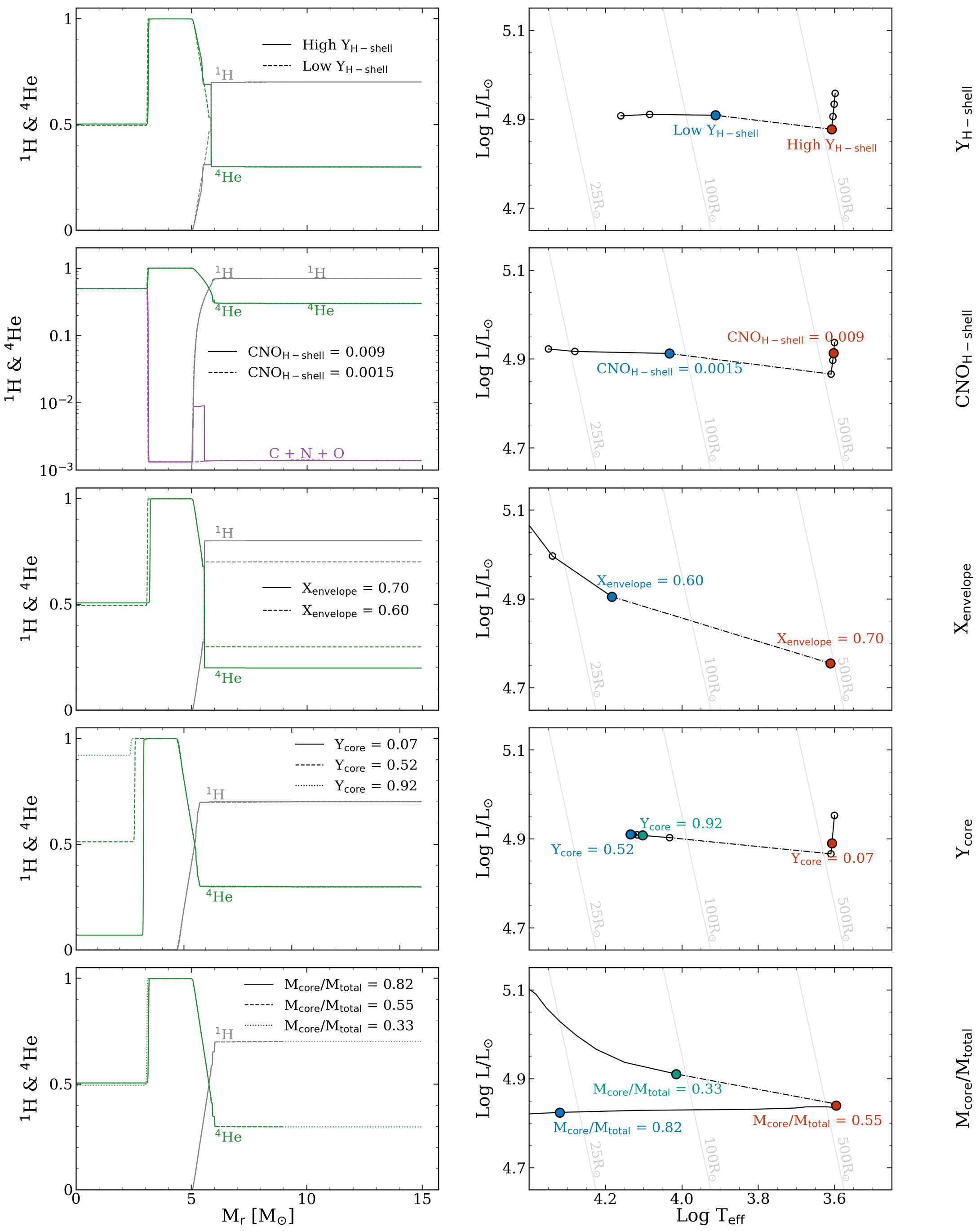

Figure 43: Isolating the effect of key features of the internal abundance profile on the location of a 15 $M_\odot$ star in the HR diagram. In each case, we plot the internal abundance profiles of hydrogen and helium for two or three stellar models in which only one property changes and the rest of the star remains the same. We also plot the location in the HR diagram of each of these models (circles) with a black line joining intermediate models (not plotted in the upper panels). The dash-dot line indicates the bi-stability transition between a BSG and RSG.

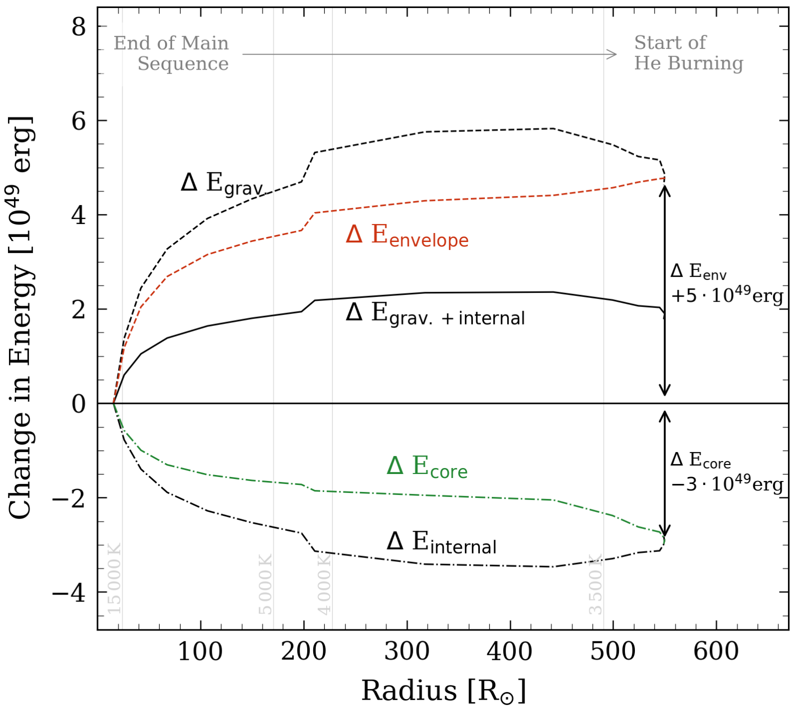

Figure 44: The change in internal energy (dash-dot), gravitational energy (dashed) and total energy (solid) of a representative 12 M$_\odot$ model as it expands from the end of the main sequence to the beginning of core helium burning (T-21). Also included are the total gravitational + internal energy of the core (green) and the envelope (red).

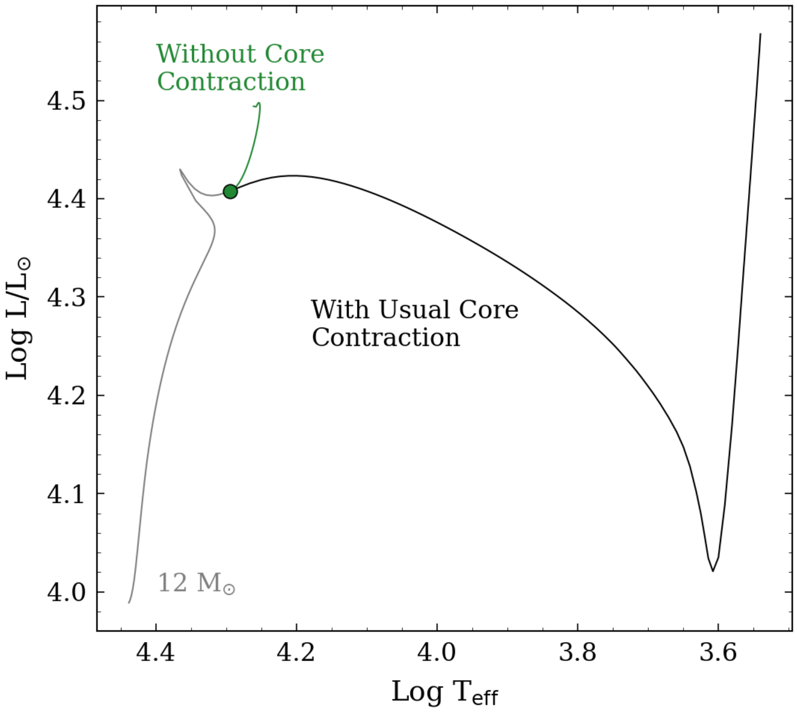

Figure 45: Effect on the surface properties if we artificially suppress the contraction of the core during the crossing of the HR diagram after core hydrogen exhaustion (green line, T-22) compared to the usual expansion (black line) in a representative 12 M$_\odot$ star at solar metallicity (T-21).

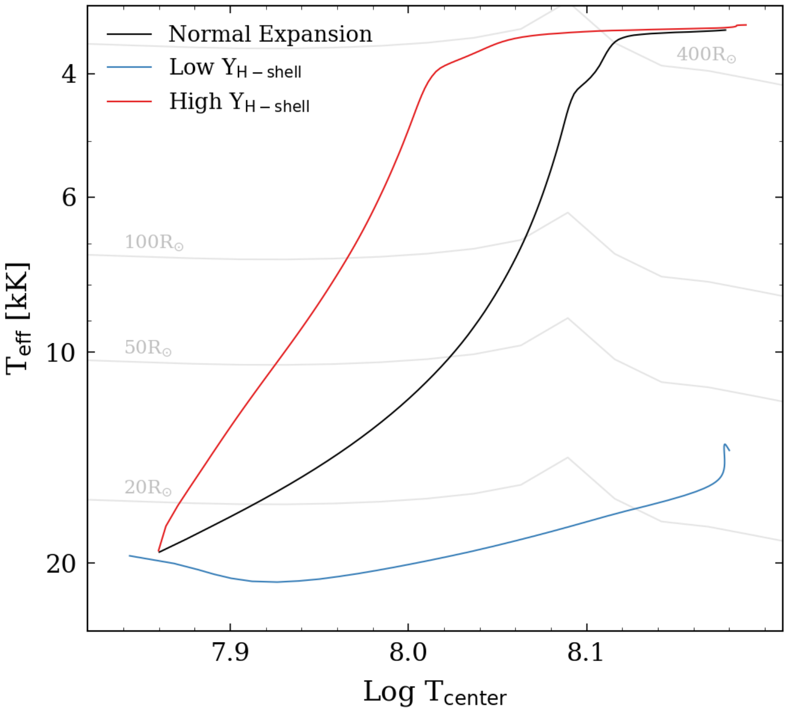

Figure 46: The effect of the helium abundance in the H-burning shell Y_{shell} on the expansion of a 12 $M_\odot$ star from the end of the MS to the start of core helium burning (T-23). The usual stellar evolution model is shown in black as well as models with a higher (red) and lower (blue) value of Y_{shell}.

5.5 The Crossing of the HR diagram after the main sequence

When hydrogen is exhausted in the core at the end of the main sequence phase, most stars expand significantly to become giants or supergiants. A simple explanation for why this happens currently appears somewhat elusive, despite extensive discussion in the literature (Hoppner & Weigert, 1973; Eggleton et al., 1981; Yahil & van den Horn, 1985; Applegate, 1988; Eggleton & Cannon, 1991; Renzini et al., 1992; Iben, 1993; Sugimoto & Fujimoto, 2000; Stancliffe et al., 2009; Ball et al., 2012). To investigate this expansion in massive stars, we perform numerical tests on representative 12 $M_\odot$ stellar models and apply our understanding of what sets L and T_{eff} from Sec. 5.2, 5.3, 5.4. One point we would like to emphasise is that any compelling explanation for why stars expand after the main sequence should also describe why some stars (or stellar models) expand more than others. For example, comparing Fig. 48 and Fig. 49 the 16 $M_\odot$ stellar model expands to about 80 $R_\odot$ at SMC metallicity (Z = 0.002), compared to 600 $R_\odot$ at a metallicity ten times larger (Z = 0.020).

When the central hydrogen abundance decreases below about $X_c = 0.05$ in our standard (unmodified) 12 $M_\odot$ stellar evolution model, the entire star contracts due to the decrease in the central fuel supply, decreasing the total (gravitational + internal) energy of the star. The region above the hydrogen depleted core heats up and begins to burn hydrogen,

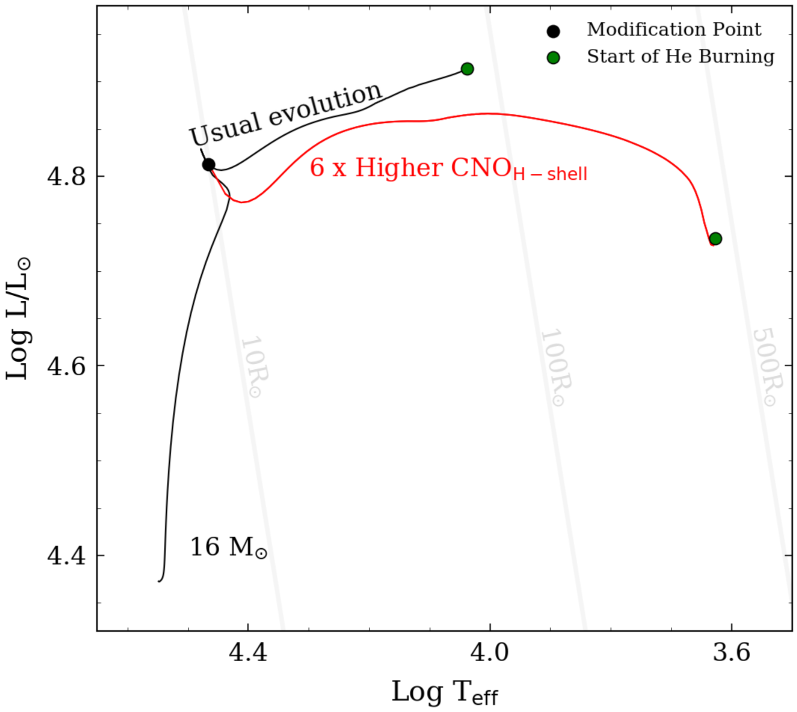

Figure 47: Effect of the CNO abundance in the H-burning shell CNO$_{\rm shell}$ on the expansion across the HR diagram after core hydrogen exhaustion in a 16 M$_\odot$ model at a metallicity of Z = 0.002 (T-24). The usual evolution to the beginning of core helium burning in shown in black. The red line shows the expansion when we artificially increase the CNO abundances in the hydrogen shell at the black point by a factor of 6.

forming the hydrogen burning shell. The hydrogen burning shell prevents that region from contracting due to the stabilising feedback of nuclear burning (Maeder, 2009). However, the hydrogen depleted core continues to contract as it has no other way to support itself. The contraction of the core has two effects. Firstly, it moves the radial position of the hydrogen shell inwards, increasing the temperature and density of the hydrogen shell and, hence, increasing $L_{\rm nuc}$. As discussed in Sec. 5.2, this favours evolution to a larger radius and a lower $T_{\rm eff}$. Secondly, it transfers some energy from the core (due to the decrease in gravitational potential energy) to the envelope. At any given point during the expansion, the envelope can only transport a certain amount of energy. This excess energy cannot be transported by the envelope, so it cools and expands.

In our 12 M$_\odot$ model, 60% of the increase of the energy of the envelope is accounted for by the decrease in the energy of the core and 40% is accounted for by increased nuclear energy generation in the hydrogen shell as a result of the contraction. Of course, these fractions will likely be different for models of different masses. A consequence of this is that the effect of a given amount of core contraction on the total stellar radius will depend on other features of the internal abundance profile including Y$_{\rm shell}$, CNO$_{\rm shell}$, X$_{\rm env}$ and $M_{\rm core}/M_{\rm total}$. Any property of the envelope that favours a larger radius when the whole star is in thermal equilibrium will also cause the star to expand by more for a given amount of contraction by the core (i.e. a given change in the central temperature or radius of the core).

To test this explanation, we perform three tests using modified stellar evolution models. Fig. 45 shows the effect on the surface properties if we artificially suppress the contraction of the core during the crossing of the HR diagram after core hydrogen exhaustion (green line) compared to the usual expansion (black line) in a representative 12 $M_\odot$ star at solar metallicity. The evolution during the main sequence phase is plotted in grey. Just after core hydrogen exhaustion (green circle), we effectively "remove the core" by inserting fixed inner boundary conditions equal to the values at the boundary of the core. For this purpose, we define the core as the central region that is contracting. Maintaining fixed inner boundary conditions, we follow the response of the star in the HR diagram, indicated by the green line in Fig. 45. The star does not expand, remaining in the blue region of the HR diagram. The luminosity increases slightly due to the position of the hydrogen shell artificially moving slightly inwards. However, the star does not expand. This supports the understanding that if the hydrogen shell is not continually forced to contract and heat up by the core, the star will simply not expand. We also perform a test (not plotted) in which we turn off the hydrogen shell burning. In this test, the star does not expand, but rather stays in the blue region of the HR diagram and contracts. The lack of the stabilising feedback provided by nuclear burning in the hydrogen shell means that the whole star continues to contract.

We now investigate how the abundance profile in the hydrogen shell ($\mathrm{Y_{shell}}$ from Sec. 5.4.1) affects the expansion across the HR diagram. Along with the standard $12\,M_\odot$ evolutionary model from Fig. 45, we compute two models with larger and smaller amounts of helium in the hydrogen burning shell. In Fig. 46, we plot the value of T_eff, representing the expansion of the envelope across the HR diagram, as a function of the central temperature, representing the contraction of the core. In all three models, the timescale of the expansion is the same. The expansion of the star proceeds on the Kelvin-Helmholtz timescale of the core. As the core mass is the same for each model, the timescale of the expansion is also the same for each model. The expansion of the standard, unmodified model is plotted in black. The high $\mathrm{Y_{shell}}$ model with a higher abundance of helium in the hydrogen shell expands at a faster rate as a function of the contraction of the core than the standard, unmodified model (in black). Conversely, the low $\mathrm{Y_{shell}}$ model expands at a slower rate than the standard model and actually begins core helium burning as a blue rather than a red supergiant. This can be understood by considering that a given contraction of the core will cause a given increase in the temperature and density in the hydrogen shell. However, the quantitative effect on L_nuc, and therefore on the stellar radius, depends on the properties of the hydrogen shell. As discussed in Sec. 5.4.1, a larger value of $\mathrm{Y_{shell}}$, i.e. a shallower hydrogen gradient, favours a redder star.

We perform a similar investigation for the abundance of the CNO elements in the hydrogen shell $\mathrm{CNO_{shell}}$ (Fig. 47). We begin with a $16\,M_\odot$ stellar model with a metallicity of $\mathrm{Z} = 0.002$. Just after core hydrogen exhaustion (black point), we increase the abundance of the CNO elements just in the region of the hydrogen shell (similar to Fig. 43) by a factor of 6. We then observe the response of the model as it expands to begin core helium burning (red line). It expands to much larger radii and lower $T_{\rm eff}$ than the original model, beginning helium burning as a red supergiant rather than a blue supergiant. This can be understood in a similar way to the effect on $\rm Y_{shell}$. Stellar evolution models of low metallicity stars tend to favour beginning core helium burning as blue supergiants, compared to higher metallicity models which favour core-He ignition as a RSG. This is not because their cores are hotter so they take less time to contract to become hot enough to ignite helium and therefore have less time to expand. Rather it is the effect of the lower CNO abundance in the hydrogen burning shell, combined with the lower metal opacity in the envelope. In fact, there is kind of a coincidence here: the core is hotter because there is a lower CNO abundance in the core and the star begins helium burning at a higher $T_{\rm eff}$ because there is a lower CNO abundance in the hydrogen shell. Of course, the lower CNO abundances are both due to the lower metallicity.

5.6 Cause and Effect in the HR Diagram

In this section, we apply our results from Sections 5.3, 5.4 and 5.5 to explain which features of the internal abundance profiles dominate the change in L and $T_{\rm eff}$ at different points in the evolution of a star. We select three representative cases at intermediate and high masses: a 16 $\rm M_\odot$ star at solar metallicity (Z = 0.020), a 16 $\rm M_\odot$ star at SMC metallicity (Z = 0.002) and a 6 $\rm M_\odot$ star at solar metallicity.

5.6.1 The Evolution of a 16 Solar Mass Star at Z = 0.020

Point I in Fig. 48 indicates the zero-age main sequence for a 16$\rm M_\odot$ star at solar metallicity (Z = 0.020). Our SNAPSHOT models (Fig. 36) recover the well-known results for the MS (e.g. Kippenhahn & Weigert, 1990; Maeder et al., 2009). As hydrogen is converted to helium via the CNO cycle during the MS phase, the average mean molecular weight increases which causes an increase in the surface luminosity and the stellar radius. When the central hydrogen mass fraction $X_{\rm c}$ drops below about $X_{\rm c} = 0.05$ (point II), the entire star contracts, causing the star to evolve to the left in the HR diagram (the Henyey hook). This is caused by the decrease in the central fuel supply. The luminosity continues to increase due to the additional energy released from the gravitational contraction in the outer layers of the star. The increase in temperature just above the hydrogen-depleted core due to the contraction creates a hydrogen burning shell (point III).

Due to the feedback effect of nuclear burning (Maeder, 2009), the H-burning shell acts to limit any further contraction (or expansion) in its vicinity. The core continues to contract, which has two main effects (Sec. 5.5). Firstly, it converts the core's gravitational potential energy partly to internal energy and partly to the luminosity which supports the core (Fig. 44). Secondly, it changes the hydrostatic structure of the star, increasing the temperature and density at the base of the hydrogen burning shell. This increases the rate of nuclear energy generation in the shell. The extra energy produced in the shell cannot be transported by the envelope in a timescale shorted than the core contraction timescale, so the envelope cools and expands. The cooling and expanding of the envelope is reflected in the increase of the stellar radius from $10R_\odot$ to $500R_\odot$ (from points III to IV). This expansion proceeds on the Kelvin-Helmholtz (KH) timescale of the core.

When the central temperature and density are high enough to burn helium via the triple-alpha reaction, the core stops contracting (point IV). This stops the increase in temperature and density at the H-burning shell. As a result, the envelope stops expanding and the star begins to evolve on a nuclear burning timescale again. At this point, the hydrogen and helium abundance profiles in the H-burning shell are defined mainly by the one left behind from the core hydrogen burning phase. As the hydrogen shell burns through this profile, the abundance profiles of hydrogen and helium in the burning region change. The amount of helium in the shell initially decreases, causing a decrease in the stellar radius and the star evolves back down the Hayashi track to higher $T_{\rm eff}$ (Sec. 5.4.1). At point V, the evolution in the HR diagram reverses and the star evolves back toward larger radii and lower $T_{\rm eff}$, due to the the decrease in central helium abundance (Sec. 5.4.3). At point VI, the star depletes its core helium.

5.6.2 The Evolution of a 16 Solar Mass Star at Z = 0.002

A $16\,M_\odot$ star at SMC metallicity (Z = 0.002) begins its evolution with a smaller radius at a higher $T_{\rm eff}$ and a higher luminosity than at solar metallicity (Fig. 49, point I) . A lower abundance of CNO elements in the center of the star and of metals in the envelope results in a smaller radius that at solar metallicity (Sec. 5.4.5). The higher luminosity is a result of higher T and ρ in the outer parts of the nuclear burning region. The evolution during the MS is the similar to the solar metallicity model until core hydrogen depletion (point III). After the main sequence, the rate of expansion of the envelope with the contraction of the core is smaller than for the solar metallicity model. Again, this is due to lower CNO abundances in the H-burning shell and metals in the envelope (Sec. 5.4.5).

Due to the lower CNO abundance in the H-burning shell, the low metallicity model begins burning helium as a BSG (point IV). Similar to the solar metallicity model, the H-shell burns through the profile left behind from the MS and the expansion after the MS, changing the amount of helium in the H-shell, $Y_{\rm shell}$. The envelope contracts and the star evolves to higher $T_{\rm eff}$ as $Y_{\rm shell}$ decreases (Sec. 5.4.1). Once $Y_{\rm shell}$ remains relatively constant, the contraction stops and the star begins to evolve back towards the red region of the HR diagram. The increase in $M_{\rm core}/M_{\rm total}$ as a result of the growth of the mass of the core drives the evolution to lower $T_{\rm eff}$ (Sec. 5.4.4). Subsequently, the decrease in $Y_{\rm c}$ dominates, which also drives evolution to lower $T_{\rm eff}$ (Sec. 5.4.3) until it becomes a RSG. Our models indicate that a massive star at solar metallicity (Z = 0.020) may expand to become a RSG for a different reason than a star of the same mass at SMC metallicity (Z

= 0.002).

5.6.3 The Evolution of a 6 Solar Mass Star at Z = 0.020

An intermediate mass $6\,\mathrm{M}_{\odot}$ star evolves similarly to the $16\,\mathrm{M}_{\odot}$ model beginning of helium burning (Fig. 50). Once core helium burning begins, the hydrogen shell burns through the profile above the core driving the star to lower radii and higher $T_{\rm eff}$, as for $16\,\mathrm{M}_{\odot}$ model (Sec. 5.4.1). However in the $6\,\mathrm{M}_{\odot}$ case, due to the lower core mass ratio $M_{\rm core}/M_{\rm total}$, the star evolves to much lower radii than the $16\,\mathrm{M}_{\odot}$ model. It evolves away from the Hayashi line and toward the blue region of the HR diagram and the beginning of a blue loop is formed. The model spends about 70% of its helium burning lifetime as a BSG at higher $T_{\rm eff}$. The combination of the subsequent increase in $M_{\rm core}/M_{\rm total}$ and decrease in $Y_{\rm c}$ makes the star evolve back to the Hayashi line (Sections 5.4.4 and 5.4.3).

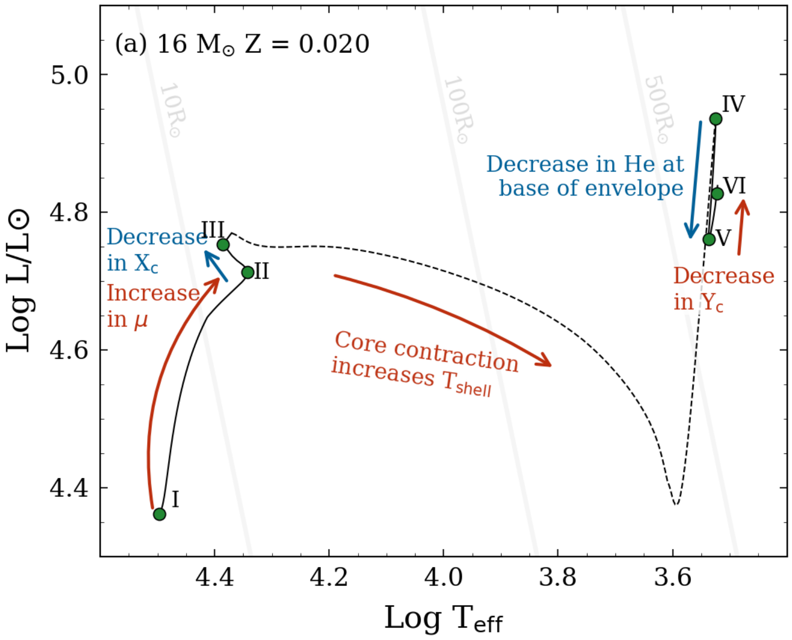

Figure 48: The evolution of a 16 $\mathrm{M}_{\odot}$ star at solar metallicity (Z = 0.020) in the HR diagram, with arrows and text indicating the primary cause for the evolution in each direction. The dashed line indicates the transition from the MS to core helium burning. The following six stages of the evolution are highlighted: I is at the zero-age main-sequence, II is at the terminal-age main-sequence when the star begins to contract, III is when the star begins to expand and cross the HR diagram, IV is the beginning of core helium burning, V is when $Y_{\rm c} = 0.30$ and VI is at the end of core helium burning.

5.7 Other Discussion Points

5.7.1 Blue Loops in the Hertzsprung-Russell Diagram

Stellar evolution models in the mass range 5 - 12 $\mathrm{M}_{\odot}$ sometimes exhibit a "blue loop", in which a star evolves from a RSG to the blue region of the HR diagram and back to the

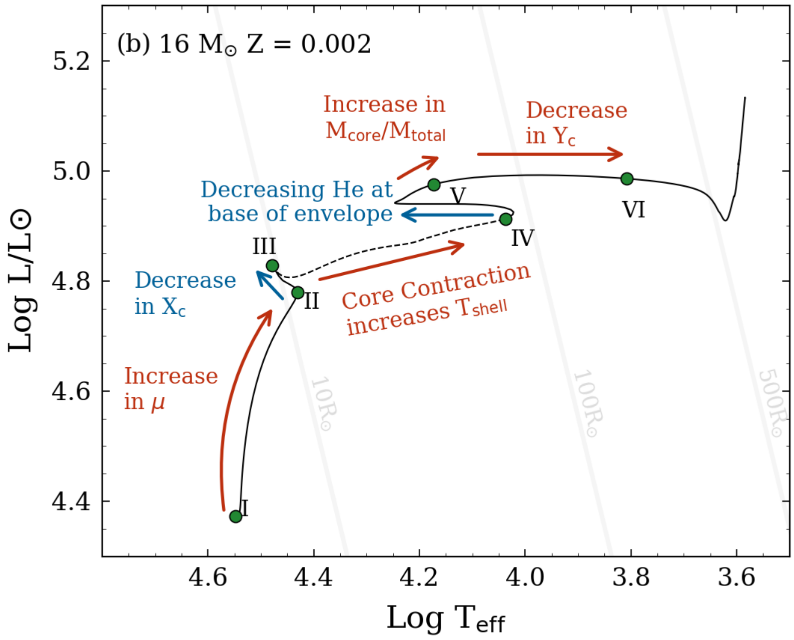

Figure 49: Same as Fig. 48, but for a 16 $M_\odot$ star at SMC metallicity (Z = 0.002).

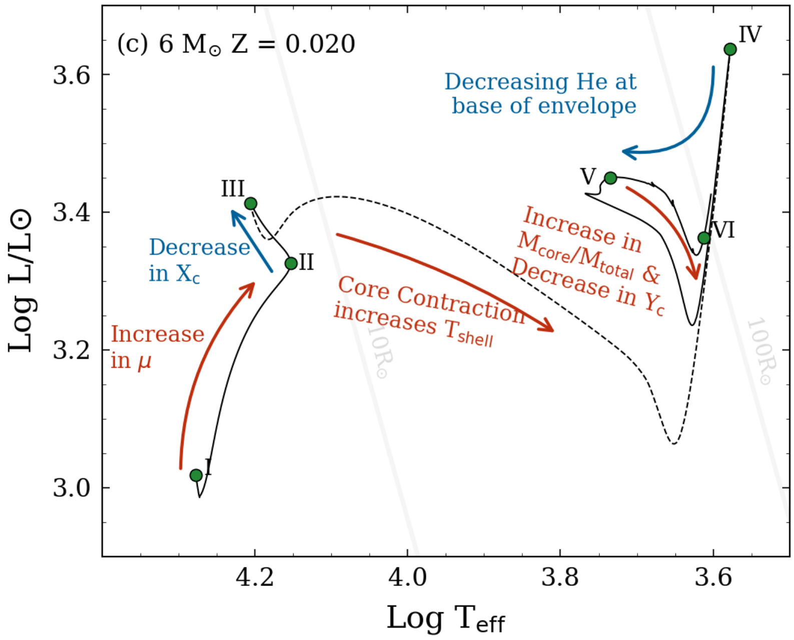

Figure 50: Same as Fig. 48, but for a 6 $M_\odot$ star at solar metallicity (Z = 0.020).

red, completing a loop in the HR diagram (e.g. Fig. 50). Their existence has been known for a long time (Hayashi & Cameron, 1962; Hofmeister et al., 1964) and they have been extensively discussed in the literature (Schlesinger, 1977; Stothers & Chin, 1979; Maeder & Mermilliod, 1981; Walmswell et al., 2015). The properties of blue loops are known to be highly sensitive to processes such as convective overshooting, mass loss and semi-convection. They are especially important in the context of the production of Cepheids. In the following paragraph, we use the model from Fig. 50 and our results from Sec. 5.4

to explain why blue loops occur.

As a RSG evolves, its helium core increases in mass as hydrogen burns in a thin shell around the core. As it burns outwards, the helium abundance profile in the hydrogen shell may change, which can affect the stellar radius (Sec. 5.4.1). In typical stellar evolution models at these masses, the change in the helium profile during helium burning favours a bluer star. At the beginning of core helium burning, the helium profile in the shell favours a large radius due to its high helium content. As the shell moves outwards through the helium profile, the profile in the burning region changes to favour a blue star. If this effect outweighs the other effects of the core mass ratio, affected by e.g. convective overshooting, mass loss and rotation, and the CNO abundance in the hydrogen shell, then the star evolves back towards the blue and may become a BSG. After the initial decrease in radius, the combined effect of decreasing Y_c and increasing core mass ratio due to hydrogen shell burning favour evolution to a larger radius. At some point, this effect wins out and the star evolves back to the red. Our results suggest that blue loops in intermediate and massive stars should be favoured at relatively lower masses because of their intrinsic lower core mass ratios. This is consistent with what we find in stellar evolution models and in observations of Cepheids. Our models also suggest that processes that increase the core mass ratio such as increased convective overshooting or post-MS mass loss will disfavour the production or extent of blue loops, which is also consistent with previous studies.

The "mirror effect" has been invoked as a phenomenological description of the blue loops (Hayashi & Cameron, 1962; Hofmeister et al., 1964; Sandage & Schwarzschild, 1952). In this description the expansion of the core causes a contraction of the envelope as the cause of the star evolving back to the blue, in the opposite way to a star expanding across the HR gap. Our results indicate that the slight expansion of the edge of the core is an effect of the changing helium profile above the core star, rather than a cause of the blue loop.

5.7.2 Why do stars tend to become more luminous and expand as they evolve?

The temperature and density in the nuclear energy generation regions increase as a star evolves. This is primarily due to either an increased higher mean molecular weight in the burning region or a change in the hydrostatic structure due to the contraction of the core when it runs out of fuel. The increased temperature and density cause an increase in L_nuc. As a consequence, stars usually produce slightly more energy than they can transport, causing a cooling and expansion of the envelope. The luminosity goes up if the increase in L_nuc outweighs the effect of the expansion on the burning region. This is always the case during MS and sometimes the case during post-MS. Additionally, the evolution of most of the key features of the internal abundance profile e.g. $M_\mathrm{core}/M_\mathrm{total}$, Y_c, $\mathrm{Y}_\mathrm{shell}$ favour a larger radius as the star becomes more evolved. This means that the more a star evolves, the harder it is to maintain a small radius.

5.8 Conclusions

In this paper, we aimed to isolate the key features of the internal abundance profile that drive stellar evolution during different evolutionary stages. We summarise the key findings below.

1. We devised a framework to qualitatively understand cause and effect in the evolution of the surface properties of stars that is ultimately based on an argument from conservation of energy. We discussed how changes in L_{nuc}, the cumulative internal luminosity distribution generated by nuclear reactions, and L_{actual}, the actual internal luminosity distribution, can help to provide an qualitative understanding for why a star evolves to a given L and T_{eff}. Beginning in thermal equilibrium, any change to the internal abundance profile, the hydrostatic structure or the energy transport that causes an increase in L_{nuc} or a decrease in L_{actual} will favour evolution to a larger radius, and vice versa.

2. We isolated and quantified the key features of the internal abundance profile that set the surface properties for stars during the main sequence, the core helium burning phase and the short-lived expansion in between. Our results provide a new way to interpret observations of individual stars and stellar populations in terms of the structural properties that favour a given set of observed properties.

3. Massive stars with lower metallicity tend to have higher T_{eff} for two reasons: (i) lower CNO abundances in the core (hydrogen burning) and the H-shell (helium burning) which affects nuclear energy generation and (ii) lower opacity in the envelope. During the post-main sequence, the effect of the CNO abundances dominates for BSGs while the effect of opacity dominates for RSGs.

4. Models of massive main sequence stars with the same mass and very similar surface properties can have different internal distributions of hydrogen and different convective core masses. This degeneracy might be broken with current and future asteroseismology observations.

5. Massive stars expand after the main sequence because the contraction of the core heats up the hydrogen-burning shell, generating more energy than the envelope can transport in a typical core contraction timescale. Whether a star begins helium burning as a blue or red supergiant depends on the helium and CNO abundances in the hydrogen shell, the core mass ratio and opacity due to hydrogen and metals in the outer envelope. Each of these properties affect the rate of expansion of the envelope for a given contraction of the core.

6. We discuss the cause of blue loops in the HR diagram during the post-main sequence. Consistent with previous works, we find that the key factor is the shape of helium profile in the hydrogen burning shell as the shell moves outwards during core helium

burning. We also discuss the cause for why other factors, including the core mass ratio and metallicity, can cause stellar evolution models to exhibit blue loops. This has important implications for interpreting observations of Cepheids.

7. We present a numerical test that clearly demonstrates that small changes in the stellar interior can cause very large changes in the surface properties. We conclude that much of the sensitivity seen in post-main sequence massive star models is ultimately due to the strong dependence of the CNO cycle energy generation rate on temperature in the hydrogen burning shell, which can be modified by very small changes in the helium abundance profile.

Consistent with previous work, our results show that a careful analysis of the internal abundance profiles is important for understanding how stars evolve. Given current uncertainties in the internal mixing of massive stars, it is possible that the abundance profiles in the current state-of-the-art stellar evolution models differ substantially from actual stars. This may have significant impacts for our overall picture of stellar evolution, including studies of binary interaction and gravitational wave progenitors. In the next chapter, we investigate recent observations of gravitational waves that indicate the production of a pair of BHs in the PI mass gap. We use stellar evolution models to explore whether it is possible that low metallicity stars could produce an 85 $M_\odot$ BH.

Chapter 6

Is GW190521 the merger of black holes from the first stellar generations?

The contents of this chapter were published in Farrell et al. (2021), MNRAS Letters, 502, 1, L40.

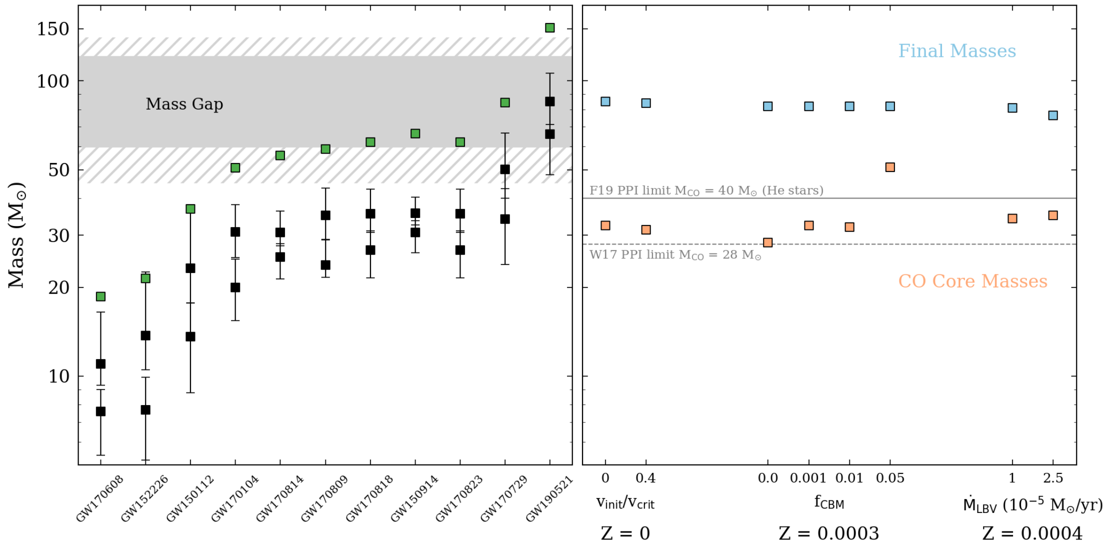

Figure 51: *Left panel:* Pre-merger and final BH masses from LIGO/Virgo observations in O1/O2 with GW190521 and the predicted region of the mass gap due to pair-instability. *Right panel:* Final masses (blue) and CO core masses (red) of selected 85M$_\odot$ models listed in Table 6.1. We also include the maximum CO core mass found by Woosley (2017) that avoids any pulsations due to pair-instability.

6.1 Stellar Evolution Models

We present a series of new stellar evolution models computed with the Geneva Stellar Evolution code, GENEC (Ekström et al. 2012; Murphy et al. in prep) and with MESA (r10398, Paxton et al., 2011, 2013, 2015). We also discuss the results from existing GENEC model grids (Ekström et al. 2012; Georgy et al. 2013; Groh et al. 2019). Except where otherwise stated, the input physics for the GENEC and MESA models are similar to those described in Ekström et al. (2012) and Choi et al. (2016), respectively. In our MESA models, we use the Ledoux criterion for convection with an exponential overshooting parameterised by $f_{\rm CBM}$, while in our GENEC models, we use the Schwarzschild criterion with step-overshooting parameterised by $\alpha_{\rm ov}$. In most models, we compute the evolution until at least the end of central C burning. For some GENEC rotating models, the computation is stopped at the end of He burning due to convergence difficulties. We define the CO core mass as the region where the helium abundance $Y < 0.01$ at the end of the evolution. The outputs from our models are summarised in Table 6.1.

Figure 51 compares the LIGO binary black hole (BBH) masses (Abbott et al., 2019) with the final masses and CO core masses of our models. The 85 $M_\odot$ models with Z in the range 0 to 0.0004 have final masses ranging from 76 to 85 $M_\odot$ and CO core masses ranging from 28 to 51 $M_\odot$. In this metallicity range, the final mass depends on assumptions about convective boundary mixing and post-MS mass loss. Not surprisingly, the model with the lowest amount of convective boundary mixing ($f_{\rm CBM}$= 0 and with the Ledoux criterion) produces the lowest CO core mass of 28 $M_\odot$. Increasing convective boundary mixing tends to produce higher CO core masses, however this depends on whether H-He shell interactions modify the convective core mass during Helium burning. For instance, H-He shell interactions impact the model with $f_{\rm CBM} = 0.01$ at $Z = 0.0003$ so that despite the larger overshooting, its final CO core mass is lower than the model with $f_{\rm CBM} = 0.001$.

H-He shell interactions are an interesting possibility to reduce the final CO core masses of massive stars at low and zero Z (Ekström et al., 2008; Clarkson & Herwig, 2020). This is relevant as it may allow a star to avoid the pulsational-pair instability regime, depending on initial mass and metallicity. To demonstrate this, we plot the Kippenhahn diagram of the evolution of our non-rotating 85$M_\odot$ $Z = 0$ stellar model (Fig. 52). As expected, the convective core mass decreases during the MS evolution and increases following the onset of He-burning. However, shortly after the beginning of He-burning, the H-shell burning region becomes convective. This causes the convective core mass to decrease by $\sim 5M_\odot$ (inset plot in Fig. 52) and prevents any subsequent increase as the star evolves to the end of He-burning.

Figure 53 shows the evolutionary tracks in the Hertzsprung-Russell diagram of three 85$M_\odot$ models with metallicities of $Z = 0$, 10^{-6} and 0.0003. The qualitative evolution during the MS is similar for all models. The location of the zero-age main sequence moves to higher $T_{\rm eff}$ and luminosity with decreasing metallicity due the lower CNO abundances in the core. The post-MS evolution is affected in a similar way by the metallicity. At lower metallicites, a lower CNO abundance in the hydrogen-burning shell favours a more compact envelope and a higher $T_{\rm eff}$. This trend continues until the pre-supernova stage, so that the maximum radii that the models reach are 142, 672 and 794 $R_\odot$ for $Z = 0$, 10^{-6} and 0.0003 respectively.

Previous works have focused on the context of producing BHs in close binary systems that could easily merge in the Hubble time and as a result assume that the entire H envelope will be lost to some combination of stellar winds, LBV eruptions or binary interaction (e.g. Farmer et al., 2019). As a result, they focus on the evolution and deaths of helium stars (e.g. Woosley, 2019). For single stars with hydrogen envelopes, a maximum BH mass of 60-65 $M_\odot$ has been suggested for non-rotating models (Woosley, 2017; Mapelli et al., 2020; Spera & Mapelli, 2017). In their models, strong mass loss of the higher mass models coupled with higher core masses prevented the formation of higher mass BHs. Rotating models were found to have lower maximum BH masses. The models presented in this paper indicate black hole masses of up to 70 - 75 $M_\odot$, and possibly up to 85 $M_\odot$ depending on uncertainties related to convective mixing, mass loss, H-He shell interactions and pair-instability pulsations. Our models leave open the possibility of a mass gap above 85$M_\odot$. To properly infer the actual limits of the pair instability mass gap based on these models, we would need to compute a large grid of models with different initial masses, rotation rates and metallicities. We defer this to future work.

6.2 Implications for black hole masses from the first stellar generations

Our models with $Z = 0$ to 0.0004 have three properties which favour higher BH masses as compared to higher metallicity models. These are (i) lower mass-loss rates, in particular during the post-MS phase, (ii) possible H-He shell interactions which lower the CO core mass and (iii) a more compact star disfavouring binary interaction.

6.2.1 Lower Mass Loss During the Evolution

The amount of mass that a star retains until the pre-supernova stage depends strongly on its metallicity (e.g., Groh et al., 2019). This is a result of the strong dependence of mass loss from radiative-driven winds on metallicity (Vink et al., 2001). For solar metallicity stars, the time-averaged mass-loss rate during the LBV phase and the presence of surface magnetic fields are important factors that determine the final BH mass of massive stars, which can range from 35 to 71 $M_\odot$ for an 85 $M_\odot$ star (Groh et al., 2020). At low metallicity, mass loss by stellar winds during the main-sequence phase becomes very low. Our 85 $M_\odot$ models at $Z = 0.0003$ lose only 1.5 $M_\odot$ during the MS assuming the Vink et al. (2001) prescription. Further mass loss occurs during the post-MS and is strongly dependent on how cool the surface becomes. Our $Z = 0.0003$ MESA models stay hot and lose 1.5 $M_\odot$ during the post-MS, while our GENEC models can become spectroscopically similar to

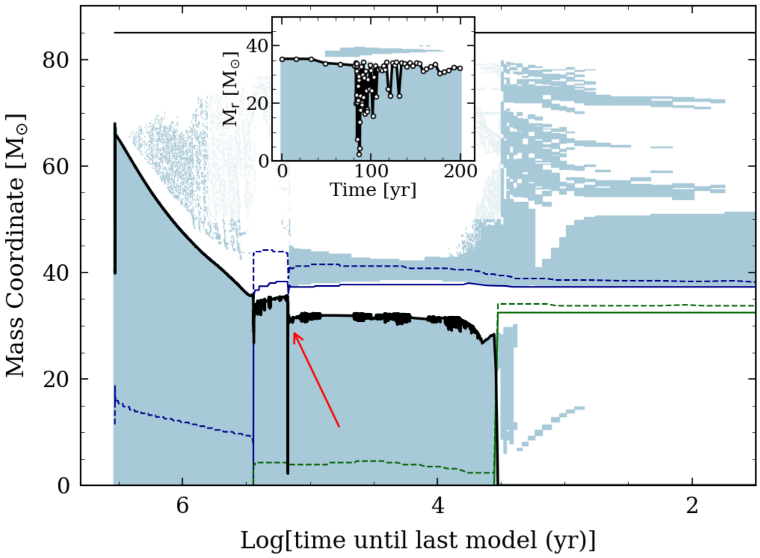

Figure 52: Kippenhahn diagram of a GENEC non-rotating 85 M$_\odot$ model at $Z = 0$. Solid (dashed) lines correspond to the peak (100 erg/g/s) of the energy generation rate for H burning (blue) and He burning (green). The red arrow indicates the H-He shell interaction. An inset is included at the top of the figure to show that the interaction is resolved, where white circles indicate each timestep.

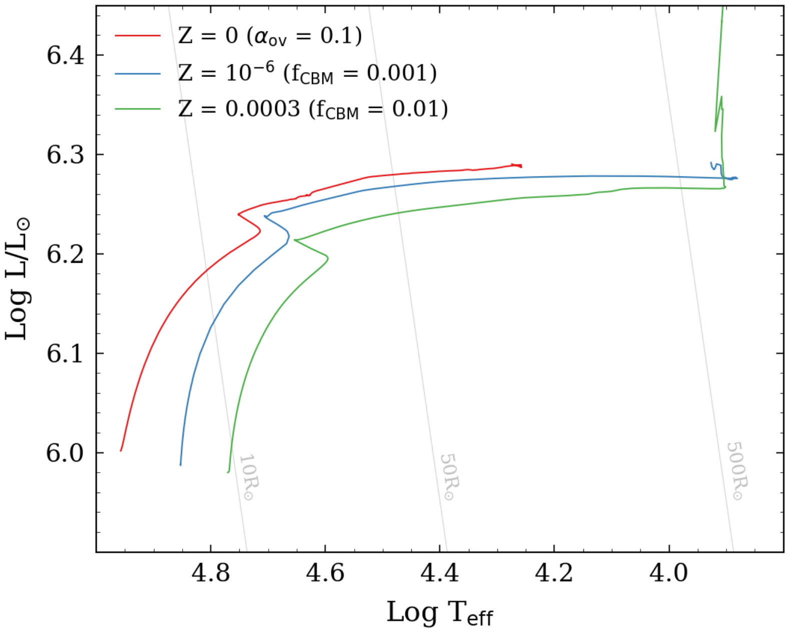

Figure 53: Evolutionary tracks of selected 85 M$_\odot$ models in the Hertzsprung-Russell diagram with $Z = 0$, $Z = 10^{-6}$ and $Z = 0.0003$.

LBVs (Groh et al., 2014). As a result, they may lose significantly more mass at that stage (7.5 M$_\odot$ for $\dot{M}_{\rm LBV,max} = 2.5\text{x}10^{-5}M_\odot$/yr), even at low metallicity (Smith & Owocki, 2006; Allan et al., 2020).

At zero metallicity, radiatively driven mass loss becomes negligible throughout the evolution (Krtička & Kubát, 2006), although for fast rotating stars there can be some

Table 6.1: Summary of our stellar evolution models. CBM refers to the free parameter regulating convective boundary mixing.

Z	M_{zams}	CBM	Mass lost	$M_{\mathrm{final}}^{\mathrm{tot}}$	$M_{\mathrm{final}}^{\mathrm{CO}}$	R_{max}
	$\mathrm{M}_\odot$	$\alpha_{\mathrm{ov}}/f_{\mathrm{CBM}}$	$\mathrm{M}_\odot$	$\mathrm{M}_\odot$	$\mathrm{M}_\odot$	$\mathrm{R}_\odot$
Standard GENEC non-rotating models (α_{ov} value given for CBM)						
0	60	0.1	0.0	60.0	24.0	35
0	85	0.1	0.0	85.0	32.4	142
0	120	0.1	0.0	120.0	54.4	219
Standard GENEC rotating models (v = 0.4 v_{crit})						
0	60	0.1	0.3	59.7	20.9	56
0	85	0.1	1.0	84.0	31.3	90
0	120	0.1	3.5	116.5	56.4	107
MESA models (f_{CBM} value given for CBM)						
10^{-6}	85	0.001	0.30	84.7	34.4	794
0.0003	85	0.0	3.0	82	28.3	766
0.0003	85	0.001	3.2	81.7	32.3	1169
0.0003	85	0.01	3.0	82	32.0	672
0.0003	85	0.05	7.0	78	51.0	984

small mass loss if the critical rotation limit is reached. Zero or negligible mass loss has been customarily used in stellar evolution grids at zero metallicity such as Marigo et al. (2001); Ekström et al. (2008); Yoon et al. (2012); Windhorst et al. (2018) and Murphy et al. 2020, in prep. As such, our zero-metallicity models retain most of their mass until core collapse. There is little observational constraints for mass-loss rates at these extremely low-Z values, in particular for the post-MS stages, and we should regard our assumptions about mass-loss rates as highly uncertain. Uncertainties related to mass-loss rates may affect both the final mass, the CO core mass and the maximum radius.

6.2.2 Possibility of H-He Shell Interactions

Some of our models at low/zero metallicity experience strong H-He shell interactions (Fig. 52). This behaviour has been seen in previous low metallicity stellar evolution models (e.g. Chieffi & Limongi, 2004; Ekström et al., 2008; Ritter et al., 2018; Clarkson & Herwig, 2020). During He-burning, a low or zero abundance of CNO elements in the H-burning shell favours a bluer star which increases the likelihood of the H-burning region becoming convective and subsequently reducing the convective core mass. In models with $Z = 0$, diffusion of C from the He-burning core to the H-burning shell can trigger a strong CNO cycle boost, make the shell convective and lead to H-He shell interactions. By comparing the GENEC models for metallicites of $Z = 0.0004$, 0.002 and 0.014, Groh et al. (2019) discuss that the occurrence of H-He shell interactions may be favoured at lower metallicities. Clarkson & Herwig (2020) find different types of H-He shell interactions that occur at different times during the evolution. Some of these interactions, particularly during the late stages, may dramatically reduce the CO core mass and allow the star to avoid the pulsational pair instability regime. We encourage further work on the effects of convective boundary mixing and rotation on H-He shell interactions as this is crucial for understanding the fate of massive stars at low and zero metallicity.

Some of our models assume a relatively low amount of convective overshooting. The extent and implementation of convective overshooting in stellar models has a large impact on the mass of the He and CO cores (e.g. Kaiser et al., 2020). Three-dimensional models of lower mass stars favour the existence of such mixing at convective boundaries (e.g. Cristini et al., 2017), although it is still unclear how it is affected by other parameters such as mass and metallicity. In addition, for stars of initial mass $7 < M_{\rm init} < 25 {\rm M}_\odot$ a high value of $f_{\rm CBM}$ is favoured (Martinet et al. 2020, in prep) as well as for masses of $\sim 35{\rm M}_\odot$ (Higgins & Vink, 2019). However, these constraints are for core-H burning stars. The value of $f_{\rm CBM}$ is not as well constrained for other burning phases or for stars of $\sim 85{\rm M}_\odot$ which have different internal structures to $\sim 15{\rm M}_\odot$ stars and larger core mass ratios.

6.2.3 Smaller Radius disfavours Binary Interaction

Zero-metallicity models favour the retention of the H-envelope in binary systems because they are more compact than higher metallicity stars. For example, the maximum radius of our $85{\rm M}_\odot$ rotating model at Z = 0 is $R_{\rm max} = 142{\rm R}_\odot$, as compared to $952{\rm R}_\odot$ at Z = 0.0004 and $815{\rm R}_\odot$ at Z = 0.014. The radius of stellar models at these masses depends greatly on the assumptions for convection in the envelope (e.g. Gräfener et al., 2012; Jiang et al., 2018). Additionally, the radius is strongly impacted by uncertainties related to the chemical abundance profile in the envelope (Farrell et al., 2020b), which is impacted by the properties of mixing (e.g. Schootemeijer et al., 2019). The size and interaction of convective shells above the core during the MS and between the MS and He-burning greatly affect the radius of the star during He-burning. If these processes result in hydrogen being mixed into the H-shell burning region, the star will remain more compact for longer during He-burning.

Binary interactions may also provide a mechanism to produce a pre-supernova structure with a high hydrogen envelope mass (e.g. Justham et al., 2014). Mass gainers or products of mergers during the post-MS that do not fully rejuvenate could have low core masses and large envelope masses, potentially avoiding the PPI regime and collapsing to a black hole with the H envelope falling back onto the BH (Spera et al., 2019; Di Carlo et al., 2019).

6.2.4 Pulsational Pair-Instability

Models suggest that stars with a CO core mass of $\gtrsim 28{\rm M}_\odot$ will undergo pair-instability driven pulsation during their final stages (Woosley, 2017). For example, Woosley (2017) present a model (T80D) with a final mass of 80 ${\rm M}_\odot$ and a CO core mass of 32.6 ${\rm M}_\odot$ that, due to pulsations, will produce a final BH mass of $34.9\,{\rm M}_\odot$. The exact value of the maximum CO core mass of this boundary that will avoid the pair-instability is uncertain (e.g. Woosley, 2017; Farmer et al., 2019; Marchant et al., 2019) and effects related to convective boundary mixing, stellar winds and the $^{12}C(\alpha,\gamma)^{16}O$ reaction rate may increase this value. Our 60 $M_{\odot}$ models with Z = 0 have CO core masses between 21 and 24 $M_{\odot}$. Most of our 85$M_{\odot}$ models are just above this strict limit with CO core masses of 31 – 35 $M_{\odot}$. We computed a test model with no convective boundary mixing that finishes with a CO core mass of 28 $M_{\odot}$. By interpolating between our 60 and 85 $M_{\odot}$ models, we compute that a 72 $M_{\odot}$ model will have a final CO core mass of 28 $M_{\odot}$ under the standard assumptions for convection in the GENEC models.

For a pulse of a given energy, the amount of mass that a star loses depends on the binding energy of the envelope. More compact, hotter stars are less likely to lose their entire H envelope compared to extended envelopes, such as in RSGs. For this reason, $Z = 0$ models are favoured to retain large masses as they remain compact until the end of their evolution. Farmer et al. (2019) find a CO core mass limit for the onset of PPI of $\sim 40M_{\odot}$ for highly compact helium stars. Since our models are hydrogen rich, with a lower binding energy than helium stars, it is unclear if this limit would apply to our 85 $M_{\odot}$ models. Further studies could investigate the impact of the uncertainties discussed by Farmer et al. (2019), such as the $^{12}C(\alpha,\gamma)^{16}O$ reaction rate, in hydrogen-rich models that are blue and relatively compact, such as our $Z = 0$ models. If the pulses are not present and/or do not remove the H envelope, this may allow the formation of 85 $M_{\odot}$ BHs.

6.3 Impacts for Binary Black Hole Mergers

Due to their lower mass-loss rates, smaller radii and the possibility of H-He shell interactions that reduce the CO core mass, stars in the first stellar generations are ideal candidates to produce BHs in the mass gap such as GW190521, with masses of 70 – 75 $M_{\odot}$. In order to produce a BBH merger observable by LIGO/Virgo, such a BH would need to be in a close binary system. Due to uncertainties in the evolution of massive stars and in how these stars behave in binary systems, it is difficult to perfectly constrain the possible evolutionary pathways that would lead to a system. Despite their large H-envelope mass, our models at $Z = 0$ expand only to radii $\sim 100R_{\odot}$. If the star has a binary companion and avoids Roche-Lobe overflow, the merging timescale would likely exceed the Hubble time. However, if the orbital separation were to reduce after the more massive star dies (e.g. due to a common envelope phase) this may reduce the merging timescale. Alternatively, if the BH is in a dense stellar cluster, it could dynamically capture a companion and form a close binary system (e.g. Sigurdsson & Hernquist, 1993; Portegies Zwart & McMillan, 2000; Downing et al., 2010; Rodriguez et al., 2016). We leave the details of the binary evolution scenario or dynamical capture to future work (e.g. Belczynski, 2020). Binary interaction is complex and can have a wide range of impacts on the evolution of stars. In the next chapter, we investigate the impact of binary interaction on the evolution of blue supergiants and, in particular, on the application to distance measurement.

Chapter 7

Impact of binary interaction on the evolution of blue supergiants: The flux-weighted gravity luminosity relationship and extragalactic distance determinations

The contents of this chapter were published in Farrell et al. (2019), A&A 621, A22.

7.1 Stellar evolution models

We use the BPASS suite of binary models and the MESA stellar evolution code to study the properties of BSGs in binary systems. To reproduce the bulk of the observed population, we focus on a mass range of 9 – 30 $M_\odot$. We study models with initial orbital periods in the range $\log(P/\text{days}) = 1.0 - 3.4$ (i.e. P = 10 – 2511 days). As we discuss in Sect. 7.3.1, the mass ratio q (where $q = m_\text{sec}/m_\text{pri}$) has little effect on the evolution of the primary star in the BSG stage and on the FGLR plot over a wide range of initial masses and periods. For this reason, we discuss only a mass ratio of $q = 0.9$ throughout this paper.

7.1.1 BPASS models

We select models with initial primary masses of 9, 15, 20 and 30 $M_\odot$, metallicity Z = 0.020 and mass ratio $q = 0.9$ from the v2.1 BPASS suite of binary models (see Eldridge et al., 2017, for details). To examine the effects of the initial period, we choose models with initial orbital periods of $\log(P/\text{days}) = 1.4$, 2.0, 2.4, 3.0, 3.2 and 3.4.

7.1.2 MESA models

To complement the BPASS models, we use the MESA stellar evolution code to compute our own models (Paxton et al., 2015, 2013, 2011). The models in the BPASS suite follow only the primary star with detailed calculations (Eldridge et al., 2017). It is important to investigate whether the secondary will produce a BSG and how these BSGs compare with the observed data. For this reason, we compute a small grid of models using MESA. Our models have initial primary masses of 12, 15, 20 and 30 $M_\odot$ with metallicity $Z = 0.020$ and a mass ratio of $q = 0.9$. We choose a range of initial orbital periods of $\log(P/\mathrm{days}) =$ 1.0, 2.0, 2.6, 3.0, 3.1, 3.3 and 3.4. We exclude very short periods as the system is likely to enter common envelope evolution, which is difficult to model accurately. We also exclude systems with initial orbital periods $P > 2511$ days, because the stars in these systems would evolve very similarly to single stars.

7.1.3 Physical ingredients of models

In this section, we summarise the physical ingredients we use in our MESA models and provide a comparison with the ingredients in the BPASS models.

- We use the Schwarzschild criterion for convection (as in BPASS).

- We consider convective core overshoot using a step function over a layer of thickness 0.3 H_P above the hydrogen core, where H_P is the pressure scale height at the outer boundary of the core. The BPASS models include convective overshooting with $\delta_\mathrm{ov} = 0.12$, which results in an overshooting length of around 0.3 H_P for massive stars.

- We use a mixing length for convection of 1.5 H_P. The BPASS models use a mixing length for convection of 2.0 H_P. We use the MLT++ scheme (Paxton et al., 2013) in MESA to assist with the convergence of the models. We note that this may impact the properties of BSGs after mass transfer.

- We use the ‘Dutch’ wind mass loss scheme in MESA with the scaling factor of 1.0. This scheme involves a combination of results from de Jager et al. (1988); Nugis & Lamers (2000); Vink et al. (2001) for different regimes. A similar mass loss scheme is used in BPASS.

- We use the ‘Kolb’ (Kolb & Ritter, 1990) mass transfer prescription to calculate the mass transfer rate. The BPASS models use a method inspired by Hurley et al. (2002) with a Roche lobe radius defined by Eggleton (1983).

– We do not consider rotation or tidal interactions, but assume non-conservative mass transfer as in Yoon et al. (2017) and as predicted by previous binary models including the effects of rotation (Yoon et al., 2010; Petrovic et al., 2005). In these studies, the accretor is quickly spun up to critical rotation during mass transfer and in response, the stellar wind mass loss increases dramatically. This effectively results in highly non-conservative mass transfer. Our models all undergo Case B mass transfer and we use a mass accretion efficiency of $\beta = 0.2$ as suggested by previous results (e.g. Yoon et al., 2010). The BPASS models assume a maximum accretion rate $\dot{M}_{\rm sec,\,max} = M_{\rm sec}/\tau_{\rm KH}$, where $\tau_{\rm KH}$ is the Kelvin-Helmholz timescale.

– We evolve the stars to a central temperature of $T_{\rm c} = 10^9$ K, corresponding to the end of carbon burning. The luminosity and effective temperature remain almost constant after $T_{\rm c}$ increases beyond 10^9 K (Hirschi et al., 2004; Groh et al., 2013c; Yoon et al., 2017).

In this work, we define the BSG stage for the primary stars as post-main sequence stars with an effective temperature between 8 000 and 25 000 K, and hydrogen surface fraction X ¿ 0.5. Due to mass accretion, the secondary stars may expand and look like BSGs before the completion of core hydrogen burning. For this reason, we define the secondary stars with $T_{\rm eff}$ between 8 000 and 25 000 K, and X ¿ 0.5, as BSGs if they have accreted mass due to mass transfer, even if they are still core-hydrogen burning stars.

In Fig. 54 we compare the BPASS and MESA evolutionary tracks for models with the same initial mass of the primary, mass ratio and initial orbital period. For the 20 $M_\odot$ models, BPASS and MESA produce similar qualitative evolution, however there are some quantitative differences between the models due to differences in physical ingredients. The main sequence (MS) track in the MESA model is slightly longer than the BPASS model because the MESA models were computed with a different overshoot implementation, creating a larger convective core during the core-H burning phase. At this point it is worth noting that different stellar evolution codes use different values for the overshooting parameter as well as different implementations of convective-core overshooting. This has consequences for the MS lifetime and the width of the MS (Martins & Palacios, 2013). Increased overshooting results in larger cores and an extension of the MS to cooler temperatures. The extension of the MS also depends on other complex mechanisms such as rotation and magnetic fields.

The 20 $M_\odot$ MESA model undergoes a sharp drop in luminosity before the RSG stage due to a mass transfer episode. Such a sharp drop in luminosity is not present in the BPASS models. This is likely due to differences in mass transfer prescriptions adopted in the MESA models and the BPASS models. The evolutionary point at which X drops below 0.5 occurs during the RSG stage in the MESA model and in the blue part of the HR diagram in the BPASS model. This difference is also likely largely due to overshooting. Larger cores (as in the MESA models) make the star evolve more rapidly to the red part of

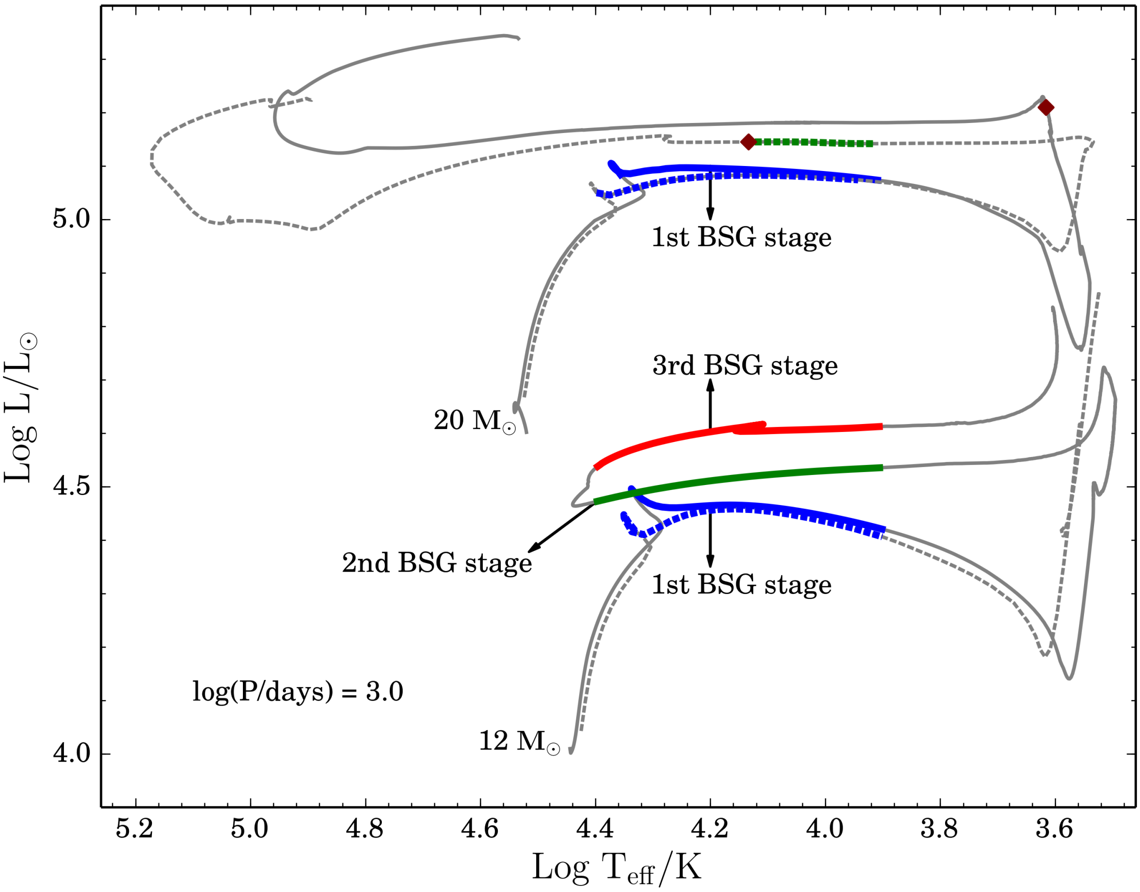

Figure 54: Evolutionary tracks for primary stars of masses 12 and 20 $M_\odot$ for BPASS models (dashed line) and MESA models (solid line). The initial orbital period is $\log(P/\text{days}) = 3.0$. Blue, green and red indicate the first, second and third BSG stages respectively. The maroon diamond indicates the evolutionary point at which the hydrogen surface abundance drops below 0.5.

the HR diagram after the MS phase. This means that a larger fraction of the core helium burning phase occurs during the RSG phase where strong mass losses occur. These strong mass losses favour a more rapid appearance of deep layers at the surface. We also note that the BPASS model produces a hotter Wolf-Rayet (WR) star than the MESA model. A possible explanation is that the two models have different surface compositions due to different mass-loss histories.

The 12 $M_\odot$ BPASS and MESA models differ qualitatively in their post-MS evolution. The MESA model produces a well developed loop but the BPASS model remains in the RSG phase. This is a result of the fact that the MESA models are redder and more extended than the BPASS models (due to differences in mixing lengths for convection) and therefore more prone to go through a stronger mass transfer episode during the RSG phase.

7.2 Impacts of binary interaction on blue supergiants

In this section we discuss the impact of binary interaction on BSGs under the assumption that the BSG can be observed without spectral contamination from its companion. In Sect. 7.3.5, we discuss the impact of the presence of a secondary on the quantities inferred from a combined unresolved spectrum.

7.2.1 Primary stars

The left panels of Figs. 55 and 56 show the evolutionary tracks of the primary stars in the HR diagram from the BPASS models and the MESA models respectively. A star can exist as a BSG either when crossing the HR diagram from the main sequence to the RSG stage (first stage), or after the RSG stage (second stage).

First stage BSGs

With both the BPASS and MESA models, BSGs that form during the first crossing of the HR diagram after the main sequence (first stage) produce characteristics mostly consistent with the observed FGLR (right panels of Figs. 55 and 56). In systems with initial periods $P > 100$ days, the first BSG stage is not affected by binarity as the mass transfer does not begin until after the BSG stage, when $\log(T_{\rm eff}/{\rm K}) < 3.9$. In these cases, these blue supergiants present similar characteristics to those obtained from a single star.

However, in systems with short initial periods, P $\leq$ 100 days, the mass transfer begins during or before the first BSG stage (e.g. see dashed blue part of tracks in Fig. 56). This is evident in the HR diagram from the drop in luminosity as a result of the mass loss. In the BPASS models, despite the change in mass (which results in a change in $g_{\rm F}$), the BSGs are still compatible with the observed FGLR due to a corresponding change in luminosity. For the MESA models, this large mass transfer produces tracks outside the observed FGLR. However, because Roche-lobe overflow (RLOF) is taking place, the spectrum of the star would probably be modified because of the high accretion and mass-loss rate (see discussion for post-mass transfer systems in Sect. 7.3.7). As a result, these stars would probably not appear as a normal BSG and therefore the FGLR would not apply to them. In this case, the duration of the BSG stage would be shortened because of the beginning of the mass transfer episode.

Second stage BSGs

Our models show that not all evolutionary tracks going back to the blue after a RSG stage produce a BSG phase. This is because some models have low hydrogen surface abundances, X, and we only consider stars with $X > 0.5$ as BSGs.

If we compare the post-RSG evolution of the 15 $M_{\odot}$ models computed with MESA for different initial periods (see left panel of Fig. 56), we find that there are three different evolutionary outcomes. For a system with a short initial period (e.g. $\log(P/\mathrm{days}) = 2.0$), the star evolves back to the blue after the RSG stage, but with X ¡ 0.5 so we do not classify it as a BSG. These stars with hydrogen-poor envelopes would likely be classified as blue hypergiants or luminous blue variables. For a system with an intermediate period (e.g. $\log(P/\mathrm{days}) = 3.0$), the star evolves back towards the blue with $X \geqslant 0.5$ creating a second BSG stage. For a system with a long period (e.g. $\log(P/\mathrm{days}) = 3.4$), the star does not evolve back to the blue. This trend is due to a general decrease in mass loss due to mass transfer, with increasing initial orbital period.

Interestingly, BSGs that result from a post-RSG stage evolution are produced with characteristics far away from the observed FGLR (see the green parts of the tracks in the FGLR planes in Figs. 55 and 56). In the BPASS models, these BSGs occur for only a relatively narrow range of parameters; only the 9 and 20 $M_{\odot}$ models produce a second BSG stage and these are only produced for a limited range of periods. More second stage BSGs are produced in the MESA models. This is due to different ingredients in the physical models such as mixing and mass transfer. These second stage BSGs are produced after undergoing strong mass loss during the RSG stage. Recalling that $g_{\mathrm{F}} = g/T_{\mathrm{eff}}^4 \propto M/L$, we see that the combination of the decreased mass and slightly increased luminosity results in a lower flux-weighted gravity, g_{F}. Because g_{F} decreases and the luminosity increases only slightly, the track in the FGLR plane is shifted to the right. With the BPASS models, Eldridge et al. (2017) reproduced the FGLR for primary stars using a population synthesis. In general they found that their models were consistent with the observed FGLR, but they also noted the presence of stars to the right of the observed scatter in the FGLR plane. This is consistent with the results obtained here.

Whether a primary star of a given mass will produce a second BSG stage depends on the initial period of the system. Using this, we can estimate the percentage of primary stars, for a given mass, that are positioned away from the observed FGLR. We can combine the initial period distribution for binary systems, the range of periods that produce a second BSG stage given by the models (Figs. 55 and 56) and the lifetimes of these stages.

We use the initial period distribution for binary systems reported by Sana et al. (2012), $f(\log(P/\mathrm{days})) \propto \log(P)^{-0.55}$ for $\log(P/\mathrm{days}) \in [0.15, 3.5]$. Based on the MESA models, we approximate that 30 $M_\odot$ primary stars will produce a second BSG stage for 2.8 ¡ $\log(P/\mathrm{days})$ ¡ 3.5. The lifetime of this second BSG stage as a percentage of the total BSG lifetime of the star is typically 80% in the MESA models. Given the above period range, period distribution and lifetime, and assuming all 30 $M_\odot$ stars are primary stars that exist in binary systems with $\log(P/\mathrm{days}) \in [0.15, 3.5]$, we expect 10% of 30 $M_\odot$ primary stars to be located away from the tight scatter in the FGLR plane. This percentage is an upper limit, as not all stars are in a binary system (Moe & Di Stefano, 2017; Sana et al., 2012). This percentage is similar for other primary masses in the MESA models investigated in this paper. Applying the same method to the BPASS models, we estimate that 4% of 9 $M_\odot$ and 1% of 20 $M_\odot$ primary stars should be located away from the tight scatter in the FGLR plane. Therefore, based on the stellar evolution models and the above assumptions, we would expect to see some stars located away from the observed FGLR in the sample of ˜140 BSGs shown in the M_{bol} vs. $\log g/T_{\mathrm{eff}}^4$ diagrams in Figs. 55 and 56. A few such objects have been detected and proposed to be products of binary interaction (U et al., 2009), however they are not included in the sample of BSGs shown in Figs. 55, 56, 57. We discuss this further in Sect. 7.3.

7.2.2 Secondary stars

The left panel of Fig. 57 shows the evolution of the secondary stars during the lifetime of the primary. The secondary stars begins its evolution on the MS, the same as single stars. When mass transfer begins due to RLOF from the primary, the luminosity and temperature increase. For systems with shorter periods, the secondary stars stay in the blue part of the HR diagram. For some systems with larger periods, the secondary stars may expand rapidly towards the red and then contract back towards the blue as they readjust to the increased mass (e.g. 13.5 $M_\odot$ with $\log(P/\mathrm{days}) = 3.3$). The consequences of mass accretion for the evolution of the secondary stars depend on the amount of mass transferred, the structure of the envelope when mass transfer takes place and the mass transfer mechanism used in the evolution code (see Sect. 7.1.3). For classical studies of accretion onto secondary stars, we refer the reader to Ulrich & Burger (1976); Kippenhahn & Meyer-Hofmeister (1977). We also note the topic has been more recently discussed by de Mink et al. (2007); Cantiello et al. (2007).

The predicted FGLR sequences for these secondary stars (assuming the BSG definition given above) are in good agreement with the observed data. This agreement with the observations is helped by the low mass accretion efficiency (0.2) that we use in our MESA models. As indicated by the dashed lines in Fig. 57, almost all of the BSG stages occur during a regime where the secondary is technically (according to our criteria) a BSG, but it is interacting with the primary. During this interaction, the models indicate that, for a short period of time, the mass accretion rates can reach $10^{-2} M_\odot/\mathrm{yr}$ which may obscure the star. The secondary may be spun up to the critical rotation as the transferred matter carries angular momentum. The high mass accretion rate may also produce a dense, flattened keplerian disk around the secondary, as in the case of HD327083 (Wheelwright et al., 2012a,b). Furthermore, some B[e] stars have been resolved in binaries (Meilland, 2017). Detailed radiative transfer models would be needed to test this scenario.

When the primary star dies, a system composed of a neutron star and the secondary star is formed. We continue to follow the evolution of the binary system with MESA (treating the neutron star as a point mass) until the secondary reaches the end of carbon burning. We estimate the mass of the neutron star using the final CO core mass of the primary and the relationship between the remnant mass and the CO core mass given in Table 4 in Georgy et al. (2012). We calculate the initial separation for the post-supernova evolution using the final separation from the pre-supernova models and taking the envelope mass ejected by the primary during the neutron star formation into account. We assume circular orbits and no neutron star kick due to the supernova. A significant fraction of such binary systems would be unbound because of the neutron star kick, and the secondary would become a single star. For detailed studies of the consequences of neutron star kicks and non-circular orbits see, for example, Tauris & Takens (1998) and Renzo et al. (2019).

We compute the remaining evolution of the secondary after the primary explodes for all models with an initial secondary mass of 13.5 $M_{\odot}$. We stop the evolution if the radius of the secondary star is greater than the distance between the two stars (i.e. the secondary star goes into contact with the remnant). This occurs for models with initial periods of $\log(P/\text{days}) = 1.0$ and 2.0. For the models with larger initial periods, $\log(P/\text{days})$ ¿ 2.0, the separation between the secondary and the neutron star is so large that mass transfer does not occur. This means that the evolution of the secondary, after the explosion of the primary, is somewhat similar to a single 13.5 $M_{\odot}$ star, but with an increased mass and a different internal structure due to previously accreted mass from the primary. The evolutionary track of a 13.5 $M_{\odot}$ secondary star from zero-age main sequence (ZAMS) to the end of carbon burning is shown in Fig. 58 and the track of the secondary (after the explosion of the primary) in the FGLR plane is shown in Fig. 59. The location of the tracks in the FGLR plane for the the secondary, after the primary explodes, are in good agreement with the observed FGLR. We conclude, at least for these cases under our assumptions, that a secondary that has accreted mass is expected to follow the FGLR.

7.3 Discussion

7.3.1 Effect of mass ratio

In our analysis above, we assumed a mass ratio of $q = 0.9$ for the models. We use the outputs from the BPASS models to investigate the effect of the mass ratio, q, on the evolution of the BSGs and the tracks produced in the FGLR. Varying the mass ratio q from 0.1 to 0.9, for the same primary mass and initial period, we find the tracks in the

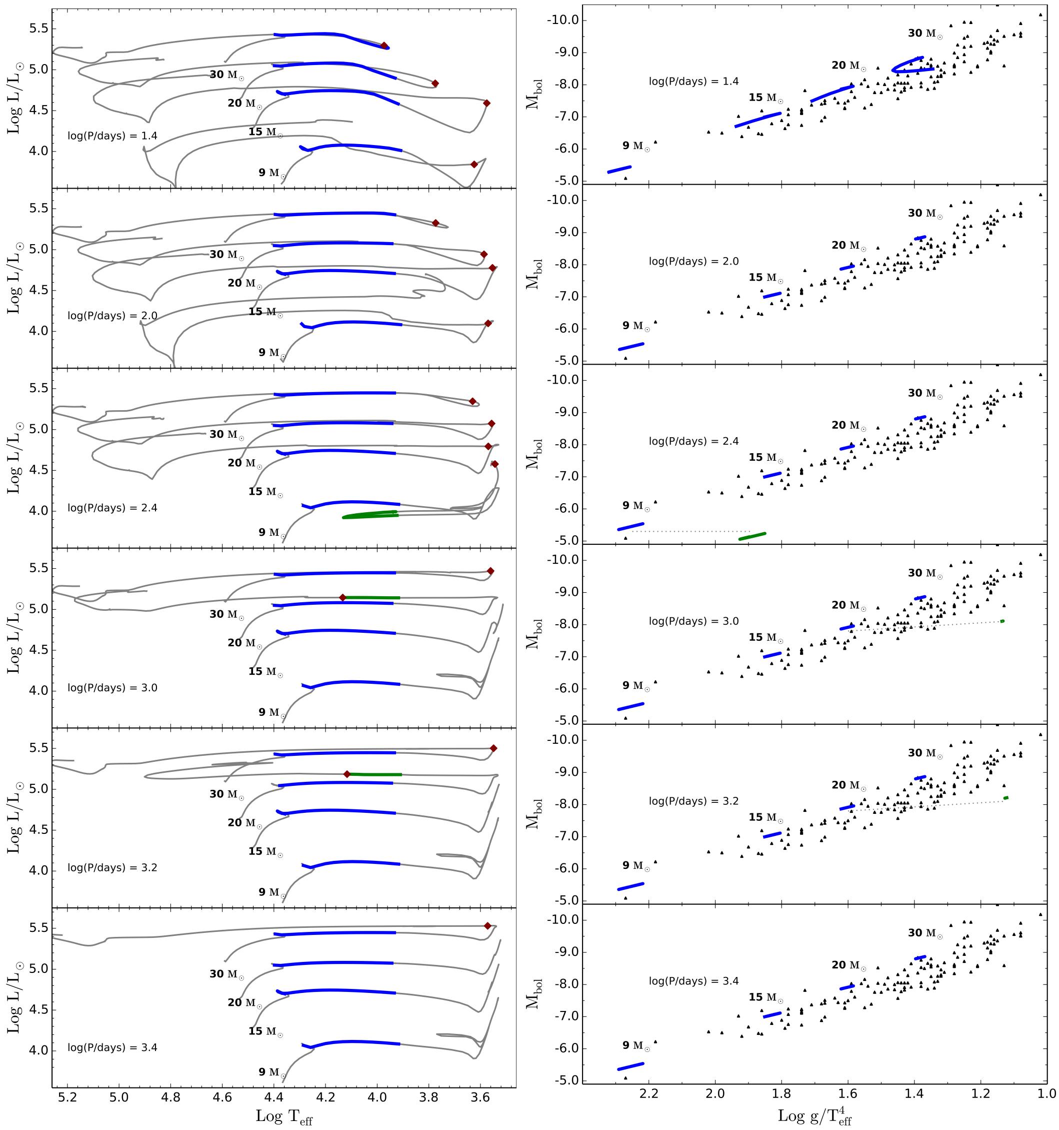

Figure 55: *Left panel:* HR diagram for BPASS models (primary stars only) with initial periods of $\log(P/\text{days}) = 1.4, 2.0, 2.4, 3.0, 3.2, 3.4$, where P is in days. Initial masses are 9, 15, 20 and 30 $M_\odot$ with a mass ratio of 0.9. Blue and green indicate first and second BSG stages respectively. Not all parts of the track crossing the BSG after a RSG stage are in green. This is because we define that a BSG has a hydrogen surface fraction X ¿ 0.5. The maroon diamond indicates the evolutionary point at which the hydrogen surface abundance drops below 0.5. *Right panel:* $M_{\rm bol}$ vs. Log $g/T_{\rm eff}^4$ planes for the same models as in the left panel. The colours have the same meaning as the left panel. Black triangles represent observations of individual BSGs. The observations are taken from NGC 300 (Kudritzki et al., 2008b), other galaxies (Kudritzki et al., 2008a), M33 (U et al., 2009), M81 (Kudritzki et al., 2012), WLM (Urbaneja et al., 2008), NGC 3109 (Hosek et al., 2014), NGC 3621 (Kudritzki et al., 2014) and NGC 4258 (Kudritzki et al., 2013). Light grey dashed lines join the first and second BSG stages from the same model.

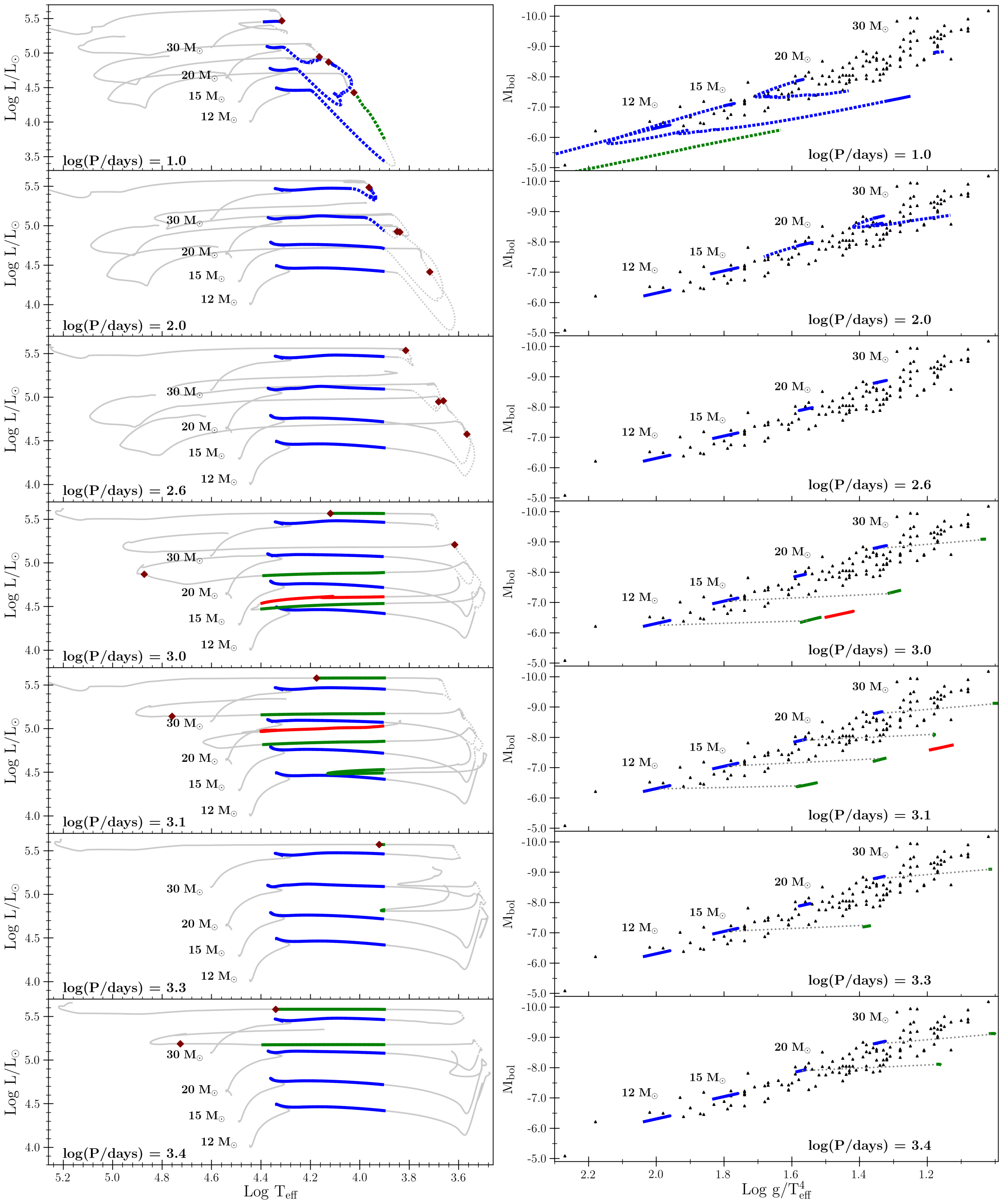

Figure 56: *Left panel:* HR diagrams for primary stars in MESA models, with initial masses of 12, 15, 20 and 30 $M_\odot$, mass ratio of $q = 0.9$ and Z = 0.020. Blue, green and red indicate first, second and third BSG stages respectively. The dashed line indicates the period during which mass transfer takes place. Not all parts of the track crossing the BSG after a RSG stage are in green. This is because we define that a BSG has a hydrogen surface fraction X ¿ 0.5. The maroon diamond indicates the evolutionary point at which the hydrogen surface abundance drops below 0.5. *Right panel:* $M_{\rm bol}$ vs. Log $g/T^4_{\rm eff}$ planes for same models as in left panel. The colours have the same meaning as the left panel. Observations sources are listed in caption of Fig. 55. Light grey dashed lines join the first and second BSG stages from the same model.

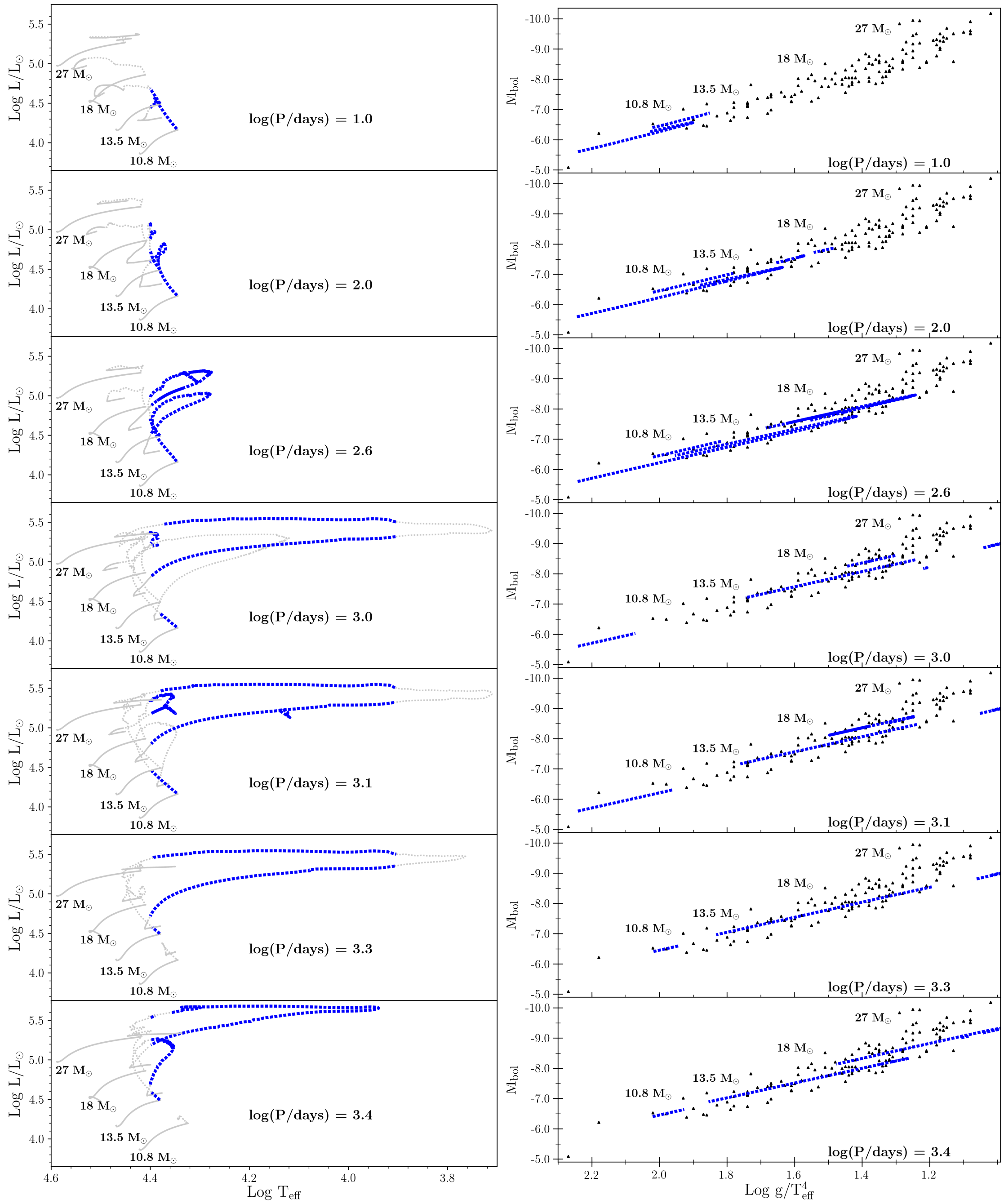

Figure 57: *Left panel:* HR diagrams for secondary stars in MESA models, with initial masses of 10.8, 13.5, 18 and 27 $M_{\odot}$. See caption of Fig. 56 for other details. *Right panel:* $M_{\rm bol}$ vs. Log $g/T^4_{\rm eff}$ planes for same models as in left panel. Observations sources are listed in caption of Fig. 55.

Table 7.1: Selected quantities for primary stars from MESA models taken at $\log(T_{\rm eff}) = 4.1$. 'Stage' column denotes if star is moving to the red in the HR diagram (first stage) or moving to the blue (second stage). '$\rm f_{BSG}$' indicates the time spent between $\log(T_{\rm eff}) = 3.9$ and 4.4 for a given stage as a fraction of the total BSG lifetime of each model. $\tau_{\rm BSG}$ indicates the lifetime of the BSG stage in kyr. Not all of these evolutionary points are considered BSGs (see X surface fractions). The rows in italics correspond to models that return to the blue due to mass loss, at a temperature $\log(T_{\rm eff})$ > 3.9 and therefore technically produce only one BSG stage. We include the parameters of these models when it has $\log(T_{\rm eff}) = 4.1$ in the stage 2 rows.

Initial details			Quantities for Primary star								Quantities for Secondary star		
$M_{\rm initial}$ $M_\odot$	$\log(P)$ days	Stage	$M_{\rm prim}$ $M_\odot$	$\rm f_{BSG}$	$\tau_{\rm BSG}$ kyr	$X_{\rm surf}$	$C/H_{\rm surf}$	log g cm s^{-2}	log P days	$v_{\rm orb}^{\rm prim}$ km s^{-1}	$M_{\rm sec}$ $M_\odot$	$L_{\rm pri}/L_{\rm sec}$	log g cm s^{-2}
12	1.0	1	10.43	0.24	18.57	0.70	4.92×10^{-3}	2.70	1.06	133	10.81	0.63	3.57
12	1.0	2	3.90	0.76	58.86	0.28	4.52×10^{-4}	1.68	1.84	98	12.10	2.64	3.89
12	2.0	1	11.59	0.31	21.96	0.70	4.92×10^{-3}	2.35	2.02	60	10.57	1.98	3.63
12	2.0	2	3.98	0.69	49.91	0.31	3.97×10^{-4}	1.72	2.81	46	12.08	2.74	3.86
12	2.6	1	11.59	0.28	22.09	0.70	4.92×10^{-3}	2.35	2.62	38	10.57	1.98	3.63
12	2.6	2	4.18	0.72	56.85	0.40	3.61×10^{-4}	1.73	3.34	30	12.01	2.59	3.84
12	3.0	1	11.59	0.07	22.09	0.70	4.92×10^{-3}	2.35	3.02	28	10.57	1.98	3.63
12	3.0	2	4.56	0.80	236.91	0.57	2.29×10^{-3}	1.95	3.60	24	11.84	1.75	3.72
12	3.1	1	11.59	0.04	22.10	0.70	4.92×10^{-3}	2.35	3.12	25	10.57	1.98	3.63
12	3.1	2	4.72	0.96	497.86	0.61	2.69×10^{-3}	2.01	3.65	23	11.76	1.58	3.66
12	3.3	1	11.59	1.00	22.09	0.70	4.92×10^{-3}	2.35	3.32	22	10.57	1.98	3.63
12	3.3	2	does not produce stage that reaches $\log(T_{\rm eff}/{\rm K}) = 4.1$										
12	3.4	1	11.59	1.00	22.09	0.70	4.92×10^{-3}	2.35	3.42	20	10.57	1.98	3.63
12	3.4	2	does not produce stage that reaches $\log(T_{\rm eff}/{\rm K}) = 4.1$										
15	1.0	1	10.53	1.00	50.73	0.70	4.87×10^{-3}	2.54	1.17	144	14.04	0.38	3.45
15	1.0	2	*5.49*	*1.00*	*50.73*	*0.50*	2.54×10^{-4}	*1.72*	*1.72*	*114*	*15.05*	*1.40*	*3.72*
15	2.0	1	14.42	0.31	15.81	0.70	4.92×10^{-3}	2.17	2.02	65	13.30	1.83	3.54
15	2.0	2	5.76	0.69	35.78	0.32	3.79×10^{-4}	1.45	2.67	54	14.99	2.66	3.75
15	2.6	1	14.42	0.38	15.78	0.70	4.92×10^{-3}	2.17	2.62	41	13.30	1.84	3.54
15	2.6	2	5.85	0.62	25.85	0.44	2.87×10^{-4}	1.62	3.23	35	14.96	2.58	3.77
15	3.0	1	14.42	0.28	15.79	0.70	4.92×10^{-3}	2.17	3.02	30	13.30	1.83	3.54
15	3.0	2	6.02	0.72	40.58	0.59	2.13×10^{-3}	1.73	3.55	27	14.83	2.01	3.70
15	3.1	1	14.42	0.18	15.79	0.70	4.92×10^{-3}	2.17	3.12	28	13.30	1.83	3.54
15	3.1	2	6.13	0.78	67.92	0.61	2.55×10^{-3}	1.74	3.62	25	14.76	1.84	3.68
15	3.3	1	14.42	0.14	15.78	0.70	4.92×10^{-3}	2.17	3.32	24	13.30	1.84	3.54
15	3.3	2	does not produce stage that reaches $\log(T_{\rm eff}/{\rm K}) = 4.1$										
15	3.4	1	14.42	1.00	15.79	0.70	4.92×10^{-3}	2.17	3.42	22	13.30	1.83	3.54
15	3.4	2	does not produce stage that reaches $\log(T_{\rm eff}/{\rm K}) = 4.1$										
20	1.0	1	does not produce stage that reaches $\log(T_{\rm eff}/{\rm K}) = 4.1$										
20	1.0	2	does not produce stage that reaches $\log(T_{\rm eff}/{\rm K}) = 4.1$										
20	2.0	1	18.73	0.39	12.41	0.70	4.92×10^{-3}	1.94	2.04	71	17.69	1.80	3.42
20	2.0	2	8.02	0.30	9.39	0.48	4.34×10^{-4}	1.58	2.63	61	19.83	1.47	3.84
20	2.6	1	18.73	0.37	11.81	0.70	4.92×10^{-3}	1.94	2.64	45	17.69	1.80	3.42
20	2.6	2	8.41	0.52	16.72	0.46	3.71×10^{-4}	1.59	3.18	39	19.73	1.61	3.70
20	3.0	1	18.73	0.11	12.01	0.70	4.92×10^{-3}	1.95	3.04	33	17.69	1.70	3.42
20	3.0	2	9.14	0.89	96.61	0.47	8.58×10^{-4}	1.59	3.46	31	19.44	1.92	3.74
20	3.1	1	18.73	0.13	12.01	0.70	4.92×10^{-3}	1.95	3.14	30	17.69	1.70	3.42
20	3.1	2	9.07	0.87	81.64	0.51	1.38×10^{-3}	1.59	3.54	29	19.35	1.76	3.65
20	3.3	1	18.73	1.00	12.25	0.70	4.92×10^{-3}	1.93	3.34	26	17.69	1.76	3.42
20	3.3	2	does not produce stage that reaches $\log(T_{\rm eff}/{\rm K}) = 4.1$										
20	3.4	1	18.73	0.18	10.92	0.70	4.92×10^{-3}	1.96	3.44	24	17.69	1.71	3.42
20	3.4	2	8.94	0.82	51.01	0.62	3.02×10^{-3}	1.57	3.75	24	18.85	1.78	3.41
30	1.0	1	does not produce stage that reaches $\log(T_{\rm eff}/{\rm K}) = 4.1$										
30	1.0	2	does not produce stage that reaches $\log(T_{\rm eff}/{\rm K}) = 4.1$										
30	2.0	1	25.86	1.00	48.56	0.70	4.92×10^{-3}	1.70	2.09	79	25.55	1.53	3.19
30	2.0	2	*15.03*	*1.00*	*48.56*	*0.44*	4.19×10^{-4}	*1.39*	*2.42*	*75*	*27.66*	*1.76*	*3.53*
30	2.6	1	25.86	0.09	8.07	0.70	4.92×10^{-3}	1.70	2.69	49	25.55	1.56	3.19
30	2.6	2	15.83	0.91	76.96	0.49	3.14×10^{-4}	1.46	2.96	48	27.35	1.73	3.43
30	3.0	1	25.86	0.09	8.08	0.70	4.92×10^{-3}	1.70	3.09	36	25.55	1.56	3.19
30	3.0	2	16.15	0.91	80.47	0.53	3.40×10^{-4}	1.46	3.32	36	27.04	1.76	3.34
30	3.1	1	25.86	0.13	7.90	0.70	4.92×10^{-3}	1.68	3.19	34	25.55	1.51	3.19
30	3.1	2	15.02	0.87	54.56	0.50	8.64×10^{-4}	1.40	3.45	33	27.03	1.79	3.31
30	3.3	1	25.86	0.14	7.93	0.70	4.92×10^{-3}	1.70	3.39	29	25.55	1.54	3.19
30	3.3	2	15.46	0.86	47.79	0.46	9.80×10^{-4}	1.43	3.60	29	26.55	1.78	3.22
30	3.4	1	25.86	0.22	8.03	0.70	4.92×10^{-3}	1.70	3.49	27	25.55	1.55	3.19
30	3.4	2	15.65	0.78	29.06	0.60	2.48×10^{-3}	1.41	3.68	27	26.15	1.82	3.14

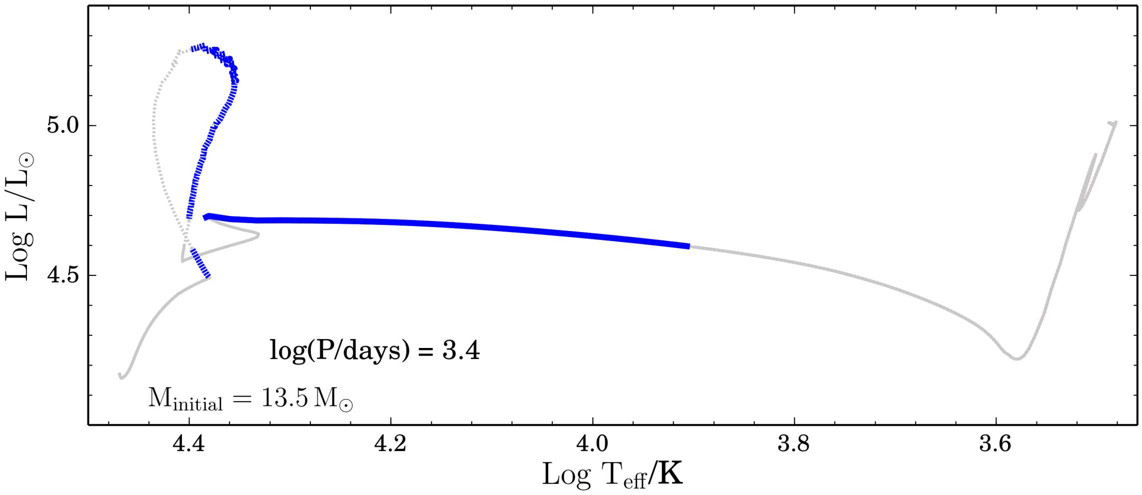

Figure 58: HR diagram for secondary stars in MESA models from the ZAMS to end of carbon burning with initial secondary mass of 13.5 $M_\odot$, mass ratio of $q = 0.9$, Z = 0.020 and an initial orbital period of $\log(P/\mathrm{days}) = 3.4$. The BSG stages are indicated in blue. The dashed part of the track indicates when mass transfer takes place.

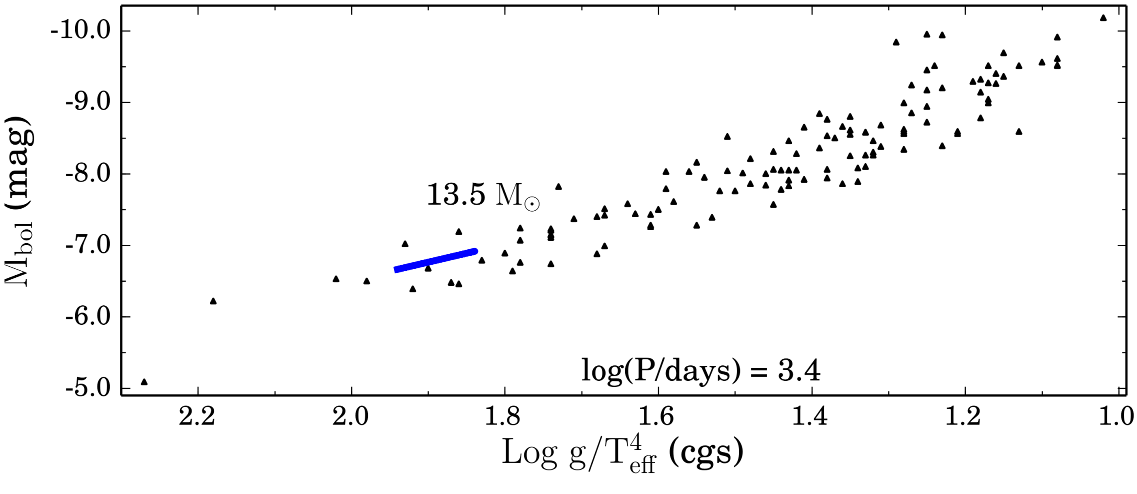

Figure 59: $M_{\rm bol}$ vs. log $g/T_{\rm eff}^4$ plane corresponding to the BSG stage for secondary stars orbiting a compact remnant for the same model as Fig. 58.

FGLR plane are almost coincidental, indicating that the mass ratio of the system has very little effect on the predicted FGLR sequence. Some of these systems may go into contact, especially those with a small mass ratio, for a given initial orbital period and an initial mass of the primary. However as we have not modelled such scenarios, we cannot say much further about these systems. These systems are potentially important as previous studies have indicated that binary systems with short initial periods resulting in Case B mergers are a promising channel for BSG production (Podsiadlowski et al., 1992; Justham et al., 2014; Menon & Heger, 2017).

7.3.2 Range of orbital Periods leading to BSGs

The range of initial orbital periods we study is limited to 100 – 2,500 days. By studying the BPASS suite of models for larger initial periods, we find that primary stars of mass 30 $M_\odot$ in binary systems with initial periods $P \gtrsim$ 4,000 days ($\log(P/\mathrm{days}) = 3.6$) will not undergo mass transfer to the secondary. Therefore, while some binary systems will have periods $\gtrsim$ 4,000 days, the stars will not exchange mass due to RLOF and will evolve similarly to single stars. The discussion of the shorter period system is more complicated because different physical processes become important. At short distances, tidal interactions occur and systems are more prone to go into contact during their evolution. Although these effects are very important for the evolution of these stars, they will likely not produce bona fide BSGs, because they may induce chemically homogeneous evolution (CHE) and thus move the stars away from the BSG region of the HR diagram (Song et al., 2016; Yoon et al., 2010; de Mink et al., 2009a). To induce CHE by tidal interaction, a very short initial orbital period is needed and therefore the parameter space for CHE is rather small (Song et al., 2016). Also, at solar metallicity, strong stellar winds tend to widen the orbit, which can prevent CHE. While a large fraction of Case A mass transfer systems would also produce BSGs (see, for example Yoon et al., 2010), the parameter space for Case A systems is much smaller than for Case B systems and therefore we expect that Case A systems would only have a minor contribution to the production of BSGs. The Case A fraction depends on how large stars become on the main sequence and this is influenced by both rotation and uncertain amounts of extra-mixing in stellar models.

7.3.3 Hydrogen abundance at the surface

The minimum hydrogen surface fraction X, that we assume in our definition of a BSG stage, significantly affects the fraction of stars that produce a second BSG stage. For this work, we define the BSG stage with X ¿ 0.5. Decreasing or increasing the minimum X surface abundance results in a respective increase or decrease in the fraction of stars that produce a second BSG stage. For example, following the same method as in Sect. 7.2.1, assuming a BSG for X ¿ 0.3 (X ¿ 0.6) predicts 24% (2%) of 15 – 30 $M_\odot$ primary stars to be located away from the tight scatter in the FGLR plane. The evolution as a function of time of the hydrogen surface fractions depend on the stellar models, and in particular on how mass loss and mixing are treated.

In principle, the fraction of outliers could be used to constrain the models if a complete observational sample were available. However we note that the target selection for spectroscopic FGLR distance determinations is heavily biased towards brighter objects to enable spectroscopy with a decent signal-to-noise. To assess the statistical effect of this selection bias on the fraction of outliers is difficult without population synthesis. The observations suggest a very small fraction of such objects. For nearby galaxies with distances smaller than 2 Mpc (M33, WLM, NGC3109, NGC300), only two objects out of a total of 81 (or 2.5%) where found to be low mass FGLR outliers.

7.3.4 Impact of stellar rotation

In this subsection, we discuss how stellar rotation and its effects on mixing and core size may affect the formation and properties of BSGs. Meynet et al. (2015b) compare the observed FGLR to single star models with and without rotation. They conclude that single star models with rotation showed a slightly better agreement with the observed FGLR than those without rotation. We chose to compute all the MESA models in this study without rotation in order to isolate the effect of mass transfer via RLOF on the FGLR. For long period binary systems, we would expect the inclusion of rotation in the models to have the same effect on the FGLR sequences as in the case of single stars and hence a slightly better reproduction of the observed FGLR. In very short period systems (with an orbital period of the order of one day), tides rapidly cause the period of rotation of the star to become equal to the orbital period (a process called synchronisation). Since the orbital period is short, stars may be rotating so quickly that they may follow a homogeneous evolution (Song et al., 2016; Yoon et al., 2010; de Mink et al., 2009a). Stars in these systems will likely not evolve to a BSG.

Rotation has an impact of the duration of the RSG phase and thus impacts the probability that a system will undergo RLOF during that phase. This will have further consequences on the evolution of the star. Some effects of rotation, such as the increase of the mass of the core during the MS phase, favour a rapid redward evolution after the MS phase causing the beginning of the RSG phase at an early stage of the core He-burning process. This may favour RLOF during the RSG phase. Other processes, such as the mixing of He into the H-rich envelope, has mixed effects that can both favour and disfavour a rapid redward evolution after the MS phase. On one hand, helium mixing into the external H-rich layers reduces the mass fraction of hydrogen in the H-burning shell. This tends to decrease the efficiency of the H-burning shell, to reduce the size of the intermediate convective zone attached to it and to favour a rapid redward evolution (Maeder & Meynet, 2001). On the other hand, the helium mixing makes the star more homogeneous, tending to keep it in a bluer region of the HR diagram. This disfavours the evolution into a RSG phase, at least at an early stage of the core He-burning phase (Goupil et al., 2013).

It is worth noting that the treatment of convection also plays a crucial role in producing BSGs, for instance using the Ledoux criterion instead of the Schwarschild criterion makes a difference as discussed by Georgy et al. (2014a). The choice of the convection criterion also affects the surface chemical composition and possibly the timing of the mass transfer episodes in binary systems.

This interplay between the mass of the core, the behaviour of the convective zone associated to the H-burning shell and the degree of overall mixing is complex and remains to be more thoroughly explored. Rotation does affect the duration of the RSG phase and thus, at least in an indirect way, any RLOF that will occur at that stage. At the moment, the quantitative effects of rotation on the properties of BSGs that appear after the RSG phase is still an open question. However, it is difficult to say more quantitatively how it affects the properties and the frequency of the stage 2 BSGs. This question remains largely open.

7.3.5 Impact of an unresolved secondary on photometry and spectroscopy of a BSG primary star

For the range of initial orbital periods chosen in the binary models produced using MESA, the typical separation between the primary and secondary stars during the BSG stage ranges from 200 – 1200 $R_{\odot}$. As the FGLR is used as an extragalactic distance indicator with BSGs at distances of the order of ˜Mpc, the primary and secondary stars are unresolved at these distances.

Because of this, it is important to study the impact of the presence of an unresolved secondary star on the observed quantities obtained for the primary star. It is possible that the presence of a secondary companion will contaminate the spectrum and affect quantities derived from the spectrum such as the $B-V$ colour used for reddening corrections, the value obtained for log g or for $T_{\rm eff}$. The increased flux from an unresolved secondary may also contribute to the bolometric magnitude assigned to the primary.

In the context of post-interaction binary systems, Götberg et al. (2017, 2018) looked at the detectability of stripped stars and found that they may be challenging to detect at optical wavelengths, but easier to detect at UV wavelengths. Here, we look at the pre-interaction detectability of binary systems and in particular how the flux from a secondary may impact the spectrum of a primary BSG.

Determination of log g and $T_{\rm eff}$

We first look at how the presence of an unresolved secondary would affect the values obtained from the spectrum for log g and $T_{\rm eff}$.

In the analysis of observed BSG spectra, stellar gravities are constrained through a model atmosphere fit of the higher Balmer lines. For the determination of effective temperatures, different methods are applied depending on the spectral type. For BSGs of spectral type B0 to B5, the ionisation equilibrium of Si II/III/IV is used (e.g. Urbaneja

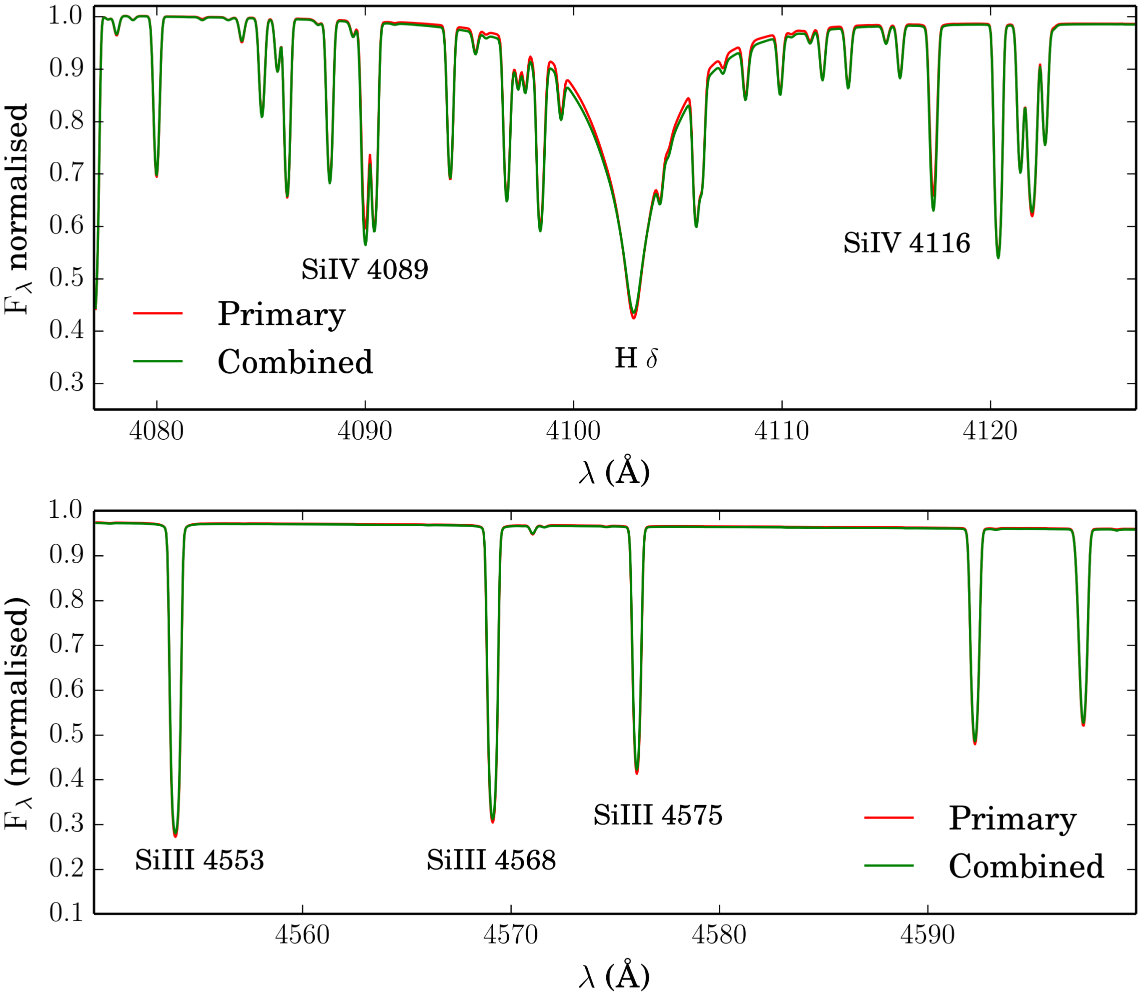

Figure 60: CMFGEN model spectrum computed at the beginning of the BSG stage using outputs from our MESA binary models for a representative system of a 20 $M_\odot$ BSG primary and an 18 $M_\odot$ (MS) secondary. The red line profiles indicate the CMFGEN model spectrum of a primary star with T = 23 000 K and log(g) = 3.0 dex. The green line indicates a combination of the model spectrum of the primary star with T = 23 000 K and log(g) = 3.00 dex and the secondary star with T = 26 000 K and log(g) = 3.50 dex. The flux ratio of the primary to the secondary in the B band at the stage when the spectra are computed is $F_{B,\mathrm{pri}}/F_{B,\mathrm{sec}} = 2.3$. *Top panel:* Spectral region around the Hδ line which is one of the diagnostics for log g. *Bottom panel:* Spectral region around SiII lines at 4553, 4568 and 4575 Å, which are T_{eff}^4 diagnostics along with SiII and SiIV lines.

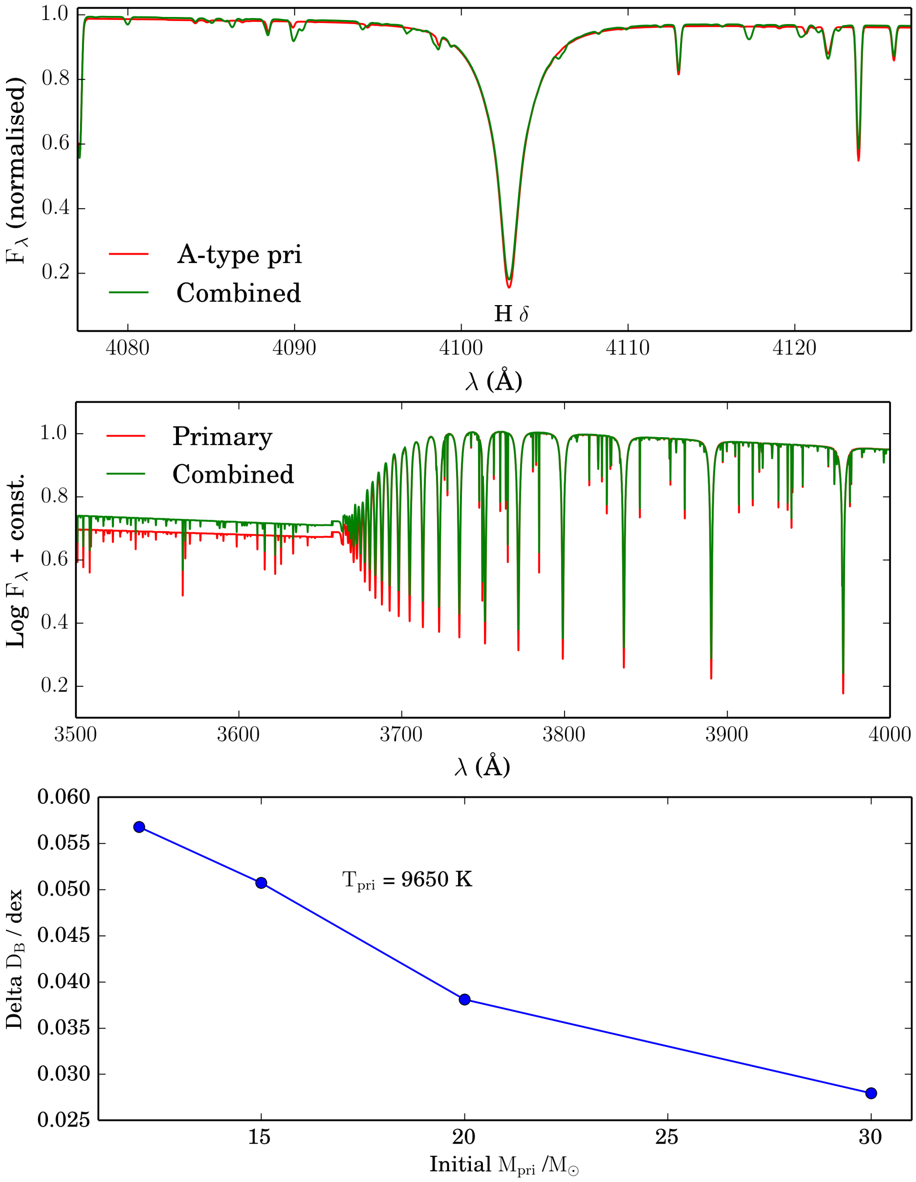

Figure 61: CMFGEN model spectra computed at the end of the BSG stage using outputs from our MESA binary models, taken from the same binary models as in Fig. 60, but at a later evolutionary stage. The red line profiles indicate the CMFGEN model spectrum of a primary star with T = 9 650 K and log(g) = 1.50 dex. The green line indicates a combination of the model spectrum of the primary star with T = 9 650 K and log(g) = 1.50 dex and the secondary star with T = 26 000 K and log(g) = 3.50 dex. The flux ratio of the primary to the secondary below the Balmer jump is 3.0. *Top panel:* Hδ line for the primary (red) and combined spectra (green). *Middle panel:* Balmer jump for the primary (A-type supergiant; red) and combined spectrum (green). Fluxes are normalised at 3790 Å for clarity. *Bottom panel:* Change in Balmer jump in the combined spectrum relative to the primary spectrum, as a function of initial primary mass. The combined spectrum has the lower Balmer jump.

et al., 2005). For later spectral types (B6 to A4), $T_{\rm eff}$ was originally obtained from a fit of the Balmer jump in the earlier FGLR work (see Kudritzki et al., 2008b, for details), however this method has since been replaced by a χ^2 fit of the total metal line spectrum between 4000 and 5500 Å which constrains $T_{\rm eff}$ and metallicity simultaneously (Hosek et al., 2014; Kudritzki et al., 2013). To study the effect of the secondary on these spectral features, we select a representative case from our MESA binary models ($M_{\rm pri} = 20\ M_\odot$, $M_{\rm sec} = 18\ M_\odot$, $\log(P/{\rm days}) = 3.0$) and use the radiative transfer code CMFGEN (Hillier & Miller, 1998) to compute synthetic spectra of a primary and secondary at the beginning (Fig. 60) and the end (Fig. 61) of the first BSG stage of the primary (before mass transfer takes place).

We compute spectra when the primary has a temperature of $T_{\rm eff}$ = 23,000 K with log(g) = 3.00 dex (beginning of BSG stage) and when the primary has a temperature of $T_{\rm eff}$ = 9,650 K with log(g) = 1.50 dex (end of BSG stage). The secondary has a temperature of $T_{\rm eff}$ = 26,000 K with log(g) = 3.50 dex in both cases. The radiative transfer models are similar to those described in Groh et al. (2014) and Smith et al. (2017). The CMFGEN spectra we compute in this paper are based on BSG models presented in Smith et al. (2017) and YSG models presented Groh et al. (2014), using a similar atomic model. In this paper, we computed a small grid of models around the values of $\log g$, $T_{\rm eff}$ and luminosity predicted by the binary models for the primary and secondary with $\dot{M}$ similar to that of the MESA models. The abundances are also the same as those from the MESA models at the appropriate evolutionary state. We note that this choice of mass ratio ($q = 0.9$) and $T_{\rm eff}$ of the primary represent a 'worst case scenario' (i.e. maximising the relative contribution of flux from the secondary in the V band). We would expect that other binary systems containing a 20 $M_\odot$ BSG would show a lower contamination due to the secondary. We combine the spectrum of the primary and secondary using their luminosities and compare the combined spectrum to that of the primary to study the effect of the presence of the secondary.

As an example of a Balmer line used to determine log g, we compare the Hδ line for the primary and combined spectra (top panels of Figs. 60 and 61). At the beginning of the BSG stage, a small amount of increased broadening in the Hδ line is noticeable in the combined spectrum due to the higher $\log g$ of the secondary. However, this difference is too small to significantly affect the $\log g$ determination, especially at the spectral resolution of 5 Å which is used for the extragalactic studies of BSGs. The effect on the Si III/IV lines is also very small which suggests that the presence of a secondary has little influence on the temperature and gravity diagnostics of early BSG types. At the end of the BSG stage, when the primary has $T_{\rm eff}$ = 9 650 K, the Balmer lines and the metal lines, and hence the determination of $\log g$ and $T_{\rm eff}$, are practically unaffected by the presence of the secondary (upper panel of Fig. 61). This is because the ratio of the flux in the V-band of the primary to the secondary is 16 (see Sect. 7.3.5).

We also investigate the temperature diagnostic for later spectral types using the Balmer jump, as it has been applied in the earlier FGLR work. In Fig. 61, we compare the Balmer jump for the primary star with the combined spectral energy distribution at the end of the BSG stage when the primary is an A-type BSG. At wavelengths lower than the Balmer jump, the flux ratio of the primary to the secondary is 3.0 because of the higher T_{eff} of the secondary. As a result, the Balmer jump of the combined spectral energy distribution is slightly decreased, as compared the the Balmer jump of the primary. In the bottom panel of Fig. 61, we plot the difference in Balmer jump inferred from the primary and combined spectra, Δ DB, for models with different initial primary masses by computing CMFGEN spectra for the primary when $T_{\text{pri}} = 9\,650$ K and for secondaries of different masses. The value of Δ DB increases with increasing initial mass because the values for log g of the primary at $T_{\text{pri}} = 9\,650$ K decrease with increasing mass. The lower log g of the primary then results in a smaller value of DB of the primary which means the UV flux of the secondary is less important when the energy distributions of the primary and secondary are combined. As can be inferred from Fig. 30 in Kudritzki et al. (2008b), this reduced Balmer jump will result in an increase of T_{eff} of up to 300 K and also an increase of g_{F} of up to 0.05 dex. This is within the uncertainties of the temperature and gravity diagnostics, but it will be a systematic effect as the secondaries are always hotter than the primary in our models with $q = 0.9$. As noted at the beginning of this section, this is the most extreme case. Population synthesis, taking into account the distribution of mass fractions and initial orbital periods will be needed to assess this effect in detail.

We conclude that there is a small systematic bias in the determinations of log g and T_{eff} from spectra of primary BSGs in binary systems due to the presence of unresolved secondary stars.

Determination of $B-V$ colour

Secondly, we discuss how the presence of an unresolved secondary may affect the $B-V$ colour used to calculate reddening corrections. As the secondary has a temperature of about $T_{\text{eff}} = 26,000$K throughout the BSG stage of the primary, its relative contributions in the B and V band may cause a hotter inferred $B-V$ colour. A changed $B-V$ colour due to the secondary may result in incorrect reddening corrections and hence incorrect bolometric magnitudes assigned to the primary. To check this, we plot the change in $B-V$ that would be observed due to the presence of the secondary star using colours from Worthey & Lee (2011), as a function of T_{eff} of the primary star during the first BSG stage (Fig. 62). The flux contribution of the secondary has little effect on the $B-V$ colour of the unresolved system, causing a maximum change in $B-V$ colour of -0.023 mag. This is also encouraging because it shows that the reddening corrections are not strongly affected by the presence of the secondary. While this is a small effect, it is also systematic. A systematic error of 0.02 mag in $B-V$ would result in an error of 0.06 mag in extinction and, thus, in the apparent bolometric magnitude M_{bol}. As a result, the distance modulus determined would be slightly biased towards smaller values. This

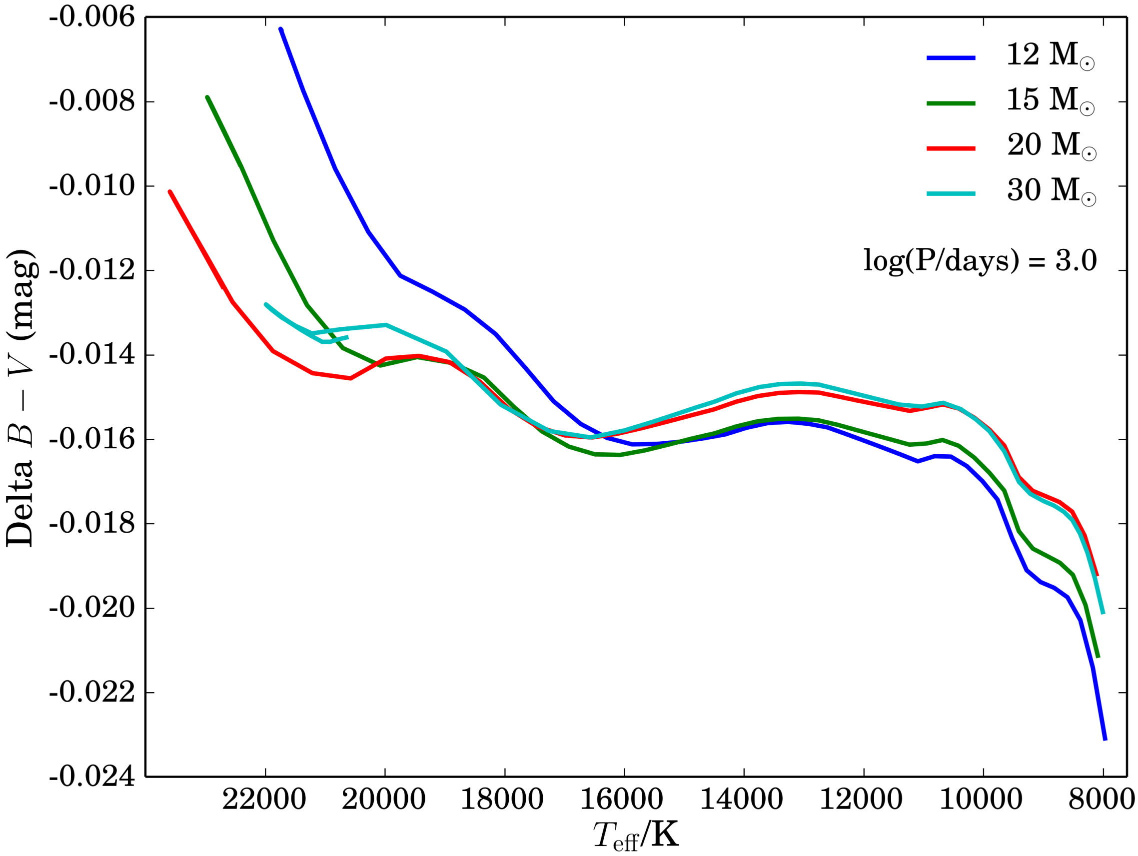

Figure 62: Change in $B-V$ colour due to presence of secondary as a function of the effective temperature of the primary star during the first BSG stage of the primary (before mass transfer takes place). The values were computed for our MESA models with initial primary masses of 12, 15, 20 and 30 $M_{\odot}$, $\log(P/\mathrm{days}) = 3.0$ and mass ratio $q = 0.9$.

implies that the FGLR method applied to BSGs that are in unresolved binaries would slightly underestimate the distance to their host galaxies. However, we note again that the mass ratio considered here $q = 0.9$ is the most extreme case.

Determination of the bolometric magnitude

It is also important to check how the increased flux from an unresolved secondary affects the bolometric magnitude assigned to the primary and the consequences of this increased flux on the FGLR. As described in Kudritzki et al. (2008b), the effective temperatures, gravities and metallicities obtained in the spectral analysis of each individual BSG are used to calculate bolometric corrections (BCs), which are then combined with the dereddened observed V-band magnitudes to obtain apparent bolometric magnitudes M_{bol}. Therefore, the secondary can affect M_{bol} either due to additional flux in the V band, or due to spectral contamination causing an incorrect determination of log g or T_{eff}, which are used to calculate the BCs. As we have discussed above, the determinations for log g and T_{eff} of the primary BSG are not significantly affected by the presence of an unresolved secondary. However, increased flux in the V band from an unresolved secondary may cause an increase in the calculated bolometric luminosity and an increased scatter of the FGLR. This increase in apparent bolometric luminosity may result in underestimates of distances to BSGs.

To study the effect of increased flux in the V band, we investigate the ratio of the flux in the V band of the primary to the secondary, $F_{V,\mathrm{pri}}/F_{V,\mathrm{sec}}$, during the main BSG stage of the primary (Fig. 63). We select some representative models to illustrate the behaviour for other systems. Again, we note that this mass ratio of $q = 0.9$ represents a worst case scenario in terms of contribution of flux from the secondary. During the BSG stage, the bolometric luminosities of both the primary and secondary and the temperature of the secondary remain approximately constant over the timescale of the BSG stage. The value of $F_{V,\mathrm{pri}}/F_{V,\mathrm{sec}}$ increases as the temperature of the primary decreases and its output in the V band increases. For much of the BSG stage of the primary, the flux ratio of the primary to the secondary is so large that the secondary will have a negligible impact on the total flux in the V band or on the spectrum in the visual range. This means that even for a BSG in a binary system with mass ratio $q = 0.9$, the presence of an unresolved secondary will only impact the V band flux from the system during the beginning of the BSG stage of the primary. For systems with lower mass ratios, we expect much larger flux ratios $F_{V,\mathrm{pri}}/F_{V,\mathrm{sec}}$.

Based on the conclusions above that there is little systematic bias in determinations of log g and T_{eff} from spectra of primary BSGs in binary systems, we expect that the the presence of unresolved secondary stars will not shift the tracks in the FGLR diagram horizontally. However, the analysis of the values of $F_{V,\mathrm{pri}}/F_{V,\mathrm{sec}}$, suggests that changes in M_{bol} assigned to the primary may shift the tracks vertically in the FGLR diagram. To study the effect of the presence of a secondary star on the M_{bol} assigned to the primary

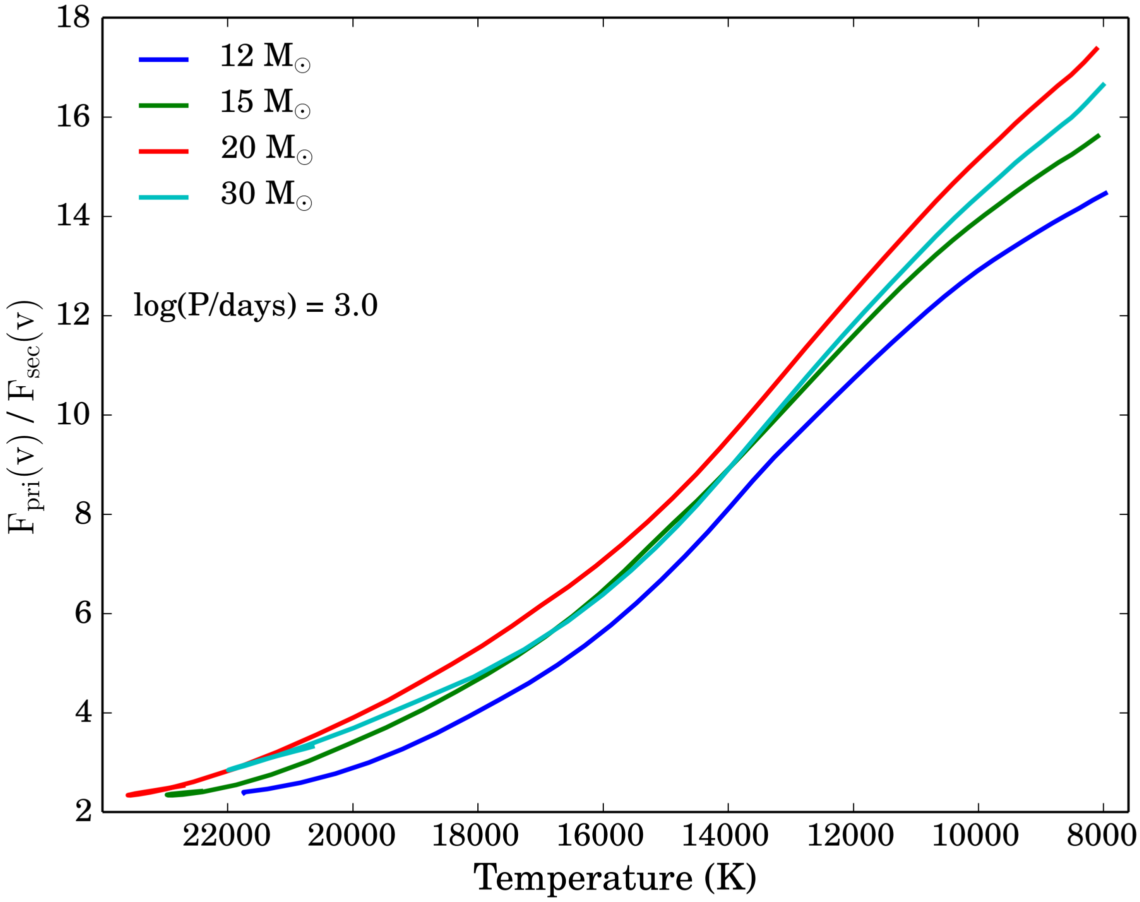

Figure 63: The ratio of the flux of the primary to the secondary in the V band, $F_{V,\mathrm{pri}}/F_{V,\mathrm{sec}}$, as a function of the temperature of the primary star during the main BSG stage of the primary (before mass transfer takes place). The values were computed for our MESA models with initial primary masses of 12, 15, 20 and 30 $M_{\odot}$, $\log(P/\mathrm{days}) = 3.0$ and mass ratio $q = 0.9$.

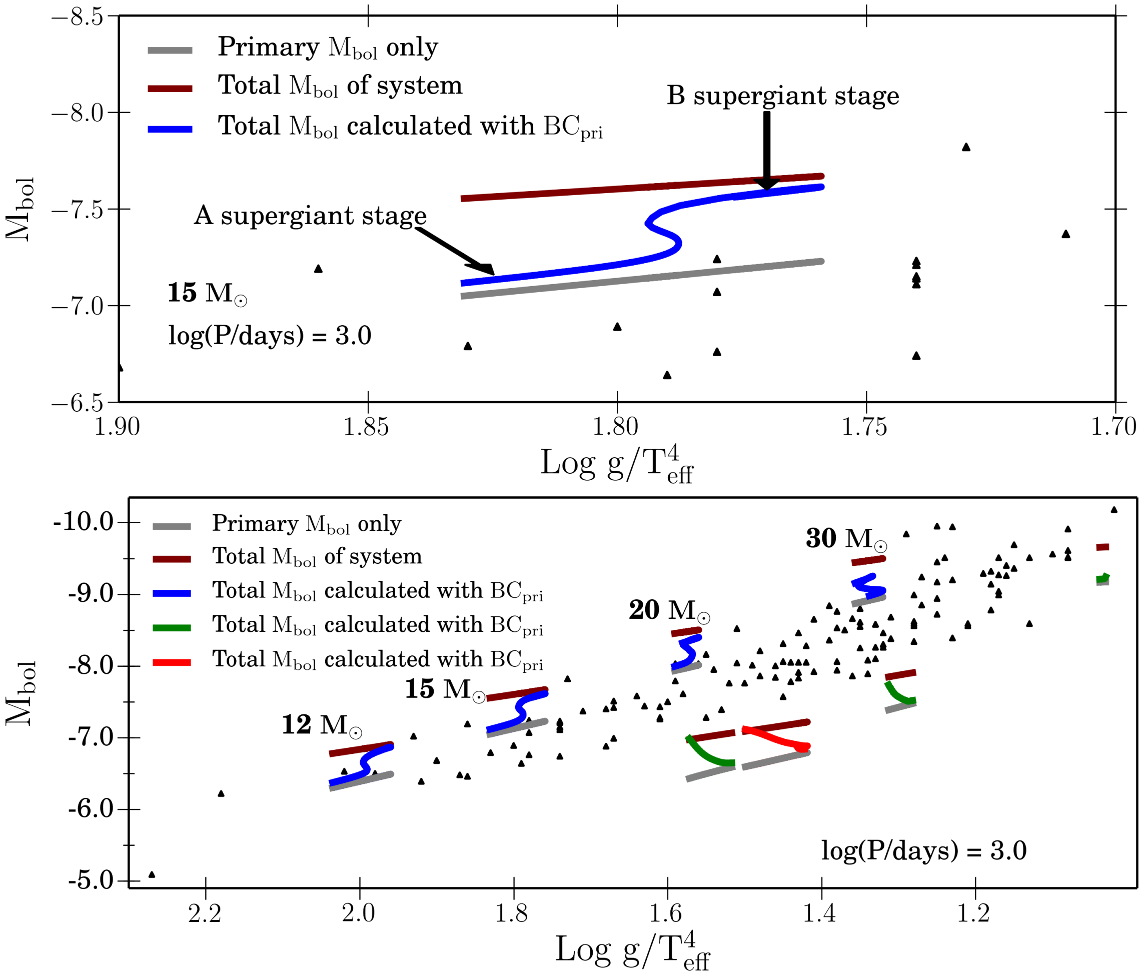

Figure 64: Tracks in $M_{\rm bol}$ vs. Log g/T$^4_{\rm eff}$ plane for BSG stages, using both a modified and unmodified bolometric magnitude due to the presence of the secondary. Grey tracks are original tracks with unmodified $M_{\rm bol}$ (as in Fig. 56). Blue, green and red tracks correspond to the first, second and third BSG stages with modified $M_{\rm bol}$ calculated by combining the V band flux of the primary and secondary and applying the bolometric correction (BC) based on the log g and $T_{\rm eff}$ of the primary. Maroon tracks use a modified $M_{\rm bol}$ calculated by computing the bolometric magnitude for the sum of the luminosities of the primary and secondary. *Top panel:* Close-up track of the 15 $M_\odot$ model to more clearly illustrate the changes in the modified tracks. *Bottom panel:* Models with initial masses of 12, 15, 20 and 30 $M_\odot$, mass ratio of $q = 0.9$ and initial period of $\log(P/\text{days}) = 3.0$.

on the FGLR, we compute tracks in the M_{bol} vs. Log g/T$^4_{\mathrm{eff}}$ plane for a representative sample of MESA models in Fig. 63, using a modified bolometric magnitude due to the presence of the secondary (Fig. 64). The modified M_{bol} is calculated by combining the V band flux of the primary and secondary and applying the BC based on the log g and T_{eff} of the primary. The values of the BCs are taken from Worthey & Lee (2011).

Comparing the tracks with modified and unmodified M_{bol}, the increased flux from the secondary has the systematic effect of raising the tracks in the FGLR plane (Fig. 64). Because $F_{V,\mathrm{pri}}/F_{V,\mathrm{sec}}$ varies during the BSG stage (Fig. 63), the effect of the secondary on the modified M_{bol} also varies. The effect of the secondary on M_{bol} is more pronounced when the primary is a B-type supergiant than when it is an A-type supergiant. When taking into account the binary fraction and the distribution of mass ratios, additional flux from secondary stars will produce a natural scatter in the FGLR plane. This may be some of the source of the observed scatter in the FGLR. Similar results are obtained for different orbital periods. Although this natural scatter is still within the error bars obtained from observations and remains consistent with the observed scatter, it is a systematic increase in bolometric luminosity which could be important when using the FGLR to determine distances. Of course, if the calibration of the FGLR is equally affected, then the systematic effect would not affect distance determinations. It is important to note that Fig. 64 represents the maximum effect and we expect a smaller effect for smaller mass ratios.

7.3.6 Identifying BSGs in binary systems

One way to deconstruct a composite spectrum from an unresolved binary system containing a BSG is through radial velocity measurements. The orbital velocities expected in the binary systems are indicated in Table 7.1. From Table 7.1, we see that the maximum amplitude of the orbital velocity is between 40 and 60 km s^{-1}, therefore only a fraction of these systems could be detected to be composite. The extragalactic FGLR studies work with a resolution of 5 Å and will therefore not be able to identify most binaries through radial velocity variations. In addition, some systems will present eclipses and thus might be distinguished through their photometric variability. We note, however, that for many of these systems the period is of the order of one year or more thus implying longer term observing campaigns.

Figure 65 shows the expected trend between the C/H surface abundance and the orbital velocity for primary stars at $T_{\mathrm{eff}} = 12\,500$ K (see Table 7.1). The group of stars located at the top of the diagram have a similar C/H surface abundance to their initial value. These correspond to the stars evolving from the MS towards the RSG stage. They show no C depletion at the surface. A second group of stars show lower C/H surface abundances, indicating depletion of C at the surface. These stars are evolving towards the blue after experiencing strong mass loss in the RSG stage. The mass loss reveals the inner layers of the star which are depleted in C due to CNO processes. We see a trend of decreasing C/H surface abundances with increasing orbital velocity. Stars with smaller initial periods (and

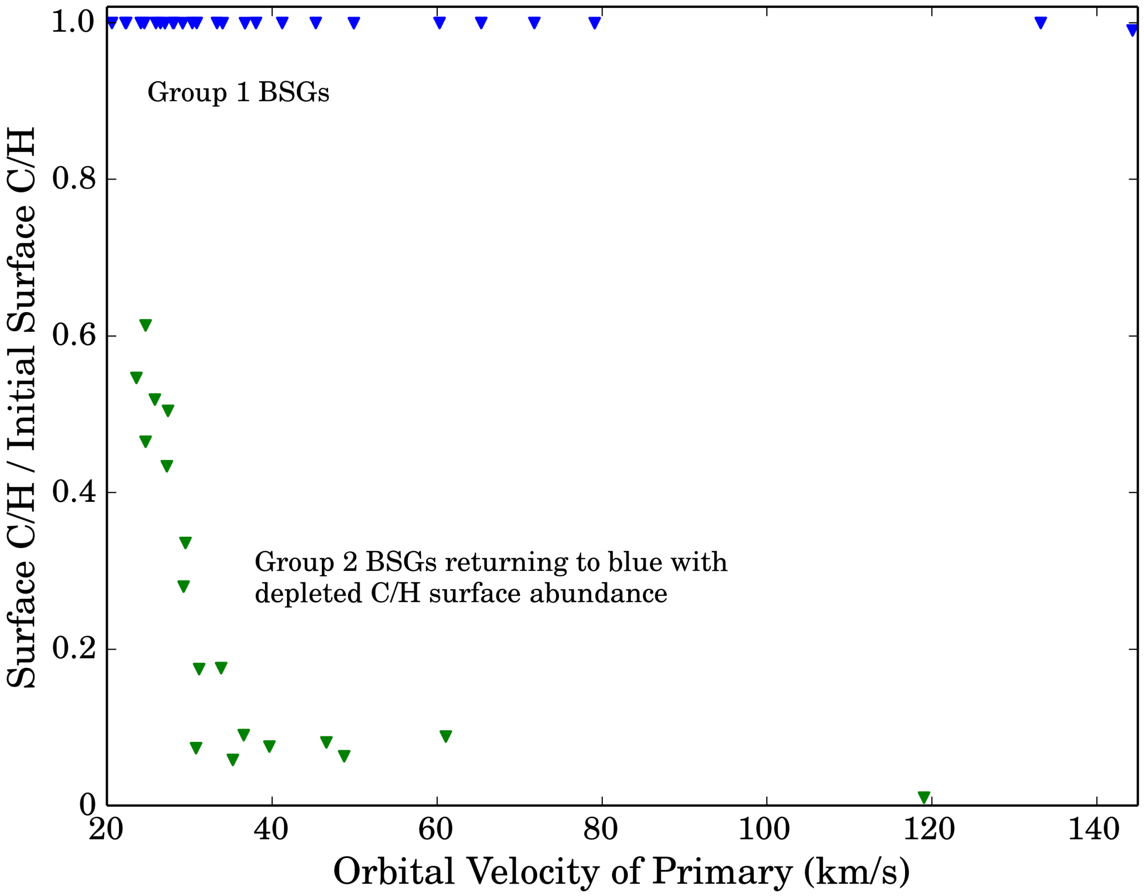

Figure 65: C/H surface abundance vs. orbital velocity for primary stars in our MESA binary models. The values were computed at a temperature of $T_{\text{eff}} = 12\,500$ K (see Table 7.1). The blue and green points represent stars moving towards the red and towards the blue in the HR diagram respectively. Not all of the stars moving towards the blue are considered BSGs by our criteria, due to low hydrogen surface abundances.

hence higher orbital velocities) undergo stronger mass loss (due to mass transfer) in the RSG stage, revealing deeper, more C depleted layers in the star. This trend, combined with radial velocities, could be used to identify blue stars that exist in binary systems. We note, however, that rotational mixing could affect this trend. Not all of these blue stars will necessarily be a BSG, as some may show strongly depleted surface hydrogen. To be tested, the two spectra should be distinguishable and relatively high resolution is needed to infer the radial velocity. Due to the high resolution required, this is more promising for nearby BSGs as observations of extragalactic BSGs typically use a spectral resolution of about 1000.

7.3.7 Further Work

Based on the results of this paper, we have determined that most BSGs in close binaries follow the observed FGLR and that the presence of unresolved secondary stars does not significantly affect the value of $M_{\rm bol}$, log g or $T_{\rm eff}$ measured for primary BSGs. We find that BSGs that form after mass transfer episodes (2nd or 3rd stage BSGs) are, in general, not consistent with the observed FGLR. As these stars have lost a substantial amount of mass, they may have in different wind properties. For instance, they may have extended atmospheres and show significant Balmer line emission, which would make the star observationally recognised as a blue hypergiant or a luminous blue variable (LBV). A similar effect has been found for single stars of 20 – 25 $M_\odot$ by Groh et al. (2013a). We will explore the spectroscopic evolution of binary systems in a forthcoming paper.

We used the MLT++ (mixing length theory) scheme (Paxton et al., 2013) to avoid numerical issues. It remains to be seen whether this implementation is valid over the mass range we explored. Recently Chun et al. (2018) investigated the impact of the MLT++ on post-MS stars, in particular RSGs. Based on the results in that paper, it is possible that using MLT++ may affect the post mass transfer effective temperatures. The treatment of radiation-dominated envelopes in 1-D stellar evolution models is challenging and we expect that future models would benefit from improved physical implementation of radiation dominated envelopes.

Population synthesis calculations are needed to more precisely compare the predictions from these binary stellar evolution models with the observed FGLR. This would properly take into account the distribution of initial periods and mass ratios. It is worth noting that Eldridge et al. (2017) present a population synthesis based on the BPASS models to study primary BSGs in binary systems. Given the difference we have discussed between the BPASS and MESA models, it would be warranted to do similar work with the MESA models. While a full population synthesis of the same scale as BPASS would take significant time to complete, creating the necessary grid to focus on the FGLR is a feasible next step. We note that MESA has recently been used to do population synthesis of single stars (Choi et al., 2016). As we discuss above, rotation may significantly impact close binary systems and should be accounted for in future models.

7.4 Conclusions

In this paper we investigated how binary evolution affects the properties of blue supergiants. In particular, we explored the effects on the bolometric luminosity and flux-weighted gravity (g/$T_{\rm eff}^4$). We initially assumed that the stars can be observed as individual objects, and then examined the impact of an unresolved secondary star on the spectrum of a primary BSG and the implications for the FGLR. Our main results and their implications are summarised below.

1. Based on the BPASS suite and a grid of models we computed with MESA, we find that most BSGs in close binary systems follow the observed FGLR. This is encouraging as it means that the FGLR is robust not only with respect to changes in the mass, metallicity and rotation but also with respect to multiplicity.

2. Our models indicate the possibility that there are some BSGs outside the FGLR observed scatter. These are produced when primary stars in a binary system undergo a mass transfer episode during the RSG stage and evolve back to the blue with a greatly reduced mass, and hence reduced flux-weighted gravity $g_{\rm F}$. Such systems may actually also be produced by single star evolution with strong mass losses during the RSG phase. In their spectroscopic FGLR studies, Kudritzki et al. (2008b) and (U et al., 2009) each found one such object in the galaxies NGC 300 and M33 respectively.

3. We estimate the frequency of these systems to be between 1 and 24% depending on, among other factors, the surface fraction of hydrogen that an evolved blue star can have to still be considered a BSG. These percentages were estimated under the assumption that all stars exist in binary systems with periods between 1.4 and 3,000 days. If we take into account the existence of longer period binary systems and single stars, these percentages will decrease by an amount depending on the binary fraction and the initial period distribution of binary systems. The observations suggest a very small fraction of such objects. For nearby galaxies with distances smaller than 2 Mpc (M33, WLM, NGC3109, NGC300), only two objects out of a total of 81 (or 2.5%) were found to be low mass FGLR outliers. However, we note that the target selection for spectroscopic FGLR distance determinations is heavily biased towards brighter objects to enable spectroscopy with a decent signal-to-noise. To assess the statistical effect of this selection bias on the fraction of outliers is difficult without population synthesis.

4. In the context of extragalactic observations, the systems studied here would be unresolved by a 10 m telescope. Therefore, we studied the impact of the presence of a secondary on the inferred magnitude, $B-V$ colour, log g and effective temperature of a primary BSG in a binary system with a mass ratio of $q = 0.9$. A high mass ratio will, in general, maximise the effects of the secondary on the primary spectrum. We find that, for a mass ratio of $q = 0.9$, the contribution of a secondary star to the

spectrum of a primary BSG has only a very small effect on the determination of T_{eff} and log g. The effects on the determination of interstellar reddening and bolometric magnitude are also small but systematic in the sense that the brightness will be overestimated by a few hundredths of a magnitude. In addition to this systematic effect, a natural scatter may be introduced to the FGLR. Detailed population synthesis calculations are needed to investigate this effect.

5. Our models suggest that some outliers to the FGLR could be the product of binary evolution. These come from systems with periods 2.8 ¡ log(P/days) ¡ 3.5 as these systems produce BSGs returning from the RSG stage after a mass transfer episode. Interestingly, all these outliers would present strongly depleted C surface abundances.

In conclusion, we find that most BSGs in close binary systems should be suitable for extragalactic distance determinations using the flux-weighted gravity luminosity relationship, although some possible outliers exist. The contribution of flux from an unresolved secondary has small systematic effect on the FGLR and also produces a natural scatter in the relationship.

After mass transfer and interaction with the companion, our results indicate that massive stars may only be recognised as blue supergiants in binary systems with a certain range of orbital periods, which depends on the mass ratio of the two components. For shorter orbital periods, different post-interaction spectra could be produced as the surface H abundances are significantly reduced compared to normal BSGs. These post-interacting systems could be observationally classified as blue hypergiants or LBVs. During or shortly after the mass transfer, the companion stars could be recognised as B[e] stars given the dense circumstellar medium that could be produced as a result of high mass-transfer rates, possibly coupled with the spin up of these companion stars by mass accretion. These evolutionary connections illustrate that the properties of blue supergiants evolving in binary systems analysed in this paper, and how they are connected to other classes of massive stars and supernova progenitors, remain an important topic for further exploration.

Binary interaction can produce strong magnetic fields in stars. However, for low mass stars, most magnetic fields are thought to be of fossil origin, thought the details of their formation are unknown. In the next chapter, we combine observations with theoretical predictions to infer the initial fossil field distribution in AB stars.

Chapter 8

Inferring the Initial Fossil Field Distribution in A/B Stars

The contents of this chapter are in preparation for submission to ApJ.

8.1 Methods

8.1.1 Observations

Sikora et al. (2019a) recently produced a volume-limited survey of all identified intermediate mass MS stars within a heliocentric distance of 100pc as determined using Hipparcos parallaxes. Sikora et al. (2019b) then measured the magnetic field strengths of the magnetic chemically peculiar stars (mCP) in their sample using spectropolarimetry. Figure 66 shows their sample in the Hertzsprung–Russell (HR) diagram.

We infer the mass of each star in this survey by matching the HR diagram position against stellar evolution models, computed as described in Section 8.1.2. We then choose to divide the data into five mass bins. Using less than five bins limits the power of our inference method, while more than five larger leads to limited sample sizes of $1-2$ stars in the upper mass bins. In each bin we compute the fraction of strongly-magnetized stars. We identify objects as strongly magnetic if Sikora et al. (2019b) were able to measure a magnetic field and weak otherwise, associating these with the two modes of the present-day field distribution. Table 8.1 summarises the number of magnetic stars $\mathrm{n_B}$, non-magnetic stars $\mathrm{n_{nonB}}$ and fraction of magnetic stars $\mathrm{f_B} = \mathrm{n_B}/\mathrm{n_{nonB}}$ in the five mass bins. These five values of $\mathrm{f_B}$, along with the mass bins, form the data which we use to infer the Initial Field Distribution (IFD).

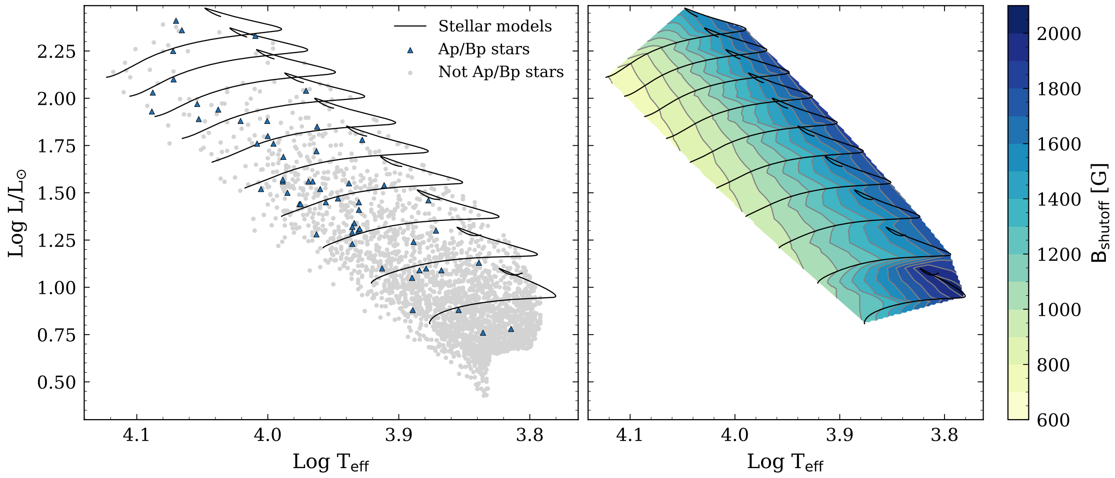

Figure 66: *Left:* A Hertzsprung–Russell diagram with observed sample (Sikora et al., 2019a,b) and our MESA stellar evolution models over-plotted. Non-magnetic AB stars are plotted in grey and strongly-magnetized stars are shown in red. *Right:* The critical magnetic field strength computed using Equation 8.1.

Table 8.1: Characteristics of stars in the volume limited survey by Sikora et al. (2019a,b), binned by mass as derived from our stellar evolution models.

Mass bin ($M_\odot$)	Number of mCP stars	Total Number	f_B
1.44 - 1.87	10	1384	0.007
1.87 - 2.30	19	544	0.034
2.30 - 2.72	13	192	0.068
2.72 - 3.15	7	53	0.132
3.15 - 3.58	6	26	0.231

8.1.2 Theory

We begin by noting that there is a critical vertical magnetic field strength above which systems are *stable* to convection. MacDonald & Petit (2019) compute this as

$$B_{\mathrm{crit}}^2 = \frac{4\pi\rho c_s^2 Q(\nabla_{\mathrm{rad}} - \nabla_{\mathrm{ad}})}{1 - Q(\nabla_{\mathrm{rad}} - \nabla_{\mathrm{ad}}) + d\ln\Gamma_1/d\ln p}, \tag{8.1}$$

where c_s is the sound speed, Γ_1 is the first adiabatic index and

$$Q = \frac{4 - 3p_{\mathrm{gas}}/p}{p_{\mathrm{gas}}/p}. \tag{8.2}$$

Here p_{gas} is the gas pressure and p is the total pressure. Using this criterion, we model magnetic fields as evolving according to a few simple rules:

1. The magnetic field is uniform near the surface of a star.
2. So long as $B > B_{\mathrm{crit}}$, convection is suppressed and the field evolves according to flux conservation ($B \propto R^{-2}$, where R is the stellar radius).
3. If the magnetic field is ever $B < B_{\mathrm{crit}}$, near-surface convective motions begin and quickly erase the surface magnetic field.

These rules implement the story described by Jermyn & Cantiello (2020). Note that stable fossil fields can survive underneath the convective regions (Jermyn & Cantiello, 2021), but they are not detectable at the surface.

We calculated stellar evolutionary tracks for stars ranging from $1.6 - 3.4 M_\odot$ using revision 15140 of the Modules for Experiments in Stellar Astrophysics (MESA, Paxton et al., 2011, 2013, 2015, 2018, 2019) software instrument. Details on the MESA microphysics inputs are provided in an Appendix. We swept the mass range in increments of $0.2 M_\odot$ and used solar metallicity ($Z = 0.02$). The evolutionary tracks of our models are plotted in the HR diagram in Fig. 66. In these calculations we forced the temperature gradient to be the radiative one in the outer envelope where subsurface convective layers would otherwise form. This allows us to simulate the inhibition of convection by a strong magnetic field in those regions. This choice has a very small effect on the surface properties, as shown by Jermyn & Cantiello (2020). However, it does impact the thermodynamic properties of the subsurface convection regions, which are relevant for computing B_{crit}.

We evaluate B_{crit} for each model at each point in time using equation (8.1) and taking the maximum value inside the subsurface convective layers, because in our scenario even a small convective region is enough to erase the surface magnetic field. For the stars observed by (Sikora et al., 2019a) the relevant subsurface convective regions are driven by hydrogen (H CZ) and helium ionization (HeI CZ, HeII CZ) (Cantiello & Braithwaite, 2019). We note that the HeI CZ is frequently stabilized by viscosity and thermal diffusion (Jermyn et al., 2022, submitted), so formally we should exclude its contribution to B_{crit}, though in practice we do not need to do anything because as far as we can tell the HeI CZ never produces the largest $B_{\rm crit}$ among available convection zones.

Fig. 67 (upper) shows $B_{\rm crit}$ as a function of mass and evolutionary stage in our models. Similar to Jermyn & Cantiello (2020), we find that the critical field strength decreases with increasing stellar mass. We also see that forcing the transport by radiation in the subsurface convective layers typically decreases $B_{\rm crit}$ by about 1 % relative to what Jermyn & Cantiello (2020) calculated, though this can increase to 10% for low-mass models at towards the late main-sequence.

Stars expand during the main-sequence. Assuming conservation of magnetic flux, the surface magnetic field B decrease with radius R as $B \propto 1/R^2$. Therefore the initial field strength required to produce a strong (super-critical) magnetic field for a given mass and MS fractional age is the cumulative maximum of $B_{\rm crit}$ from the upper panel in Fig. 67 scaled by the square of the increase of the radius. This *initial* $B_{\rm crit}$ is plotted in lower panel of Fig. 67, where the increase as a function of MS age is due to the expansion of the star. As in the upper panel, the critical field strength decreases with increasing mass.

8.1.3 Approximate Bayesian Computation

We use an Approximate Bayesian Computation (ABC) method to perform likelihood-free inference of the initial field distribution. The ABC method allows us to reconstruct the IFD as a probability density function $I(B) = dN/dB$ from the observed fraction of strongly magnetised stars $\mathrm{f_B}(M_\star)$. We do this as follows. First, we choose a parameterised, functional form for $I(B)$. We write this as $I_{\mu,\sigma,\ldots}(B)$, where the subscripts denote the parameterization. For simplicity, we assume that the fossil field distribution is mass independent throughout. We discuss the implications of this assumption later on. Next, we choose an appropriate prior distribution $p(\mu,\sigma,\ldots)$ over these free parameters. For example, one of our parameterizations is a Gaussian distribution described by a mean μ and a standard deviation σ, and we choose flat priors over μ and σ. Next, we enter a loop:

- Sample values for the free parameters of our distribution from the prior.
- Construct a population of stars sampling the resulting IFD ($I_{\ldots}(B)$). These stars have masses and ages chosen to match those in the observed volume-limited sample described above.
- For each star, we use MESA models to determine if the magnetic field is weaker than the critical field at any point between the pre-main-sequence and the age of the star inferred from observations. If this occurs, we mark that star as 'not magnetic', on the assumption that convection will erase the fossil field. Otherwise we mark the star as 'magnetic'.
- We bin the stars by mass and compute the magnetic fraction $f_{\rm B}$ in each bin.

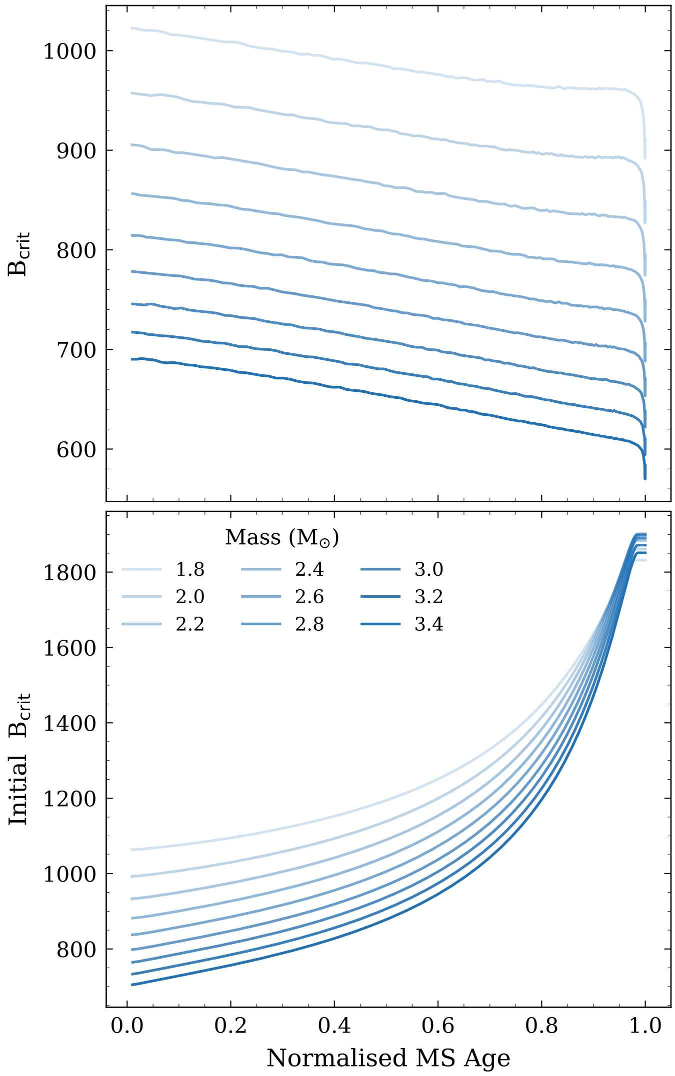

Figure 67: *Upper panel*: Critical magnetic field required to prevent the formation of subsurface convective layers as a function of normalised main sequence age for models of different masses. *Lower panel*: The critical initial magnetic field required to suppress the formation of subsurface convective layers and maintain a strong magnetic field until a given age as a function of normalised main sequence age. The trend in age is due to the expansion during the main sequence.

Table 8.2: Details of a range of distributions that we tested, including the free parameters, prior distributions, means and standard deviations (σ) of the posterior distributions and the 'distance' between the threshold 1000th best simulation and the observations (D_{1000}).

Distribution	Parameters	Priors	Posterior Mean	Posterior Standard Deviation	D_{1000}
		Standard Assumptions			
Linear	m (slope)	U(-1, 1)	-0.12	0.01	0.39
Trapezoidal	m (slope)	U(-1, 1)	-0.086	0.48	0.07
	B_{min}	U(300, 850)	551	106	
	B_{max}	U(850, 1350)	1028	53	
Gaussian	μ	U(500, 1000)	770	44	0.06
	σ	U(10, 230)	146	37	
Triangular	Midpoint	U(500, 1000)	767	131	0.05
	B_{min}	U(300, 600)	445	85	
	B_{max}	U(800, 1300)	1107	79	
		Additional Tests			
Gaussian + f_0	μ	U(500, 1000)	843	64	0.07
	σ	U(10, 230)	115	49	
	f_0	U(0, 1)	0.34	0.20	
Gaussian + mass dependence ($\mu = \mu_0 + \beta * m$)	μ_0	U(500, 1000)	731	172	0.03
	σ	U(10, 230)	150	47	
	β	U(-100, 100)	14	52	

- We compare f_B to that reported from observations by computing the sum of the differences between the fractions in each mass bin.
- If this difference is less than some threshold distance, the values of the parameters chosen at the beginning are saved, otherwise they are rejected.

We perform this loop 10^5 times for each functional form of $I(B)$. The accepted samples form our posterior distribution over the free parameters of each functional form. We verified that the accepted posterior distributions did not change substantially when we increased the number of iterations in the loop.

8.2 Inferred Initial Field Distribution

For simplicity, we begin by assuming that all stars are born with some non-zero magnetic field and that the distribution is independent of stellar mass. We will discuss the impact of relaxing these assumptions later on.

Magnetohydrodynamics is complicated, so we do not have a strong physical prior for the functional form of the IFD, and have tested several different ones. Below we compare four different forms:

1. Linear: A distribution over $B \in [300, 1500]$G of the form $I(B) = I_0 + mB$, where I_0 is determined to normalize the distribution. We assign the slope m a uniform prior distribution over $[-1, 1]$.
2. Trapezoidal: A variant of the linear distribution but with variable left and right

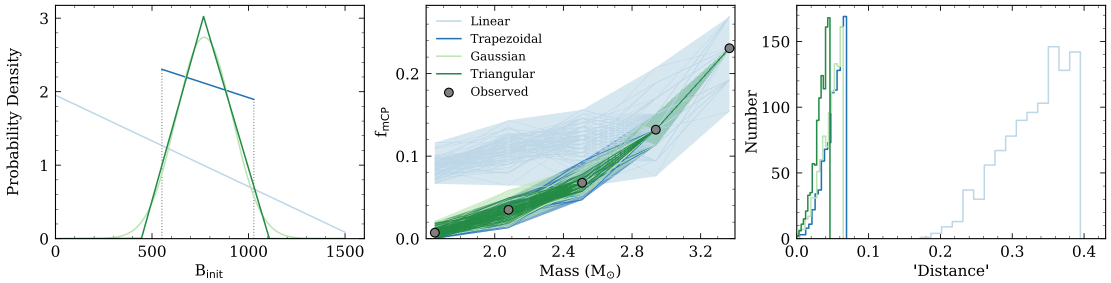

Figure 68: Comparing the results from the ABC simulations for different functional forms of the fossil field distribution. *Left panel:* Plots of the fossil field distributions with the free parameters equal to the means of their posterior distributions. *Middle panel:* Comparison between outputs of simulations and observations. *Right panel:* The distribution of the “distance” between the observations and simulations for each distribution type.

endpoints, resulting in two additional free parameters (B_{min}, B_{max}), which we assign broad uniform priors.

3. Gaussian: A Gaussian distribution characterized by a mean μ and variance σ^2. Both μ and σ are given uniform priors.

4. Triangular: A distribution with a single peak, dropping to zero linearly on either side. Both the peak location and the left and right roots are allowed to vary, with all three having uniform priors.

These functional forms are summarized in the upper half of Table 8.2.

To properly compare these different forms we performed our ABC procedure over 10^5 distributions of each form, sampling the distribution parameters from their priors. We chose our acceptance tolerance separately for each form so as to accept the best 10^3 samples, and used these to construct the posterior distributions for each parameter. Corner plots of these posteriors are provided in an Appendix.

The left panel of Fig. 68 shows examples of all four forms, with their respective parameters set to the means of their respective posterior distributions. The middle panel then compares the distributions from the 100 best simulations for each functional form with the observations. Finally, the lower panel shows the distribution of the “distance” between the observations and simulations for each distribution type. The ‘distance’ is the sum of the distance between each of the observational data points in the middle panel and the corresponding simulated points.

We find that a linear distribution from 300 G to 1500 G is inconsistent with the observed data (Fig. 68, middle). The distribution of distances in the lower panel of Fig. 68 confirms that linear distributions perform poorly compared with the other distributions. The reason for this is that the linear distribution produces many more strongly-magnetized $\sim 1.8\mathrm{M}_\odot$ stars than are actually observed. By contrast, the trapezoidal, Gaussian and triangular forms are all able to reproduce the observations within a much tighter tolerance, and visually reproduce the observed trend in f_{B} much more closely (Fig. 68, middle).

The trapezoidal form is a useful one for building intuition about our inference procedure. This form favours a relatively uniform distribution from 500 G to 1100 G. Because the critical magnetic field strength decreases with increasing stellar mass, the lower bound of the distribution is sensitive to higher mass stars and the upper bound of the distribution is sensitive to lower mass stars. The upper bound of the trapezoidal distribution is relatively strongly constrained due to they very low fraction of strongly magnetised $\sim 1.8\mathrm{M}_{\odot} stars$. The lower bound is somewhat less well constrained due to the fact that the fraction of strongly magnetised $\sim 3\mathrm{M}_{\odot}$ stars is higher than for lower masses.

The Gaussian and triangular forms are very similar in shape, and both rather different from the trapezoidal form. They both favour a peak around 800G and a similar width as that of the trapezoidal distribution (e.g. $\sigma \sim 130\mathrm{G}$). This suggests that the initial field distribution could have a peak at 800 G and a width of around 600 G, with very few stars born with magnetic fields of less than 500 G or greater than 1100 G. However given that Gaussian, triangular, and trapezoidal all fit the data similarly well we cannot tell much else about the shape of the distribution.

The trapezoidal and triangular forms, with their sharp kinks and discontinuities, seem less likely to be found in nature than the Gaussian Therefore, given the similarity between their performance and that of the Gaussian, we choose to explore the Gaussian form in more detail below.

The posterior distribution for the Gaussian form has mean $\mu = 770 \pm 44\,\mathrm{G}$ and standard deviation $\sigma = 145 \pm 77\,\mathrm{G}$. These are anti-correlated, such that we see that distributions with higher mean tend to be narrower, and those with higher variance tend to have lower means. Fig. 69 shows samples of distributions drawn from this posterior, as well as the average over these samples, which broadly tells the same story as above: initial field distribution is peaked around 800 G and has a full-width of around 600 G, with very few stars born below 500 G or above 1100 G.

8.3 Uncertainties

We now consider various uncertainties in our approach.

8.3.1 Bimodal IFDs

We have assumed that all stars were born with some non-zero initial magnetic field. While this is almost certainly the case, it could well be that the IFD is itself bimodal, and observations of young stars suggest the possibility of a second mode at very weak field strengths (Villebrun et al., 2019).

To explore this possibility we investigated distributions in which some fraction of stars are born with an initial magnetic field of $B_{\mathrm{init}} = 0$, while the rest have initial fields distributed according to a Gaussian form. We refer to this as the Gaussian+f_0 form.

Fig. 71 shows the posterior distribution over f_0, μ, and σ for this form. We see that

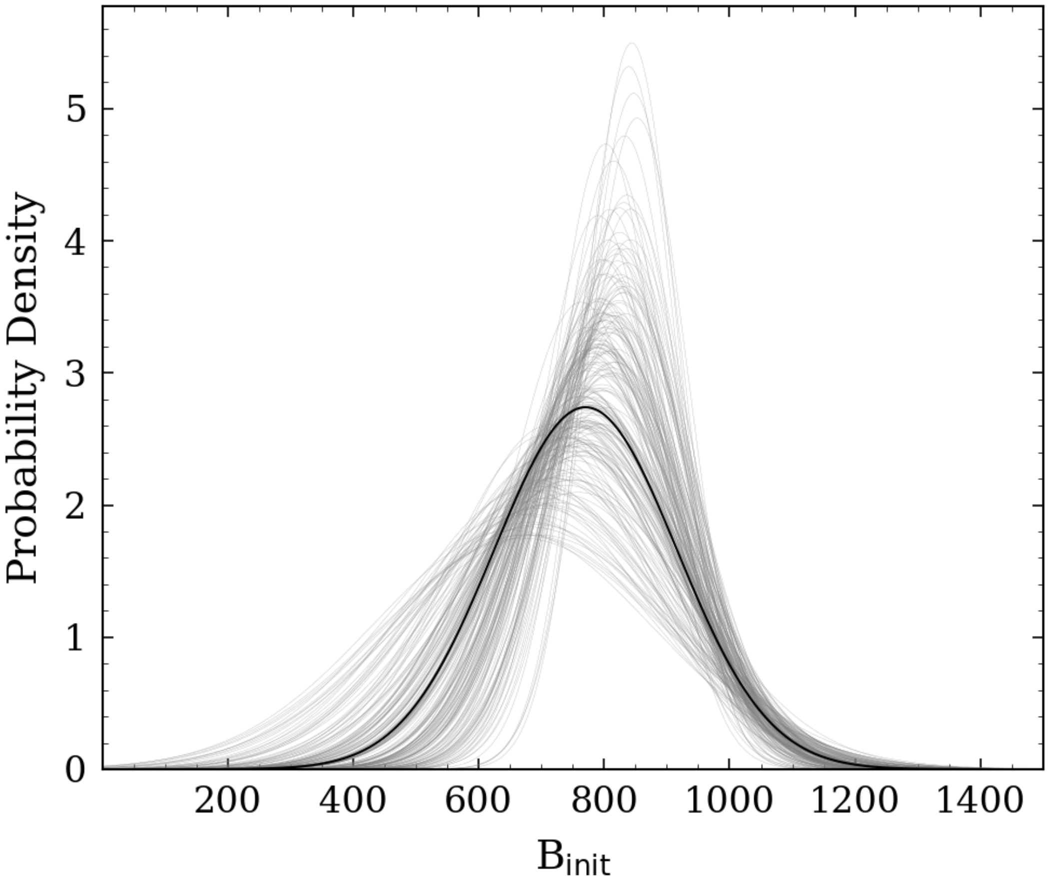

Figure 69: The black line indicates the IFD using the means from the posterior distributions. A selection of samples from the posterior distribution over Gaussian IFDs are shown in grey.

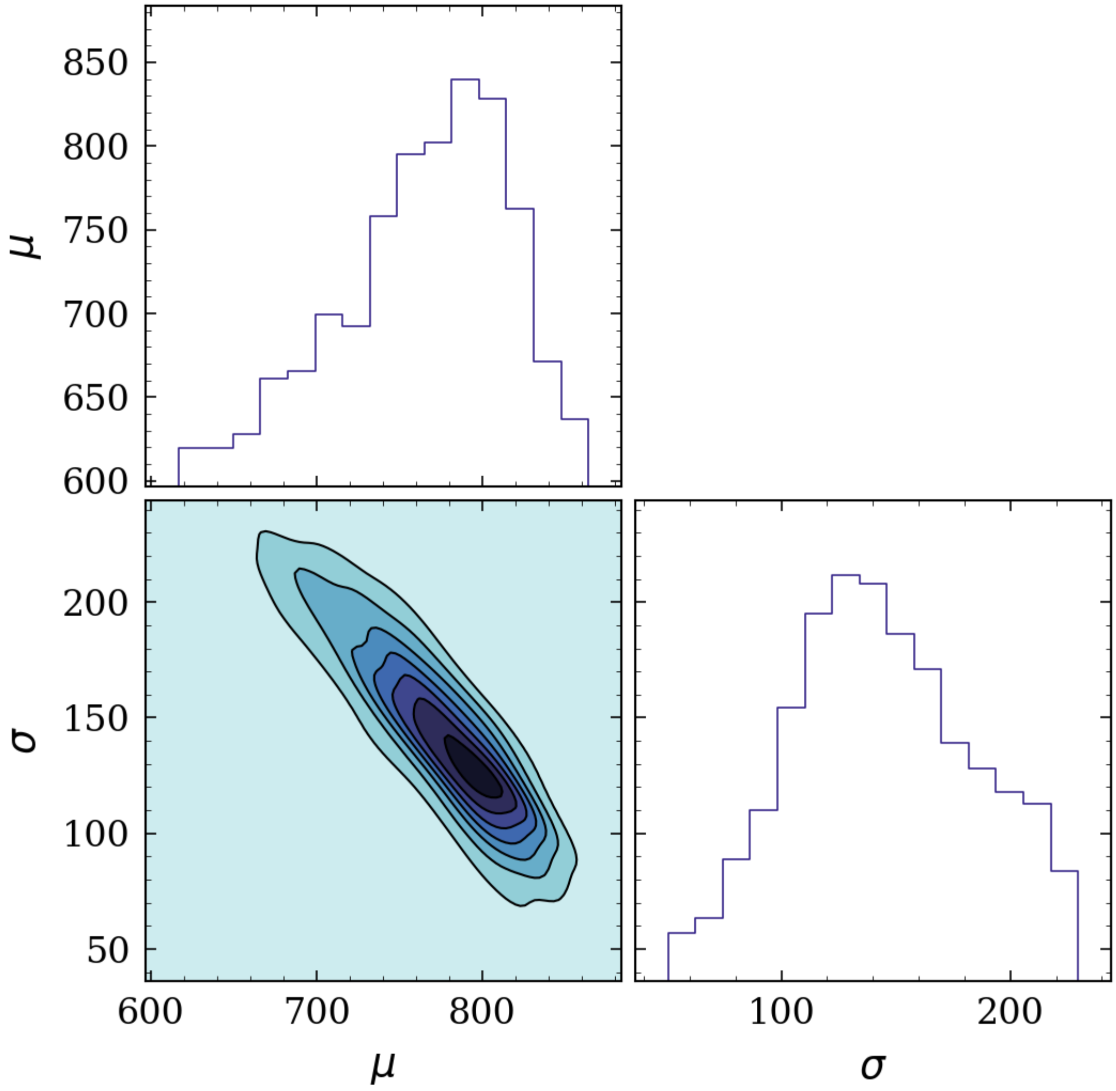

Figure 70: Posterior distributions for the mean μ and the standard deviation σ are shown for the Gaussian form.

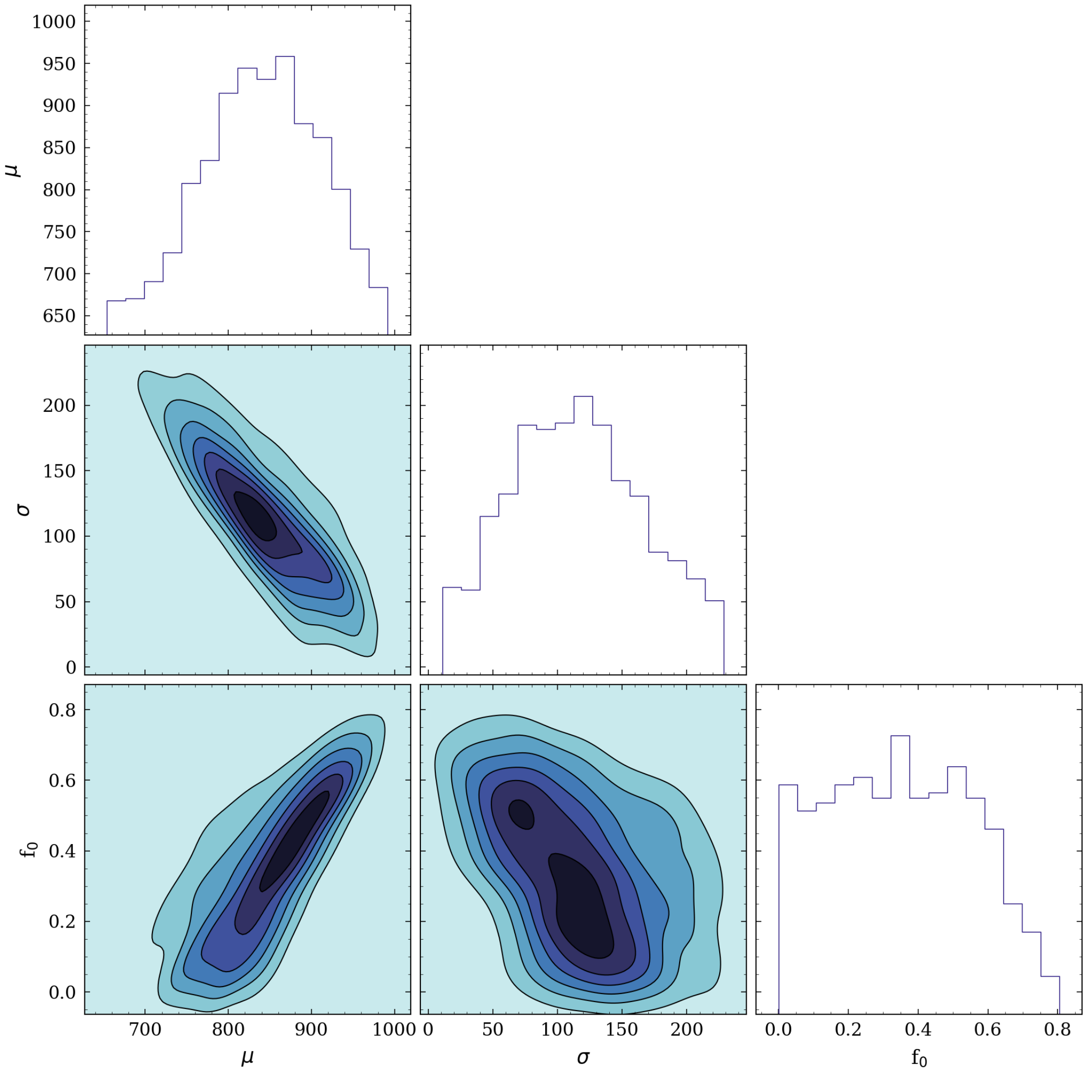

Figure 71: Posterior distribution of the mean μ and standard deviation σ and fraction of stars born with no strong magnetic field (f_0) for a Gaussian initial field distribution.

while σ is mostly uncorrelated with f_0, μ and f_0 are strongly correlated. This makes sense: as the fraction of stars with zero initial field strength increases, more stars with strong magnetic fields are needed to match the observed magnetic fraction f_B. For this reason, regardless of the precise form we choose, any functional form allowing an additional mode at weak field strengths will exhibit such a degeneracy. We cannot exclude such forms, and this degeneracy introduces an additional uncertainty to our models.

8.3.2 Sensitivity to overshooting

To study the sensitivity of our results to the details of our stellar evolution calculations, we computed a grid of models with a higher value for convective overshooting ($f_\mathrm{ov} = 0.020$ compared to $f_\mathrm{ov} = 0.014$). We find that the fossil field distribution inferred using models with larger overshooting is consistent with the distribution inferred using the original models to within 1%.

8.3.3 Magnetic Field Evolution

We have assumed that, so long as the magnetic field is strong enough to shut off convection, the field strength evolves according to flux conservation from the beginning of the main sequence phase onward. This neglects a variety of different possible phenomena, including

- Magnetic diffusion
- Differential rotation
- Stellar mergers

We think it is safe to neglect magnetic diffusion, as the diffusion time across a star is long compared with its main-sequence lifetime. We likewise suspect that differential rotation can be neglected, as super-critical magnetic fields are likely strong enough to inhibit any significant shears from developing on the main-sequence.

We do, however, think that stellar mergers pose a challenge to our analysis. Stellar mergers may produce a population of stars with strong magnetic fields without those fields being present at the ZAMS. As a result we are not necessarily inferring the IFD at the ZAMS, but rather the IFD at *either* the ZAMS or the point of merger.

8.3.4 Possible Mass Dependence

We investigated the possibility of a dependence of the distribution of initial fossil field distribution on mass. To do this, we tested a Gaussian IFD with a mean that scales linearly with the stellar mass m such that $\mu = \mu_0 + \beta * m$. We found that μ_0 and β are strongly degenerate (Fig. 72).

To understand this note that our approach is primarily using the fact that B_crit varies with mass, and so differences in the magnetic fraction between different mass bins tell us

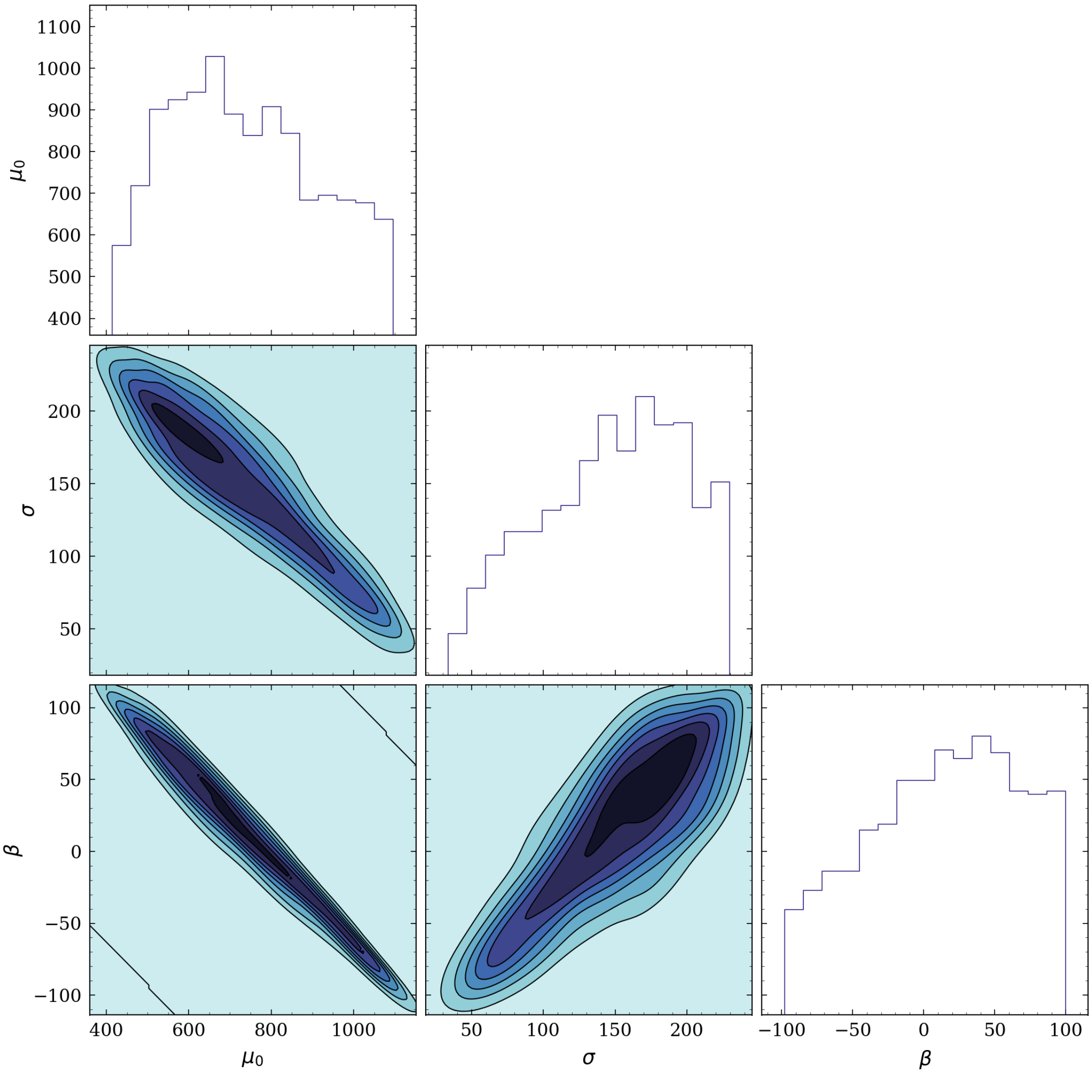

Figure 72: Posterior distribution of IFD parameters for a Gaussian form and allowing a dependence of the mean of the Gaussian with the mass through $\mu = \mu_0 + \beta * m$.

about the IFD. As a result if we permit our parameterized IFD to vary with mass we effectively lose our ability to constrain the distribution. What little inferential power we retain comes from the evolution of B_{crit} across the main-sequence, but we do not have a large enough sample of stars to also bin by age and so this is only minimally constraining.

As a result, we emphasize that our results are strongly contingent on the assumption of a mass-independent IFD over the range from $1.6-3.4\mathrm{M}_\odot$.

8.4 Discussion

We have inferred the initial distribution of magnetic field strengths (IFD) from a volume-limited sample of A/B stars with magnetic field measurements. To do this we have assumed that the IFD is independent of stellar mass and that convection erases near-surface subcritical magnetic fields. Our favoured distribution is a Gaussian with mean $\mu = 770\,\mathrm{G}$ and standard deviation $\sigma = 145\,\mathrm{G}$. We now turn to the astrophysical implications of this distribution.

8.4.1 Magnetic Desert

Jermyn & Cantiello (2020) proposed that the observed distribution of magnetic fields - and the ”magnetic desert“ – can be explained in a scenario where some fraction of stars are born with a smooth distribution of initial fields and these fields are modified by convection. The fact that our preferred IFD reproduces the observed magnetic fraction in AB stars is consistent with this hypothesis.

It is important to note that this did not need to be the case: we could not have successfully fit arbitrary data. For instance this story would have trouble reproducing a non-monotone magnetic fraction as a function of mass, and would need to invoke more complicated assumptions such as a mass-dependent IFD.

8.4.2 Connection to Star Formation

It is unclear what physical mechanism sets the IFD. It is possible that the IFD reflects some frozen-in flux present in the molecular cloud a star formed from. However, that story runs into trouble explaining the mean of the IFD. Typical molecular clouds are have strong enough magnetic fields that they cannot collapse without shedding magnetic energy (Troland & Crutcher, 2008). If just enough magnetic field is shed to allow the cloud to collapse then we should expect initial magnetic fields in approximate equipartition with gas pressure, predicting field strengths which are orders of magnitude stronger than what is observed.

On the other hand if convection indeed erases any magnetic fields that came before then we would expect the magnetic field on the ZAMS to be generated by a convective dynamo as the star descends the Hayashi track. Villebrun et al. (2019) compiled measurements of magnetic fields on the pre-main-sequence in their figure 1. For fully convective stars at the base of the Hayashi track they see a broad distribution of magnetic field strengths ranging from $\sim 100\,\mathrm{G}$ to $\sim 800\,\mathrm{G}$. These field strengths are in equipartition with the kinetic energy of convection in the outer layers of a star carrying luminosity $L \sim L_{\odot}$, and occur for stars with luminosities of that order, so it is at least plausible that the these fields are dynamo-generated.

From that point on though the story becomes unclear. These relatively strong fields persist through the development of a radiative interior, though they mostly vanish by the time early-type stars develop convective cores and radiative envelopes (Villebrun et al., 2019), so there could well be non-trivial field evolution happening in the immediate run-up to the ZAMS.

8.4.3 Solar Magnetism

If the IFD we have inferred holds at lower masses, we should expect the Sun to have been born with a $\sim 800\,\mathrm{G}$ magnetic field, and the portion of that field below the solar convection zone could well have survived to this day (Cowling, 1953).

So far as we know the fossil field in the interior of the Sun has not been measured. There are, however, various upper bounds which have been obtained. Reasoning from measurements of the solar oblateness, Friedland & Gruzinov (2004) found an upper bound of $7 \times 10^6\,\mathrm{G}$, which is certainly consistent with our prediction. By contrast Boruta (1996) inferred an upper bound of $\sim 30\,\mathrm{G}$ in the radiative zone based on the lack of bias in the solar cycle, contingent on some assumptions including that the dynamo is localized to the tachocline. If their assumptions hold then this tight limit is evidence against our IFD, and favours more complicated models like the bimodal Gaussian+f_0 forms we considered in Section 8.3.

8.4.4 Compact Remnants

Our results predict that some early-type stars with subcritical surface magnetic fields may have strong fossil fields hiding just beneath their subsurface convection zones (Jermyn & Cantiello, 2021). Assuming simple flux conservation, a field of $\sim$ 800 G would give rise to fields of order $10^6\,\mathrm{G}$ in Red Giant Cores and White Dwarfs and $10^{15}\,\mathrm{G}$ in Neutron Stars. Asteroseismology has revealed magnetic fields of order $10^6\,\mathrm{G}$ in Red Giant cores (Fuller et al., 2015), and roughly 20% of White Dwarfs have $10^{5-6}\,\mathrm{G}$ fields (Landstreet & Bagnulo, 2019), so these hidden fossil fields provide a simple explanation for the observations. This does not mean that all Magnetars and magnetic White Dwarfs inherit their fields from the IFD, as there are other mechanisms for generating or destroying magnetic fields in the course of stellar evolution (Spruit, 2002; Fuller et al., 2019), but it does at least provide a very simple mechanism for compact remnants to end up with strong magnetic fields.

Chapter 9

Conclusion & Outlook

9.1 Key Conclusions

While a century of research has produced well-established descriptions of the evolution of massive stars, many important questions remain unsolved. The research in this thesis used a variety of techniques to model the structure and evolution of massive stars, with the goal of making progress towards answering these questions. We touched on a range of topics including the key evolutionary sequences for massive stars as a function of mass and metallicity, the structural differences between blue and red supergiants, the impact of binary interaction, the formation channels for binary black holes detectable by LIGO/Virgo and the magnetic field strengths in stellar interiors. In addition to using stellar evolution models and models of binary interaction, both widely-used modelling techniques, we found it useful to develop a new stellar modelling approach that we called SNAPSHOT. The SNAPSHOT approach allows us to systematically isolate the impact of different properties of the internal abundance profiles on the surface properties, L and T_{eff}. It involves computing grids of numerical stellar structure models in hydrostatic and thermal equilibrium covering key phases of stellar evolution, varying one property of the internal abundance profile at a time.

In our first investigation, we systematically computed SNAPSHOT stellar structure models in hydrostatic and thermal equilibrium based on 3 structural properties – the core mass M_{core}, the envelope mass M_{env} and the core composition. Models with $M_{\mathrm{core}}/M_{\mathrm{total}}$ from 0.2 to 0.8 have convective envelopes, low T_{eff} and will appear as red supergiants. For a given M_{core}, they exhibit a small variation in luminosity (0.02 dex) and T_{eff} ($\sim 400\,\mathrm{K}$) over a wide range of M_{env} ($\sim 2-20\,\mathrm{M}_{\odot}$). At $M_{\mathrm{core}}/M_{\mathrm{total}} \approx 0.2$, our models exhibit a bistability and jump from a RSG to a BSG structure. Our models with $M_{\mathrm{core}}/M_{\mathrm{total}} > 0.8$, which correspond to stripped stars produced by mass loss or binary interaction, show that T_{eff} has a strong dependence on M_{env}, M_{core} and the core composition. Secondly, we used the SNAPSHOT approach to investigate the relationship between the surface properties and the mass of red supergiants at the pre-supernova stage. Our models indicate that it is not possible to determine the final mass M_{fin} of a red supergiant (RSG) at the pre-supernova

(SN) stage from its luminosity L and effective temperature T_{eff} alone. We found that for a given value of L and T_{eff}, a RSG can have a range of M_{fin} as wide as 3 to 45 $\text{M}_{\odot}$. While the probability distribution within these limits is not flat, any individual determination of M_{fin} for a RSG will be degenerate. However, the final Helium core mass $M_{\text{He-core}}$ is well determined by the final luminosity and we find $\log(M_{\text{He-core}}/\text{M}_{\odot}) = 0.659 \log(L/\text{L}_{\odot}) - 2.630$. Using this relationship, we derived $M_{\text{He-core}}$ for directly imaged SN progenitors and one failed SN candidate. Given the initial mass function, our results apply to the majority of progenitors of core collapse SNe, failed SNe and direct collapse black holes. Finally, we used the SNAPSHOT approach along with a series of numerical experiments to help understand cause and effect in massive star evolution. For the main sequence, we demonstrated that models with the same mass and very similar surface properties can have different internal distributions of hydrogen and convective core masses. We discussed why massive stars expand after the main sequence and the fundamental reasons for why they become red, blue or yellow supergiants. For the post-main sequence, we demonstrated that small changes in the abundance profile can cause very large effects on the surface properties.

A key recent development in the understanding of the evolution of massive stars is the observation of black holes using gravitational waves by the LIGO Virgo Collaboration. The properties of the black holes left behind by massive stars are useful observational constraints for the late evolutionary stages. For instance, the binary black hole merger GW190521 reported by the LIGO VIRGO Collaboration contains unexpectedly high component masses of 85 and 66 $\text{M}_{\odot}$. We investigated the possibility that stars at low or zero metallicity could retain most of their hydrogen envelope until the pre-supernova stage, avoid the pulsational pair-instability regime and produce a black hole with a mass in the mass gap by fallback. We discussed the fact models with a metallicity in the range 0 – 0.0004 could favour higher black hole masses due to (i) lower mass-loss rates during the post-MS phase, (ii) a more compact star disfavouring binary interaction and (iii) possible H-He shell interactions which lower the CO core mass. We conclude that it is possible that GW190521 may be the merger of black holes produced directly by massive stars from the first stellar generations.

A large fraction of massive stars evolve in interacting binary systems, which dramatically modifies the outcome of stellar evolution. We investigated the properties of blue supergiants in binary systems and whether they are suitable for extragalactic distance determinations using the flux-weighted gravity luminosity relationship (FGLR). We computed a grid of binary stellar evolution models with MESA and found that the majority of primary stars that produce blue supergiant stages are consistent with the observed FGLR, with a small offset towards brighter bolometric magnitudes. A very small number of such stars have been found in extragalactic FGLR studies, suggesting that they may have evolved through binary interaction. Some models with shorter periods could resemble blue hypergiants and luminous blue variables.

Our previous investigations neglected the effects of magnetic fields due to the limited observational evidence of the properties of magnetic fields in massive stars. However, the situation is different for low mass AB stars, where there is a lot more data. Therefore, we investigated the initial distribution of magnetic field strengths in AB stars. We combined observations with theoretical models of magnetic field evolution to infer the initial distribution of magnetic fields for AB stars in the mass range $1.6-3.4M_{\odot}$. We find that a distribution with a mean of ~ 800 G and a full-width of ~ 600 G is most consistent with the observed fraction of strongly magnetized stars as a function of mass. Our most-favoured distribution is a Gaussian with a mean $\mu = 770\,\mathrm{G}$ and standard deviation $\sigma = 146\,\mathrm{G}$. Evolution of this magnetic field distribution under the assumption of flux-freezing, results in field strengths of $10^6\,\mathrm{G}$ in White Dwarfs and $10^{15}\,\mathrm{G}$ in Neutron Stars, in broad agreement with the observations.

9.2 Possible Future Directions

9.2.1 Pre-Supernova Models

The SNAPSHOT method can be applied to explore a range of further questions in stellar astrophysics. For instance, evolving a large grid of SNAPSHOT models to the pre-supernova stage and using 1-D explosion models would allow us to systematically study the appearance of supernovae as a function of the internal structure at the moment of core collapse. This type of investigation is usually done with single and binary stellar evolution models (e.g. Müller et al., 2016; Woosley, 2017; Sukhbold et al., 2018; Chieffi & Limongi, 2020). For example, Yoon et al. (2017) modelled the properties of Type Ib and IIb SN progenitors that are produced by stable mass transfer in binary systems (Fig. 73) and connected the progenitor appearance, final envelope masses and evolutionary histories. The advantage of the SNAPSHOT method is that it would allow a much greater diversity of stellar structures at the pre-supernova stage than with stellar evolution models. In Farrell et al. (2020a), we explored the connections between a given location in the HR diagram with one or more internal structure models based on variations in the core and envelope mass. Stellar interiors are, of course, quite complex and a range of other properties of the internal abundance profile could also be studied in a similar way. For instance, the impact of internal properties such as the mass of the inert helium shell, the properties of the hydrogen burning shell (in blue supergiants) or the mass fraction of the CO core are unknown. An extension of the work done in Farrell et al. (2020a) could investigate how these properties affect L and T_{eff} at the pre-supernova stage. This would allow a more detailed exploration of the degeneracy between internal and surface properties at the pre-supernova stage. It may also provide new information to interpret images of progenitors of core-collapse supernovae.

On top of the surface appearance at the pre-supernova stage, the outcome of the explosion following core collapse and the photometric and spectroscopic evolution of the supernova can also be modelled using 1-D explosion models (e.g. Goldberg et al., 2019; Ertl et al., 2020). A large diversity of stellar structures provided in a systematic way by the SNAPSHOT models may shed new light on our understanding of the interpretation of a wide range of transient phenomena. This is especially useful given the ongoing and future large scale transient surveys, which provide another useful way to understand and constrain the behaviour of massive stars. Along this line of study, the SNAPSHOT approach could also be useful to study the mass function of compact remnants and the boundaries between white dwarfs and neutron stars, and neutron stars and black holes.

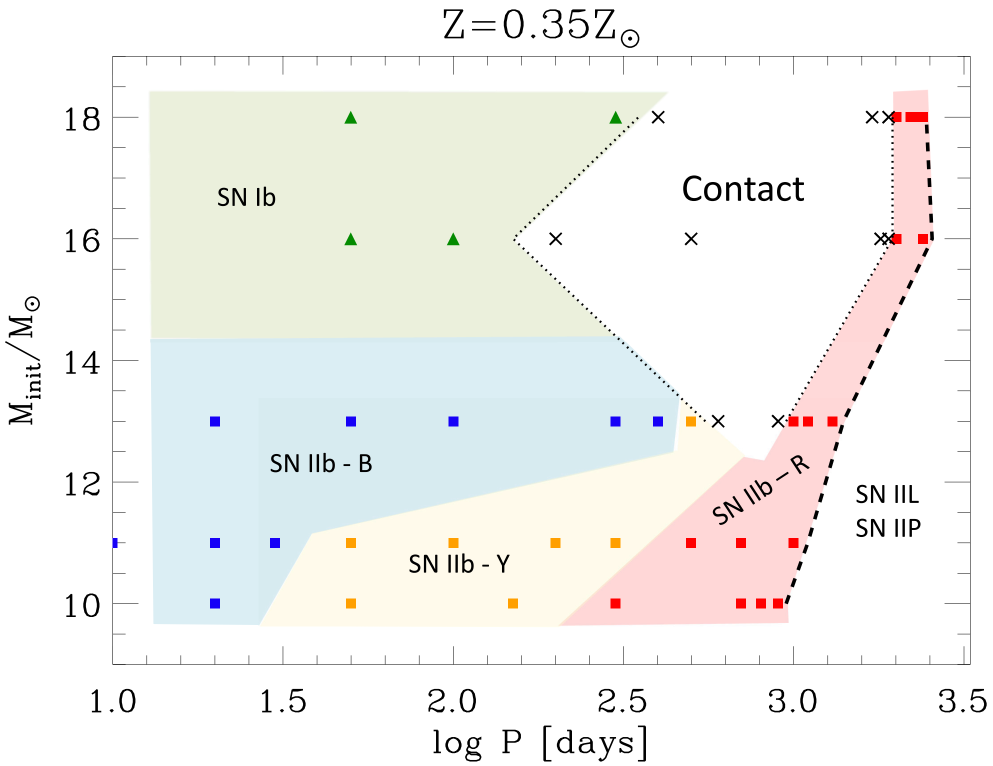

Figure 73: Predicted final fates of the primary stars for different initial masses and orbital periods at LMC metallicity from Yoon et al. (2017). Triangle and square symbols denote SN Ib and SN IIb, respectively. Blue, orange, and red squares indicate the colour of the SN IIb progenitors. Sequences where the binary system becomes a contact binary are marked by a black cross.

9.2.2 Black Holes Masses

Further detections of neutron stars and black holes are expected by the LIGO Virgo Collaboration. The recently launched James Webb Space Telescope will also provide a range of new observational constraints on the first stellar generations. Future observations of binary black hole and neutron star mergers will likely shed further light on the existence of a pair-instability mass gap, although the latest results from The LIGO Scientific Collaboration et al. (2021d) suggest the possibility that this mass gap may not exist as expected. Furthermore, the distribution of black hole masses and spins may help to distinguish between two possible origins: isolated evolution in a binary or multiple star system and growth of black hole masses by dynamical captures in dense stellar systems like globular clusters. A more complete understanding of the impact of binary interaction will also be necessary to fully piece together the wide range of evolutionary pathways that massive stars can take.

However, even in single star evolution, unknowns regarding convection, rotation and mass loss may have significant impacts on the stellar population synthesis models that are used to interpret black holes masses detected by LIGO/Virgo. In Farrell et al. (2021b), we performed a simple, exploratory investigation into whether the existence of an 85 $M_\odot$ black hole could plausibly be explained by stellar evolution models within the typical uncertainties of massive star evolution. Many other works have performed more a detailed analysis on the expected black hole masses (e.g. Belczynski et al., 2016; Woosley, 2017, 2019; Marchant et al., 2019; Stevenson et al., 2019; Farmer et al., 2019; Renzo et al., 2020a). Given that the observations detected by LIGO/Virgo are produced by a population of stars, it is common to use rapid population synthesis models to compare the observational constraints with theoretical expectations (e.g. Eldridge et al., 2017; Stevenson et al., 2019; van Son et al., 2020; Mapelli et al., 2020; Broekgaarden et al., 2021; Belczynski et al., 2022). Most of these models rely on prescriptions from Hurley et al. (2000) for the rapid stellar evolution calculations and from Hurley et al. (2002) for the rapid binary interaction calculations. These prescriptions have served as a useful way to quickly generate population models to compare to observations. A useful new project would be to investigate the impact of convection, rotation and mass loss on the expected final black hole mass distributions from the population synthesis models. This would allow a more complete interpretation of the latest results from The LIGO Scientific Collaboration et al. (2021d), taking the detailed evolutionary effects into account.

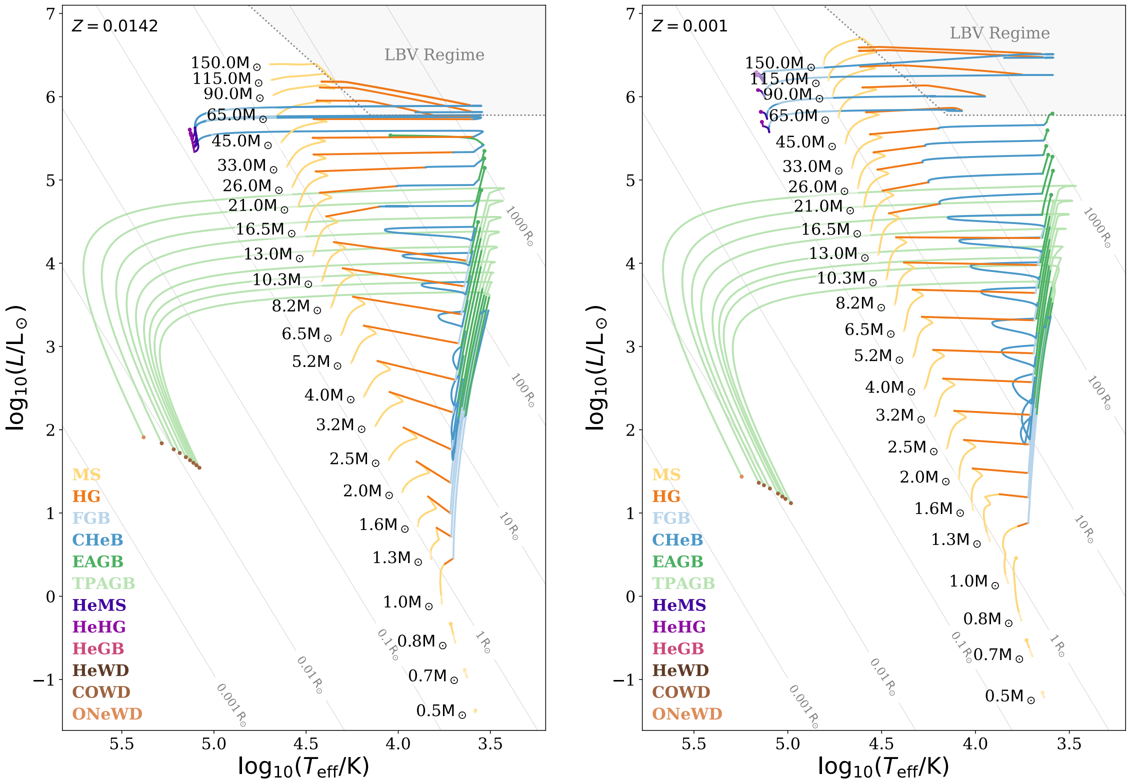

Figure 74: Evolutionary tracks in the Hertzsprung–Russell diagrams for single stars from Team COMPAS: J. Riley et al. (2022) with ZAMS masses between 0.5 and 150 $M_\odot$ at solar ($Z = 0.0142$) and low ($Z = 0.001$) metallicity using COMPAS default settings based on prescriptions from Hurley et al. (2000).

Bibliography

Abbott D. C., 1982, ApJ, 259, 282

Abbott D. C., Conti P. S., 1987, ARA&A, 25, 113

Abbott B. P., et al., 2009, Reports on Progress in Physics, 72, 076901

Abbott B. P., et al., 2016a, Physical Review X, 6, 041015

Abbott B. P., et al., 2016b, Phys. Rev. Lett., 116, 061102

Abbott B. P., et al., 2016c, Phys. Rev. Lett., 116, 221101

Abbott B. P., et al., 2016d, ApJ, 818, L22

Abbott B. P., et al., 2017a, Phys. Rev. Lett., 119, 161101

Abbott B. P., et al., 2017b, Nature, 551, 85

Abbott B. P., et al., 2017c, ApJ, 848, L12

Abbott B. P., et al., 2017d, ApJ, 848, L13

Abbott B. P., et al., 2018, Phys. Rev. Lett., 121, 161101

Abbott B. P., et al., 2019, Physical Review X, 9, 031040

Abbott B. P., et al., 2020a, Classical and Quantum Gravity, 37, 045006

Abbott R., et al., 2020b, Phys. Rev. Lett., 125, 101102

Abbott B. P., et al., 2020c, ApJ, 892, L3

Abbott R., et al., 2020d, ApJ, 900, L13

Abdul-Masih M., et al., 2019, ApJ, 880, 115

Abdul-Masih M., et al., 2021, A&A, 651, A96

Abramovici A., et al., 1992, Science, 256, 325

Adams S. M., et al., 2013, ApJ, 778, 164

Adams S. M., et al., 2017a, MNRAS, 468, 4968

Adams S. M., Kochanek C. S., Gerke J. R., Stanek K. Z., 2017b, MNRAS, 469, 1445

Aerts C., et al., 2019, A&A, 624, A75

Aghakhanloo M., Murphy J. W., Smith N., Hložek R., 2017, MNRAS, 472, 591

Agliozzo C., et al., 2019, A&A, 626, A126

Agliozzo C., et al., 2021, A&A, 655, A98

Agrawal P., Szécsi D., Stevenson S., Hurley J., 2021a, arXiv e-prints, 0, arXiv:2112.02800

Agrawal P., Stevenson S., Szécsi D., Hurley J., 2021b, arXiv e-prints, 0, arXiv:2112.02801

Aguilera-Dena D. R., Langer N., Moriya T. J., Schootemeijer A., 2018, ApJ, 858, 115

Aguilera E. F., et al., 2006, Phys. Rev. C, 73, 064601

Akmal A., Pandharipande V. R., Ravenhall D. G., 1998, Phys. Rev. C, 58, 1804

Aldering G., Humphreys R. M., Richmond M., 1994, AJ, 107, 662

Allan A. P., et al., 2020, MNRAS, 496, 1902

Almeida L. A., et al., 2017, A&A, 598, A84

Alongi M., Bertelli G., Bressan A., Chiosi C., 1991, A&A, 244, 95

Alongi M., et al., 1993, A&AS, 97, 851

An Z.-D., et al., 2015, Phys. Rev. C, 92, 045802

An F., et al., 2016, Journal of Physics G Nuclear Physics, 43, 030401

Applegate J. H., 1988, ApJ, 329, 803

Arnett W. D., 1978, ApJ, 219, 1008

Arnett W. D., Bahcall J. N., Kirshner R. P., Woosley S. E., 1989, ARA&A, 27, 629

Arnett W. D., et al., 2018, arXiv e-prints, 0, arXiv:1810.04659

Arnett W. D., et al., 2019, ApJ, 882, 18

Atkinson R. D. E., Houtermans F. G., 1929, Zeitschrift fur Physik, 54, 656

Aurière M., et al., 2007, A&A, 475, 1053

Baade W., Zwicky F., 1934, Physical Review, 46, 76

Bailey J. E., et al., 2015, Nature, 517, 56

Ball W. H., Tout C. A., Żytkow A. N., 2012, MNRAS, 421, 2713

Barrón-Palos L., et al., 2006, Nucl. Phys. A, 779, 318

Beals C. S., 1929, MNRAS, 90, 202

Beasor E. R., Davies B., Smith N., Bastian N., 2019, MNRAS, 486, 266

Beasor E. R., et al., 2020, MNRAS, 492, 5994

Becker G. D., Bolton J. S., 2013, MNRAS, 436, 1023

Becker H. W., Kettner K. U., Rolfs C., Trautvetter H. P., 1981, Zeitschrift fur Physik A Hadrons and Nuclei, 303, 305

Belczynski K., 2020, ApJ, 905, L15

Belczynski K., Kalogera V., Bulik T., 2002, ApJ, 572, 407

Belczynski K., et al., 2008, ApJS, 174, 223

Belczynski K., et al., 2016, A&A, 594, A97

Belczynski K., et al., 2017, MNRAS, 471, 4702

Belczynski K., et al., 2022, ApJ, 925, 69

Bertelli G., Nasi E., Girardi L., Marigo P., 2009, A&A, 508, 355

Bessel F. W., 1838, Astronomische Nachrichten, 16, 65

Bestenlehner J. M., 2020, MNRAS, 493, 3938

Bestenlehner J. M., et al., 2014, A&A, 570, A38

Bestenlehner J. M., et al., 2021, arXiv e-prints, 0, arXiv:2112.00022

Bethe H. A., 1939, Physical Review, 55, 434

Bethe H. A., Critchfield C. L., 1938, Physical Review, 54, 248

Björklund R., Sundqvist J. O., Puls J., Najarro F., 2021, A&A, 648, A36

Blanchard P. K., et al., 2021, ApJ, 921, 64

Böhm-Vitense E., 1958, ZAp, 46, 108

Boian I., Groh J. H., 2018, A&A, 617, A115

Bolton C. T., 1972, Nature, 235, 271

Bono G., Caputo F., Castellani V., 2006, Mem. Soc. Astron. Italiana, 77, 207

Boothroyd A. I., Sackmann I. J., 1988, ApJ, 328, 653

Boruta N., 1996, ApJ, 458, 832

Bouret J. C., et al., 2013, A&A, 555, A1

Bouvier J., et al., 2007, A&A, 463, 1017

Braun H., Langer N., 1995, A&A, 297, 483

Bresolin F., et al., 2016, ApJ, 830, 64

Britavskiy N., et al., 2019, A&A, 624, A128

Broekgaarden F. S., et al., 2021, arXiv e-prints, p. arXiv:2112.05763

Brott I., et al., 2011a, A&A, 530, A115

Brott I., et al., 2011b, A&A, 530, A116

Brown G. E., et al., 2001, New A, 6, 457

Bucher B., et al., 2015, Phys. Rev. Lett., 114, 251102

Buchler J. R., Yueh W. R., 1976, ApJ, 210, 440

Buemi C. S., et al., 2017, MNRAS, 465, 4147

Buldgen G., Reese D. R., Dupret M. A., 2015, A&A, 583, A62

Burbidge E. M., Burbidge G. R., Fowler W. A., Hoyle F., 1957, Reviews of Modern Physics, 29, 547

Cameron A. G. W., 1957, PASP, 69, 201

Cannon A. J., Pickering E. C., 1901, Annals of Harvard College Observatory, 28, 129

Cantiello M., Braithwaite J., 2011, A&A, 534, A140

Cantiello M., Braithwaite J., 2019, ApJ, 883, 106

Cantiello M., Langer N., 2010, A&A, 521, A9

Cantiello M., Yoon S. C., Langer N., Livio M., 2007, A&A, 465, L29

Carson T. R., 1976, ARA&A, 14, 95

Cassisi S., et al., 2007, ApJ, 661, 1094

Castor J. I., Abbott D. C., Klein R. I., 1975, ApJ, 195, 157

Castro N., et al., 2014, A&A, 570, L13

Castro N., Oey M. S., Fossati L., Langer N., 2018, ApJ, 868, 57

Chabrier G., 2003, PASP, 115, 763

Charbonnel C., Zahn J. P., 2007, A&A, 467, L15

Chatzopoulos E., Wheeler J. C., 2012, ApJ, 760, 154

Chatzopoulos E., Wheeler J. C., Couch S. M., 2013, ApJ, 776, 129

Chen K.-J., et al., 2014, ApJ, 792, 28

Chevalier R. A., Fransson C., 2006, ApJ, 651, 381

Chevalier R. A., Irwin C. M., 2011, ApJ, 729, L6

Chiappini C., et al., 2011, Nature, 474, 666

Chieffi A., Limongi M., 2004, ApJ, 608, 405

Chieffi A., Limongi M., 2013b, ApJ, 764, 21

Chieffi A., Limongi M., 2013a, ApJ, 764, 21

Chieffi A., Limongi M., 2020, ApJ, 890, 43

Chieffi A., et al., 2021, ApJ, 916, 79

Chin C.-W., Stothers R. B., 1990, ApJS, 73, 821

Chini R., et al., 2012, MNRAS, 424, 1925

Chiosi C., 1986, Progress in Particle and Nuclear Physics, 17, 173

Chiosi C., Nasi E., 1974, A&A, 35, 81

Chiosi C., Nasi E., Sreenivasan S. R., 1978, A&A, 63, 103

Choi J., et al., 2016, ApJ, 823, 102

Chojnowski S. D., et al., 2018, ApJ, 865, 76

Chomiuk L., et al., 2011, ApJ, 743, 114

Christy R. F., 1966, ARA&A, 4, 353

Christy R. F., 1968, QJRAS, 9, 13

Chugunov A. I., Dewitt H. E., Yakovlev D. G., 2007, Phys. Rev. D, 76, 025028

Chun S.-H., et al., 2018, ApJ, 853, 79

Clark J. S., Larionov V. M., Arkharov A., 2005, A&A, 435, 239

Clarkson O., Herwig F., 2020, arXiv e-prints, 0, arXiv:2005.07748

Conroy C., van Dokkum P. G., 2012, ApJ, 760, 71

Conti P. S., 1975, Memoires of the Societe Royale des Sciences de Liege, 9, 193

Conti P. S., 1997. p. 387

Conti P. S., Dupre D. R., Massey P., Rensing M., 1984, ApJ, 282, 693

Cowling T. G., 1935, MNRAS, 96, 42

Cowling T. G., 1953, in Kuiper G. P., ed., , The Sun. p. 532

Cox J. P., Giuli R. T., 1961, ApJ, 133, 755

Cox J. P., Giuli R. T., 1968, Principles of stellar structure

Cranmer S. R., Saar S. H., 2011, ApJ, 741, 54

Cristini A., et al., 2017, MNRAS, 471, 279

Cristini A., et al., 2019, MNRAS, 484, 4645

Croon D., McDermott S. D., Sakstein J., 2020, arXiv e-prints, 0, arXiv:2007.07889

Cucchiara A., et al., 2011, ApJ, 743, 154

Cyburt R. H., et al., 2010, ApJS, 189, 240

Davidson K., Humphreys R. M., 1997, ARA&A, 35, 1

Davies B., 2017, Philosophical Transactions of the Royal Society of London Series A, 375, 20160270

Davies B., Beasor E. R., 2018, MNRAS, 474, 2116

Davies B., Plez B., 2021, MNRAS, 508, 5757

Davies B., Oudmaijer R. D., Vink J. S., 2005, A&A, 439, 1107

Davies B., et al., 2007, ApJ, 671, 781

Davies B., et al., 2008, ApJ, 676, 1016

Davies B., Kudritzki R.-P., Figer D. F., 2010, MNRAS, 407, 1203

De Loore C., De Greve J. P., Lamers H. J. G. L. M., 1977, A&A, 61, 251

De Luca V., et al., 2021, Phys. Rev. Lett., 126, 051101

Decin L., et al., 2011, A&A, 534, A1

Decressin T., et al., 2009, A&A, 505, 727

Dessart L., Hillier D. J., 2011, MNRAS, 415, 3497

Dessart L., Hillier D. J., 2019, A&A, 625, A9

Dessart L., Hillier D. J., Waldman R., Livne E., 2013, MNRAS, 433, 1745

Deutsch A. J., 1956, ApJ, 123, 210

Di Carlo U. N., et al., 2019, MNRAS, 487, 2947

Doherty C. L., Gil-Pons P., Siess L., Lattanzio J. C., 2017, PASA, 34, e056

Donati J. F., Landstreet J. D., 2009, ARA&A, 47, 333

Dorda R., Patrick L. R., 2021, MNRAS, 502, 4890

Downing J. M. B., Benacquista M. J., Giersz M., Spurzem R., 2010, MNRAS, 407, 1946

Drout M. R., et al., 2009, ApJ, 703, 441

Drout M. R., Massey P., Meynet G., 2012, ApJ, 750, 97

Dufton P. L., et al., 2019, A&A, 626, A50

Duncan R. C., Thompson C., 1992, ApJ, 392, L9

Dunstall P. R., et al., 2015, A&A, 580, A93

Eddington A. S., 1920, Nature, 106, 14

Eddington A. S., 1924, Nature, 113, 786

Eddington A. S., 1926, The Internal Constitution of the Stars

Eddington A. S., 1959, The internal constitution of the stars

Eggenberger P., Meynet G., Maeder A., 2002, A&A, 386, 576

Eggenberger P., et al., 2017, A&A, 599, A18

Eggleton P. P., 1983, ApJ, 268, 368

Eggleton P., 2006, Evolutionary Processes in Binary and Multiple Stars

Eggleton P. P., Cannon R. C., 1991, ApJ, 383, 757

Eggleton P. P., Tout C. A., 1989, Space Sci. Rev., 50, 165

Eggleton P. P., Faulkner J., Iben I. J., Renzini A., 1981, Why do stars become red giants. Physical processes in red giants; Proceedings of the Second Workshop, pp 179–182, doi:10.1007/978-94-009-8492-9˙18

Eggleton P. P., Fitchett M. J., Tout C. A., 1989, ApJ, 347, 998

Eggleton P. P., Faulkner J., Cannon R. C., 1998, MNRAS, 298, 831

Eichler D., Livio M., Piran T., Schramm D. N., 1989, Nature, 340, 126

Einstein A., 1916, Sitzungsberichte der Königlich Preußischen Akademie der Wissenschaften (Berlin, 0, 688

Einstein A., 1918, Sitzungsberichte der Königlich Preußischen Akademie der Wissenschaften (Berlin, 0, 154

Ekström S., et al., 2008, A&A, 489, 685

Ekström S., et al., 2012, A&A, 537, A146

Eldridge J. J., Stanway E. R., 2009, MNRAS, 400, 1019

Eldridge J. J., Xiao L., 2019, MNRAS, 485, L58

Eldridge J. J., Mattila S., Smartt S. J., 2007, MNRAS, 376, L52

Eldridge J. J., Izzard R. G., Tout C. A., 2008, MNRAS, 384, 1109

Eldridge J. J., et al., 2013, MNRAS, 436, 774

Eldridge J. J., et al., 2017, PASA, 34, e058

Eldridge J. J., et al., 2018, PASA, 35, e049

Eldridge J. J., et al., 2019, PASA, 36, e041

Elmegreen B. G., 2011, ApJ, 731, 61

Emden R., 1907, Gaskugeln

Emden R., 1927, Naturwissenschaften, 15, 769

Ertl T., Woosley S. E., Sukhbold T., Janka H. T., 2020, ApJ, 890, 51

Farmer R., et al., 2019, ApJ, 887, 53

Farmer R., et al., 2020, ApJ, 902, L36

Farr W. M., Fishbach M., Ye J., Holz D. E., 2019, ApJ, 883, L42

Farrell E. J., Groh J. H., Meynet G., Eldridge J. J., 2020a, MNRAS, 494, L53

Farrell E. J., et al., 2020b, MNRAS, 495, 4659

Farrell E., Groh J., Meynet G., Eldridge J., 2021a, arXiv e-prints, 0, arXiv:2109.02488

Farrell E., et al., 2021b, MNRAS, 502, L40

Faucher-Giguère C.-A., Lidz A., Hernquist L., Zaldarriaga M., 2008, ApJ, 688, 85

Faucher-Giguère C.-A., Lidz A., Zaldarriaga M., Hernquist L., 2009, ApJ, 703, 1416

Ferguson J. W., et al., 2005, ApJ, 623, 585

Ferrario L., Pringle J. E., Tout C. A., Wickramasinghe D. T., 2009, MNRAS, 400, L71

Fields C. E., et al., 2016, ApJ, 823, 46

Filippenko A. V., 1997, ARA&A, 35, 309

Fishbach M., Holz D. E., 2020, ApJ, 904, L26

Fishbach M., Holz D. E., Farr B., 2017, ApJ, 840, L24

Forbes J. E., 1968, ApJ, 153, 495

Fossati L., et al., 2015, A&A, 582, A45

Fowler W. A., Hoyle F., 1964, ApJS, 9, 201

Fragione G., Loeb A., Rasio F. A., 2020, ApJ, 902, L26

Fraser M., 2016, MNRAS, 456, L16

Fraser M., et al., 2011, MNRAS, 417, 1417

Fraser M., et al., 2013, ApJ, 779, L8

Freedman W. L., et al., 2001, ApJ, 553, 47

Fricke K., Stobie R. S., Strittmatter P. A., 1971, MNRAS, 154, 23

Friedland A., Gruzinov A., 2004, ApJ, 601, 570

Friščić I., Donnelly T. W., Milner R. G., 2019, Phys. Rev. C, 100, 025804

Fryer C. L., Woosley S. E., Heger A., 2001, ApJ, 550, 372

Fuller J., 2017, MNRAS, 470, 1642

Fuller G. M., Fowler W. A., Newman M. J., 1985, ApJ, 293, 1

Fuller J., et al., 2015, Science, 350, 423

Fuller J., Piro A. L., Jermyn A. S., 2019, MNRAS, 485, 3661

Gagnier D., et al., 2019a, A&A, 625, A88

Gagnier D., et al., 2019b, A&A, 625, A89

Gal-Yam A., 2012, Science, 337, 927

Gal-Yam A., et al., 2009, Nature, 462, 624

Gal-Yam A., et al., 2014, Nature, 509, 471

Gamow G., 1938, Physical Review, 53, 595

Gamow G., 1939a, Physical Review, 55, 718

Gamow G., 1939b, Physical Review, 55, 796

Gamow G., Schoenberg M., 1941, Physical Review, 59, 539

Garmany C. D., Conti P. S., Massey P., 1980, ApJ, 242, 1063

Gautschy A., Saio H., 1995, ARA&A, 33, 75

Gautschy A., Saio H., 1996, ARA&A, 34, 551

Gayathri V., et al., 2020, arXiv e-prints, 0, arXiv:2009.05461

Georgy C., 2012, A&A, 538, L8

Georgy C., et al., 2012, A&A, 542, A29

Georgy C., et al., 2013, A&A, 558, A103

Georgy C., Saio H., Meynet G., 2014a, MNRAS, 439, L6

Georgy C., et al., 2014b, A&A, 566, A21

Georgy C., Saio H., Meynet G., 2021, A&A, 650, A128

Gerosa D., Berti E., 2017, Phys. Rev. D, 95, 124046

Giacobbo N., Mapelli M., Spera M., 2018, MNRAS, 474, 2959

Giannone P., Weigert A., 1967, ZAp, 67, 41

Giannone P., Kohl K., Weigert A., 1968, ZAp, 68, 107

Gies D. R., et al., 1998, ApJ, 493, 440

Gilkis A., et al., 2021, MNRAS, 503, 1884

Glatzel W., Fricke K. J., El Eid M. F., 1985, A&A, 149, 413

Glebbeek E., Gaburov E., Portegies Zwart S., Pols O. R., 2013, MNRAS, 434, 3497

Goldberg J. A., Bildsten L., Paxton B., 2019, ApJ, 879, 3

Goldberg J. A., Jiang Y.-F., Bildsten L., 2021, arXiv e-prints, 0, arXiv:2110.03261

Goldreich P., Julian W. H., 1969, ApJ, 157, 869

Goldstein A., et al., 2017, ApJ, 848, L14

González-Gaitán S., et al., 2015, MNRAS, 451, 2212

González-Torà G., Davies B., Kudritzki R.-P., Plez B., 2021, arXiv e-prints, 0, arXiv:2106.01807

Gordon M. S., Humphreys R. M., Jones T. J., 2016, ApJ, 825, 50

Götberg Y., de Mink S. E., Groh J. H., 2017, A&A, 608, A11

Götberg Y., et al., 2018, A&A, 615, A78

Götberg Y., et al., 2020, A&A, 634, A134

Gough D. O., Tayler R. J., 1966, MNRAS, 133, 85

Goupil M., et al., 2013, Studying Stellar Rotation and Convection

Gräfener G., Hamann W. R., 2008, A&A, 482, 945

Gräfener G., Vink J. S., de Koter A., Langer N., 2011, A&A, 535, A56

Gräfener G., Owocki S. P., Vink J. S., 2012, A&A, 538, A40

Grevesse N., Sauval A. J., 1998, Space Sci. Rev., 85, 161

Groh J. H., 2014, A&A, 572, L11

Groh J. H., Oliveira A. S., Steiner J. E., 2008, A&A, 485, 245

Groh J. H., Hillier D. J., Damineli A., 2011, ApJ, 736, 46

Groh J. H., Meynet G., Ekström S., 2013a, A&A, 550, L7

Groh J. H., Georgy C., Ekström S., 2013b, A&A, 558, L1

Groh J. H., Meynet G., Georgy C., Ekström S., 2013c, A&A, 558, A131

Groh J. H., Meynet G., Ekström S., Georgy C., 2014, A&A, 564, A30

Groh J. H., et al., 2019, A&A, 627, A24

Groh J. H., et al., 2020, ApJ, 900, 98

Grunhut J. H., et al., 2013, MNRAS, 428, 1686

Grunhut J. H., et al., 2017, MNRAS, 465, 2432

Gvaramadze V. V., Langer N., Mackey J., 2012, MNRAS, 427, L50

Haehnelt M. G., Madau P., Kudritzki R., Haardt F., 2001, ApJ, 549, L151

Hagen Bauer W., Bennett P. D., 2014, ApJS, 211, 27

Haiman Z., Loeb A., 1997, ApJ, 483, 21

Hainich R., et al., 2015, A&A, 581, A21

Hammache F., et al., 2016. p. 012007, doi:10.1088/1742-6596/665/1/012007

Hammer J. W., et al., 2005, Nucl. Phys. A, 752, 514

Härm R., Schwarzschild M., 1955, ApJ, 121, 445

Harper G. M., Griffin R. E. M., Bennett P. D., O'Riain N., 2016, MNRAS, 456, 1346

Harrington P. Z., Garaud P., 2019, ApJ, 870, L5

Hawcroft C., et al., 2021, A&A, 655, A67

Hawking S., 1971, MNRAS, 152, 75

Hayashi C., Cameron R. C., 1962, ApJ, 136, 166

Hayashi C., Jugaku J., Nishida M., 1959, Progress of Theoretical Physics, 22, 531

Hayashi C., Hōshi R., Sugimoto D., 1962, Progress of Theoretical Physics Supplement, 22, 1

Heger A., Langer N., 2000, ApJ, 544, 1016

Heger A., Woosley S. E., 2002, ApJ, 567, 532

Heger A., Langer N., Woosley S. E., 2000, ApJ, 528, 368

Heger A., et al., 2003, ApJ, 591, 288

Heger A., Woosley S. E., Spruit H. C., 2005, ApJ, 626, 350

Heine M., et al., 2018, Nuclear Instruments and Methods in Physics Research A, 903, 1

Hellings P., 1983, Ap&SS, 96, 37

Hellings P., 1984, Ap&SS, 104, 83

Henyey L. G., Lelevier R., Levée R. D., 1955, PASP, 67, 154

Henyey L. G., Lelevier R., Levee R. D., 1959a, ApJ, 129, 2

Henyey L. G., et al., 1959b, ApJ, 129, 628

Henyey L. G., Forbes J. E., Gould N. L., 1964, ApJ, 139, 306

Henyey L., Vardya M. S., Bodenheimer P., 1965, ApJ, 142, 841

Hertzsprung E., 1905, Zeitschrift Fur Wissenschaftliche Photographie, 3, 442

Hertzsprung E., 1907, Zeitschrift Fur Wissenschaftliche Photographie, 5, 86

Hertzsprung E., 1911, Publikationen des Astrophysikalischen Observatoriums zu Potsdam, 63

Herwig F., 2000, A&A, 360, 952

Herwig F., Bloecker T., Schoenberner D., El Eid M., 1997, A&A, 324, L81

Higgins E. R., Vink J. S., 2019, A&A, 622, A50

Higgins E. R., Sander A. A. C., Vink J. S., Hirschi R., 2021, MNRAS, 505, 4874

High M. D., Čujec B., 1977, Nucl. Phys. A, 282, 181

Hillier D. J., Dessart L., 2019, A&A, 631, A8

Hillier D. J., Miller D. L., 1998, ApJ, 496, 407

Hiramatsu D., et al., 2021, ApJ, 913, 55

Hirata K., et al., 1987, Phys. Rev. Lett., 58, 1490

Hirschi R., Meynet G., Maeder A., 2004, A&A, 425, 649

Hofmeister E., Kippenhahn R., Weigert A., 1964, ZAp, 60, 57

Holgado G., et al., 2020, A&A, 638, A157

Holt R. J., Filippone B. W., Pieper S. C., 2018, arXiv e-prints, 0, arXiv:1809.10176

Holt R. J., Filippone B. W., Pieper S. C., 2019, Phys. Rev. C, 99, 055802

Holzwarth V., Jardine M., 2007, A&A, 463, 11

Hoppner W., Weigert A., 1973, A&A, 25, 99

Horst L., et al., 2021, A&A, 653, A55

Hosek Matthew W. J., et al., 2014, ApJ, 785, 151

Hoyle F., 1945, MNRAS, 105, 23

Hoyle F., 1954, ApJS, 1, 121

Hoyle F., Lyttleton R. A., 1942, MNRAS, 102, 177

Hoyle F., Schwarzschild M., 1955, ApJS, 2, 1

Huang W., Gies D. R., McSwain M. V., 2010, ApJ, 722, 605

Humphreys R. M., 1978, ApJS, 38, 309

Humphreys R. M., Davidson K., 1979, ApJ, 232, 409

Humphreys R. M., Davidson K., 1994, PASP, 106, 1025

Humphreys R. M., Helton L. A., Jones T. J., 2007, AJ, 133, 2716

Hunter I., et al., 2008a, A&A, 479, 541

Hunter I., et al., 2008b, ApJ, 676, L29

Hurley J. R., Pols O. R., Tout C. A., 2000, MNRAS, 315, 543

Hurley J. R., Tout C. A., Pols O. R., 2002, MNRAS, 329, 897

Iben I. J., 1974, ARA&A, 12, 215

Iben Icko J., 1993, ApJ, 415, 767

Iglesias C. A., Rogers F. J., 1993, ApJ, 412, 752

Iglesias C. A., Rogers F. J., 1996, ApJ, 464, 943

Irwin A. W., 2004, The FreeEOS Code for Calculating the Equation of State for Stellar Interiors

Itoh N., Hayashi H., Nishikawa A., Kohyama Y., 1996, ApJS, 102, 411

Izzard R. G., et al., 2006, A&A, 460, 565

Jeans J. H., 1925, MNRAS, 85, 914

Jermyn A. S., Cantiello M., 2020, ApJ, 900, 113

Jermyn A. S., Cantiello M., 2021, ApJ, 923, 104

Jermyn A. S., Anders E. H., Cantiello M., 2022, A Transparent Window into Early-Type Stellar Variability

Jiang Y.-F., et al., 2018, Nature, 561, 498

Johnson H. L., Hiltner W. A., 1956, ApJ, 123, 267

Johnson H. L., Mitchell R. I., 1958, ApJ, 128, 31

Justham S., Podsiadlowski P., Vink J. S., 2014, ApJ, 796, 121

Kaiser E. A., et al., 2020, MNRAS, 496, 1967

Kasen D., Bildsten L., 2010, ApJ, 717, 245

Kasen D., Woosley S. E., Heger A., 2011, ApJ, 734, 102

Kasliwal M. M., et al., 2011, ApJ, 730, 134

Kee N. D., et al., 2021, A&A, 646, A180

Keller S. C., 2008, ApJ, 677, 483

Keszthelyi Z., et al., 2019, MNRAS, 485, 5843

Keszthelyi Z., et al., 2020, MNRAS, 493, 518

Keszthelyi Z., et al., 2021, MNRAS, 504, 2474

Kienzle F., Burki G., Burnet M., Meynet G., 1998, A&A, 337, 779

Kiewe M., et al., 2012, ApJ, 744, 10

Kilpatrick C. D., et al., 2017, MNRAS, 465, 4650

Kinugawa T., Nakamura T., Nakano H., 2020, MNRAS, 498, 3946

Kinugawa T., Nakamura T., Nakano H., 2021, MNRAS, 501, L49

Kippenhahn R., Meyer-Hofmeister E., 1977, A&A, 54, 539

Kippenhahn R., Weigert A., 1967, ZAp, 65, 251

Kippenhahn R., Weigert A., 1990, Stellar Structure and Evolution. Springer

Klement R., et al., 2017, A&A, 601, A74

Klencki J., Nelemans G., Istrate A. G., Pols O., 2020, A&A, 638, A55

Klencki J., Nelemans G., Istrate A. G., Chruslinska M., 2021, A&A, 645, A54

Kobulnicky H. A., Fryer C. L., 2007, ApJ, 670, 747

Kobulnicky H. A., et al., 2014, ApJS, 213, 34

Kochanek C. S., 2011, ApJ, 743, 73

Köhler K., et al., 2015, A&A, 573, A71

Kolb U., Ritter H., 1990, A&A, 236, 385

Kosirev N. A., 1934, MNRAS, 94, 430

Kotak R., Vink J. S., 2006, A&A, 460, L5

Kozyreva A., Yoon S. C., Langer N., 2014, A&A, 566, A146

Kroupa P., 2001, MNRAS, 322, 231

Krtička J., Kubát J., 2006, A&A, 446, 1039

Krumholz M. R., 2015, The Formation of Very Massive Stars. p. 43, doi:10.1007/978-3-319-09596-7_3

Kudritzki R. P., et al., 1999, A&A, 350, 970

Kudritzki R. P., Bresolin F., Przybilla N., 2003, ApJ, 582, L83

Kudritzki R. P., Urbaneja M. A., Bresolin F., Przybilla N., 2008a, Physica Scripta Volume T, 133, 014039

Kudritzki R.-P., et al., 2008b, ApJ, 681, 269

Kudritzki R.-P., et al., 2012, ApJ, 747, 15

Kudritzki R.-P., et al., 2013, ApJ, 779, L20

Kudritzki R.-P., et al., 2014, ApJ, 788, 56

Kudritzki R. P., et al., 2016, ApJ, 829, 70

Kulkarni S. R., et al., 2007, Nature, 447, 458

Kushwaha R. S., 1957, ApJ, 125, 242

Lamers H. J. G. L. M., de Groot M. J. H., 1992, A&A, 257, 153

Landstreet J. D., Bagnulo S., 2019, A&A, 628, A1

Langanke K., Martínez-Pinedo G., 2000, Nuclear Physics A, 673, 481

Langer N., 1989, A&A, 210, 93

Langer N., 1991, A&A, 252, 669

Langer N., 1992, A&A, 265, L17

Langer N., 2012, ARA&A, 50, 107

Langer N., Maeder A., 1995, A&A, 295, 685

Langer N., Fricke K. J., Sugimoto D., 1983, A&A, 126, 207

Langer N., El Eid M. F., Fricke K. J., 1985, A&A, 145, 179

Langer N., El Eid M. F., Baraffe I., 1989, A&A, 224, L17

Laplace E., et al., 2020, A&A, 637, A6

Laplace E., et al., 2021, A&A, 656, A58

Lattimer J. M., 2012, Annual Review of Nuclear and Particle Science, 62, 485

Lattimer J. M., Prakash M., 2004, Science, 304, 536

Lauterborn D., Refsdal S., Weigert A., 1971a, A&A, 10, 97

Lauterborn D., Refsdal S., Roth M. L., 1971b, A&A, 13, 119

Leavitt H. S., 1908, Annals of Harvard College Observatory, 60, 87

Leavitt H. S., Pickering E. C., 1912, Harvard College Observatory Circular, 173, 1

Leung S.-C., Nomoto K., Blinnikov S., 2019, ApJ, 887, 72

Levesque E. M., et al., 2006, ApJ, 645, 1102

Levesque E. M., et al., 2012, ApJ, 751, 67

Li L.-X., Paczyński B., 1998, ApJ, 507, L59

Loeb A., Barkana R., 2001, ARA&A, 39, 19

Lovekin C. C., Guzik J. A., 2014, MNRAS, 445, 1766

Lucy L. B., Solomon P. M., 1970, ApJ, 159, 879

MacDonald J., Mullan D. J., 2009, ApJ, 700, 387

MacDonald J., Petit V., 2019, Monthly Notices of the Royal Astronomical Society, 487, 3904

MacMillan W. D., 1918, ApJ, 48, 35

Maeder A., 1974, A&A, 32, 177

Maeder A., 1975, A&A, 40, 303

Maeder A., 1976, A&A, 47, 389

Maeder A., 1980, A&A, 92, 101

Maeder A., 1981a, A&A, 99, 97

Maeder A., 1981b, A&A, 102, 401

Maeder A., 1985, A&A, 147, 300

Maeder A., 1987, A&A, 178, 159

Maeder A., 2009, Physics, Formation and Evolution of Rotating Stars

Maeder A., Mermilliod J. C., 1981, A&A, 93, 136

Maeder A., Meynet G., 1987, A&A, 182, 243

Maeder A., Meynet G., 1988, A&AS, 76, 411

Maeder A., Meynet G., 1989, A&A, 210, 155

Maeder A., Meynet G., 1994, A&A, 287, 803

Maeder A., Meynet G., 2000, ARA&A, 38, 143

Maeder A., Meynet G., 2001, A&A, 373, 555

Maeder A., Meynet G., Ekström S., Georgy C., 2009, Communications in Asteroseismology, 158, 72

Maguire K., et al., 2010, MNRAS, 403, L11

Maguire K., et al., 2012, MNRAS, 426, 2359

Mapelli M., et al., 2020, ApJ, 888, 76

Marchant P., Moriya T. J., 2020, A&A, 640, L18

Marchant P., et al., 2019, ApJ, 882, 36

Margolin L. G., Rider W. J., Grinstein F. F., 2006, Journal of Turbulence, 7, 15

Marigo P., Girardi L., Chiosi C., Wood P. R., 2001, A&A, 371, 152

Martinet S., et al., 2021, A&A, 648, A126

Martins F., Palacios A., 2013, A&A, 560, A16

Martins F., Palacios A., 2021, A&A, 645, A67

Martins F., Depagne E., Russeil D., Mahy L., 2013, A&A, 554, A23

Mason B. D., et al., 2009, AJ, 137, 3358

Massey P., Olsen K. A. G., 2003, AJ, 126, 2867

Massey P., et al., 2021, AJ, 161, 79

Mauerhan J., Smith N., 2012, MNRAS, 424, 2659

Maund J. R., 2019, ApJ, 883, 86

Maund J. R., et al., 2011, ApJ, 739, L37

Maund J. R., et al., 2015, MNRAS, 447, 3207

Maury A. C., Pickering E. C., 1897, Annals of Harvard College Observatory, 28, 1

McClintock J. E., Remillard R. A., 2006, Black hole binaries. pp 157–213

McCray R., Fransson C., 2016, ARA&A, 54, 19

McDonald S. L. E., Davies B., Beasor E. R., 2021, MNRAS, 0

McLaughlin D. B., 1950, ApJ, 111, 449

Meakin C. A., Arnett D., 2007, ApJ, 667, 448

Meilland A., 2017. p. 163

Menon A., Heger A., 2017, MNRAS, 469, 4649

Mestel L., 1953, MNRAS, 113, 716

Meylan G., Maeder A., 1983, A&A, 124, 84

Meynet G., Maeder A., 2000, A&A, 361, 101

Meynet G., et al., 1994, A&AS, 103, 97

Meynet G., Eggenberger P., Maeder A., 2011, A&A, 525, L11

Meynet G., et al., 2015a, A&A, 575, A60

Meynet G., Kudritzki R.-P., Georgy C., 2015b, A&A, 581, A36

Miller M. C., Hamilton D. P., 2002, MNRAS, 330, 232

Minkowski R., 1941, PASP, 53, 224

Minkowski R., 1964, ARA&A, 2, 247

Modjaz M., et al., 2008, AJ, 135, 1136

Moe M., Di Stefano R., 2017, ApJS, 230, 15

Monpribat E., et al., 2021, arXiv e-prints, 0, arXiv:2111.15224

Morel T., et al., 2015. pp 342–347, doi:10.1017/S1743921314007054

Moriya T. J., 2021, MNRAS, 503, L28

Moriya T. J., et al., 2014, MNRAS, 439, 2917

Morozova V., et al., 2015, ApJ, 814, 63

Morozova V., Piro A. L., Valenti S., 2018, ApJ, 858, 15

Morris M., 1987, PASP, 99, 1115

Morse J. A., et al., 1998, AJ, 116, 2443

Morton D. C., 1967a, ApJ, 147, 1017

Morton D. C., 1967b, ApJ, 150, 535

Motte F., Bontemps S., Louvet F., 2018, ARA&A, 56, 41

Muijres L. E., et al., 2012, A&A, 537, A37

Müller B., Heger A., Liptai D., Cameron J. B., 2016, MNRAS, 460, 742

Munari U., et al., 2002, A&A, 389, L51

Murphy L. J., et al., 2021, MNRAS, 501, 2745

Neugebauer M., Snyder C. W., 1962, Science, 138, 1095

Neugent K. F., 2021, ApJ, 908, 87

Neugent K. F., Massey P., 2011, ApJ, 733, 123

Neugent K. F., Massey P., 2014, ApJ, 789, 10

Neugent K. F., et al., 2010, ApJ, 719, 1784

Neugent K. F., Massey P., Skiff B., Meynet G., 2012a, ApJ, 749, 177

Neugent K. F., Massey P., Georgy C., 2012b, ApJ, 759, 11

Neugent K. F., Levesque E. M., Massey P., 2018, AJ, 156, 225

Neugent K. F., Levesque E. M., Massey P., Morrell N. I., 2019, ApJ, 875, 124

Neugent K. F., et al., 2020, ApJ, 900, 118

Nieuwenhuijzen H., et al., 2012, A&A, 546, A105

Nomoto K., et al., 1993, Nature, 364, 507

Nugis T., Lamers H. J. G. L. M., 2000, A&A, 360, 227

Ober W. W., El Eid M. F., Fricke K. J., 1983, A&A, 119, 61

Oda T., et al., 1994, Atomic Data and Nuclear Data Tables, 56, 231

Ofek E. O., et al., 2014, ApJ, 789, 104

Oke J. B., Schwarzschild M., 1952, ApJ, 116, 317

Owocki S. P., 2015. p. 113, doi:10.1007/978-3-319-09596-7_5

Paczyński B., 1966, Acta Astron., 16, 231

Paczyński B., 1967a, Acta Astron., 17, 1

Paczyński B., 1967b, Acta Astron., 17, 193

Paczyński B., 1969, Acta Astron., 19, 1

Paczyński B., 1971, Acta Astron., 21, 1

Paczyński B., Ziółkowski J., 1967, Acta Astron., 17, 7

Pastorello A., et al., 2007, Nature, 447, 829

Pastorello A., et al., 2010, ApJ, 724, L16

Patterson J. R., Winkler H., Zaidins C. S., 1969, ApJ, 157, 367

Paxton B., et al., 2011, ApJS, 192, 3

Paxton B., et al., 2013, ApJS, 208, 4

Paxton B., et al., 2015, ApJS, 220, 15

Paxton B., et al., 2018, ApJS, 234, 34

Paxton B., et al., 2019, ApJS, 243, 10

Pedersen M. G., et al., 2021, Nature Astronomy, 5, 715

Perrin J., 1922, L'Astronomie, 36, 49

Peters G. J., et al., 2013, ApJ, 765, 2

Petrovic J., Langer N., van der Hucht K. A., 2005, A&A, 435, 1013

Podsiadlowski P., Joss P. C., Hsu J. J. L., 1992, ApJ, 391, 246

Podsiadlowski P., Hsu J. J. L., Joss P. C., Ross R. R., 1993, Nature, 364, 509

Pols O. R., Tout C. A., Eggleton P. P., Han Z., 1995, MNRAS, 274, 964

Pols O. R., et al., 1998, MNRAS, 298, 525

Portegies Zwart S. F., McMillan S. L. W., 2000, ApJ, 528, L17

Portegies Zwart S. F., van den Heuvel E. P. J., 2016, MNRAS, 456, 3401

Porter J. M., Rivinius T., 2003, PASP, 115, 1153

Potekhin A. Y., Chabrier G., 2010, Contributions to Plasma Physics, 50, 82

Prentice S. J., et al., 2021, MNRAS, 508, 4342

Puls J., Vink J. S., Najarro F., 2008, A&A Rev., 16, 209

Rakavy G., Shaviv G., Zinamon Z., 1967, ApJ, 150, 131

Ramachandran V., et al., 2019, A&A, 625, A104

Ramírez-Agudelo O. H., et al., 2013, A&A, 560, A29

Ramírez-Agudelo O. H., et al., 2015, A&A, 580, A92

Reiz A., Otzen Petersen J., 1964, Astrophysica Norvegica, 9, 214

Ren Y., et al., 2021, ApJ, 907, 18

Renzini A., Greggio L., Ritossa C., Ferrario L., 1992, ApJ, 400, 280

Renzo M., Ott C. D., Shore S. N., de Mink S. E., 2017, A&A, 603, A118

Renzo M., et al., 2019, A&A, 624, A66

Renzo M., et al., 2020a, MNRAS, 493, 4333

Renzo M., et al., 2020b, A&A, 640, A56

Riess A. G., et al., 1998, AJ, 116, 1009

Riess A. G., et al., 2011, ApJ, 730, 119

Ritossa C., 1996, MNRAS, 281, 970

Ritter C., et al., 2018, MNRAS, 480, 538

Rivinius T., Carciofi A. C., Martayan C., 2013, A&A Rev., 21, 69

Robertson J. W., 1971, ApJ, 164, L105

Rodriguez C. L., et al., 2016, ApJ, 832, L2

Rodriguez C. L., et al., 2019, Phys. Rev. D, 100, 043027

Rogers F. J., Nayfonov A., 2002, ApJ, 576, 1064

Romero-Shaw I., Lasky P. D., Thrane E., Calderón Bustillo J., 2020, ApJ, 903, L5

Rosenberg H., 1910, Astronomische Nachrichten, 186, 71

Rublev S. V., 1965, AZh, 42, 347

Ruderman M. A., Sutherland P. G., 1975, ApJ, 196, 51

Russell H. N., 1914a, Popular Astronomy, 22, 275

Russell H. N., 1914b, The Observatory, 37, 165

Russell H. N., 1925, Nature, 116, 209

Sakashita S., Ôno Y., Hayashi C., 1959, Progress of Theoretical Physics, 21, 315

Sakstein J., et al., 2020, Phys. Rev. Lett., 125, 261105

Salaris M., et al., 1997, ApJ, 486, 413

Salasnich B., Bressan A., Chiosi C., 1999, A&A, 342, 131

Salpeter E. E., 1952, ApJ, 115, 326

Salpeter E. E., 1955, ApJ, 121, 161

Sana H., et al., 2012, Science, 337, 444

Sana H., et al., 2013, A&A, 550, A107

Sandage A. R., Eggen O. J., 1959, MNRAS, 119, 278

Sandage A. R., Schwarzschild M., 1952, ApJ, 116, 463

Sander A. A. C., Vink J. S., Hamann W. R., 2020, MNRAS, 491, 4406

Saslaw W. C., Schwarzschild M., 1965, ApJ, 142, 1468

Saumon D., Chabrier G., van Horn H. M., 1995, ApJS, 99, 713

Savaglio S., Glazebrook K., Le Borgne D., 2009, ApJ, 691, 182

Scalo J. M., 1986, Fund. Cosmic Phys., 11, 1

Schaerer D., 1996, A&A, 309, 129

Schaerer D., de Koter A., Schmutz W., Maeder A., 1996, A&A, 310, 837

Schaller G., Schaerer D., Meynet G., Maeder A., 1992, A&AS, 96, 269

Schlesinger B. M., 1977, ApJ, 212, 507

Schneider F. R. N., et al., 2014, ApJ, 780, 117

Schneider F. R. N., et al., 2016, MNRAS, 457, 2355

Schneider F. R. N., et al., 2019, Nature, 574, 211

Schönberg M., Chandrasekhar S., 1942, ApJ, 96, 161

Schootemeijer A., Langer N., 2018, A&A, 611, A75

Schootemeijer A., Langer N., Grin N. J., Wang C., 2019, A&A, 625, A132

Schultz W. C., Bildsten L., Jiang Y.-F., 2021, arXiv e-prints, 0, arXiv:2110.13944

Schulze S., et al., 2018, MNRAS, 473, 1258

Schwarzschild M., 1958, Structure and evolution of the stars.

Schwarzschild M., 1961, ApJ, 134, 1

Schwarzschild M., Härm R., 1958, ApJ, 128, 348

Schwarzschild M., Howard R., Härm R., 1957, ApJ, 125, 233

Scott L. J. A., et al., 2021, MNRAS, 503, 4208

Shaviv G., Salpeter E. E., 1973, ApJ, 184, 191

Shen Y. P., et al., 2020, Phys. Rev. Lett., 124, 162701

Shenar T., et al., 2016, A&A, 591, A22

Shultz M. E., et al., 2018, MNRAS, 475, 5144

Sigurdsson S., Hernquist L., 1993, Nature, 364, 423

Sikora J., Wade G. A., Power J., Neiner C., 2019a, MNRAS, 483, 2300

Sikora J., Wade G. A., Power J., Neiner C., 2019b, MNRAS, 483, 3127

Smartt S. J., 2009, ARA&A, 47, 63

Smartt S. J., 2015, PASA, 32, e016

Smartt S. J., et al., 2004, Science, 303, 499

Smartt S. J., Eldridge J. J., Crockett R. M., Maund J. R., 2009, MNRAS, 395, 1409

Smith N., 2007, AJ, 133, 1034

Smith N., 2013, MNRAS, 429, 2366

Smith N., 2014, ARA&A, 52, 487

Smith N., 2019, MNRAS, 489, 4378

Smith N., Frew D. J., 2011, MNRAS, 415, 2009

Smith N., Owocki S. P., 2006, ApJ, 645, L45

Smith N., Vink J. S., de Koter A., 2004, ApJ, 615, 475

Smith R. J., et al., 2011, MNRAS, 414, 3633

Smith B. D., et al., 2015, MNRAS, 452, 2822

Smith N., Groh J. H., France K., McCray R., 2017, MNRAS, 468, 2333

Soderberg A. M., et al., 2012, ApJ, 752, 78

Song H. F., et al., 2016, A&A, 585, A120

Sota A., et al., 2011, ApJS, 193, 24

Sota A., et al., 2014, ApJS, 211, 10

Spera M., Mapelli M., 2017, MNRAS, 470, 4739

Spera M., et al., 2019, MNRAS, 485, 889

Spillane T., et al., 2007, Phys. Rev. Lett., 98, 122501

Spruit H. C., 2002, A&A, 381, 923

Sreenivasan S. R., Wilson W. J. F., 1985, ApJ, 290, 653

Stancliffe R. J., Eldridge J. J., 2009, MNRAS, 396, 1699

Stancliffe R. J., Chieffi A., Lattanzio J. C., Church R. P., 2009, PASA, 26, 203

Stanway E. R., Eldridge J. J., Becker G. D., 2016, MNRAS, 456, 485

Stark D. P., 2016, ARA&A, 54, 761

Steiner J. E., Oliveira A. S., 2005, A&A, 444, 895

Stencel R. E., et al., 1984, ApJ, 281, 751

Stevenson S., et al., 2019, ApJ, 882, 121

Stobie R. S., 1969a, MNRAS, 144, 485

Stobie R. S., 1969b, MNRAS, 144, 511

Stothers R., 1963, ApJ, 138, 1074

Stothers R., 1964, ApJ, 140, 510

Stothers R., 1966, ApJ, 143, 91

Stothers R., 1970, MNRAS, 151, 65

Stothers R., 1974, ApJ, 194, 699

Stothers R. B., 1991, ApJ, 383, 820

Stothers R., Chin C.-W., 1968, ApJ, 152, 225

Stothers R., Chin C.-W., 1973, ApJ, 179, 555

Stothers R., Chin C. W., 1975, ApJ, 198, 407

Stothers R., Chin C. W., 1976, ApJ, 204, 472

Stothers R., Chin C. W., 1979, ApJ, 233, 267

Stothers R. B., Chin C. W., 1985, ApJ, 292, 222

Stothers R. B., Chin C.-W., 1995, ApJ, 440, 297

Stothers R. B., Chin C.-w., 2001, ApJ, 560, 934

Straniero O., Domínguez I., Imbriani G., Piersanti L., 2003, ApJ, 583, 878

Sturrock P. A., 1971, ApJ, 164, 529

Sugimoto D., Fujimoto M. Y., 2000, ApJ, 538, 837

Sukhbold T., Adams S., 2020, MNRAS, 492, 2578

Sukhbold T., et al., 2016, ApJ, 821, 38

Sukhbold T., Woosley S. E., Heger A., 2018, ApJ, 860, 93

Sweet P. A., 1950, MNRAS, 110, 548

Szécsi D., et al., 2015, A&A, 581, A15

Tan J. C., et al., 2014. p. 149, doi:10.2458/azu_uapress_9780816531240-ch007

Tanikawa A., et al., 2021, ApJ, 910, 30

Tanvir N. R., et al., 2009, Nature, 461, 1254

Tauris T. M., Takens R. J., 1998, A&A, 330, 1047

Tayler R. J., 1954, ApJ, 120, 332

Team COMPAS: J. Riley T., et al., 2022, The Journal of Open Source Software, 7, 3838

Thackeray A. D., 1950, MNRAS, 110, 343

The LIGO Scientific Collaboration et al., 2021a, arXiv e-prints, 0, arXiv:2107.03701

The LIGO Scientific Collaboration et al., 2021b, arXiv e-prints, 0, arXiv:2107.13796

The LIGO Scientific Collaboration et al., 2021c, arXiv e-prints, 0, arXiv:2111.03606

The LIGO Scientific Collaboration et al., 2021d, arXiv e-prints, 0, arXiv:2111.03634

Thielemann F.-K., Nomoto K., Hashimoto M.-A., 1996, ApJ, 460, 408

Timmes F. X., Swesty F. D., 2000, ApJS, 126, 501

Tolstoy E., Hill V., Tosi M., 2009, ARA&A, 47, 371

Tout C. A., Pols O. R., Eggleton P. P., Han Z., 1996, MNRAS, 281, 257

Tout C. A., Aarseth S. J., Pols O. R., Eggleton P. P., 1997, MNRAS, 291, 732

Troland T. H., Crutcher R. M., 2008, ApJ, 680, 457

Trundle C., Lennon D. J., 2005, A&A, 434, 677

Trundle C., Lennon D. J., Puls J., Dufton P. L., 2004, A&A, 417, 217

Tur C., Heger A., Austin S. M., 2007, ApJ, 671, 821

Tylenda R., et al., 2011, A&A, 528, A114

U V., et al., 2009, ApJ, 704, 1120

Ud-Doula A., Owocki S. P., Townsend R. H. D., 2009, MNRAS, 392, 1022

Ugliano M., Janka H.-T., Marek A., Arcones A., 2012, ApJ, 757, 69

Ulrich R. K., Burger H. L., 1976, ApJ, 206, 509

Umeda H., Nomoto K., 2002, ApJ, 565, 385

Urbaneja M. A., et al., 2005, ApJ, 622, 862

Urbaneja M. A., et al., 2008, ApJ, 684, 118

Vamvatira-Nakou C., et al., 2015, A&A, 578, A108

Van Dyk S. D., 2017, Philosophical Transactions of the Royal Society of London Series A, 375, 20160277

Van Dyk S. D., et al., 2013, ApJ, 772, L32

Vanbeveren D., De Loore C., Van Rensbergen W., 1998, A&A Rev., 9, 63

Vanbeveren D., Van Bever J., Belkus H., 2007, ApJ, 662, L107

Vazdekis A., et al., 2010, MNRAS, 404, 1639

Vidotto A. A., et al., 2013, A&A, 557, A67

Villante F. L., Serenelli A., 2021, Frontiers in Astronomy and Space Sciences, 7, 112

Villebrun F., et al., 2019, A&A, 622, A72

Vink J. S., Sander A. A. C., 2021, MNRAS, 504, 2051

Vink J. S., de Koter A., 2002, A&A, 393, 543

Vink J. S., de Koter A., Lamers H. J. G. L. M., 2001, A&A, 369, 574

Vink J. S., et al., 2011, A&A, 531, A132

Vinter Hansen J. M., 1944, ApJ, 100, 8

Vogelsberger M., et al., 2014, Nature, 509, 177

Wade G. A., et al., 2014. pp 265–269, doi:10.1017/S1743921314002233

Wade G. A., et al., 2016, MNRAS, 456, 2

Walborn N. R., Fitzpatrick E. L., 2000, PASP, 112, 50

Walmswell J. J., Eldridge J. J., 2012, MNRAS, 419, 2054

Walmswell J. J., Tout C. A., Eldridge J. J., 2015, MNRAS, 447, 2951

Wang L., Gies D. R., Peters G. J., 2017, ApJ, 843, 60

Wang C., et al., 2020, ApJ, 888, L12

Wang T., et al., 2021, ApJ, 912, 112

Weaver T. A., Woosley S. E., 1993, Phys. Rep., 227, 65

Weaver R., et al., 1977, ApJ, 218, 377

Weber E. J., Davis Leverett J., 1967, ApJ, 148, 217

Webster B. L., Murdin P., 1972, Nature, 235, 37

Weiss A., 1989, ApJ, 339, 365

West C., Heger A., Austin S. M., 2013, ApJ, 769, 2

Whalen D. J., et al., 2013, ApJ, 762, L6

Wheelwright H. E., de Wit W. J., Oudmaijer R. D., Vink J. S., 2012a, A&A, 538, A6

Wheelwright H. E., et al., 2012b, A&A, 543, A77

Windhorst R. A., et al., 2018, ApJS, 234, 41

Wise J. H., et al., 2014, MNRAS, 442, 2560

Wolf C. J. E., Rayet G., 1867, Academie des Sciences Paris Comptes Rendus, 65, 292

Woosley S. E., 2010, ApJ, 719, L204

Woosley S. E., 2017, ApJ, 836, 244

Woosley S. E., 2019, ApJ, 878, 49

Woosley S. E., Heger A., 2007, Phys. Rep., 442, 269

Woosley S. E., Weaver T. A., 1986, ARA&A, 24, 205

Woosley S. E., Weaver T. A., 1994, ApJ, 423, 371

Woosley S. E., Weaver T. A., 1995, ApJS, 101, 181

Woosley S. E., Heger A., Weaver T. A., 2002, Reviews of Modern Physics, 74, 1015

Worthey G., Lee H.-c., 2011, ApJS, 193, 1

Wright K. O., 1970, Vistas in Astronomy, 12, 147

Yahil A., van den Horn L., 1985, ApJ, 296, 554

Yaron O., et al., 2017, Nature Physics, 13, 510

Yoon S.-C., 2015, PASA, 32, e015

Yoon S.-C., Cantiello M., 2010, ApJ, 717, L62

Yoon S. C., Langer N., 2005, A&A, 443, 643

Yoon S. C., Langer N., Norman C., 2006, A&A, 460, 199

Yoon S. C., Woosley S. E., Langer N., 2010, ApJ, 725, 940

Yoon S. C., Dierks A., Langer N., 2012, A&A, 542, A113

Yoon S.-C., Dessart L., Clocchiatti A., 2017, ApJ, 840, 10

Zapartas E., et al., 2017, A&A, 601, A29

Zapartas E., et al., 2019, A&A, 631, A5

Zhevakin S. A., 1963, ARA&A, 1, 367

de Groot M., 1988, Irish Astronomical Journal, 18, 163

de Jager C., Nieuwenhuijzen H., van der Hucht K. A., 1988, A&AS, 72, 259

de Koter A., Heap S. R., Hubeny I., 1997, ApJ, 477, 792

de Mink S. E., Belczynski K., 2015, ApJ, 814, 58

de Mink S. E., Pols O. R., Hilditch R. W., 2007, A&A, 467, 1181

de Mink S. E., et al., 2009a, A&A, 497, 243

de Mink S. E., Pols O. R., Langer N., Izzard R. G., 2009b, A&A, 507, L1

de Mink S. E., et al., 2013, ApJ, 764, 166

de Mink S. E., et al., 2014, ApJ, 782, 7

deBoer R. J., et al., 2017, Reviews of Modern Physics, 89, 035007

van Bever J., Vanbeveren D., 1998, A&A, 334, 21

van Genderen A. M., 2001, A&A, 366, 508

van Loon J. T., Cioni M. R. L., Zijlstra A. A., Loup C., 2005, A&A, 438, 273

van Son L. A. C., et al., 2020, ApJ, 897, 100

von Weizsacker C. F., 1938, Phys. Zs., 39

Chapter 10

Appendices

10.1 Core and Envelope Masses for Core-H Burning Models

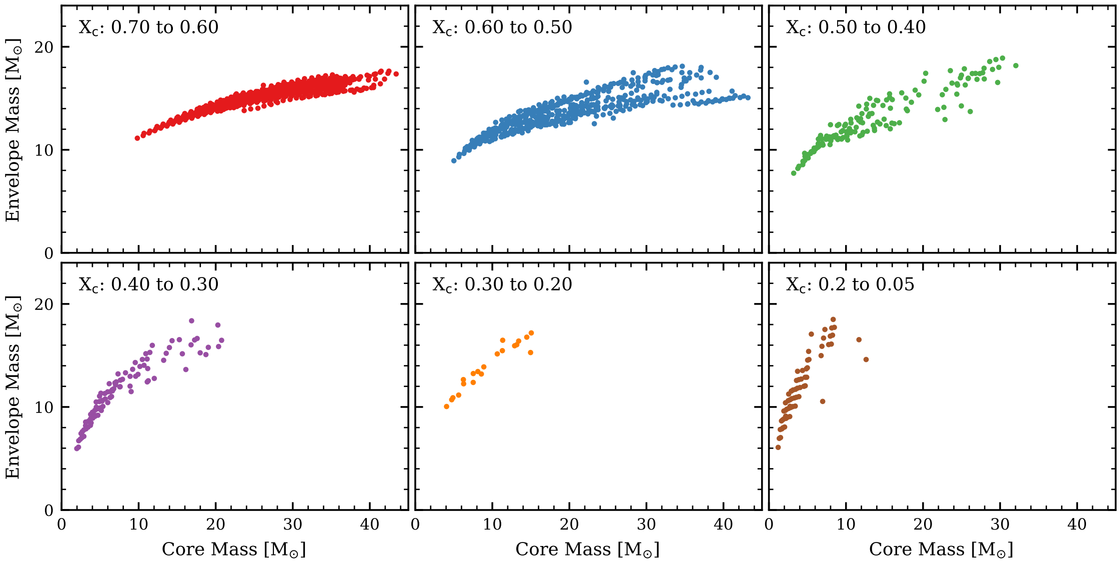

Figure 75: Summary of the 3 key structural parameters (convective core mass, envelope mass and core composition) for each of our core-H burning structure models. Each dot represents an individual core-H burning stellar structure model with the given core mass and envelope mass in $M_\odot$. The models are divided up into bins by their central H mass fraction (X_c) as indicated in each plot.

10.2 Core and Envelope Masses for Core-He Burning Models

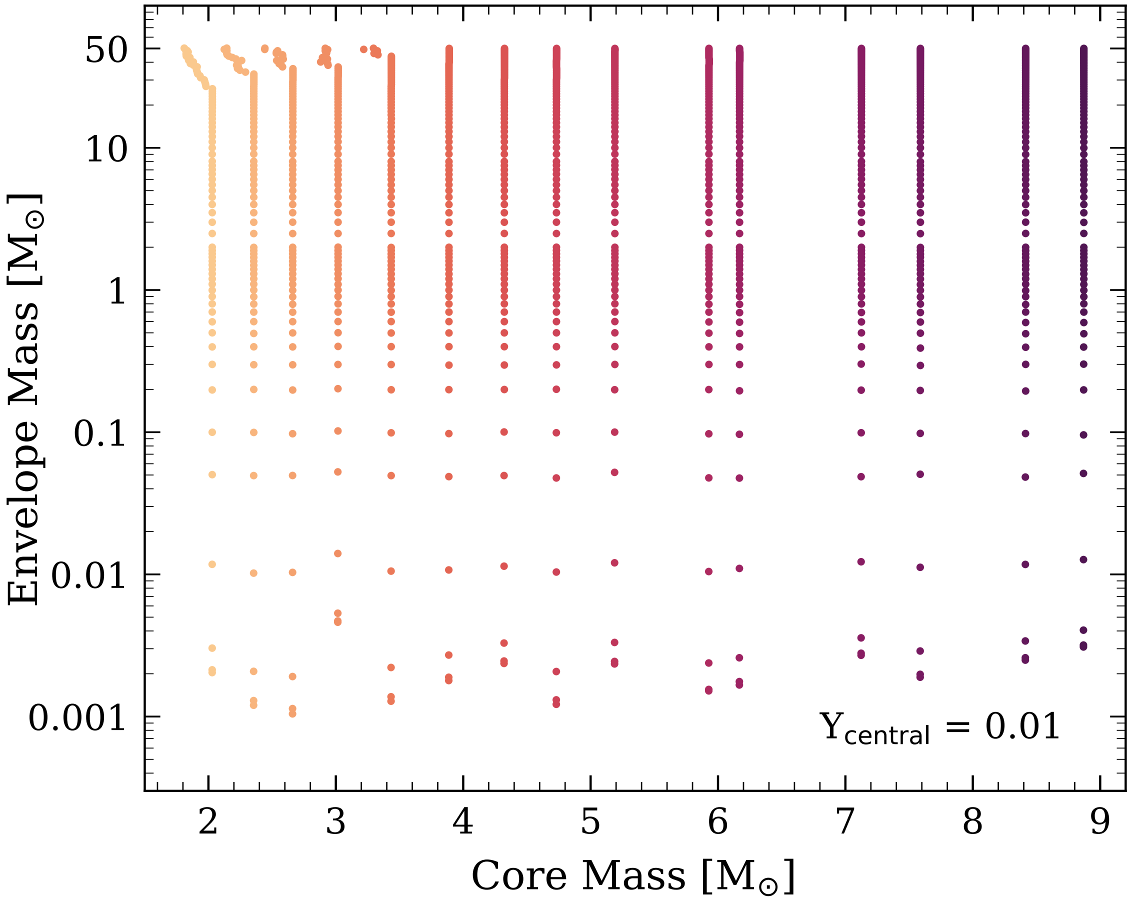

Figure 76: Each dot represents a core-He burning structure, similar to Fig. 17. but with with $Y_c = 0.01$

10.3 Central Temperature vs. Core mass ratio

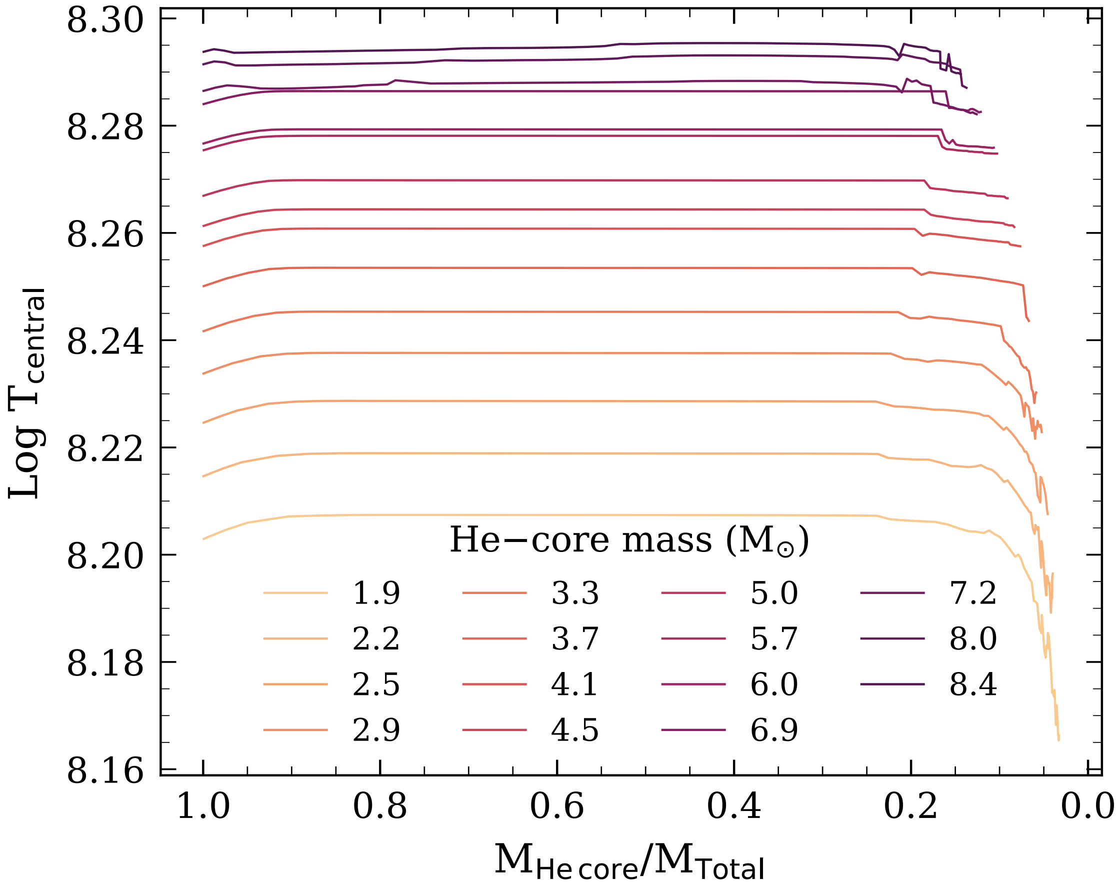

Figure 77: The central temperature as a function of envelope mass for core-He burning models of constant core mass. For most combinations of core and envelope masses, the central temperature of the core is not affected by the mass of the envelope.

10.4 Surface properties for core-He burning models

Table 10.1: Summary of surface properties for core-He burning models with a He-core mass of $4.1\mathrm{M}_\odot$, a central Helium abundance of 0.50 and envelope masses from $10^{-3} - 25\mathrm{M}_\odot$. $F_{\mathrm{H-shell}}$ refers to the fraction of the total nuclear energy generated in the H-Shell. The same table for envelope masses from $25 - 50\mathrm{M}_\odot$ can be found below in Table 10.2.

M_{core} [$\mathrm{M}_\odot$]	M_{env} [$\mathrm{M}_\odot$]	$\log T_{\mathrm{eff}}$ [K]	T_{eff} [K]	$\log \mathrm{L}/\mathrm{L}_\odot$	$\log g$	$\log \mathrm{R}/\mathrm{R}_\odot$	$F_{\mathrm{H-shell}}$
4.1	2×10^{-3}	4.96	91700	4.37	5.48	-0.21	0.00
4.1	4×10^{-3}	4.96	91700	4.37	5.48	-0.21	0.00
4.1	0.01	4.96	91750	4.38	5.48	-0.21	0.00
4.1	0.05	4.96	91680	4.39	5.48	-0.21	0.00
4.1	0.1	4.95	88160	4.40	5.40	-0.17	0.00
4.1	0.2	4.88	75700	4.43	5.11	-0.02	0.00
4.1	0.3	4.84	68800	4.46	4.93	0.08	0.03
4.1	0.4	4.62	41630	4.50	4.03	0.53	0.10
4.1	0.5	4.45	28000	4.53	3.32	0.89	0.17
4.1	0.6	4.26	18010	4.55	2.54	1.29	0.22
4.1	0.7	3.96	9200	4.56	1.37	1.88	0.24
4.1	0.8	3.62	4150	4.57	-0.01	2.57	0.26
4.1	0.9	3.57	3690	4.57	-0.21	2.67	0.26
4.1	1.0	3.55	3580	4.57	-0.26	2.70	0.26
4.1	1.1	3.55	3520	4.57	-0.28	2.72	0.27
4.1	1.2	3.54	3480	4.57	-0.29	2.73	0.27
4.1	1.3	3.54	3460	4.58	-0.29	2.73	0.27
4.1	1.4	3.54	3440	4.58	-0.30	2.74	0.27
4.1	1.5	3.53	3420	4.58	-0.30	2.74	0.28
4.1	1.6	3.53	3410	4.58	-0.30	2.75	0.28
4.1	1.7	3.53	3400	4.58	-0.29	2.75	0.28
4.1	1.8	3.53	3400	4.58	-0.29	2.75	0.28
4.1	1.9	3.53	3390	4.58	-0.29	2.75	0.28
4.1	2.0	3.53	3390	4.58	-0.28	2.76	0.28
4.1	2.5	3.53	3380	4.58	-0.26	2.76	0.29
4.1	3.0	3.53	3380	4.59	-0.23	2.76	0.29
4.1	3.5	3.53	3390	4.59	-0.19	2.76	0.29
4.1	4.0	3.53	3400	4.59	-0.16	2.76	0.30
4.1	4.5	3.53	3410	4.59	-0.13	2.75	0.30
4.1	5.0	3.53	3430	4.59	-0.10	2.75	0.30
4.1	5.5	3.54	3440	4.59	-0.07	2.75	0.30
4.1	6.0	3.54	3460	4.59	-0.04	2.74	0.30
4.1	6.5	3.54	3470	4.59	-0.01	2.74	0.31
4.1	7.0	3.54	3490	4.59	0.02	2.73	0.31
4.1	7.5	3.54	3510	4.60	0.04	2.73	0.31
4.1	8.0	3.55	3520	4.60	0.07	2.73	0.31
4.1	9.0	3.55	3550	4.60	0.12	2.72	0.31
4.1	10.0	3.55	3590	4.60	0.16	2.71	0.32
4.1	11.0	3.56	3620	4.60	0.21	2.71	0.32
4.1	12.0	3.56	3650	4.60	0.25	2.70	0.32
4.1	13.0	3.57	3680	4.60	0.29	2.69	0.32
4.1	14.0	3.57	3700	4.60	0.32	2.69	0.33
4.1	15.0	3.57	3730	4.61	0.36	2.68	0.33
4.1	16.0	3.58	3760	4.61	0.39	2.68	0.33
4.1	17.0	3.58	3800	4.61	0.42	2.67	0.34
4.1	18.0	4.29	19620	5.04	2.87	1.46	0.75
4.1	19.0	4.32	20770	5.09	2.94	1.43	0.77
4.1	20.0	4.33	21490	5.12	2.98	1.42	0.79
4.1	21.0	4.34	22080	5.15	3.02	1.41	0.80
4.1	22.0	4.36	22710	5.18	3.05	1.40	0.82
4.1	23.0	4.37	23270	5.21	3.08	1.39	0.84
4.1	24.0	4.38	23740	5.24	3.11	1.39	0.84
4.1	25.0	4.38	24260	5.26	3.13	1.39	0.85

Table 10.2: Same as Table 10.1 but for envelope masses from $25-50\mathrm{M}_\odot$.

M_{core} [$\mathrm{M}_\odot$]	M_{env} [$\mathrm{M}_\odot$]	$\log T_{\mathrm{eff}}$ [K]	T_{eff} [K]	$\log \mathrm{L}/\mathrm{L}_\odot$	$\log g$	$\log \mathrm{R}/\mathrm{R}_\odot$	$F_{\mathrm{H-shell}}$
4.1	26.0	4.39	24760	5.29	3.15	1.38	0.86
4.1	27.0	4.40	25230	5.32	3.18	1.38	0.87
4.1	28.0	4.41	25690	5.34	3.20	1.37	0.88
4.1	29.0	4.42	26120	5.36	3.22	1.37	0.89
4.1	30.0	4.42	26530	5.39	3.23	1.37	0.89
4.1	31.0	4.43	26940	5.41	3.25	1.37	0.90
4.1	32.0	4.44	27320	5.43	3.27	1.37	0.90
4.1	33.0	4.44	27690	5.45	3.28	1.36	0.91
4.1	34.0	4.45	28050	5.47	3.29	1.36	0.91
4.1	35.0	4.45	28400	5.49	3.31	1.36	0.92
4.1	36.0	4.46	28730	5.51	3.32	1.36	0.92
4.1	37.0	4.46	29060	5.53	3.33	1.36	0.92
4.1	38.0	4.47	29380	5.55	3.34	1.36	0.93
4.1	39.0	4.47	29680	5.57	3.35	1.36	0.93
4.1	40.0	4.48	29970	5.58	3.36	1.36	0.93
4.1	41.0	4.48	30250	5.60	3.37	1.36	0.93
4.1	42.0	4.48	30520	5.62	3.38	1.36	0.94
4.1	43.0	4.49	30940	5.63	3.40	1.36	0.94
4.1	44.0	4.49	31200	5.65	3.40	1.36	0.94
4.1	45.0	4.50	31450	5.66	3.41	1.36	0.95
4.1	46.0	4.50	31690	5.68	3.42	1.36	0.95
4.1	47.0	4.50	31930	5.69	3.42	1.36	0.95
4.1	48.0	4.51	32150	5.71	3.43	1.36	0.95
4.1	49.0	4.51	32370	5.72	3.44	1.36	0.95
4.1	50.0	4.51	32590	5.73	3.44	1.36	0.95